

A Precision Top Quark Mass Measurement with a Profile Likelihood Nuisance Fit

Dissertation zur Erlangung des Doktorgrades
an der Fakultät für Mathematik, Informatik und
Naturwissenschaften
Fachbereich Physik der Universität Hamburg

vorgelegt von

Christoph Andreas Garbers

Hamburg
2022

Gutachter der Dissertation:	Prof. Dr. Peter Schleper PD Dr. Andreas B. Meyer
Zusammensetzung der Prüfungskommission:	Dr. Hannes Jung PD Dr. Andreas B. Meyer Prof. Dr. Sven-Olaf Moch Prof. Dr. Arwen Pearson Prof. Dr. Peter Schleper
Vorsitzende der Prüfungskommission:	Prof. Dr. Sven-Olaf Moch
Datum der Disputation:	20.07.2022
Vorsitzender des Fach-Promotionsausschusses PHYSIK:	Prof. Dr. Wolfgang J. Parak
Leiter des Fachbereichs PHYSIK:	Prof. Dr. Günter H. W. Sigl
Dekan der Fakultät MIN:	Prof. Dr. Heinrich Graener

Abstract

In this thesis a measurement of the top quark mass in the lepton+jets final state at $\sqrt{s} = 13\text{ TeV}$ using 36 fb^{-1} of proton-proton collision data taken with the CMS detector in 2016. Events with one muon or one electron and four jets are selected. Two of the jets are identified as originating from a bottom quark. The events are further constrained by a fit of their kinematics to a top-antitop hypotheses. In difference to former analyses, uncertainties are included as nuisance parameters in a likelihood fit. Five observables are used simultaneously to reduce the impact of systematic uncertainties in the selected phase-space. The observables are the invariant masses of the top quark candidate after a kinematic fit, the reconstructed W boson and the lepton-b-jet system, split into two categories, as well as the transverse momentum ratios of bottom-flavored to light-quark-flavored jets. A model for a profile likelihood to measure the quark mass is presented. The top quark mass is measured to be $171.77 \pm 0.38\text{ GeV}$. The central values is consistent with former analyses. At the time of publishing this result is the most precise top quark mass measurement.

Kurzfassung

In dieser Arbeit wird eine Topquarkmassenmessung auf 36 fb^{-1} Lepton+Jets Daten, die 2016 aus $\sqrt{s} = 13\text{ TeV}$ Proton-Proton-Kollisionen mit dem CMS-Detektor aufgenommen wurden, präsentiert. Kollisionsereignisse mit einem Myon oder einem Elektron und vier Jets werden ausgewählt. Zwei dieser Jets können Bottomquarkzerfällen zugeordnet werden. Die Ereignisse und ihre Kinematik werden mit einer Minimierung an eine Topquarkpaarhypothese weiter eingeschränkt. Im Unterschied zu vorigen Analysen werden Unsicherheiten als zusätzliche Parameter in die Likelihoodparametrisierung eingefügt. Es werden fünf Observable benutzt, um den Einfluss von systematischen Unsicherheiten weiter zu verringern. Die Observablen sind die invariante Masse des Topquarkkandidaten nach der Minimierung der Kinematik, des W -Bosons und des Lepton-b-Jet Systems, das in zwei Kategorien unterteilt wird, sowie das Verhältnis des Transversalimpulses von b-Jets zu Jets aus leichteren Quarkzerfällen. Die Topquarkmasse $m_t = 171.77 \pm 0.38\text{ GeV}$ wurde gemessen. Dieses Ergebnis ist zur Zeit die präziseste Messung der Topquarkmasse und vereinbar mit vorherigen Analysen.

Contents

1. Introduction	1
1.1. Unit convention	2
2. Theoretical overview	3
2.1. The Standard Model of particle physics	3
2.1.1. Gauge Theory	6
2.1.2. Quantum Chromodynamics	6
2.1.3. Electroweak Interaction	7
2.2. The top quark	9
2.2.1. Phenomenology	9
2.2.2. The top quark mass	12
2.2.3. Measurements using MC templates	14
2.2.4. Measurements from cross sections	17
2.2.5. Global interest	17
3. Experimental setup	21
3.1. The Large Hadron Collider	21
3.2. The Compact Muon Solenoid detector	23
3.2.1. CMS coordinate system	24
3.2.2. CMS components	24
4. Event generation and simulation	31
5. Event reconstruction	36
5.1. Lepton identification and reconstruction	37
5.2. Jet reconstruction	38
5.2.1. Missing transverse energy	41
6. Event selection	42
6.1. Used samples	42
6.1.1. Data samples	42
6.1.2. Simulated samples	42
6.2. Semi-leptonic event selection	49
6.2.1. Lepton selection	51
6.2.2. Jet selection	52
6.2.3. Data-simulation comparison	55

6.3. Kinematic fit	60
7. Systematic Uncertainties	67
7.1. Experimental uncertainties	67
7.2. Modeling Uncertainties	70
7.2.1. Modeling of hadronization	70
7.2.2. Modeling of the scattering process	71
7.2.3. Modeling of non-perturbative QCD effects	73
8. Methodology	74
8.1. Pseudo-experiments	74
8.2. Observables	75
8.3. Templates, nuisance parameterization and fit	83
8.3.1. Toy consistency checks of the parameterization	87
8.3.2. Double counting between FSR and JEC	95
8.3.3. Single nuisance closure	96
8.3.4. Nuisance correlation	98
9. Results of the measurement	101
9.1. Nuisance impact predictions	101
9.2. Partial unblinding	105
9.2.1. Cross-checks after partial unblinding	112
9.3. Fully unblinded results	118
9.4. Comparison to former measurements	122
10. Summary	128
10.1. Outlook	129
Appendices	131
A. Observable Correlations and Independency	132
B. Example model build and measurement	146
B.1. Example model build	146
B.2. Example fit results	147
C. Predicted and measured nuisance values and impacts for different observable selections	150
C.1. Partial unblinded impacts from single observables	150
C.2. Full nuisance impacts for different observable selections	163
D. Additional model controlplots	179
D.1. Single Nuisance Closure	179
D.2. Template variation distributions	188
E. Bibliography	218

List of Figures	234
List of Tables	239
Acknowledgments	241
Eidesstattliche Versicherung	242

1. Introduction

Particle physics explores matter and radiation on the level of the smallest known, irreducible particles and their fundamental interactions. The heaviest irreducible particle discovered to date, the top quark, was measured first at the Fermilab Tevatron in 1995 [1, 2]. Its mass (m_t) is an important parameter of the standard model of particle physics. Due to its high coupling to the Higgs boson it is an important input for global theory fits and could also be a gateway to physics beyond the standard model. The value of the top quark mass has been measured by various experiments with high precision resulting among others in the 2014 world combination of $m_t = 173.4 \pm 0.76$ [3] and the CMS Run1 legacy result of $m_t = 172.44 \pm 0.49$ [4]. With an uncertainty below 1% this is among the most precise measurements at the Large Hadron Collider (LHC). The top-quark mass is a benchmark for the performance of modern high energy physics detectors like the Compact Muon Solenoid (CMS) detector [5]. The single most precise top-quark measurement, before this analysis, was performed on $t\bar{t} \rightarrow \text{lepton} + \text{jets}$ data recorded by CMS in 2012. The result of the measurement was $m_t = 172.38 \pm 0.52$ [6].

In its 2016 run at a center-of-mass energy of $\sqrt{s} = 13$ TeV the Large Hadron Collider (LHC) delivered a luminosity of about 36 fb^{-1} of proton-proton collision data. At this center-of-mass about 30 million top quark pairs are expected to have been produced, rightfully earning the LHC the moniker "top quark factory".

In this thesis the top-quark mass will be measured from $t\bar{t} \rightarrow \text{lepton} + \text{jets}$ decays in the 2016 CMS data. A m_t measurement from the same data has already resulted in $m_t = 172.25 \pm 0.08(\text{stat}) \pm 0.62(\text{syst})$ GeV [7, 8]. It was limited by systematic uncertainties while its statistical uncertainty was nearly negligible. This thesis is going to improve this measurement even further by using a new reconstructed version of the data and new theoretical calculations. Among other improvement the simulation includes for the first time an underlying event tune derived from 13 TeV CMS data. This promises a better description of the data and especially improves the jet description that is one of the limiting factors in this analysis. As in the former analysis a final state containing a lepton, two jets from bottom quarks and two jets from light quarks are selected. Kinematic properties of the selection are fit to a top-quark mass independent $t\bar{t}$ hypothesis. The fit result is used as a further selection criteria to identify the correct jet-parton assignment. The top-quark mass distribution after the fit is the most important observable. To narrow down uncertainties further multiple additional observables are included. Used are the invariant mass of the two jets associated with the hadronic decaying W boson, the invariant mass of the lepton and the bottom quark associated with the leptonic decaying top quark and the ratio of bottom- to light-quark transverse momentum. This thesis

is the first CMS analysis in this decay channel including the later two observables. From these distributions m_t dependent templates are derived. In the former analyses the effect of systematic uncertainties was evaluated with independent ideograms. In this thesis nuisance parameters for all uncertainty sources are included in the parameterization of the likelihood instead. This is going to reduce the impact from some of the systematic uncertainty sources resulting in a considerable more precise measurement.

The analysis presented in this thesis is released as preliminary result by the CMS collaboration [9]. The work on the journal paper is still going on at the time the thesis is handed in.

1.1. Unit convention

In this thesis two different unit systems will be used. Macroscopic apertures will be described in SI units. Properties of elementary particles will be described in "natural" units, in which the reduced Planck constant $\hbar = \frac{h}{2\pi}$, the speed of light c , and the Boltzmann constant k_B are set to 1. This results in the unit eV for masses, energies and momenta and the unit eV^{-1} for length and time. For example a mass of 1 eV equals in SI units 1.78×10^{-36} kg and a length of 1 eV^{-1} equals 1.97×10^{-7} m. Also the elemental charge, which is the absolute of the charge of an electron, in SI units $e = 1.602176565 \cdot 10^{-19}$ C, is used.

2. Theoretical overview

2.1. The Standard Model of particle physics

At the core of physics is the study of matter and its movement through space and time. To not only describe but predict its behavior, various theories about the composition of matter and on the forces unflinching the motion of particles have been developed.

In modern physics, all behavior of matter is described by four fundamental forces. These are the gravitation, the electromagnetic interaction, the weak nuclear force and the strong nuclear force. The model that describes the electromagnetic, the weak and the strong force and the composition of matter in a quantum field theoretical framework is the standard model of particle physics (SM). It does not include gravity, but especially considering the measurements at the LHC, it is a very successful model. In the following a short overview of the standard model of particle physics will be presented. A more mathematical description will be given in section 2.1.1.

All fundamental particles in the SM are assumed to be point-like. For every charged particle there is an anti-particle with the same attributes except the opposite charge. Fundamental particles are categorized as fermions with a spin, in units of \hbar , of $\frac{1}{2}$ and bosons with integer spin. The light fermions, except the (nearly) massless neutrinos, build solid matter, while the bosons mediate the fundamental forces between them. All SM particles are categorized and labeled with their mass, charge and spin in figure 2.1.

Fermions The fermions of the standard model are divided into six quarks, that interact via all three forces, and six leptons that interact electromagnetic and via the weak force. Both groups are divided into three generations, which are the pairs of fermions that are most likely to interact with each other.

Each generation contains two quarks, one with an electric charge of $+\frac{2}{3}e$ and one with $-\frac{1}{3}e$, both are in addition color charged. In each generation of leptons one state has an electric charge of $-1e$ and the other is an uncharged neutrino. For each fermion there is an anti-particle with the same properties but opposite charge. In most parts of this thesis no distinction between particles and anti-particles will be made so e.g. 'muon' (μ) is used as short hand for 'muon or anti-muon'.

Neutrinos carry no charge and can be considered massless for most applications. Mass limits

Standard Model of Elementary Particles

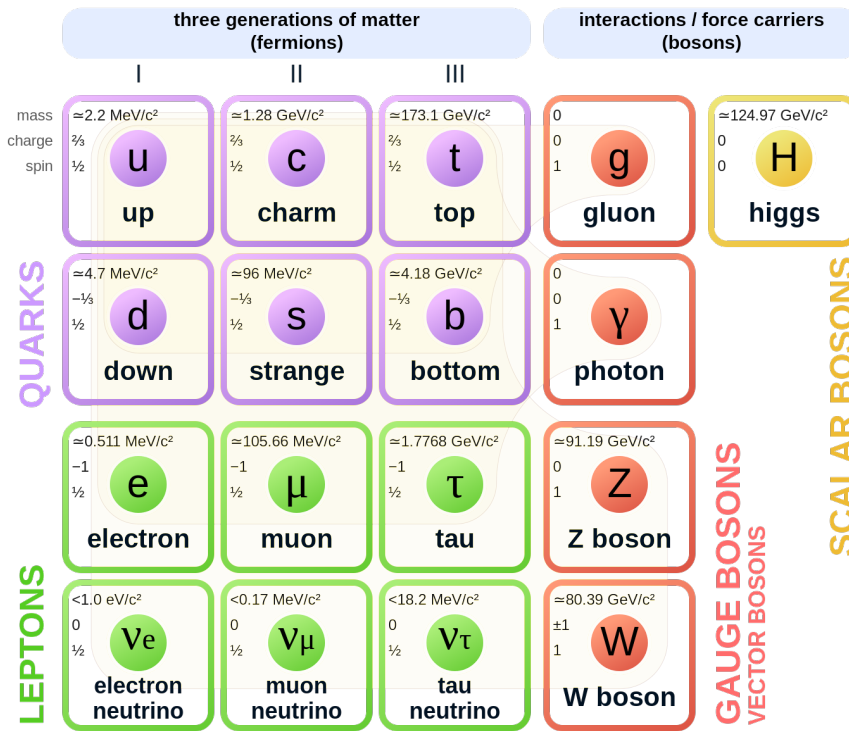


Figure 2.1.: Overview of all fundamental particles of the standard model of particle physics: The 12 fundamental fermions and 5 fundamental bosons. Brown loops indicate which bosons (red) couple to which fermions (purple and green) [10]. The cited mass values were published in 2019 by the particle data group [11]. Their latest average (August 2020) quotes the top quark mass at $172.73 \pm 0.3 \text{ GeV}$ using the 7,8 TeV combination from ATLAS [12], the lepton+jets, alljets [13], dilepton [14], t-channel single top [15] and 7,8 TeV combination [16] from CMS and the Tevatron combination [17].

and quadratic mass differences of the neutrinos were measured from neutrino flavor oscillations [18]. Neutrinos can only interact via the weak force. If neutrinos are Dirac or Majorana particles, so if they have anti-particles or are their own anti-particles, is not determined yet.

Bosons In the standard model of particle physics all bosons have a spin of one, except the Higgs boson with a spin of 0. The Higgs boson interacts with all massive particles. The mass of the Higgs boson has been measured to be $m_H = 125.4 \text{ GeV}$ [11]. It couples dominantly with the top quark. This makes the understanding of the top quark important for the Higgs boson and vice versa. The Higgs field and its mechanism introduces the mass terms of the Z and the W^\pm boson. This will be described in section 2.1.3.

The Z and W^\pm bosons are the mediators of the weak force and couple to all SM fermions. Due to the masses of its bosons the weak force is only relevant for small distances. The W^\pm boson has an electric charge of ± 1 and the Z boson is uncharged. The properties of these two bosons are excellent observables of other parts of the SM, because of their coupling to all fermions. For example, measurements of the Z boson cross section confirmed the number of neutrino generations (with small masses) to be three [19]. Concerning this thesis, the W^\pm bosons are crucial as mediator of the top-quark decay. In the SM the particle flavor cannot change via neutral currents, therefore top quarks can only decay via W^\pm and not via Z bosons. For simplicity W^+ bosons and W^- bosons will be labeled as W bosons in the following.

The boson of the electromagnetic force is the photon γ . It couples to all particles with electric charge and has no mass or charge itself. This results in a unlimited range of the electromagnetic field.

The mediator of the strong force is the gluon. Like the photon it has no mass, but it carries one color and one anti-color charge. When the energy density of the color field gets large, e.g. by increased distance of colored charged particles, quark-antiquark pairs are generated resulting in color-neutral mesons and baryons.

While the standard model of particle physics is by no means a "theory of everything", it is well suited for nearly all physics phenomena that have been observed in particle colliders so far. This does not include the abundance of additional particles that are predicted from e.g. the astrophysical observation of dark matter. Some of these predicted particles could be produced and observed by high enough energies in collider experiments [20]. The latest and most notable measurement of a deviation from the standard model is a measurement of the W boson mass, m_W , by the CDF collaboration. With 8.8 fb^{-1} of proton-antiproton collision data at $\sqrt{s} = 1.96 \text{ TeV}$ they measured $m_W = 80433.5 \pm 9.4 \text{ MeV}$ [21]. This result has a discrepancy of 7 standard deviations to the SM expectation of $80357 \pm 6 \text{ MeV}$, but also deviates from the current world average of similar but less precise direct measurements of m_W . This fuels the particle physics discussions of today.

One LHC result that is challenging the SM is from b meson decays ($b \rightarrow sl^{+1-}$), measured by the LHCb experiment. Their analysis results in a Lepton Flavor Universality violation of $> 3\sigma$ [22]. Another one is the magnetic dipole moment of the muon, g_μ . With the latest results from the Fermilab its measurements combine to $a_\mu = (116592061 \pm 41) \times 10^{-11}$, with $a_\mu = (g_\mu - 2) / 2$. That is 4.2σ away from the SM prediction of the Dirac equation (evaluated up to two loops) [23].

Gravitation is the fundamental force that is by far the weakest. Macroscopic gravitation is excellently described by Einsteins theory of general relativity, backed among other experiments by the recently discovered gravitational waves [24]. But it does not describe gravitation on the microscopic ($\mathcal{O} \leq 10^{-15} \text{ m}$) level we are looking at in high energy particle physics.

There are several theories trying to unify general relativity and the SM into a relativistic quantum theory but additional particles and forces predicted by them could not be discovered yet. Further precise measurements finding inconsistencies in the SM could hint at which

of these theories could be implemented in nature.

2.1.1. Gauge Theory

Mathematically the Standard Model is formulated as a Quantum Field Theory. Its formulation can be deduced by the quantization of the fields derived by Gauge theories. Gauge theories are based on the association of conservation laws with invariances of a system under specific symmetry transformations. In the group theory framework these symmetry transformations are described by Lie groups. One important Lie group is the Lorentz group. It is employed for the theory of special relativity.

If the Lagrangian density $\mathcal{L} = \mathcal{T} - \mathcal{V}$, with the kinetic energy density \mathcal{T} and the potential energy density \mathcal{V} of a particle field ψ , is known, than its classical dynamics are given by the Euler-Lagrange equation

$$\partial_\mu \left(\frac{\partial \mathcal{L}}{\partial (\partial_\mu \psi)} \right) - \frac{\partial \mathcal{L}}{\partial \psi} = 0.$$

The Lagrangian density for free particles in a scalar field contains a kinematic term $\partial^\mu \psi \partial_\mu \psi$ and a mass term $m^2 \psi^2$. Further interactions can be included into the theory by adding terms in the order of $\mathcal{O}(\psi^3)$ or $\mathcal{O}(\psi^4)$, each provided with a coupling constant.

The postulated conservation laws of the SM are the conservation of energy, momentum, angular momentum, color charge, weak isospin, electric charge, and weak hypercharge. In addition the conservation of baryon number and lepton number can be derived from symmetries of the SM without being postulated.

To ensure that all measurable quantities of the theory are finite, it has to be renormalized in such a way that predicted infinities can be absorbed into not measurable quantities. This results in 'running' coupling constants that are not constant but energy scale dependent.

2.1.2. Quantum Chromodynamics

Quantum Chromodynamics (QCD), the interaction related to the strong force, describes the interaction of particles with color charge. The underlying group is the $SU(3)_C$, fundamentally represented by the eight 3×3 Gell-Mann matrices. The three chromatic charges are typically denoted as "red", "green", and "blue". Gluons interact due to their own charge with other gluons. They carry one color and one anti-color combining to eight different charged gluon types. The gluon self-coupling leads to an effective QCD coupling constant α_s that is large for low and small for high energies. Therefore the potential energy between separated quarks increases with distance and new quark-antiquark pairs are generated until all quarks are part of color neutral mesons and baryons. At the high energies of modern particle colliders this phenomenon results in collimated streams of particles called 'jet'.

The precision on the detection of the energy of these jets is one of the major limiting factors in the style of analyses that is presented in this thesis.

At leading order the strong coupling constant is given by

$$\alpha_s(Q^2) = \frac{\alpha_s(\mu^2)}{1 + \frac{\alpha_s(\mu^2)}{12\pi} (33 - 2n_f) \log\left(\frac{Q^2}{\mu^2}\right)}$$

with the energy scale of interest Q , given the strength at a reference energy scale μ , assuming the number of available flavors n_f . At the scale of the Z boson mass m_Z the world average of strong coupling constant measurements is $\alpha_s(m_Z) = 0.1181 \pm 0.0011$ [11].

2.1.3. Electroweak Interaction

The electroweak interaction ties together the weak and the electromagnetic force into a $SU(2)_L \times U(1)_Y$ gauge group. The coupling constant of the electromagnetic interaction in leading order is given by

$$\alpha(Q^2) = \frac{\alpha(\mu^2)}{1 - \frac{\alpha(\mu^2)}{3\pi} \log\left(\frac{Q^2}{\mu^2}\right)}.$$

At the scale of m_Z the coupling constant was calculated to be $\alpha(m_Z)^{-1} = 127.934 \pm 0.026$ [25]. The gauge eigenstates W^1, W^2, W^3 and B mix into the observable mass eigenstates γ, Z and W^\pm with the Weinberg angle θ_W , with $\sin^2 \theta_W \approx 0.23$ [11] by

$$\begin{bmatrix} \gamma \\ Z \end{bmatrix} = \begin{bmatrix} \cos \theta_W & \sin \theta_W \\ -\sin \theta_W & \cos \theta_W \end{bmatrix} \begin{bmatrix} B \\ W^3 \end{bmatrix}, \quad W^\pm = \frac{1}{\sqrt{2}} (W^1 \mp W^2).$$

Quarks can change flavor when decaying via the strong interaction or the W boson. The transition probabilities between them are given as $|V_{ij}|^2$ by the Cabibbo-Kobayashi-Maskawa Matrix [11]:

$$V_{CKM} = \begin{pmatrix} |V_{ud}| & |V_{us}| & |V_{ub}| \\ |V_{cd}| & |V_{cs}| & |V_{cb}| \\ |V_{td}| & |V_{ts}| & |V_{tb}| \end{pmatrix} = \begin{pmatrix} 0.974 & 0.225 & 0.004 \\ 0.221 & 0.987 & 0.041 \\ 0.008 & 0.038 & 0.999 \end{pmatrix}.$$

Especially for heavy quarks the transition within the same generation is dominating. In addition to the four vector boson gauge fields there is one complex scalar field, the Higgs field. The Higgs field has a potential of $V_H = \mu^2 \phi^\dagger \phi - \lambda (\phi^\dagger \phi)^2$ with $\mu^2 > 0$, $\lambda > 0$ and a ground state at $v = 246 \text{ GeV}$ [11], the vacuum expectation value. The symmetry of the Higgs field is broken spontaneously, generating the masses of $m_Z = 91.2 \text{ GeV}$ and $m_{W^\pm} = 80.4 \text{ GeV}$. This is called the Higgs mechanism. One of the four degrees of freedom of the

field ϕ are identified as the Higgs boson. Scenarios with more than one Higgs boson are considered in theory but could not be observed yet. The Higgs boson couples to fermions via the Yukawa coupling y_f proportional to their mass $m_f = \frac{1}{\sqrt{2}}v y_f$ [11]. Therefore the Higgs couples the most to the top quark and their respective masses become a precision test for the standard model of particle physics as a whole. Examples for such tests will be presented in section 2.2.2.

The Higgs boson mass is much lighter than the Planck mass. This gives rise to the hierarchy problem, the incredible fine-tuning cancellations between the quadratic radiative corrections and the bare mass of the Higgs boson needed for a particle physics model to work on scales from the weak force up to gravitation.

2.2. The top quark

The top quark is the up-type quark of the third generation with a charge of $+\frac{2}{3}e$. It was predicted together with the bottom quark in 1973 by Makoto Kobayashi and Toshihide Maskawa to explain the CP-violation of the Kaon decay. In 1995 the CDF and DØ experiments at Fermilab discovered the top quark and measured its mass to be $m_t = 176 \pm 18 \text{ GeV}$ [26–28]. With this mass in the same order of magnitude as a gold atom it is the heaviest elementary particle observed and the only observed fermion heavier than the gauge bosons. Because of this high mass it couples strongly to the Higgs boson and possibly also to hypothetical particles from theories extending the SM. Knowledge of the top quark properties is important in many searches for new physics and for consistency checks of the SM and new theory models. Due to its small lifetime of $\tau_t = 5 \times 10^{-25} \text{ s}$ the top quark, unlike other quarks, does not hadronize before its decay [29]. This provides on the one hand the opportunity to measure properties of a "bare" quark, such as spin-correlations, which are lost in a bound state. On the other hand it makes the definition of its mass more complicated, which will be elaborated in section 2.2.2.

2.2.1. Phenomenology

In the following the top quark phenomenology, especially in proton-proton colliders at center-of-mass energies of several TeV, will be described.

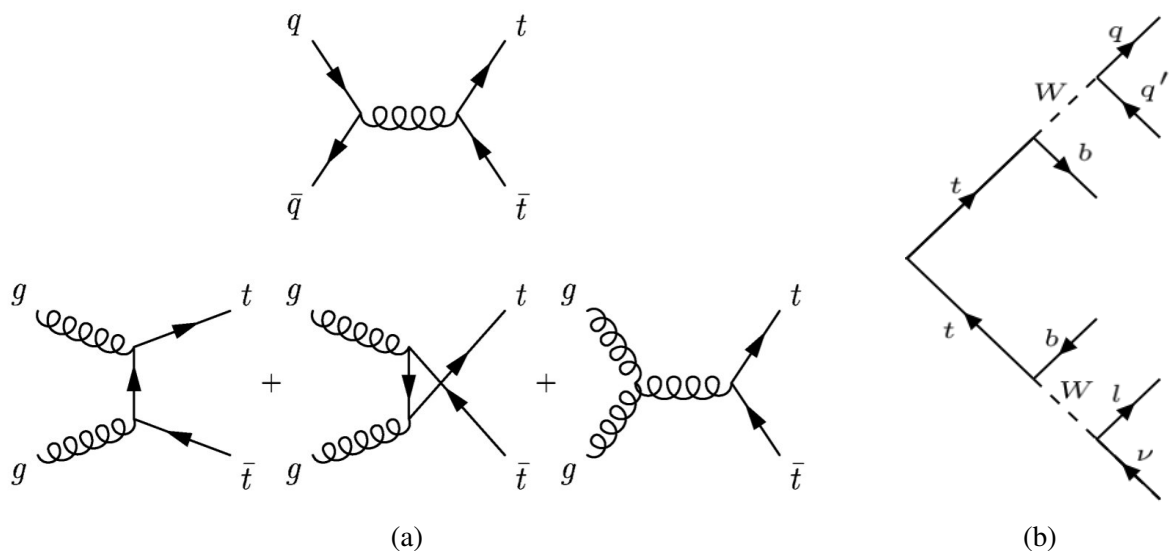


Figure 2.2.: a: Leading order $t\bar{t}$ production diagrams through quark-antiquark (top) and gluon-gluon (bottom) interaction [29]. b: Leading order decay of a top quark pair in the lepton+jets channel.

Top quark production In high-energy hadron colliders top quark pairs can be generated in leading order (LO) through gluon-gluon and quark-antiquark interaction. Top-anti-top quark pairs can be produced through QCD and single (anti-)top quarks through electroweak interaction. Single top (ST) production appears at a lower rate than pair production and will be considered as a background event source in this analysis. Other rare modes are top-quark pair production associated with a vector or Higgs boson and four top quark production. All possible LO top-quark pair production diagrams are shown in figure 2.2a. The predicted

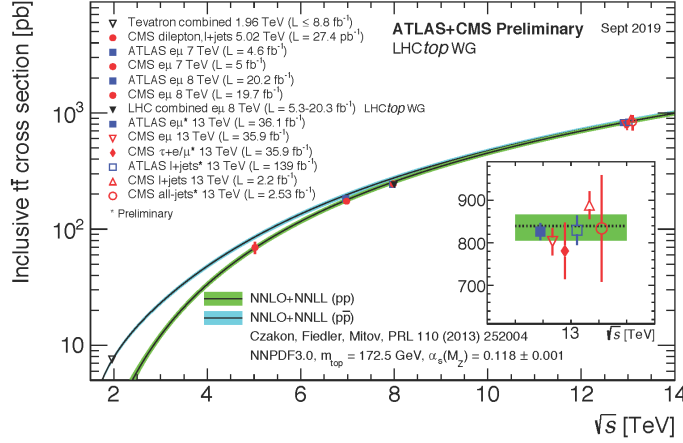


Figure 2.3.: Summary of LHC and Tevatron measurements of the top-pair production cross section as a function of the center-of-mass energy \sqrt{s} compared to the NNLO QCD calculation complemented with NNLL re-summation (top++2.0). The theory band represents uncertainties due to the renormalization and factorization scale, parton density functions and the strong coupling. The measurements and the theory calculation are quoted at $m_t = 172.5$ GeV. Measurements made at the same center-of-mass energy are slightly offset for clarity [30].

and measured cross section of top-quark pair production at hadron colliders is shown in figure 2.3. For a top quark mass of $m_t = 172.5$ GeV the production cross section at a proton-proton collider with a center-of-mass energy of $\sqrt{s} = 13$ TeV is predicted at NNLO+NNLL order to be $\sigma_{t\bar{t}}^{\text{NNLO+NNLL}} = 832_{-46}^{+40}$ pb. With the CMS experiment at $\sqrt{s} = 13$ TeV a cross section of $\sigma_{t\bar{t}} = 803 \pm 2(\text{stat}) \pm 25(\text{syst}) \pm 20(\mathcal{L})$ pb has been measured. The measurement was performed with dilepton events from a data sample corresponding to an integrated luminosity of 35.9 fb^{-1} [31] that was recorded in 2016.

Top quark decay Because flavor changing neutral currents are absent in the standard model, a (anti-)top quark can decay only into a down-type (anti-)quark and a W^\pm . The relative probabilities of the three possible decays are given by the CKM matrix shown in equations 2.1.3. Only the decay $t \rightarrow b W$ has a relevant probability for this analysis of approximately 0.998. The subsequent decay of the W boson occurs into one lepton and one neutrino (leptonic) or into a quark-antiquark pair (hadronic). The latter further develops due

to confinement into jets containing a multitude of light particles. Top quark pair decays are categorized by the subsequent decays of the two W bosons. The combinatoric branching ratios of possible LO top quark pair decays are listed in table 2.1. The branching fraction of

Table 2.1.: Combinatoric branching ratios for all top quark pair decay modes in dependence of the W boson decays.

BR($t\bar{t} \rightarrow b\bar{b} + X$)	$e^+ \nu_e$	$\mu^+ \nu_\mu$	$\tau^+ \nu_\tau$	$q\bar{q}'$
$e\bar{\nu}_e$	1/81	1/81	1/81	2/27
$\mu\bar{\nu}_\mu$	1/81	1/81	1/81	2/27
$\tau\bar{\nu}_\tau$	1/81	1/81	1/81	2/27
$q\bar{q}'$	2/27	2/27	2/27	4/9

a $t\bar{t}$ -decay with two leptons in the final state (dilepton) is approximately 1/9, the ratio of no leptons in the final state (all-jets or all-hadronic) 4/9, and the ratio of final states containing exactly one lepton (lepton+jets or semi-leptonic) 4/9. The branching fractions predicted via Monte Carlo generators at NLO accuracy in QCD, including possible off-shell effects, differ slightly from pure combinatorics and are 10.5% dilepton, 45.7% all-jets and 43.75% lepton+jets [11]. The latest measurement of the branching fraction performed by ATLAS with $\sqrt{s} = 7$ TeV data agrees with the combinatoric branching fractions within a few percent [32]. Each channel has its own benefits and challenges for selecting top quark events and extracting m_t dependent observables. The dilepton channel provides a rather clean sample when Drell-Yan background is suppressed, but has a small branching ratio and, due to the two neutrinos in the event, a higher energy uncertainty than the other channels. The all-jets channel has a higher statistic due to its branching ratio and the entire energy in an event can be collected, but the QCD-multijet background has to be controlled. In this thesis decays with one muon or electron and four jets in the final state will be analyzed. With b-jet identification it features a clean selection and a well constrained kinematic. Although only muons and electron are considered, the channel will be called lepton+jets and 'lepton' will refer in most parts of this thesis to 'muon or electron'.

A diagram of a possible LO decay in this channel is shown in figure 2.2b.

For high partonic center-of-masses the decay products from a top quark can appear boosted, so that all bundle into one jet. In this analysis these events will not be selected .

2.2.2. The top quark mass

Mass definition The mass of macroscopic, classical particles is easily defined by relativistic kinematics and can be calculated out of their energy and momentum as $m^2 = E^2 - \vec{p}^2$. It is called an "invariant" mass due to its invariance under Lorentz transformation. This definition will be used technically for the studied event hypotheses and parton candidate properties. For most quarks it is useful to determine an effective mass of the quark in a bound state and calculating a rest mass from estimations of their bond energy. This is not possible for the top quark as it decays too quickly and the bare quark mass is, due to the confinement in QCD, not a physical observable but a parameter of the QCD Lagrangian. If not only the LO interaction of the quark is taken into account, but also possible particle loops that can appear due to quantization, then the Lagrangian has to be renormalized to stay finite. This mass definition depends on the scheme with which the renormalization is performed. The conventional choice for many QCD applications is the pole mass. With the introduction of additional orders of perturbation, the propagator of the particle changes as

$$\frac{i}{\not{p} - m_0} \Rightarrow \frac{i}{\not{p} - \underbrace{m_0(\Lambda)}_{\text{'bare' mass}} - \underbrace{\delta m_0(\Lambda)}_{\text{divergent}} - \underbrace{\Sigma' m_0(\Lambda)}_{\text{finite}}} := \frac{i}{\not{p} - m^{\text{pole}}}$$

with the renormalization scale Λ and the four momentum in Dirac basis $\not{p} = \sum_{\mu=0}^3 \gamma^\mu p_\mu$ with the Dirac matrices γ^μ .

For heavy quarks this definition has shortcomings. Since quarks in asymptotic states do not appear as free particles, non-perturbative corrections must be added. This leads to an uncertainty of the pole mass in the order of $\Lambda_{\text{QCD}} \approx 200 \text{ MeV}$ [33]. Below Λ_{QCD} the strong coupling becomes large and perturbation theory is no longer applicable.

Therefore alternative mass schemes, that are physically and theoretically well described, are of interest. One of them is the $\overline{\text{MS}}$ scheme. It is a short-distance mass scheme, based on running masses, that depend on a cut off scale μ , which is typically chosen to be in the order of the mass itself so that $\mu = m_t$. The difference between the $\overline{\text{MS}}$ mass \bar{m} and m^{pole} can be approximated by perturbation theory but depends on how many loops of QCD and QED corrections are taken into account.

More generally than the $\overline{\text{MS}}$ scheme, a short-distance mass scheme can introduce an associated scale R . This MSR mass can be related to m^{pole} through the perturbative series

$$m^{\text{pole}} = m^{\text{MSR}}(R, \mu) + R \sum_{n=1}^{\infty} \sum_{k=0}^n a_{nk} \alpha_s^n(\mu) \ln^k \left(\frac{\mu^2}{R^2} \right),$$

with the correction coefficients a_{nk} .

The MSR mass is also convenient, as it is directly related to the $\overline{\text{MS}}$ scheme through

$$m^{\text{MSR}}(\mu, \mu) = m^{\overline{\text{MS}}}(\mu)$$

and interpolates to the pole mass

$$\lim_{R \rightarrow 0} m^{\text{MSR}}(R, \mu) = m^{\text{pole}}.$$

Examples for the top quark mass in different schemes for up to three QCD loops were calculated by reference [34] and are given in table 2.2. The calculation including the fourth QCD loop can be found in reference [35]. The running of the top quark mass was measured to agree with the theoretical prediction within 1.1σ in the $t\bar{t}$ dilepton channel at CMS from differential $t\bar{t}$ cross section as a function of the invariant mass of the $t\bar{t}$ system [36]. The influence of QED correction in the relation between pole and running masses is analyzed in reference [37].

Table 2.2.: The top quark mass in the MSR scheme at different scales, in the $\overline{\text{MS}}$ scheme at $\mathcal{O}(\alpha_s^3)$ for $\alpha_s(M_Z) = 0.1185$ converted from $m^{\text{MSR}}(3 \text{ GeV})$, and the pole mass at 1, 2, and 3 loop converted from the $\overline{\text{MS}}$ mass. All numbers are given in GeV and $m_t^{\text{MSR}}(R) := m_t^{\text{MSR}}(R, \mu = m_t)$ [34].

$m_t^{\text{MSR}}(1)$	$m_t^{\text{MSR}}(3)$	$m_t^{\text{MSR}}(9)$	$m_t^{\overline{\text{MS}}}(m_t)$	$m_{t,1\text{-loop}}^{\text{pole}}$	$m_{t,2\text{-loop}}^{\text{pole}}$	$m_{t,3\text{-loop}}^{\text{pole}}$
173.72	173.40	172.78	163.76	171.33	172.95	173.45

There are concerns that m_t determinations, that rely on a calibration based on Monte-Carlo (MC) simulations, can not be easily translated into a mass that is theoretically well motivated. One approach for such a translation is to take a short-distance mass definition, where the range R is adjusted to the energy threshold of the perturbative shower description in the Monte-Carlo simulation. This leads to an uncertainty in the order of 1 GeV [34,38]. In ref. [34] the Monte-Carlo mass was translated into a MSR mass and then, via the $\overline{\text{MS}}$ scheme, into a pole mass. This procedure resulted in a numerical difference for the world average top quark mass of $m_t^{\text{pole}} - m_t^{\text{MC}} = 0.05^{+0.32}_{-0.62} \pm 0.50 \text{ GeV}$, with the conclusion that MC mass results are expected to be close to the pole mass.

Another approach was taken by Hoang et al. in ref. [38]. There the dependence of the top-quark MC mass to theory mass schemes was evaluated in $e^- e^+$ collisions. This was done using the 2-Jettiness [39] distribution of events simulated with Powheg 8.205. Example results of this calibration are given in table 2.3. A Monte-Carlo mass of $m_t^{\text{MC}} = 173 \text{ GeV}$ was transferred to a pole mass at next-to-next-to-leading logarithmic order (NNLL) of $m_t^{\text{pole}} = 172.43 \text{ GeV}$ with an uncertainty of 0.28 GeV. The uncertainty is driven by the limited order of perturbation and the difference between the MC event generator results and the QCD prediction. In figure 2.4 the MSR mass for different m_t^{MC} values is shown. In it can be seen that the translation from MC to MSR mass is a simple offset.

A similar fit was performed by the ATLAS collaboration [40]. It used the jet mass of high p_T jets in hadronically-decaying $t\bar{t}$ events from proton-proton collision simulation with $\sqrt{s} = 13 \text{ TeV}$ and a particle-level calculation at next-to-leading-log precision. With this the difference between the Monte-Carlo and MSR mass at $R = 1 \text{ GeV}$ was evaluated to be

Table 2.3.: Central values and uncertainties out of the calibration of $m_t^{\text{MC}} = 173 \text{ GeV}$ into theoretical mass schemes, all in GeV and $m_{t,R}^{\text{MSR}} := m_t^{\text{MSR}}(R, \mu = m_t)$. σ combines the uncertainty due to perturbation and the incompatibility [38].

$$m_t^{\text{MC}} = 173 \text{ GeV}$$

mass scheme	order	central [GeV]	σ [GeV]
$m_{t,1}^{\text{MSR}} \text{ GeV}$	NLL	172.80	0.29
$m_{t,1}^{\text{MSR}} \text{ GeV}$	NNLL	172.82	0.22
m_t^{pole}	NLL	172.10	0.38
m_t^{pole}	NNLL	172.43	0.28

$0.08_{-0.40}^{+0.35} \text{ GeV}$. The uncertainty is mainly driven by missing higher-order corrections. Carrying out these fits with the pole mass parameter resulted in $m_t^{\text{MC}} - m_t^{\text{pole}} = 0.35_{-0.36}^{+0.30} \text{ GeV}$. While these approaches agree within their uncertainty, the question to which level they are transferable to the measurement presented in this thesis is not totally clear. But the agreement between the fits from electron-positron and proton-proton collision simulation gives confidence that the Monte-Carlo mass from semi-leptonic decays should have a similar relationship to the theoretically well defined schemes. A more in-depth review of the controversy on the connection of physical parameters with the result of direct top-quark mass measurements using templates from simulation was presented in ref. [41]. It recommends the application of additional uncertainties of 0.5 GeV for interpretation plus 0.25 GeV for the pole mass renormalon ambiguity when identifying $m_t^{\text{MC}} = m_t^{\text{pole}}$.

2.2.3. Measurements using MC templates

Most analyses measure the top quark mass not in one of these schemes but derive it directly with a template fit on mass-sensitive distributions that are calculated from observables of the top quark decay products. From these, a value that is calibrated to the top quark mass parameter in the Monte-Carlo (MC) event simulation is extracted.

Most results that will be quoted in this section are compared in figure 2.5. All quoted CMS results have a smaller value the world average, which is caused by the $D\bar{O}$ measurement included in the combination.

The top quark was discovered in 1995 at the Fermilab in $p\bar{p}$ collisions at $\sqrt{s} = 1.8 \text{ TeV}$ and its mass was measured to be $178 \pm 8(\text{stat}) \pm 10(\text{syst}) \text{ GeV}$ with the CDF [1] experiment and $199 \pm 20(\text{stat}) \pm 22(\text{syst}) \text{ GeV}$ with $D\bar{O}$ [2].

The world combination (2014) of top quark mass measurements that combines results of the experiments Atlas, CDF, CMS, and $D\bar{O}$ is $m_t = 173.34 \pm 0.27(\text{stat}) \pm 0.71(\text{syst}) \text{ GeV}$ [3]. In 2016 a combination averaged the measurements from $p\bar{p}$ collisions at the Fermilab to $m_t = 174.30 \pm 0.65 \text{ GeV}$ [17]. The CMS and ATLAS experiment combined their respective

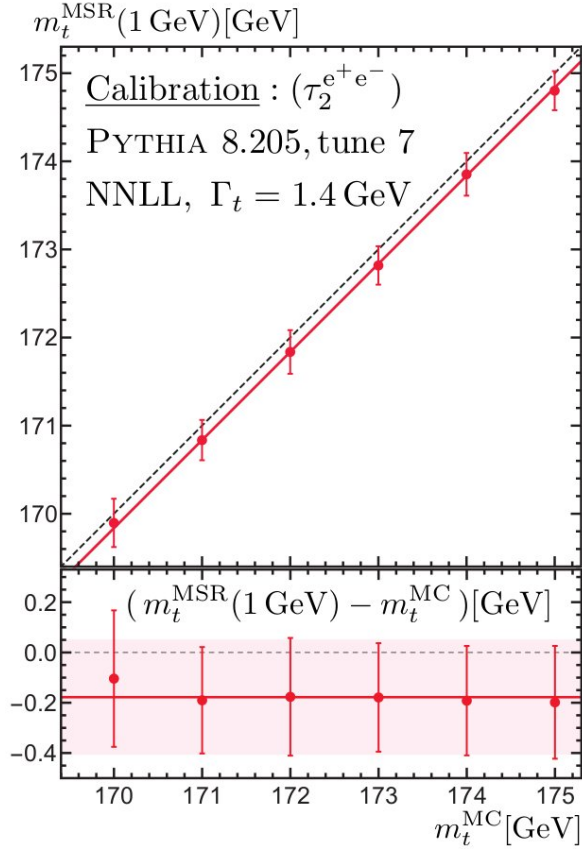


Figure 2.4.: Dependence of the NNLL fit result of the MSR mass on the input m_t^{MC} value in Pythia. The error bars show the total calibration uncertainty. The red solid lines correspond to the weighted average of the individual results. The red shaded area shows the average of the individual uncertainties [38].

measurements from 7 TeV and 8 TeV pp-collisions to 172.44 GeV (CMS) and 172.69 GeV (ATLAS) with an uncertainties of 0.48 GeV each [42, 43].

The most precise single analysis of the top quark mass, before this thesis, was done in the lepton+jets channel of the $t\bar{t}$ decay [4]. It used a fit of the event kinematics to a $t\bar{t}$ hypothesis and extracted m_t together with an additional jet scale factor (JSF) to reduce the impact of jet energy correction (JEC) uncertainties. Its approach is the baseline of the method that will be used in this analysis and is explained in chapter 8. It was published in 2015 by CMS and had a result of $m_t = 172.38 \pm 0.16(\text{stat}) \pm 0.49(\text{syst})\text{GeV}$ [6]. In the dilepton decay channel in CMS data the top quark mass was measured to be $m_t = 172.33 \pm 0.14(\text{stat})_{-0.72}^{+0.66}(\text{syst})\text{GeV}$ [31]. That analysis used a profile likelihood fit that included systematic uncertainties as nuisance parameters. A similar approach will be used in this thesis. Another similarity to this analysis is that invariant mass between the lepton and associated bottom tagged jet, $m_{l,b}^{\text{min}}$, is included in the likelihood as additional observable. Be aware that $m_{l,b}^{\text{min}}$ is not exactly defined in the same way as the m_{lb}^{reco} distribution that will be used in this thesis but uses a jet-parton assignment that conserves the hard cut-off to higher

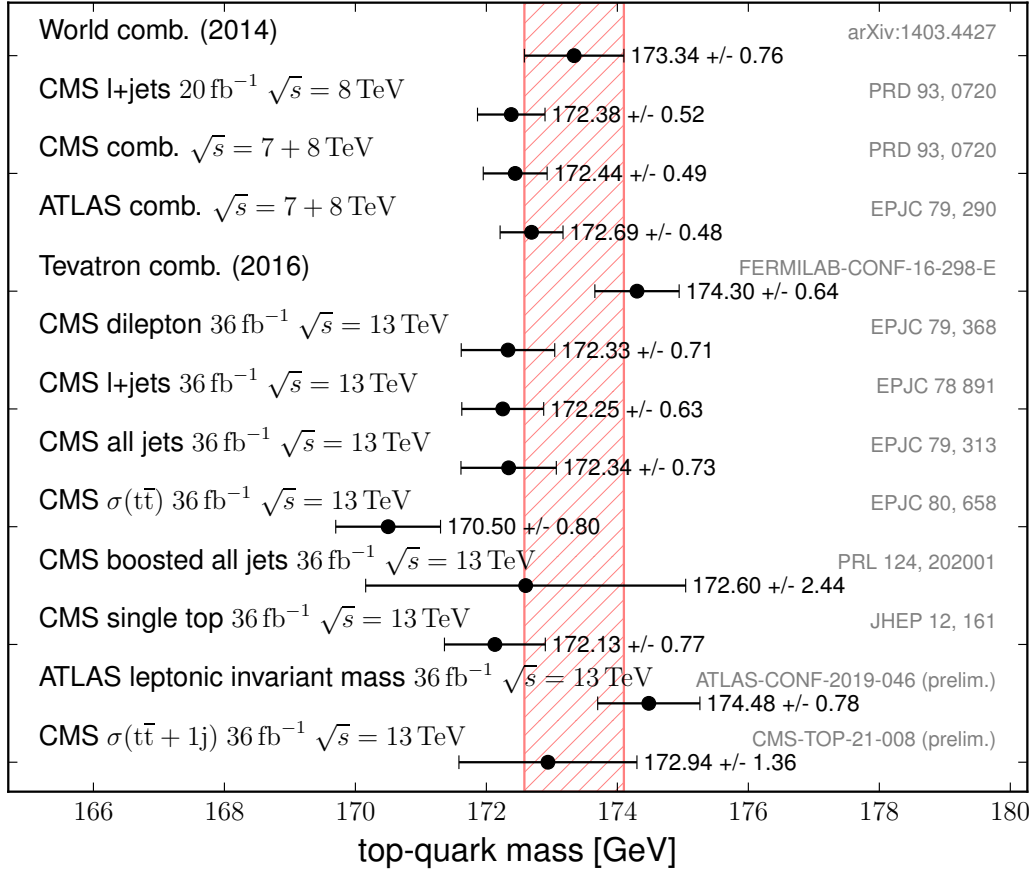


Figure 2.5.: Summary of example top-quark mass measurement results.

values. A major difference to the analysis in this thesis is that the top-quark mass in the dilepton analysis was measured simultaneous to the $t\bar{t}$ cross-section.

In the alljets decay channel in CMS data the top quark mass was measured to be $m_t = 172.34 \pm 0.20(\text{stat}) \pm 0.70(\text{syst}) \text{ GeV}$ [44]. The measurement employed a kinematic fit and fitted a JSF from the m_W^{reco} distribution, similar to the measurement in the lepton+jets channel.

The top quark mass is also measured in other channels than in $t\bar{t}$ decays. For example a measurement from single top events in 36 fb^{-1} CMS data at $\sqrt{s} = 13 \text{ TeV}$ determined the top quark mass to be $172.13_{-0.77}^{+0.76} \text{ GeV}$ [45]. That analysis used a high-momentum lepton selection, required each event to contain at least two jets and used a multivariate analysis method to separate signal events from background with high purity. The single top selection was also used to determine the ratio and difference between the mass of the top quark and antiquark. The results of $m_t/m_{\bar{t}} = 0.995_{-0.010}^{+0.008}$ and $m_t - m_{\bar{t}} = 0.83_{-1.35}^{+1.79} \text{ GeV}$ are consistent with the CPT invariance of the SM [45] and former measurements that combine to $\Delta m_t = -0.16 \pm 0.19 \text{ GeV}$ [11].

Another way to measure the top quark mass is from $t\bar{t} \rightarrow \text{lepton} + \text{jets}$ events with an additional soft muon. This approach uses templates from the invariant mass between the lepton

from the W-boson decay and a μ from the b-hadron decay. With this method the ATLAS collaboration measured $m_t = 174.48 \pm 0.78 \text{ GeV}$ in 36 fb^{-1} data at $\sqrt{s} = 13 \text{ TeV}$ [46]. This result is especially interesting as it uses events that are very similar to the events selected in the presented analysis, but has different leading uncertainties and measures a higher mass value than most other analyses from LHC experiments.

2.2.4. Measurements from cross sections

One way to avoid this ambiguity in the definition is to extract m_t^{pole} from the differential $t\bar{t}$ cross section. From multi-differential $t\bar{t}$ production cross sections in pp collisions at $\sqrt{s} = 13 \text{ TeV}$ the CMS experiment measured $m_t^{\text{pole}} = 170.5 \pm 0.8 \text{ GeV}$ using NLO calculations in a simultaneous fit with α_s [47]. Another m_t^{pole} measurement used dileptonic $t\bar{t}$ decays with at least one additional jet at $\sqrt{s} = 13 \text{ TeV}$, measured with the CMS detector, and unfolded the cross-section differential in $\rho = 2m_0/m_{t\bar{t}+\text{jet}}$ with $m_0 = 170 \text{ GeV}$ [48]. For the unfolding a likelihood maximization with nuisance parameters was employed, similar to what will be used in this thesis. It measured $m_t^{\text{pole}} = 172.94_{-1.34}^{+1.37} \text{ GeV}$. In the boosted regime of the $t\bar{t}$ alljets decay channel, where all decay products from a top quark are collimated into one jet with a transverse momentum larger than 400 GeV , it becomes feasible to unfold the $t\bar{t}$ cross section as a function of the jet mass at the particle level to extract the top quark mass. With this approach the top quark mass was measured by the CMS experiment at $172.6 \pm 2.5 \text{ GeV}$ [49].

2.2.5. Global interest

The longer no evidence for physics beyond the standard model is observed, the more interesting becomes a precise understanding of SM quantities, particles and their observables. These observables can be fitted to data in different combinations to test the consistency of the standard model. This highly affects the physics interpretation of the theory. One example for such an observable is the mass of the top quark. It is a free parameter of the SM but has relations to other parameters via all the interactions included in the SM. For example top quark loop corrections contribute to the Higgs boson mass and top-bottom quark loop corrections contribute to the W boson mass.

One application of these dependencies between different SM parameters are global fits, for example of the electroweak sector of the SM. Before the masses of the top quark and Higgs boson were measured they could be determined from other SM parameters. Now that both have been measured, such fits can be used as a cross-check for the measurements and the standard model as a whole. A recent global electroweak fit [50] using NNLO theory predictions and a top quark mass of $m_t = 172.47 \pm 0.68 \text{ GeV}$ had a fit result of $\chi^2/N_{\text{df}} = 18.6/15$. This is an important consistency demonstration of the SM. When leaving the top quark mass

free and fitting it from the other 21 included parameters m_t is indirectly determined to be $m_t = 176.4 \pm 2.1$ GeV. The uncertainty is dominated by the uncertainty on the W boson mass ($m_W = 80.379 \pm 0.013$ GeV) and would go down to ± 0.9 GeV with perfect knowledge of m_W . This puts the measured m_t at about 1.7σ of the indirect determined m_t . In figure 2.6 indirect determinations of m_W and m_t at the same time, with and without leaving the Higgs boson mass m_H free, are shown. As comparison the result of the direct measurement are also included in the figure. Both fits agree with the direct measured masses.

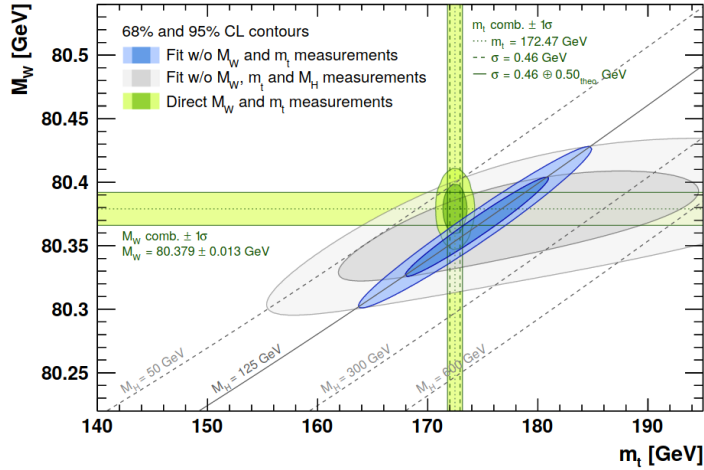


Figure 2.6.: Contours at 68% and 95% confidence level obtained from scans of M_W versus m_t in a global fit of electroweak observables including (blue) and excluding the M_H measurement (grey), as compared to the direct measurements (green vertical and horizontal 1σ bands, and two-dimensional 1σ and 2σ ellipses). The direct measurements of M_W and m_t are excluded from the fits [50].

As another crosscheck the complete lifetime of the standard model can be determined. This means calculating the quantum field theory tunneling probability and thus vacuum stability of the universe according to the SM This was done by ref. [51]. With assuming the SM, no quantum gravity and no new physics the decay rate per unit volume was calculated to be $\Gamma/V = 10^{-773_{+239}^{-638}} \text{ GeV}^4$. The top quark mass value used was $m_t^{pole} = 173.1 \pm 0.6$ GeV. The biggest part of the uncertainty, $10^{-364_{+198}}$, is caused by the uncertainty on the top quark mass. The decay rate translates into a predicted lifetime of the universe of $\tau_{SM} = (\Gamma/V)^{-1/4} = 10^{161_{-59}^{+160}}$ years. This is enormously long but the exponent is still roughly in the order of magnitude as the exponent of our universes current lifetime (10^{10} years). The stability prediction in the m_t - m_H plane is shown in figure 2.7 together with the scale Λ_{NP} of new physics that would stabilize the SM. In the m_t - m_H plane the SM sits in a narrow region of meta-stability with

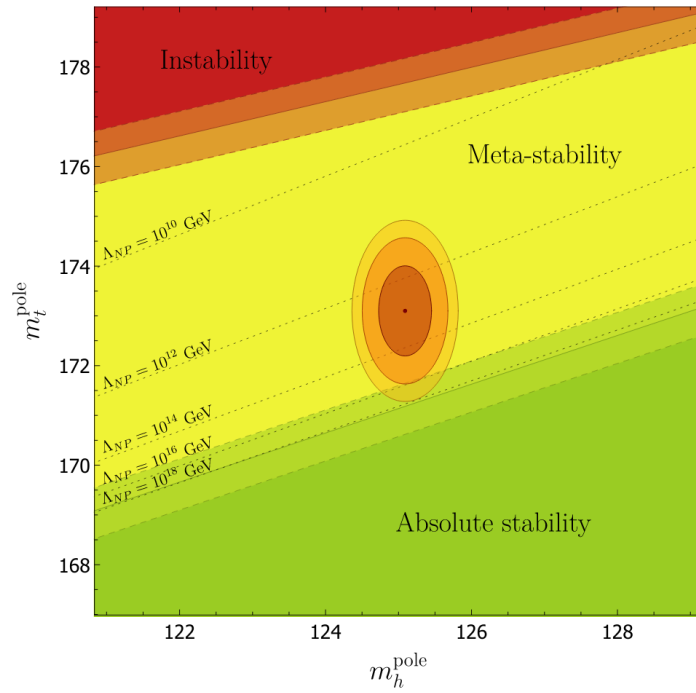


Figure 2.7.: Phase diagram for stability in the $m_t^{\text{pole}}/m_h^{\text{pole}}$ plane with dotted lines indicating the scale at which the addition of higher-dimension operators could stabilize the SM. Ellipses show the 68%, 95% and 99% contours based on the experimental uncertainties on m_t^{pole} and m_h^{pole} . The shaded bands on the phase boundaries, framed by the dashed lines and centered on the solid lines, are combinations of the α_s experimental uncertainty and the theory uncertainty [51].

the stability border at

$$\frac{m_t^{\text{pole}}}{\text{GeV}} < 171.18 + 0.12 \left(\frac{m_H^{\text{pole}} / \text{GeV} - 125.09}{0.24} \right) + 0.43 \left(\frac{\alpha_s(M_Z) - 0.1181}{0.0011} \right) + (\text{theo})_{-0.35}^{+0.17}. \quad (2.1)$$

Absolute stability is excluded at 2.48σ and a top quark mass uncertainty of $\sigma_{m_t} < 0.25 \text{ GeV}$ would be needed to exclude a stable SM universe at 3σ . Quantum gravity or new physics at arbitrary high scale could open up new tunneling directions but near stability arbitrary high scale physics also could stabilize the SM. From the current m_t , m_H and α_s measurements the relevant scale of new physics to stabilize the SM is $\Lambda_{NP} \sim 10^{13} \text{ GeV}$.

When including new physics no sensible estimation of a lower stability bound is possible. But an even more precise knowledge of m_t would help to hone in on at which energy scale new physics is expected at least if we want to assume that the universe is stable, which is not required by any physics reason.

3. Experimental setup

To produce top quarks stable particles with lower masses are collided at high enough center of mass energies (\sqrt{s}). The obvious choice are electromagnetic charged particles that can be relatively easy accelerated with electric- and collimated with magnetic fields. If circular machines are used the same acceleration apparatus can be used multiple times, but the particles lose energy in the curves by synchrotron radiation. The highest center of mass energy is achieved by colliding protons in a circular collider. The largest machine of this kind is the Large Hadron Collider.

3.1. The Large Hadron Collider

The Large Hadron Collider (LHC), at the Conseil Européen pour la Recherche Nucléaire (CERN) in Geneva, is a synchrotron and storage ring for protons and heavy ions. With a circumference of 26.7 km it is the largest single machine built. It is constructed in the same tunnel that was used for the Large Electron-Positron Collider (LEP) [52] until the year 2000. The center-of-mass energy of the LHC is designed to be 14 TeV in proton-proton collision operation. There are four experiments at the LHC, observing the particles out of the collisions. ALICE (A Large Ion Collider Experiment) is mainly focusing on the research of the products of heavy ion collisions. LHCb (LHC beauty experiment) is specialized in observing bottom hadrons produced with small angles to the beam pipe. The two other experiments, ATLAS and CMS (Compact Muon Solenoid), are multi-purpose detectors observing a broad range of proton-proton collision final states. ATLAS and CMS are valuable competitors to one another as at the moment only they are capable to confirm or falsify each others results. The first collisions at the LHC started in 2009 and lead to the discovery of a Higgs-like particle in 2012 at $\sqrt{s} = 8$ TeV. Since 2015 the LHC is running in its second run period at $\sqrt{s} = 13$ TeV, which is referred to in the following as Run II.

The protons for the collision are produced by ionizing hydrogen gas with an electron beam. In order get a high energy beam with an acceptable emittance, the protons have to run through several pre-accelerator steps before they can be injected into the LHC.

The first step of the acceleration chain is a linear accelerator that accelerates the protons from a kinetic energy of about 100 keV to 50 MeV via radio-frequency cavities. The second step

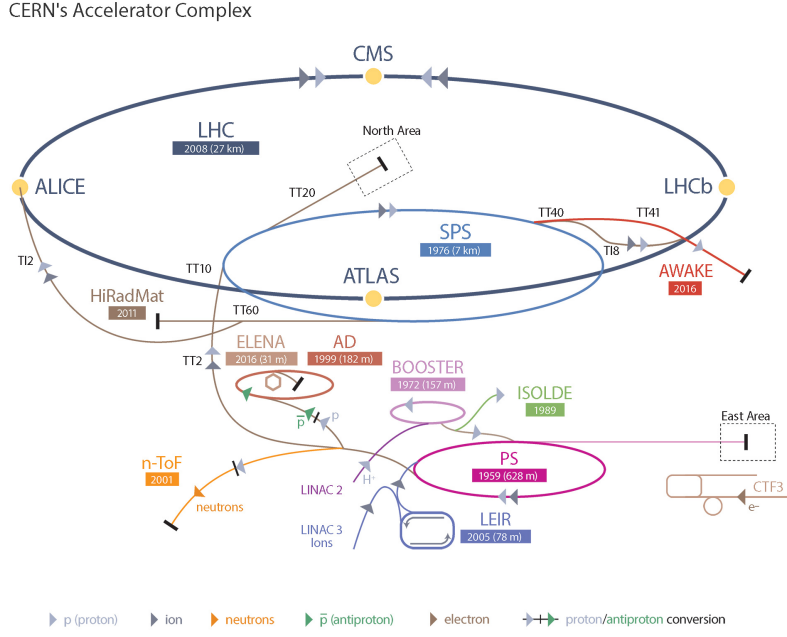


Figure 3.1.: Schematic overview of the LHC pre-accelerator chain [54].

is the Proton Synchrotron Booster. There, the head and the tail of the beam are dumped, and the middle part is separated into four bunches with 4 ns length each. In the following step these bunches are accelerated to an energy of 1.4 GeV. Thereafter the bunches are injected into the Proton Synchrotron, with a bunch spacing of 25 ns or 50 ns, as is required for the LHC operation. This analysis uses data generated on 25 ns bunch spacing. In the Proton Synchrotron, the protons are accelerated to 25 GeV and passed on to the Super Proton Synchrotron where their energy is increased to the LHC injection energy of 450 GeV [53]. Within the LHC, the beam can be stable for about 8 hours before the LHC needs to be filled again.

The characteristic property of a particle collider describing the collision activity is the *instantaneous luminosity* L . For symmetric circular colliders it can be calculated as

$$L = \frac{f N_1 N_2}{2\pi \sqrt{\sigma_{x,1}^2 + \sigma_{x,2}^2} \sqrt{\sigma_{y,1}^2 + \sigma_{y,2}^2}}$$

from the frequency of proton bunches colliding f , the number of protons per bunch N_i , and the bunch profile in the transverse directions $\sigma_{x/y,i}$. The initial LHC design planned an instantaneous luminosity at the LHC of $L = 10^{34} \text{ cm}^{-2} \text{ s}^{-1} = 10 \text{ Hz/nb}$ (using the unit Barn, $1 \text{ b} = 10^{-28} \text{ m}^2$). The LHC reached up to $L = 15.3 \text{ Hz/nb}$ in the 2016 run and even $L = 20 \text{ Hz/nb}$ in 2017, surpassing the design luminosity [55, 56].

For a given production cross section hypotheses σ , the expected event count is derived from the integrated luminosity $L_{int} = \int L dt$ as $n = \sigma L$.

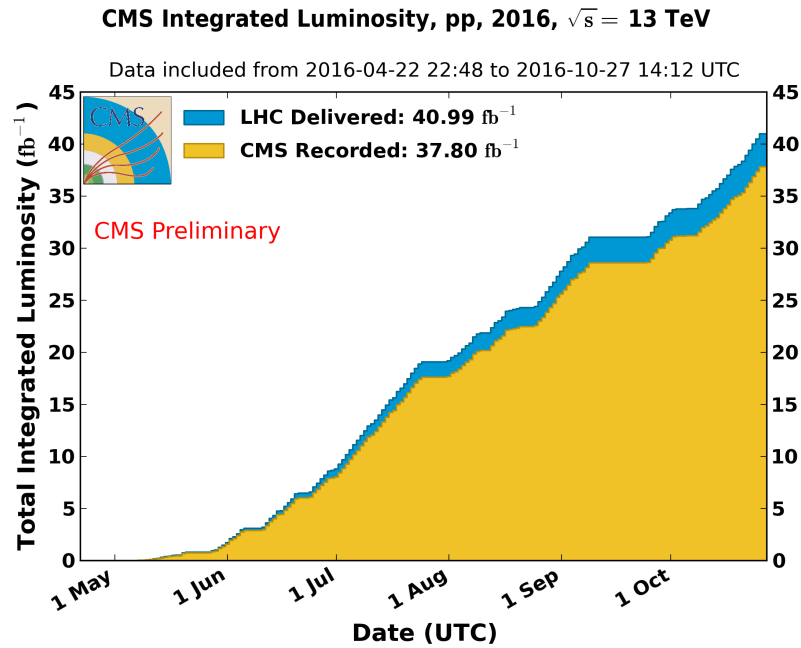


Figure 3.2.: Cumulative offline luminosity versus week delivered to (blue), and recorded by CMS (orange) during stable beams and for p-p collisions at 13 TeV center-of-mass energy in 2016 [57].

The integrated Luminosity, that was recorded by CMS in 2016, is plotted in figure 3.2. The data analyzed in this thesis corresponds to an integrated luminosity of 35.917fb^{-1} .

The nominal beam parameters of the LHC at Run II in proton-proton operation are listed in table 3.1. In Heavy Ion operations fully stripped lead ions ($^{208}\text{Pb}^{82+}$) are accelerated to 2.76 TeV per nucleon and collided with protons as well as other lead ions. A detailed description can be found in the LHC design report [59].

3.2. The Compact Muon Solenoid detector

The Compact Muon solenoid (CMS) detector is a multi-purpose particle detector at the LHC. It has a circumference of 15 m and length of 28.7 m, while weighing about 14 000 t. The detector has a onion-like structure, with each layer being specialized for detecting the observables of a distinct particle type and covering nearly all angles around the interaction point. The different layers are easily spotted in figure 3.3. The detector is capable of identifying the decay products of all particles in the standard model of particle physics except neutrinos. An illustration of how the signatures of different particle types can be distinguished by combining information from the different parts of the detector can be found In figure 3.4. Each of the layers will be described roughly in the following. A more detailed description, including

Table 3.1.: Overview of the LHC beam properties [58, 59].

parameter	value
proton energy	6.5 TeV
bunches per beam	2808
proton per bunch (at start)	1.2×10^{11}
RMS bunch length	7.55 cm
RMS bunch width	16.7 μm
instantaneous luminosity (design)	$10^{34} \text{ cm}^{-2} \text{ s}^{-1}$
collision rate	40 MHz
energy loss per round	max. 6.71 keV
beam collision angle	285 μrad
max. magnetic dipole field	0.535 \rightarrow 8.33 TeV

performance studies, can be found in the references [60, 61].

3.2.1. CMS coordinate system

All particles described in this thesis are characterized by their kinematic properties. Out of these properties the observables of interest are derived. The Lorentz vector, one time and three space coordinates or the equivalent one energy and three momentum coordinates fully describe the kinematics of a particle.

The transverse momenta of the colliding particles with respect to the beam is negligible. The resolution of the detector depends highly on the angle to the LHC beam line. For the description of particle tracks and energy deposits in the detector no Cartesian coordinates are used. Instead the azimuthal angle in the x - y plane ϕ , where x points radial into the center of the LHC and y away from the earth, and the pseudo-rapidity $\eta = -\ln \tan(\theta/2)$ are used. The polar angle θ is defined with respect to the right-handed z -axis, that points counterclockwise to the axis of the beam. $\Delta\eta$ is invariant under Lorentz transformations. Therefore $\Delta\eta$ is a very useful metric to consistently cut on angular distances between objects in the detector for different energies.

Another often used quantity in this thesis is the transverse momentum, defined as $p_T = \sqrt{p_x^2 + p_y^2}$. This coordinate system definition is the same as the commonly used at the CMS detector [60].

3.2.2. CMS components

Solenoid Magnet To be able to measure the charge per mass and momentum of particles, a magnetic field is inducted in the detector. The detector is designed for a field strength of

CMS Detector

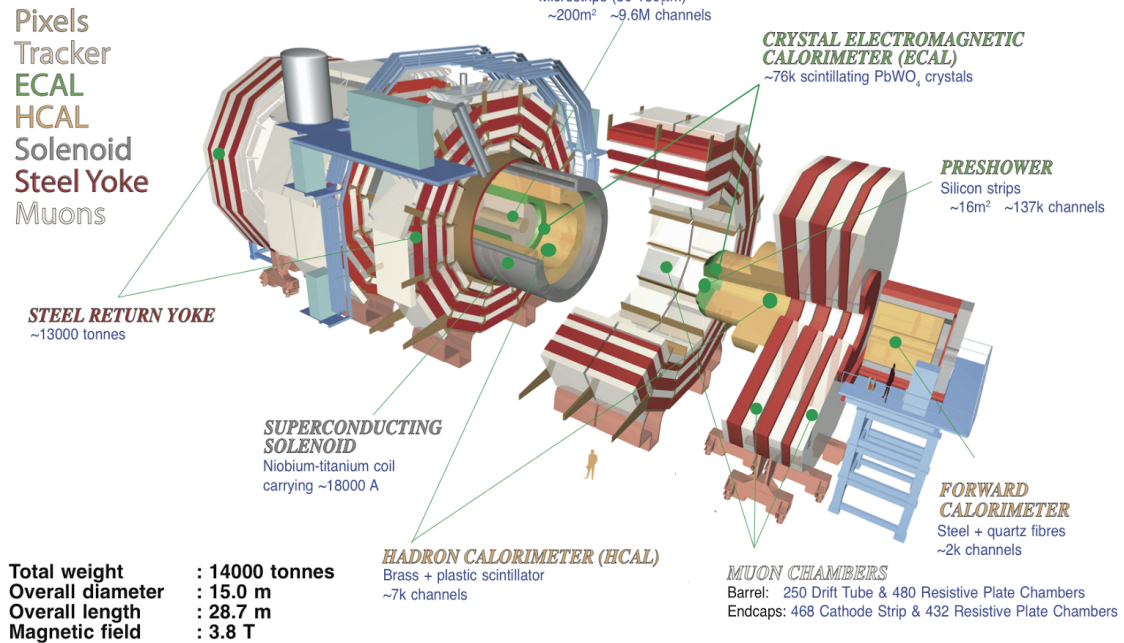


Figure 3.3.: Overview of the CMS detector with all its subsystems [62].

up to 4T in its center but operated at 3.8T for stability reasons. The field is generated by a solenoid with an inner circumference of 2.95m and a length of 12.9m, containing 53km superconducting niobium-titanium cable in 2168 windings, and is operated with a current of 19.5 kA. The structure includes an iron yoke for the magnetic return flux in which the field strength is 2T. To minimize energy absorption from the particles that are to be measured, while maximizing the field strength in the tracker, the solenoid is placed between the hadronic calorimeter and the muon system.

The strong magnetic field makes it possible to measure transverse momenta with the high resolution quoted in the following.

Tracker The first part of the detector that is passed by particles out of the collision point, is the silicon tracker. It is composed of barrels and disks of silicon-pixel and silicon-strip sensors. It covers the whole ϕ range and a pseudo-rapidity up to $|\eta| < 2.5$. The material budget of this detector part has to be minimal, so that particle tracks are altered as little as possible. The radiation length of the tracker reaches from 0.4 in the barrel to 2 in the transition between barrel and end-caps. Closest to the beam line are three barrel layers of silicon-pixels with radii of 4.4cm to 10.2cm around the detector's z-axis. There are two end-caps on either side, with distances of 34.5 cm and 46.4 cm to the interaction point. Each

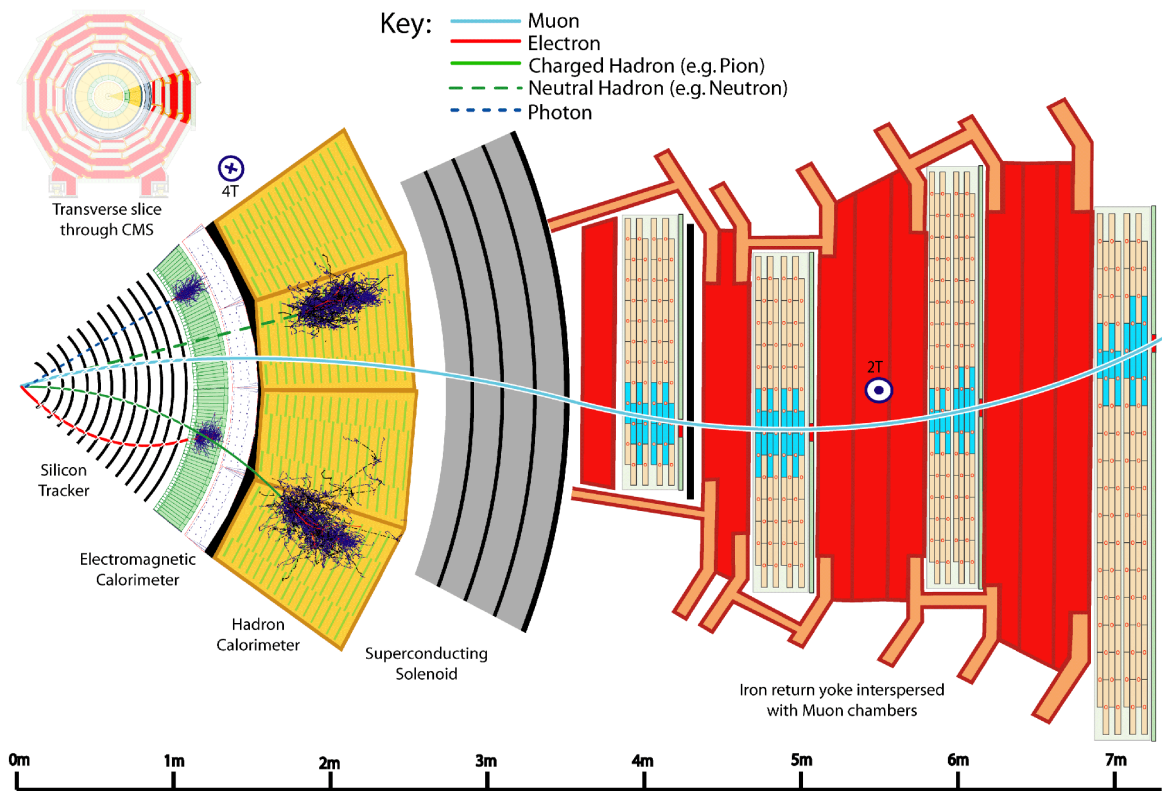


Figure 3.4.: Cut through the ϕ -plane of the CMS detector where the signatures of different particle types are illustrated [63].

of the 66 million hybrid-pixel-sensors has a size of $100 \times 150 \mu\text{m}^2$. The pixels of one layer are tiled on each other and shifted against the next layer, so that a resolution of $10 \mu\text{m}$ in r - ϕ and $20 \mu\text{m}$ in z direction is obtained. The pixels were aligned using cosmic muon radiation data as calibration reference.

The silicon strip tracker has a length of 5.8 m and a radial thickness of 0.55 m. The $320 \mu\text{m}$ and $500 \mu\text{m}$ wide strips are arranged with a spacing of $80 \mu\text{m}$ to $180 \mu\text{m}$ between them in 6 barrels around the beam pipe and in 12 caps on each side. A schematic of the tracker is shown in figure 3.5. Due to the two-dimensional hit information, a resolution of $23 \mu\text{m}$ to $52 \mu\text{m}$ orthogonal to the strips can be obtained.

Their transverse momenta are calculated from the curvature of the tracks from charged particles in the magnetic field. Their relative resolution is about $\frac{\Delta p_T}{p_T} = 1.5 \cdot 10^{-4} p_T / \text{GeV} + 0.005$. This means a p_T resolution of $\sim 2\%$ from the tracker can be expected for $p_T \sim 100 \text{ GeV}$ which is the typical p_T of leptons in this analysis. For the lowest momentum leptons in this analysis at $p_T \sim 30 \text{ GeV}$ the resolution gets better to $\sim 1\%$. The resolution is better for small and worse for high $|\eta|$.

Primary and secondary vertices of particle decays can be identified in the tracker and are used for particle identification.

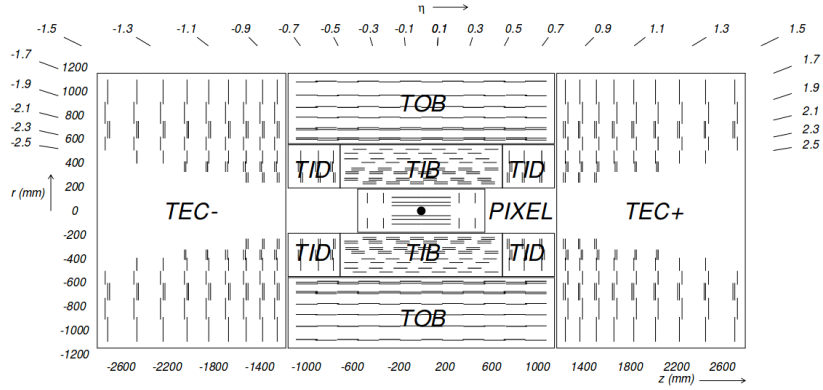


Figure 3.5.: Schematic cross section through the CMS tracker. Each line represents a detector module. Double lines indicate back-to-back modules which deliver stereo hits. The strip tracker is divided into inner and outer barrel (TIB, TOB), inner disks (TID) and end-caps (TEC) [64].

Calorimeters The next layers of the detector are the electromagnetic calorimeter (ECAL) and the hadronic calorimeter (HCAL).

The ECAL is designed to absorb as much energy from electrons and photons as possible. This is achieved by 75 848 scintillating lead tungstate crystals that are arranged in a barrel with a radius of 1.4 m, covering $|\eta| < 1.5$, and caps, covering $1.5 < |\eta| < 3.0$. Each crystal is 23 cm long with a $22 \times 22 \text{ mm}^2$ face tilted 3° towards the nominal interaction point, covering a $\Delta\phi \times \delta\eta$ surface of 0.0174 at $\eta \approx 0$. The length of the lead tungstate crystals corresponds to 25.8 radiation lengths. The scintillation light is detected by silicon avalanche photodiodes in the barrel and vacuum photodiodes in the caps.

The relative energy resolution of the ECAL was measured with an electron test beam and is parameterized for electron and photons as

$$\left(\frac{\sigma}{E}\right)^2 = \left(\frac{2.8\% \sqrt{\text{GeV}}}{\sqrt{E}}\right)^2 + \left(\frac{12\% \text{ GeV}}{E}\right)^2 + 0.30\%^2,$$

which yields a resolution of $< 1\%$ on the energies of electrons for the relevant energies $> 20 \text{ GeV}$ in this analysis [65]. The \sqrt{E}^{-1} term of the parameterization is caused mainly from the stochastic distribution of the scintillation photon count. The E^{-1} term originates from electronic and digitization noise. The constant term comes from the non-uniformity of the light collection, intercalibration uncertainty and energy leakage from the rear side of the crystals.

To identify neutral meson to double photon decays a preshower detector from lead and silicon strips is placed at $1.653 < |\eta| < 2.6$.

The ECAL is surrounded by the HCAL that measures the hadronic energy components, mainly from particle jets. In the HCAL it is crucial that the energy of all hadrons is absorbed. Therefore it is build out of 0.37 cm thick plastic scintillators as active material with 5 cm

thick brass plates as absorber between them and front and black plates out of steel. Passing particles shower in the absorber layers. The energy of the shower then produces scintillator light which is frequency shifted and channeled into hybrid photodiodes. In the barrel region $|\eta| < 1.4$ each HCAL segment covers a region of $\Delta\phi \times \delta\eta = 0.087$. In the endcaps the segmentation varies in $\Delta\phi$ from 5° to 10° and in $|\eta|$ from 0.087 to 0.35. For $|\eta| < 1.26$ there are additional scintillator layers behind the solenoid. For $3 < |\eta| < 5$ forward HCALs are installed at a distance of 11.2 m in z from the nominal interaction point. In the barrel region the HCAL is about 10 hadronic interaction length thick.

The resolution on jet energies when combining both calorimeters was parameterized from CMS measurements taken with $\sqrt{s} = 7$ TeV [66] as

$$\left(\frac{\sigma}{E}\right)^2 \approx \left(\frac{100\%\sqrt{\text{GeV}}}{\sqrt{E}}\right)^2 + (5\%)^2 .$$

This means an expected energy resolution of the jets considered in this analysis with the lowest energy 30 GeV of 19% and about 10% for the typical leading jet energy of 150 GeV. When information from all subdetectors are combined in the particle flow event-reconstruction algorithm the resolution of such jets goes down to about 5% [67] From past top quark mass measurements the uncertainty on jet energies is expected to be one of the biggest sources of uncertainty in this analysis.

Muon system Around the HCAL is the solenoid magnet coil and around the coil the muon system. Because of the density of HCAL and solenoid, the muon system has a high muon identification purity as other (known, not-neutrino) particles either scatter and are absorbed in the calorimeters or decay too fast to reach it.

The $|\eta| < 1.2$ barrel region of the muon system consists of aluminum drift tubes that provide a resolution of $100\mu\text{m}$ and resistive plate chambers that provide a fast response time. In the endcaps cathode strip tubes are installed instead of drift tubes. The cathode strip tubes provide a resolution of $100\mu\text{m} \times 100\mu\text{m}$ and are optimized for neutral background.

The time resolution of the entire system is around 3 ns, providing excellent trigger capabilities. The momentum resolution for muons is enhanced by combining information of the tracker and the muon system to $\frac{\Delta p_T}{p_T}|_{p_T=1\text{ TeV}} = 5\%$ and $\frac{\Delta p_T}{p_T}|_{p_T=100\text{ GeV}} = 1\%$.

Trigger For the data considered in this analysis the LHC operated with a 25 ns bunch spacing. This translates to a bunch crossing rate at the interaction point of 40 MHz with approximately 20 simultaneous proton-proton collisions per crossing at design luminosity. Only 1000 events per second can be written in permanent storage so a very elaborated trigger system is needed. At CMS, the trigger system is layered in two stages.

The first stage, the Level-1 trigger (L1), is built out of custom hardware with local, regional and global components. It is partially built directly onto the detector components

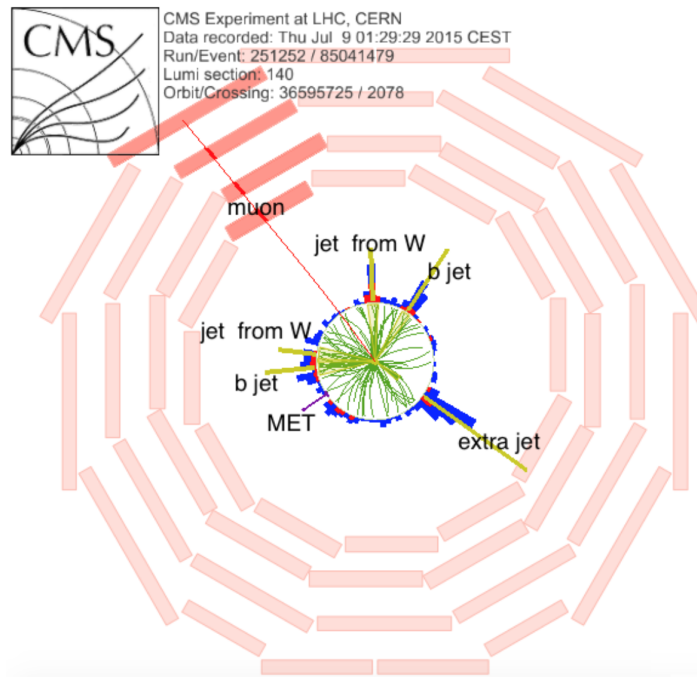


Figure 3.6.: Event display of a top-quark pair candidate in x-y views. This event has one isolated muon, transverse missing energy of 34 GeV, and five hadronic jets. Two of the jets pass the tight threshold on the b-tagging discriminant and are interpreted as originating from the b quarks from top quark decay. Two of the others form an invariant mass of 72 GeV and are interpreted as coming from a hadronically decaying W boson. Leptonic top mass: 166 GeV. Hadronic top mass: 162 GeV [68].

and partially located in an underground control room about 90m away from the detector. The detector components are used at reduced granularity performing scans for events with high-energetic particles and calculations of the total transverse energy. The L1 is designed for a continuous output rate of 30kHz and has a latency of 3.2 μ s. For the latency time the processing is pipelined and quasi deadtime free operation is accomplished.

The second trigger stage is the high-level-trigger (HLT). It uses a farm of standard processors where the information of all detector subsystems are entered and analysis-like calculations can be performed. The total rate of events passing both triggers is 920Hz. Prescales are applied to keep the rate constant for different luminosities. The fully reconstructed data is available for analysis within 48 hours except a part that is stored for reconstruction after the data taking period.

An example of how a $t\bar{t} \rightarrow \mu + \text{jets}$ event candidate impacts the CMS detector is shown in figure 3.6. The muon can be easily identified by its impact on the muon system and the jets are found from energy deposits in ECAL and HCAL. How jets from light and bottom quarks are discriminated will be explained in chapter 5.

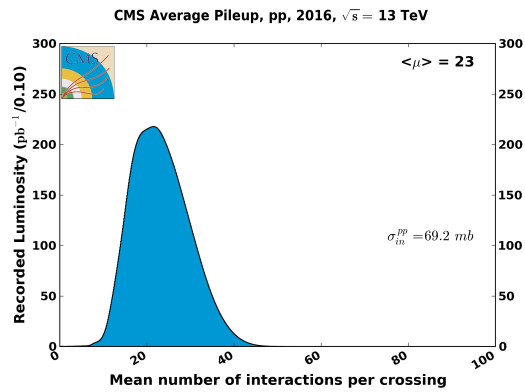


Figure 3.7.: Mean number of interactions per bunch crossing for the 2016 pp run at 13 TeV. The plot uses the CMS recommended value of 69.2 mb, which is determined by finding the best agreement with data and is recommended for CMS analyses.

Pileup Multiple proton-proton interactions per bunch crossing (pileup) happen at the interaction point of the detector during collisions. In the data recorded by CMS during 2016 the mean number of interactions per bunch crossing is 23. The pileup distribution in the data used in this analysis is shown in figure 3.7. Simulated events are weighted to match the pileup distribution in data.

4. Event generation and simulation

One vital part of all physics experiments is a well motivated prediction of their outcome. In high energy particle physics predictions are also utilized to get a hold on not directly observable parameters and to estimate signal acceptances and efficiencies. These predictions can be verified with the distribution of and dependencies on observable properties. The design and test of analysis strategies is also done on simulation in order to not bias features in the data.

The composition and distribution of outgoing partons after particle collision can be calculated by following the standard model of particle physics. These calculations include integrals in high-dimensional phase space. The method of choice for this is Monte-Carlo integration (MC). They ideally converge with $1/\sqrt{n}$, with n randomly sampled phase space points.

On top of this, parton showering and hadronization techniques are applied to predict the actual behavior of a partonic final state in the detector. The stages from the pp-collision over the parton decay, scattering and further evolution including additional radiations, are illustrated in figure 4.1. The steps that are taken to generate data-like predictions from the mathematical description of the standard model of particle physics are described in the following.

Parton distribution functions The starting point of the simulation is the initial state of the process considered. In the case of high energy proton-proton collisions this is not trivial. For low momentum transfer ($Q^2 \sim \mathcal{O}(10\text{GeV}^2)$) a large portion of the momentum is carried by the three valence quarks of the protons. At higher momentum transfers the contribution of sea (anti-)quarks and gluons increase and becomes dominant. The momentum fraction x of the different components of the proton are described by the parton distribution function (PDF) which cannot be calculated perturbatively. PDFs are mainly extracted from deep-inelastic scattering e.g. from proton-X collisions at experiments like HERA [70]. PDFs are evaluated at a factorization scale μ_F , the characteristic hard scattering scale of the investigated process. This ensures that all relevant fluctuations are contained. Extrapolations to higher Q^2 are available in different parameterizations from multiple collaborations often including LHC data in addition to HERA data in their fits. One example for two different values of Q^2 is shown in figure 4.2. For higher Q^2 the contribution of sea quarks and especially gluons increase significantly. A comparison between different PDF sets is shown in figure 4.3 with the major difference being the uncertainty on the contribution of sea quarks and gluons at small x . The use of a different PDF can have impact on the kinematic distribution of the final state of a process. If this is valid for the observables used in this analysis

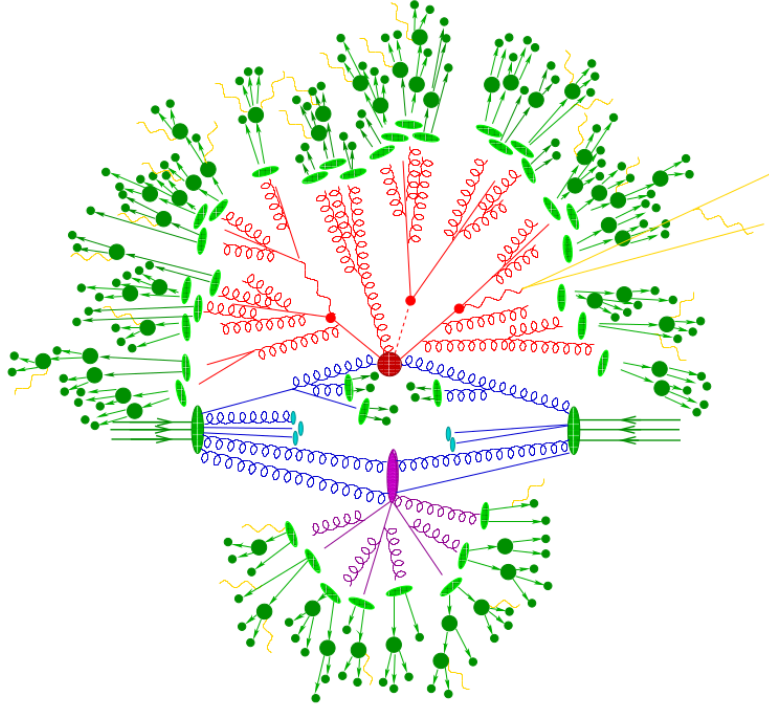


Figure 4.1.: Pictorial representation of a $t\bar{t}h$ event as produced by an event generator. The hard interaction (big red blob) is followed by the decay of both top quarks and the Higgs boson (small red blobs). In addition hard QCD radiation is produced (red) and a secondary interaction takes place (purple blob) before the final-state partons hadronize (light green blobs) and hadrons decay (dark green blobs). Photon radiation occurs at any stage (yellow) [69].

will be tested in subsection 7.2.2.

The minimal average momentum fraction to produce a top-quark pair at $\sqrt{s} = 13$ TeV is $x = \sqrt{x_1 x_2} \geq 2m_t/\sqrt{s} = 0.027$.

In this analysis the PDF set NNPDF 3.1 [71] is used as default.

Hard scattering The hard scattering differential cross section in perturbation theory for a final state fin is given by

$$d\sigma_{fin} = \sum_{k=0}^{legs} d\Phi_{fin+k} \left| \sum_{l=0}^{loops} \mathcal{M}_{fin+k}^{(l)} \right|^2,$$

where Φ_{fin+k} is the momentum configuration and $\mathcal{M}_{fin+k}^{(l)}$ the matrix element with k additional outgoing particles (legs) and l additional loops. In the samples that are used in this thesis as description of the signal, the events were calculated with up to 5 additional outgoing particles and one internal loop with Powheg v2 [74]. Additional matrix element generators that used in background samples are MADGRAPH5 [75] and AMC@NLO v2.2.2 [76].

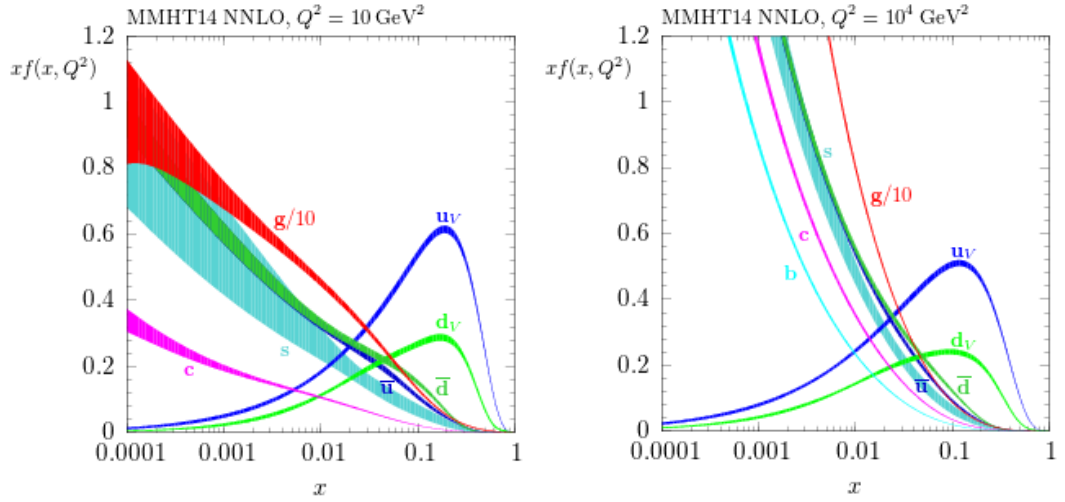


Figure 4.2.: The MMHT 2014 NNLO parton distribution function for different values of Q^2 [72].

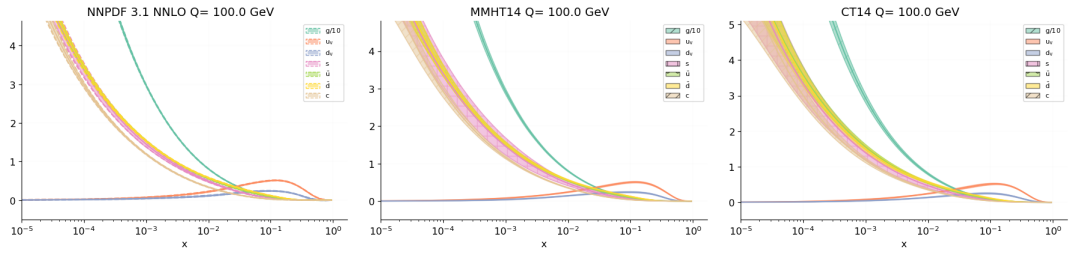


Figure 4.3.: The NNPDF 3.1 (left), MMHT 2014 (middle) and CT14 (right) parton distribution functions for $Q^2 = 100$ GeV [73].

Parton Showering The transitions of quarks and gluons into a multitude of particles in a cone-shaped stream, called jet, is simulated by a parton showering algorithm. Additional electromagnetic and QCD radiations are also included in this process. Parton showers are characterized by their 'width'. In the Pythia 8 tool the width is defined by the p_t of the shower particle in regard to the emitting parton. The showering algorithm is repeated until a cutoff scale Q_0 is reached. The Sudakov factor [77] is used to estimate the probability of no emission between two Q scales. A typical cutoff scale is $Q_0 = 1$ GeV.

Hadronization Below the cutoff scale hadrons are formed from quarks and gluons. In Pythia this is done according to the Lund string model [78]. Color strings are spanned between quark-antiquark pairs. Gluons are treated as "kinks" in these strings. The potential energy between the quarks is lowered by the production of new quark-antiquark pairs. Heavy quarks are suppressed and the transverse momentum to the string direction is smeared following a Gaussian distribution. In addition, hadron decay tables are included in the model and it is tuned e.g. to e^+e^- data. This tune can have a big impact on the prediction of events

at the LHC [79].

Underlying Event Interactions of the event of interest with additional partons from the protons, the underlying event (UE), can also have an effect on the hard scattering process and the energy deposited in the detector. This is enhanced by the geometrical overlap of the two colliding protons and is adjusted by tuning parameters of the simulation to collision data. The multi-parton interaction (MPI) parameters of the MC generators are tuned to match the energy from UE observed in data.

The UE tune **CUETP8M1** was derived by fitting parameters of PYTHIA 8 to CDF underlying event data at $\sqrt{s} = 900$ GeV and $\sqrt{s} = 1.96$ TeV [80] together with CMS data at $\sqrt{s} = 7$ TeV [81]. Unfortunately, initial measurements of the additional jet multiplicity in $t\bar{t}$ events using $\sqrt{s} = 13$ TeV CMS data have shown poor agreement [82, 83].

To mitigate this, an additional re-tune is added on top of CUETP8M1 by fitting the h_{damp} and α_s^{ISR} in PYTHIA 8 to $\sqrt{s} = 8$ TeV CMS dilepton data via the jet multiplicity and leading additional jet multiplicity distributions. This tune **CUETP8M2T4** [82] was used in the last CMS top quark mass analyses and during the earlier development of this analysis. In the presented state for all $t\bar{t}$ signal and variation simulation samples, the **CP5** underlying event tune [83] is used. This tune was obtained by fitting CDF underlying event data at $\sqrt{s} = 900$ GeV and $\sqrt{s} = 1.96$ TeV together with CMS data at $\sqrt{s} = 7$ TeV and $\sqrt{s} = 13$ TeV. In addition this tune is based on the higher-order PDF set NNPDF3.1 at NNLO, that is able to give a more reliable description of minimum-bias and UE measurements. For tuning, the parameters in PYTHIA 8 are varied to match a number of distributions in an NLO evolution. The varied parameters are the exponent of the \sqrt{s} dependence, the matter fraction contained in the core, the radius of the core, and the range of the color reconnection probability. They are varied to match the MPI, the final state radiation (FSR) and the initial state radiation (ISR) contributions from hard scattering, and the running of the ISR.

A comparison between the CUETP8M2T4 and CP5 tunes with data in the selected phase-space of this analysis will be shown in section 6.1.2.

Color reconnection Color reconnection (CR) models non-pertubatively describe changes to the color configuration of events before the hadronization stage. Each multi-parton interaction adds colored partons to the final state. This creates a dense net of color lines that overlap with the parton fields from the hard scattering and with each other, and may be connected with one another. This connection, interaction and information exchange is implemented in a color reconnection model. It can improve the mean transverse momentum description and multiplicity in minimum bias events that can be investigated for charged particles. There are different color reconnection models implemented in Pythia 8.

The CR model used as default is **MPI-based** [84]. In this model partons are classified by their MPI system, with the scale p_T of its hard interaction. The MPI system connects to systems with a harder scale with the probability $P = \frac{p_{TRec}^2}{p_{TRec}^2 + p_T^2}$ with $p_{TRec} = R \cdot p_{T0}$ where R is a tunable parameter and p_{T0} is the energy-dependent dampening parameter used for MPIs.

After reconnecting the MPI systems, their string lengths are minimized. The MPI-based model is the simplest one implemented in MC event generators and introduces only one free parameter.

As we cannot directly compare it to data, the effects of changing the CR model will be treated as an uncertainty in this analysis. The considered alternative models are the QCD-inspired [85] and the gluon-move model [86].

The **QCD-inspired** model adds color rules to the string length minimization. All pairs of dipoles that are allowed to reconnect by this color rule are iteratively reconnected until no allowed reconnection lowers the total string length anymore. In addition the creation of junction structures, which enable the inclusion of higher order effects in the CR model, are allowed. The free parameters of the QCD-inspired model are the lower limit for the mass of particles that are not allowed to be color connected and the definition of the causal contact between color strings.

In the **gluon-move** model all gluons are identified, along with all the color connected pairs of partons. For each final-state gluon attached to a parton's string piece the gluon is moved to the string which results in the smallest change of string length. This is iterated until no smaller changes are possible or a lower limit for string length or maximum reduction is reached. The main free parameters of the gluon-move model are the lower limit of the string length allowed for color connections, the fraction of gluons allowed to move or flip and the lower limit of the string length's allowed reduction.

A more in-depth comparison and a tune of these models can be found in reference [87].

Detector simulation The generated events are processed by a full CMS detector simulation with GEANT4 [88]. This includes the responses of all subsystems and effects of the support and read-out structure between them. On the result of the detector simulation the full event reconstruction, which will be described in chapter 5, is run. This results in data-like events that include generator and matching informations that are not included in data actual recorded by the CMS experiment.

5. Event reconstruction

Before the analysis dependent selections and evaluations, the data recorded by the CMS detector is reconstructed into physics-inspired high level objects. An intermediate state between the full reconstruction and raw detector output are track candidates and clusters, that were recorded and combined from different detector components. The reconstruction is done using the CMS software framework (CMSSW) based on the ROOT data analysis framework [89]. The reconstructed events are saved in Analysis Object Data (AOD) files and in the reduced format MINIAOD [90]. The reduced version includes all information needed in this analysis.

Primary vertex identification With the pileup expected at the high luminosities of the LHC operation in 2016 it is important to identify which tracks and energy clusters originate from the interaction that triggered the data recording. To identify this interaction and to exclude particles from other interactions its primary vertex is identified. The charged particle tracks closest to the beam line that cross at the same point are selected for the reconstruction. Each of these tracks has to be fitted from at least five hits in the inner tracker, including at least two hits in the pixel detector with $\chi^2_{(\text{normalized})} < 20$ of the track fit.

The tracks are then clustered by the adaptive vertex fitter [91]. It checks the compatibility of the tracks with all possible vertices. For each event, the vertices within 2 cm transverse and 24 cm longitudinal distance of the nominal interaction point are considered. A fit with at least four degrees of freedom is performed and the vertex with the highest $\sum p_T^2$ of its associated tracks is taken as the primary vertex. Using CMS data at $\sqrt{s} = 7$ TeV the primary vertex resolution was found to be smaller than $50\mu\text{m}$ in all directions [91].

Particle flow All CMS sub-detector systems are combined in the particle-flow (PF) algorithm to identify particles [92,93]. At first, all tracks associated with muons, easily identified by the muon detector, are removed. The remaining tracks are connected with calorimeter energy deposits. Energy deposits significantly larger than the momentum calculated from their associated track or without a track are identified as overlapping neutral hadrons or photons. Energies in the HCAL are corrected for deposits in the ECAL and the non-linear HCAL response. On average a jet consists of 65% charged hadrons, 25% photons, and 10% neutral hadrons.

5.1. Lepton identification and reconstruction

This analysis looks at the final particle states from pp-collisions that include exactly one lepton. Therefore a precise lepton identification is crucial. Because of the special challenges in identifying short lived taus, only muons and electrons will be considered.

At the CMS detector muons are reconstructed using the inner tracking system and the muon system outside of the solenoid. To be tagged as *global muon* a track must have at least 5 hits within the inner tracker, including one in the pixel detector, one hit in the muon chamber and a $\chi^2/N_{\text{df}} < 10$ of the track fit. The muon track has to have an impact parameter with respect to the beam spot of $|\Delta d_0| < 0.02$ cm and a maximal distance to the primary vertex of 0.5 cm in beam line direction.

The PF isolation I of a lepton, within a radius R in respect to the lepton direction, is defined as

$$I(R) = \left(\sum_{\text{ch}(R)} p_{\text{T}} + \max \left(\sum_{\text{nh}(R)} p_{\text{T}} + \sum_{\gamma(R)} p_{\text{T}} - \frac{1}{2} \sum_{\text{chPU}(R)} p_{\text{T}}, 0 \right) \right) / p_{\text{T}}^{\text{lep}}, \quad (5.1)$$

with charged hadrons $\text{ch}(R)$, neutral hadrons $\text{nh}(R)$, photons $\gamma(R)$, and charged hadrons out of pile up $\text{chPU}(R)$.

The muon momentum scale is calibrated with a precision of 2%. The relative momentum resolution of single μ is $\sigma(p_{\text{T}})/p_{\text{T}}$ between 1.5% and 5%. The performance of the CMS muon reconstruction is described in reference [94]. In addition a additional momentum scale correction based on $Z \rightarrow \mu\mu$ decays is applied following the ROCHESTER algorithm described in ref. [95,96].

Electrons are more complicated to identify than muons. Due to the combination of bremsstrahlung and photon to e^+e^- pair conversion, the basic properties of electrons and photons in the CMS detector are similar. They are reconstructed from inner tracker and calorimeter information. Based on the number of hits and the χ^2 of the track fit, a pre-selection is applied and the tracks are fit again with a Gaussian-sum filter (GSF). If the ECAL cluster is linked to less than four GSF tracks it is only used as seed for an electron candidate but not included in the track. ECAL clusters with $E_{\text{T}} > 10$ GeV without a link to a track are used as seed for photon candidates. For both cases the energy measured in the HCAL within a radius of 0.15 in the (η, ϕ) plane has to be at most 10% of the energy in the ECAL cluster. The ECAL cluster energy is E and η dependent corrected for energy that was wrongly not associated to it. At the thickest tracker part at $|\eta| \approx 1.5$ and for low electron p_{T} this correction can be on the order of 25%. To be finally identified as an electron, additional criteria have to be satisfied. The energy radiated off the GSF track, the distance between the GSF tracks to the ECAL entrance, the position of the ECAL cluster, the ratio between the energies gathered in HCAL and ECAL and the χ^2 of the GSF track and a Kalman Filtering track fit are combined in a boosted decision tree. The BDT is trained for events in the ECAL barrel and the endcaps and for isolated and non-isolated electron separately [97]. The efficiency of this identification is $> 80\%$ for $|\eta| < 2$ and $> 90\%$ for $|\eta| < 0.8$ with a mis-identification

probability to hadrons of 4% in the momentum range relevant for this analysis.

Selected electrons are required to have a PF isolation of $I(\Delta R < 0.3) < 0.15$, an impact parameter with respect to the beam spot of $|\Delta d_0| < 0.02$ cm, and a maximal distance to the primary vertex of 0.5 cm in beam line direction. The energy resolution of PF electrons is better than 4%.

5.2. Jet reconstruction

Jets are the most complex physics objects reconstructed by the particle flow algorithm. Due to confinement in QCD one gluon or quark in leading order decays into cone-shaped streams of a multitude of particles, called a 'jet'. The sum of energy in a jet is susceptible to detector effects and additional particles from pile up. Therefore the jet energy and resolution is corrected in multiple steps. Jets from bottom quark decays can be identified using b-tagging algorithms.

Jet clustering The energy deposits that were not identified as originating from leptons by the PF algorithm are clustered into jets. A sequential algorithm is used, that is defined via

$$d_{ij} = \min(p_{T,i}^{2k}, p_{T,j}^{2k}) \frac{(\eta_i - \eta_j)^2 + (\phi_i - \phi_j)^2}{R^2}$$

$$\text{and } d_i = p_{T,i}^{2k},$$

with the pseudo-rapidity η and the radius of the characteristic cluster scale R . If the d_i of a particle is smaller than its d_{ij} to every other particle, it is declared a jet and removed from the list of particles. If this is not the case, the two particles with the smallest d_{ij} are clustered together. This is repeated until no particles are left.

The momentum of a jet is determined from the vector sum of all particle momenta in the jet. This algorithm is colinear and infrared safe and results in different jet shapes for different values of k . With $k = -1$ it is called anti- k_T algorithm [98,99] and results in cone shaped jets with a maximum radius of R . The anti- k_T algorithm with $R = 0.4$ is used for this analysis.

Charged hadron subtraction (CHS) is applied. This means that charged particles that are associated with any primary vertex other than the selected primary vertex are excluded in the clustering.

To suppress fake jets an event is rejected if its charged hadron, neutral hadron or photon fraction is equal to exactly 0 or 1.

At this stage the reconstructed jet momentum in simulation is found to be typically within a 5–10% range of the true jet momentum.

Jet energy correction The important property of a jet is its energy. Its measurement is imperfect due to the finite radius in the jet clustering algorithm and energy contributions not from the same event. Such energy contributions can originate from pileup and multi-parton interactions. To correct for these effects jet energy corrections (JEC) are applied [100].¹

In the simulated samples the 'true' energy of the particles before the interaction with the detector is known. This information level is called *gen*-level. The level after recombination, including all detector effects, is called *reco*-level. This level is tuned to match the *gen*-level energy from that event, including the following calibrations.

In the first calibration step the offset of additional energy in the jet cone through electronic noise and pileup, mainly via neutral hadrons and photons, is estimated [101].

The second step balances the relative jet response for different η regions of the detector in relation to its central region ($|\eta| < 1.3$). This correction is derived from simulated events. Afterwards residual corrections are added by in-situ balancing two-jet-events in data that include jets in different η regions with the same transverse momentum, and from γ/Z +jet events. The dijet residual corrections are done η dependent and the γ/Z +jet residual corrections p_T dependent. The residual corrections are only applied to data and not to simulation. For this analysis the JEC step correcting flavor dependencies is not used but uncertainties for the differences will be considered in section 7.1. All correction stages, labeled with their reference source, are illustrated in figure 5.1 [102–106]. In figure 5.2 properties of the different correction stages are shown. In the left plot the simulated jet response is shown for different p_T - η regions. The p_T dependence gets more significant for high $|\eta|$. The middle plot shows the η dependent residual corrections. The derived corrections are different for different data taking periods in 2016, but that problem does not occur for jets with $|\eta| < 2.5$ that are used in this analysis. The right plot shows the data to simulation ratio of the p_T dependent residual response that needs about 2% correction at the typical jet p_T of this analysis.

The uncertainty on the jet energy corrections will be discussed in section 7.

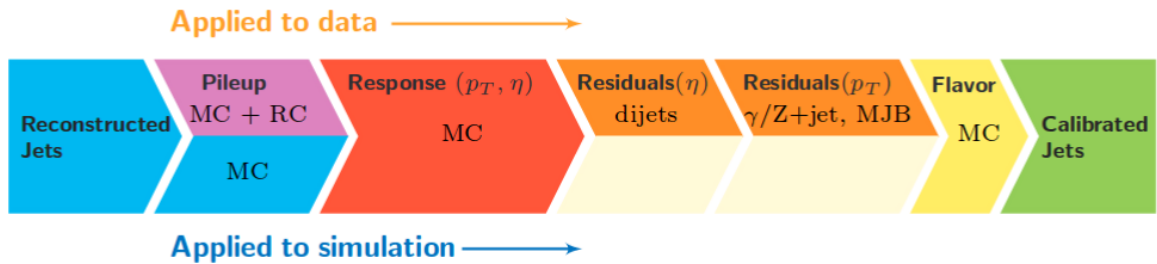


Figure 5.1.: Consecutive stages of JEC, for data and MC simulation. All corrections marked with MC are derived from simulation studies, RC stands for random cone, and MJB refers to the analysis of multi-jet events [107].

¹ In this thesis the jet energy correction labeled Summer16_07Aug2017A11_V11_DATA is used for data and Summer16_07Aug2017_V11_MC for simulation.

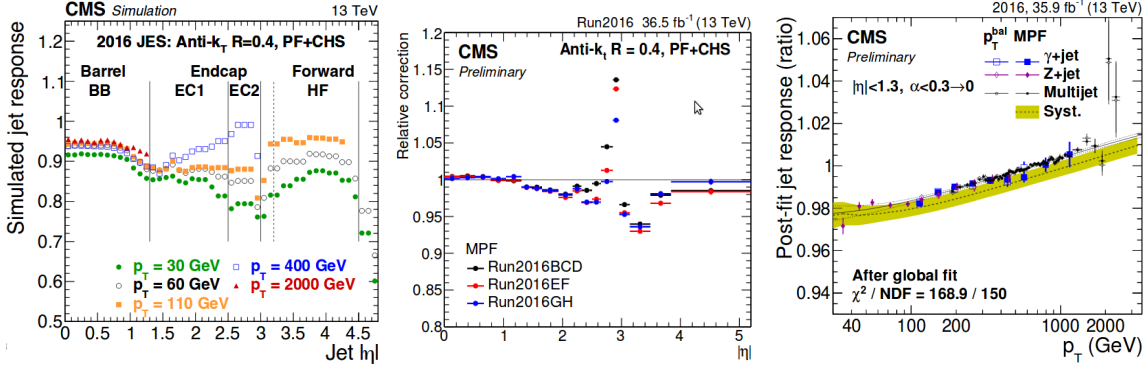


Figure 5.2.: Properties of the jet performance in $\sqrt{s} = 13$ TeV CMS data recorded in 2016. The response of jets in simulation (left), the relative residual correction for simulation to match the data (middle), and the relative response after the jet clustering (right) [102].

Jet energy resolution correction The energy resolution of jets (JER) in CMS data is worse than observed in simulation. Simulated jets are corrected to match the resolution of jets in data. This is done using the hybrid method. If the simulated jet can be matched to a generator parton, the four-momentum of the reconstructed jet is scaled by

$$c_{\text{JER}} = \max \left(1 + (s_{\text{JER}} - 1) \frac{p_{\text{T}} - p_{\text{T}}^{\text{gen}}}{p_{\text{T}}}, 0 \right).$$

with the transverse momentum of the reconstructed jet p_{T} , the transverse momentum of the corresponding parton at generator level $p_{\text{T}}^{\text{gen}}$ and the data-to-simulation core resolution scale factor s_{JER} . If no corresponding generator parton could be matched within

$$\Delta R < R_{\text{cone}}/2 \text{ and } |p_{\text{T}} - p_{\text{T}}^{\text{gen}}| < 3\sigma_{\text{JER}}p_{\text{T}}$$

with the jet cone size parameter R_{cone} from the clustering algorithm set to 0.4 for the jets used in this thesis, and the relative p_{T} resolution measured in simulation, σ_{JER} , the stochastic smearing method is applied. In the stochastic smearing method the four-momenta of the reconstructed jets are scaled by

$$c_{\text{JER}} = \max \left(1 + \mathcal{N}(0, \sigma_{\text{JER}}) \sqrt{\max(s_{\text{JER}}^2 - 1, 0)}, 0 \right)$$

with random numbers sampled from a normal distribution \mathcal{N} with a mean of zero and a variance of σ_{JER} [108].

The data-to-simulation core resolution scale factors s_{JER} , including uncertainties, were provided by the JetMET group [109] and are listed in table 7.1.

5.2.1. Missing transverse energy

The missing transverse momentum or energy (MET) is defined as

$$\vec{E}_T^{\text{miss}} = - \sum_{i \in \text{PF-particles}} \vec{p}_{T,i} ,$$

the transverse momentum imbalance of all PF particles in an event. All calibrations on jets with $p_T > 15 \text{ GeV}$ are propagated into \vec{E}_T^{miss} . In the standard model of particle physics the neutrino is the only particle that will, assuming a perfect detector, result in missing energy. One neutrino is expected in the decay channel of this analysis. Outside the SM, other particles are postulated that can cause a significant amount of missing energy. E_T^{miss} also arises from mis-measured energy e.g. from finite resolution of the identified objects. The E_T^{miss} performance of the CMS detector has been carefully validated in reference [110]. E_T^{miss} will be used in this analysis as input to the kinematic fit that will be presented in section 6.3.

6. Event selection

To enrich the fraction of $t\bar{t} \rightarrow l+jets$ signal events in the data, various phase-space selections and a fit to a $t\bar{t} \rightarrow l+jets$ hypothesis are performed. Both have been chosen carefully to avoid correlation to the top quark mass. The event selection and reconstruction is performed in CMSSW 9.4.14. For detector conditions and object calibrations, the global tags used in the analysis are 94X_dataRun2_v10 for data and 94X_mcRun2_asymptotic_v3 for simulation. A subset of the information contained in MINIAOD and some additional calculated event weights and optimizations of selected events are saved in a custom format for further analysis. This selection and event based calculations are performed on the German National Analysis Facility (NAF) infrastructure utilizing GRID-CONTROL [111] for the submission of jobs.

6.1. Used samples

6.1.1. Data samples

As this thesis considers a single lepton final state, data sets recorded by CMS at $\sqrt{s} = 13$ TeV pp collisions during 2016 that activated the single muon or the single electron trigger are considered. A list of the data sets used, their event count and integrated luminosity L_{int} is presented in Table 6.1.¹ This way 804 million single muon and 962 million single electron events are selected. For the single electron selection regions with a high trigger prescale were avoided. Because of this the selected muon events correspond to $L_{\text{int}} = 36 \text{ fb}^{-1}$ and the selected electron events only to $L_{\text{int}} = 32 \text{ fb}^{-1}$.

6.1.2. Simulated samples

The measurement technique is developed and validated with the simulated samples listed in the tables 6.3 and 6.4. Additional samples used to estimate systematic uncertainties are listed

¹The certified runs of the collected data are selected with the JSON file *Cert_271036-284044_13TeV_ReReco_07Aug2017_Collisions16_JSON.txt* corresponding to $L_{\text{int}} = 35.9 \text{ fb}^{-1}$.

Table 6.1.: Single lepton data sets for RunII data at 13 TeV recorded in 2016.

Dataset	Event count	$L_{\text{int}}[\text{fb}^{-1}]$
SingleMuonRun2016B-17Jul2018_ver2-v1MINIAOD	158 145 722	5.75
SingleMuonRun2016C-17Jul2018-v1MINIAOD	67 441 308	2.57
SingleMuonRun2016D-17Jul2018-v1MINIAOD	98 017 996	4.24
SingleMuonRun2016E-17Jul2018-v1MINIAOD	90 984 718	4.03
SingleMuonRun2016F-17Jul2018-v1MINIAOD	65 489 554	3.10
SingleMuonRun2016G-17Jul2018-v1MINIAOD	149 912 248	7.58
SingleMuonRun2016H-17Jul2018-v1MINIAOD	174 035 164	8.65
Σ single muon data	804 026 710	35.92
SingleElectronRun2016B-17Jul2018_ver2-v1MINIAOD	246 440 440	5.75
SingleElectronRun2016C-17Jul2018-v1MINIAOD	97 259 854	2.57
SingleElectronRun2016D-17Jul2018-v1MINIAOD	148 167 727	4.24
SingleElectronRun2016E-17Jul2018-v1MINIAOD	117 321 545	3.63
SingleElectronRun2016F-17Jul2018-v1MINIAOD	70 593 532	2.91
SingleElectronRun2016G-17Jul2018-v1MINIAOD	153 363 109	6.15
SingleElectronRun2016H-17Jul2018-v1MINIAOD	129 021 893	5.99
Σ single electron data	962 168 100	31.23

in table 6.5. Simulated $t\bar{t}$ signal events were generated with the POWHEG V2 matrix element generator [74], PYTHIA 8.205 parton showering [112] using the underlying CP5 tune [113] and a full simulation of the CMS detector based on GEANT 4 [114]. The CP5 tuned samples were generated separately for the different $t\bar{t}$ decay channels. The fractions of the $t\bar{t}$ decay channels were weighted according to their corresponding event based NLO generator cross sections. With the CP5 tune 107 604 800 events are available in the lepton+jets channel and ~ 60 Million in the dilepton and all-jets channel each. That are three times as many as in the sample used by the last semi-leptonic top quark mass measurement published [7]. In control distributions related to this analysis the difference in the underlying event tunes can be seen in the jet p_T distributions and number of jets as shown in figure 6.1. The plot already contains the selection that will be described later in this chapter, without the kinematic fit criteria (baseline selection). The biggest difference could be seen in the number of jets for events with five to eight jets, so for one to three additional jets on top of the $t\bar{t}$ decay, the CP5 tune agrees better with data.

Simulation samples with a top-quark mass of 169.5 GeV, 172.5 GeV 175.5 GeV are used. W/Z+jets (generated with PYTHIA8), single-top (generated with POWHEG+PYTHIA8 for the tW-channel, POWHEG+MADSPIN+PYTHIA8 for the t-channel and AMC@NLO+PYTHIA8 for the s-channel), Diboson (generated with PYTHIA 8) and QCD-multijet (generated muon and electron enriched in p_T bins with PYTHIA 8) final states are considered as background. All samples are normalized to their theoretical predicted cross sections [115–125]. The theoretical cross section σ of the $t\bar{t}$ signal with the default top-quark mass of $m_t = 172.5$ GeV is

$$\sigma = 831.76^{+19.77}_{-29.20}(\text{scale uncert.})^{+35.06}_{-35.06}(\text{PDF}+\alpha_s \text{ uncert.})^{+23.18}_{-22.45}(\text{mass uncert.})\text{pb} \quad .$$

The cross section of the top-quark mass variation samples with a top-quark mass m_t is calculated from the PDF dependent parameterization [121]

$$\sigma(m_t) = \sigma(m_{\text{ref}}) \left(\frac{m_{\text{ref}}}{m_t} \right)^4 \left[1 + a_1 \left(\frac{m_t - m_{\text{ref}}}{m_{\text{ref}}} \right) + a_2 \left(\frac{m_t - m_{\text{ref}}}{m_{\text{ref}}} \right)^2 \right]$$

with the default top quark mass $m_{\text{ref}} = 172.5$ GeV and PDF dependent a_i listed in table 6.2. Effectively a global normalization scale on the signal sample only effects the signal to back-

Table 6.2.: Result of the fit to the top-quark mass dependence for the $t\bar{t}$ cross sections at 13 TeV. The top-quark mass is set to 172.5 GeV [121].

PDF set	a_1	a_2
MSTW2008 NNLO	-0.715324	0.175732
CT10 NNLO	-0.708529	0.213963
NNPDF2.3 NNLO	-0.745047	0.127417

ground fraction that introduces, as will be show in chapter 7, no major source of uncertainty. Events in samples that were generated with AMC@NLO can have negative weights, that were accounted for in their normalization.

The simulated events include effects of additional pileup and are weighted to match their distribution in data with the best fit value of the total pp (inelastic) cross sections corresponding to $69.2 \text{ mb} \pm 4.6\%$ [104]. The simulated events are also scaled with event based weights to account for different efficiencies of the trigger, lepton identification, lepton isolation and b-tagging compared to data. The JER in the simulated samples is scaled to match the resolution observed in data using the hybrid method described in subsection 5.2. These corrections will be explained in more detail later.

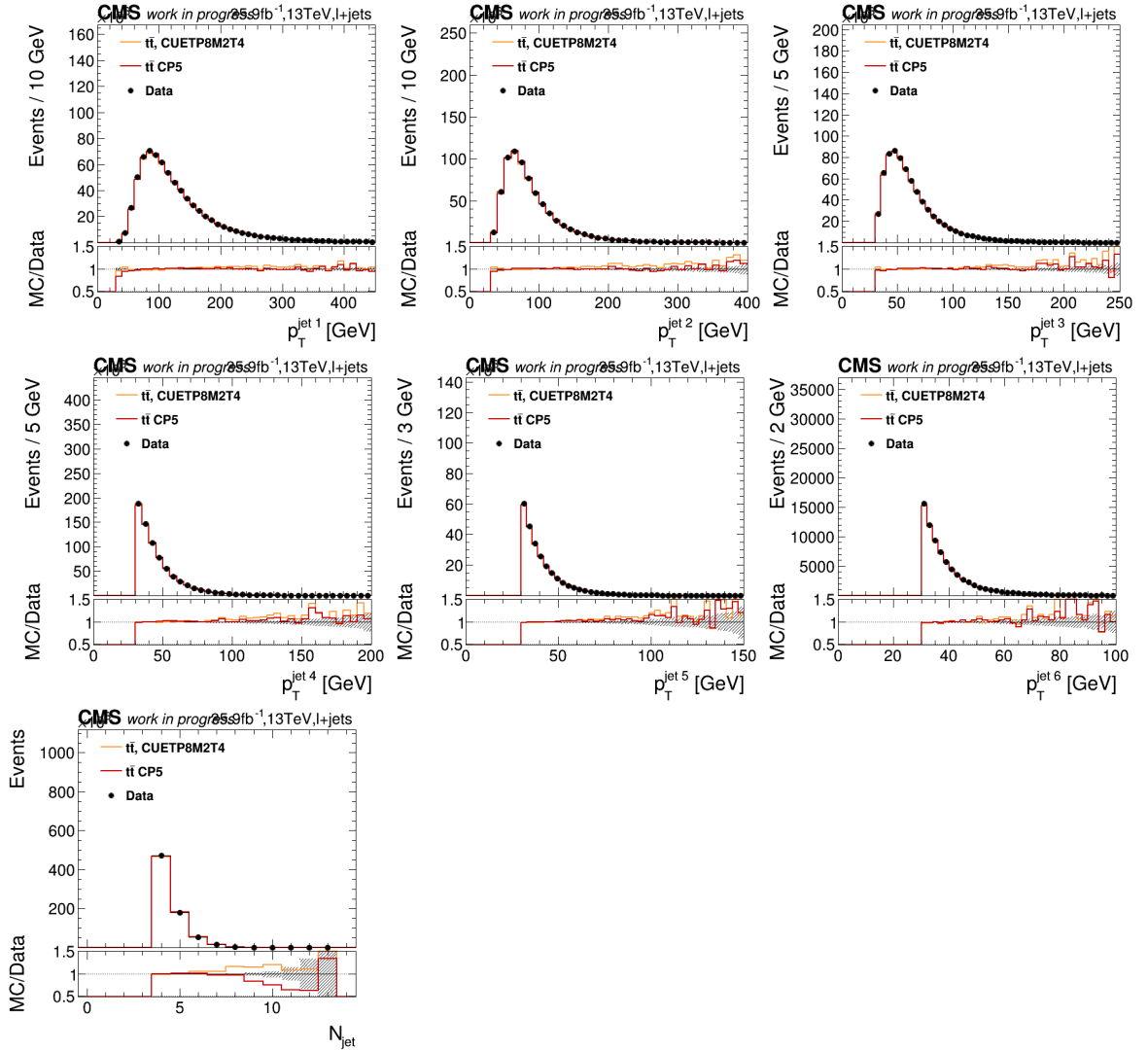


Figure 6.1.: Baseline selection lepton+jets: comparing the p_T distributions of the first six leading jets (upper two rows) and the number of (additional) jets (bottom row) for different UE tunes. The number of events in simulation was normalized to the number of events in data.

Table 6.3.: List of simulated samples used for signal, mass variation and background with the used matrix element generators and parton showering tools, the number of generated events and the corresponding expected cross-section of the final state.

Dataset	Event count	σ [pb]
t \bar{t} signal tune CP5 (POWHEG+PYTHIA8)		
TTToSemiLeptonic default ($m_t = 172.5$)	107 604 800	832
TTToHaronic default ($m_t = 172.5$)	68 518 800	832
TTTo2L2Nu default ($m_t = 172.5$)	67 926 800	832
TTToSemiLeptonic $m_t = 169.5$	26 832 000	903
TTTo2L2Nu $m_t = 169.5$	14 466 400	903
TTToSemiLeptonic $m_t = 175.5$	21 903 400	767
TTTo2L2Nu $m_t = 175.5$	11 303 600	767
background tune CUETP8M1		
WJetsToLNu (MADGRAPHMLM+PYTHIA8) (default,ext2)	29 514 020	61526.7
ST_tW_top_5f_inclusiveDecays (POWHEG+PYTHIA8)	6 952 830	35.6
ST_tW_antitop_5f_inclusiveDecays (POWHEG+PYTHIA8)	6 933 094	35.6
ST_t-channel_top_4f_inclusiveDecays (POWHEGV2-MADSPIN-PYTHIA8)	67 105 876	137.6
ST_t-channel_antitop_4f_inclusiveDecays (POWHEGV2-MADSPIN-PYTHIA8)	38 811 017	82.7
ST_s-channel_4f_leptonDecays (AMCATNLO-PYTHIA8)	1 000 000	10.4
DYJetsToLL M-10to50 (AMCATNLOFXFX-PYTHIA8) (default,ext1)	108 345 470	22 635.1
DYJetsToLL M-50 (AMCATNLOFXFX-PYTHIA8)	120 777 245	6 025.2
WW (PYTHIA8) (default,ext1)	994 012	115.0
WZ (PYTHIA8) (default,ext1)	1 000 000	47.1
ZZ (PYTHIA8) (default,ext1)	990 064	16.5

Table 6.4.: List of simulated samples used for QCD-multijet background with the used matrix element generators and parton showering tools, the number of generated events and the corresponding expected cross-section of the final state.

Dataset	Event count	σ [pb]	ϵ_{filter}
QCD-multijet background tune CUETP8M1 (PYTHIA8)			
QCD Pt-15to20 MuEnriched	4 141 251	1273190000	0.003
QCD Pt-20to30 MuEnriched	31 878 740	558528000	0.0053
QCD Pt-30to50 MuEnriched	29 954 815	139803000	0.01182
QCD Pt-50to80 MuEnriched	19 662 175	19222500	0.02276
QCD Pt-80to120 MuEnriched (default,ext1)	23 705 386	2758420	0.03844
QCD Pt-120to170 MuEnriched	7 897 731	469797	0.05362
QCD Pt-170to300 MuEnriched (default,ext1)	17 350 231	117989	0.07335
QCD Pt-300to470 MuEnriched (default,ext1,ext2)	49 005 976	7820.25	0.10196
QCD Pt-470to600 MuEnriched (default,ext1,ext2)	19 489 276	645.528	0.12242
QCD Pt-600to800 MuEnriched (default,ext1)	9 981 311	187.109	0.13412
QCD Pt-800to1000 MuEnriched (default,ext1,ext2)	19 940 747	32.3486	0.14552
QCD Pt-1000toInf MuEnriched (default,ext1)	13 628 219	10.4305	0.15544
QCD Pt-20to30 EMEnriched	9 241 500	557600000	0.009
QCD Pt-30to50 EMEnriched (default,ext1)	11 508 842	136000000	0.073
QCD Pt-50to80 EMEnriched (default,ext1)	45 789 059	19800000	0.146
QCD Pt-80to120 EMEnriched (default,ext1)	77 800 204	2800000	0.125
QCD Pt-120to170 EMEnriched (default,ext1)	78 578 415	477000	0.132
QCD Pt-170to300 EMEnriched	11 540 163	114000	0.165
QCD Pt-300toInf EMEnriched	7 380 341	9000	0.15
QCD Pt-15to20 bcToE	2 685 602	1 272 980 000	0.00020
QCD Pt-20to30 bcToE	10 987 947	557 627 000	0.000754
QCD Pt-30to80 bcToE	15 342 783	159 068 000	0.0029
QCD Pt-80to170 bcToE	14 851 987	3 221 000	0.01248
QCD Pt-170to250 bcToE	9 862 070	105 771	0.0244
QCD Pt-250toInf bcToE	9 861 593	21 094.1	0.0345

Table 6.5.: List of simulated variation samples for systematic uncertainty estimation with the used matrix element generators and parton showering tools, the number of generated events and the corresponding expected cross-section of the final state.

Dataset	Event count	σ [pb]
t \bar{t} variation tune CP5 (POWHEG+PYTHIA8)		
TTToSemiLeptonic QCDBasedCRTune	29 208 200	832
TTToHaronic QCDBasedCRTune	27 446 200	832
TTTo2L2Nu QCDBasedCRTune	14 846 400	832
TTToSemiLeptonic GluonMoveCRTune	26 468 200	832
TTToHaronic GluonMoveCRTune	28 881 600	832
TTTo2L2Nu GluonMoveCRTune	13 536 900	832
TTToSemiLeptonic erdOn	28 973 400	832
TTToHaronic erdOn	27 338 000	832
TTTo2L2Nu erdOn (default,ext1)	14 563 200	832
TTToSemiLeptonic TuneCP5up	29 239 200	832
TTToHaronic TuneCP5up	27 939 400	832
TTTo2L2Nu TuneCP5up (default,ext1)	14 838 600	832
TTToSemiLeptonic TuneCP5down	28 951 700	832
TTToHaronic TuneCP5down	27 921 200	832
TTTo2L2Nu TuneCP5down (default,ext1)	14 366 800	832
TTToSemiLeptonic hdampUp	29 671 200	832
TTToHaronic hdampUp	28 695 100	832
TTTo2L2Nu hdampUp (default,ext1)	14 889 100	832
TTToSemiLeptonic hdampDown	29 818 400	832
TTToHaronic hdampDown	28 900 700	832
TTTo2L2Nu hdampDown (default,ext1)	14 908 700	832

6.2. Semi-leptonic event selection

The selection of $t\bar{t}$ events with a cross section of only $\sigma_{t\bar{t}} \approx 0.83 \text{ nb}$ among the $\sigma_{\text{total LHC pp}} \approx 10^8 \text{ nb}$ is not a trivial task. The selection for this $t\bar{t} \rightarrow l+\text{jets}$ analysis starts with taking data that were triggered with a single muon or electron. In further selection steps, this data is filtered so that each event includes exactly one high energy lepton and at least four high energy jets, that do not overlap with the lepton. The comparison with simulated events will show that this suppresses background events at the same time.

Trigger selection The first step of the selection is to filter events that passed a high level trigger (HLT) that identifies putative leptons. Events with isolated muons are selected if they activated the *HLT_IsoMu24_v** or the *HLT_IsoTkMu24_v** high level trigger with a muon p_T threshold of 24 GeV. Events with electrons are selected with the *HLT_Ele27_WPTight_Gsf_v** trigger with a electron p_T threshold of 27 GeV and a b-tagged jet. In comparison the last $t\bar{t} \rightarrow l+\text{jets}$ top-quark mass analysis [8] used the tighter electron trigger *HLT_Ele32_eta2p1_WPTight_Gsf_v**. The combination of a more efficient b-tagging algorithm with a lower electron p_T cut lead to more selected events than in the previous analysis.

The trigger contains the isolation criteria for isolated muons following the *loose* particle flow cuts suggested in [126]. Electrons are identified using the *cutBasedElectronID_Fall17_94X_V2* on the *tight* working point and use particle flow based isolation criteria as recommended in [127]. Harder cuts on these isolation criteria will be applied for the final selection.

Scale factors for the trigger, reconstruction and selection efficiencies are applied. They were determined via the tag-and-probe method from $Z \rightarrow \ell^+ \ell^-$ decays. One of the leptons is required to activate the trigger with tight selection criteria and the invariant mass of the lepton pair has to be within a window of 15 GeV around the Z-boson mass. The efficiencies are determined by applying the selection and trigger criteria to the probe leptons and normalize to their total number. The data-to-MC scale factors are the ratios of the efficiencies in data and simulation and are evaluated dependent on the lepton p_T and η . The trigger efficiency and scale factors are shown in figure 6.2 for muons and in figure 6.3 for electrons. The electron trigger has a much softer turn on up to 50 GeV. Both triggers have a considerable η dependency of their efficiency that gets lower for $|\eta| > 1.3$. The combined average scale-factor is 0.970 ± 0.001 (stat) for muons and 0.976 ± 0.001 (stat) for electrons [128, 129].

Trigger, isolation and identification scale factors as recommended and documented in [127, 132–134] are applied on the simulated events to match the efficiencies in data as event based weights. Maps of the isolation and identification scale factors that were used in this thesis are shown in figure 6.4.

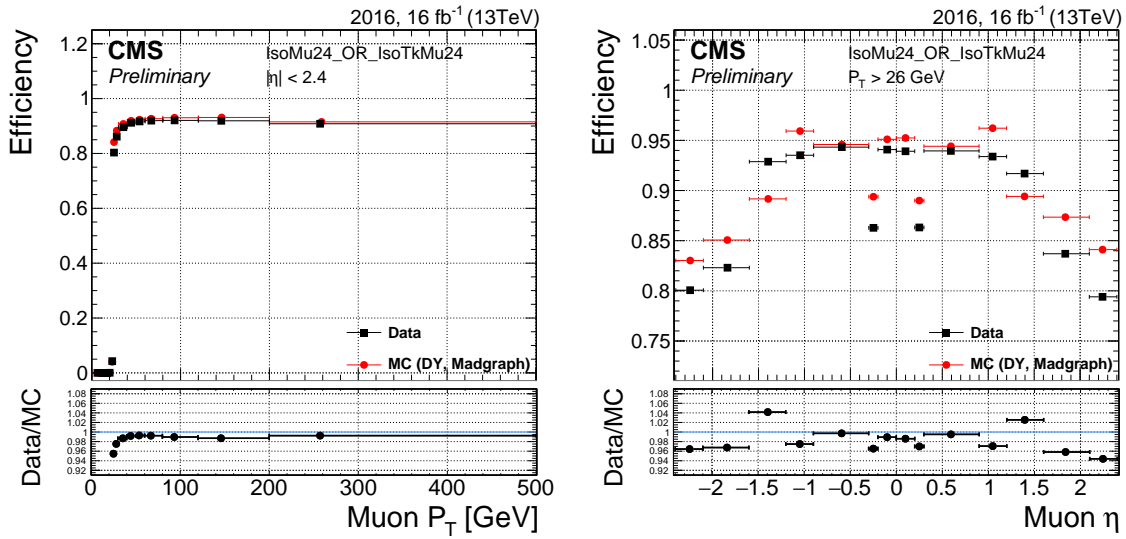


Figure 6.2.: The single-muon trigger efficiencies for MC (red) and data (black) and their ratio as a function of p_T (left), η (right). [130]

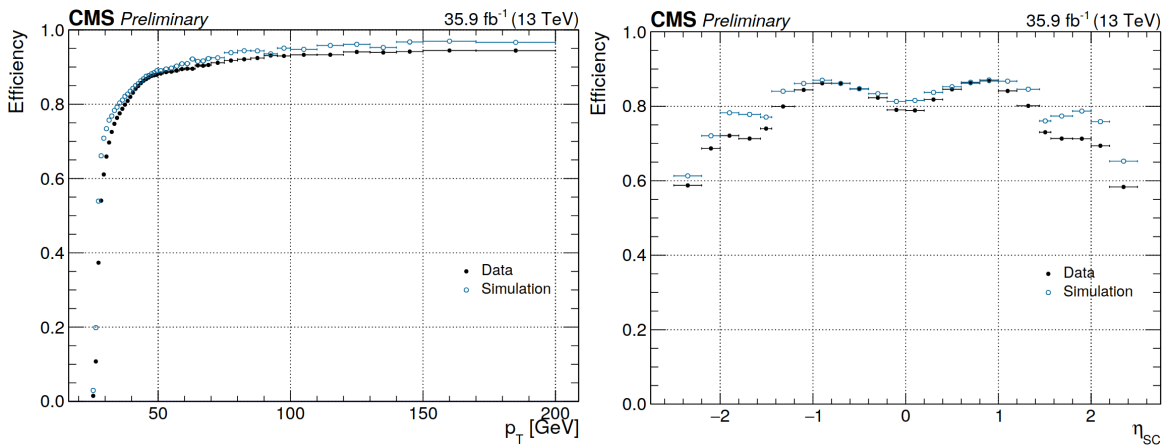


Figure 6.3.: The single-electron trigger efficiencies for MC (blue) and data (black) as a function of p_T (left) and η (right). [131]

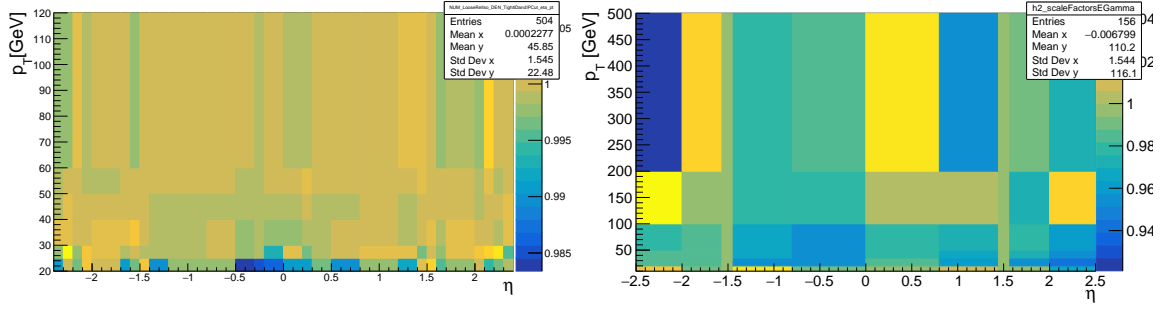


Figure 6.4.: The lepton identification efficiency scale factors in bins of p_T and η for the muon+jets (left) and electron+jets (right) channels. For muons it includes the isolation scale factor.

Primary vertex selection Only events with a primary vertex within 24 cm longitudinal and 2 cm transversal of the nominal interaction point are considered.

6.2.1. Lepton selection

Muons need to fulfill the following criteria concerning their kinematics, isolation and identification to be considered as signal muon:

- triggered the $HLT_IsoMu24_v^*$ or $HLT_IsoTkMu24_v^*$ trigger
- $|p_T| > 26$ GeV, $|\eta| < 2.4$
- PFMuon ID *tight*:
 - global muon (reconstructed in tracker and muon system)
 - valid hits in ≥ 5 tracker layers, ≥ 1 pixel layer, ≥ 1 in the muon system
 - $\chi^2/N_{df} < 10$ for the global track fit
 - impact parameter with regard to beam spot $|dB| < 0.02$ cm
 - distance to the primary vertex in z direction $d_z < 0.5$ cm
- particle flow based combined relative isolation *tight* using ΔR cone size of 0.4: $I_{PF}^\mu < 0.15$ [126] (I is defined in eq. 5.1)

Electrons need to fulfill the following criteria concerning their kinematics, isolation and identification in the detector to be considered as signal electron:

- triggered the $HLT_Ele27_WPTight_Gsf_v^*$ trigger
- $|p_T| > 29$ GeV, $|\eta| < 2.4$
- not in the barrel-endcap transition region ($1.4442 < |\eta_{supercluster}| < 1.566$)
- impact parameter with regard to beam spot $|dB| < 0.02$ cm
- impact parameter cuts:
 - in barrel region: $d_0 < 0.05$ cm, $d_z < 0.1$ cm
 - in end-cap region: $d_0 < 0.1$ cm, $d_z < 0.2$ cm

- cut-based ID *tight*
- veto on electrons from photon conversion
- relative isolation in a cone of $\Delta R < 0.3$
- particle flow based combined relative isolation *tight*: $I_{PF}^e < 0.1$ [127] (I is defined in eq. 5.1)

With the change of the electron HLT trigger path compared to the last lepton+jets top quark mass analysis, the electron p_T thresholds has been lowered from 34 GeV to 29 GeV.

In order to suppress background contributions, events are vetoed if they contain a second lepton. Events with an additional lepton identified as *global* particle flow muon with $|p_T| > 15$ GeV, $|\eta| < 2.4$ and a relative isolation smaller than 0.25 or as cut-based *veto* electron with $|p_T| > 15$ GeV, $|\eta| < 2.4$ and a relative isolation < 0.1 are vetoed.

6.2.2. Jet selection

Jets are clustered and calibrated as described in section 5.2. The four leading² PF jets have to fulfill the *tight* jet identification criteria recommended in [135]. That means they have to contain energy from charged hadrons and they must be clustered from at least two PF candidates including one charged PF candidate. Their neutral hadron energy fraction and neutral and charged electromagnetic energy fractions have to be below 90% each and their muon energy fraction has to be below 80%. In addition, the four leading jets are required to have a $|p_t| > 30$ GeV and to be within $|\eta| < 2.4$ of the detector.

All selected jets are required to have a distance of $\Delta R > 0.3$ to the signal lepton so that there is no overlap between the lepton and the jets for a cleaner signal.

The final state, that is of interest for this analysis, contains two jets originating from bottom quark decays. Algorithms for b-jet identification (b-tagging) use unique properties of the bottom quark, such as its mass of about 4.2 GeV and its lifetime in the order of 10^{-12} s. This results in a flight distance of about 7 mm on average for B-mesons when coming from a top quark decay. In the CMS software, several b-tagging algorithms are implemented, typically with working points for different efficiency/mistag -ratios. The working points are defined as loose, medium, and tight corresponding to 10%, 1% and 0.1% mistag rate. In this analysis jets originating from bottom quark (b) decay are tagged with the DEEPJET [136, 137] tagger on its medium threshold corresponding to a mistag rate of 1% and achieving an efficiency of 78%. The combined secondary vertex b tagger (CSVv2), used in the former analysis, had an efficiency of 70% at the same working point.

The **DEEPJET** tagger extends the DEEPFLAVOR [138] tagger (based on the DEEPCSV tagger) in being more inclusive in the classes and parameters learned from the jets. DEEPJET re-

²the jets or leptons with the highest p_T are called "leading"

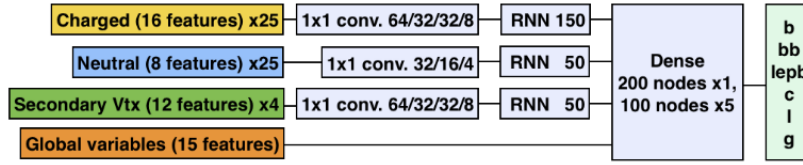


Figure 6.5.: Schematic of the DEEPJET neural network algorithm [137].

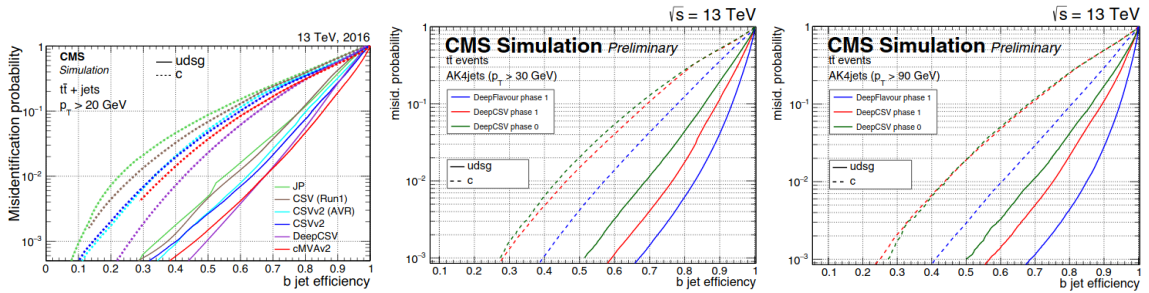


Figure 6.6.: Performance of the different heavy flavor tagging algorithms used by the CMS collaboration since the start of the data taking in 2010 (left) and comparison between the DEEPJET tagger (labeled 'Deep Flavor') and the DEEPCSV tagger evaluated on events from a $t\bar{t}$ sample with a p_T cut on the jets at 30 GeV (center) and 90 GeV (right) [137].

lies heavily on applying convolutions on lower level physics objects like individual particles, allowing the usage of much more information than former approaches. The architecture of the DEEPJET network is illustrated in figure 6.5. Instead of focusing on images the DEEPJET algorithm starts with a single particle without pre-selection to any track, secondary vertex or neutral candidate. It uses 16 features of up to 25 input tracks, 8 features of up to 25 neutral candidates, 12 features of up to 4 secondary vertices and 6 global variables. The features are passed through a set of convolution layers for each track separately before they are combined. The output of the network provides a discrimination between six classes, identifying one B hadron, two B hadrons, one leptonic decaying B hadron, a charm jet, a light quark jet or a gluon jet. The DEEPJET tagger has improved the performance in b-jet classification, especially at high jet p_T . A comparison of the performance of different tagging algorithms is shown in figure 6.6. In the left plot the DEEPJET precursor DEEPCSV is compared to other b tagging algorithms. In the central and right plot the DEEPJET can be seen surpassing the DEEPCSV algorithm for jets with $p_T > 30$ GeV and $p_T > 90$ GeV. For this analysis jets were tagged with all three output classes containing B hadrons combined.

Simulation samples are scaled with p_T and η dependent b-tagging scale factors from [139] and the p_T and η dependent b-tag efficiency [140]. An event based scale factor w is calcu-

lated as $w = P(\text{DATA})/P(\text{MC})$ with

$$P(\text{MC}) = \prod_{i=\text{tagged}} \varepsilon_i \prod_{j=\text{not tagged}} (1 - \varepsilon_j)$$

and

$$P(\text{DATA}) = \prod_{i=\text{tagged}} \text{SF}_i \varepsilon_i \prod_{j=\text{not tagged}} (1 - \text{SF}_j \varepsilon_j),$$

where ε_i is the MC b-tagging efficiency and SF_i the data-to-simulation scale factor of the b-tagging efficiency. ε_i and SF_i are both functions of the jet flavor, p_T and η . The indices i and j run over all selected jets.

At least two b-tagged jets among the four leading jets are required to be selected in an event. In the following kinematic fit the number of b-tagged jets will be further constrained to be exactly two among the four leading jets.

For the QCD multi-jet background the remaining statistic from the simulated samples is rather low after these cuts and yields single bin peaks in most distributions. Therefore this sample is used without the b-tag selection, scaled with event weights to its predicted event count that was derived from the same sample but with the b-tag selection.

The selection up to this point will be referred to as *baseline* selection.

From the 35.9 fb^{-1} of data recorded during 2016 by CMS, 451 618 $t\bar{t} \rightarrow \mu$ +jets and 287 842 e+jets events were selected. These are approximately 8% of the number of $t\bar{t} \rightarrow \mu$ /e+jets, which are expected to have occurred in 35.9 fb^{-1} of $\sqrt{s} = 13 \text{ TeV}$ proton-proton collisions. Due to the change of the b-tagging algorithm and a different electron p_T threshold more events are selected than in the former analysis [8].

The ratio of data events to the predicted number of events is with 90% rather low but matches the ratio other analyses on a similar $t\bar{t}$ phase-space in 2016 CMS data observe. One example is the energy asymmetry measurement in top quark pair production [141]. In a $t\bar{t} \rightarrow \text{lepton}+\text{jets}$ selection including two b-tagged jets and harder jet p_T cuts than this analysis, the ratio of data to predicted event numbers is 92%, roughly agreeing with our numbers. The normalization uncertainties from all considered uncertainty sources are evaluated. The uncertainty from the matrix element scale for fragmentation and renormalization is ${}_{+11\%}^{-12\%}$. This alone already covers the observed difference in event numbers. The next to leading normalization uncertainty is +5% due to B fragmentation tuning. The uncertainties will be described in detail in chapter 7. This is seen in all control distributions, for example fig 6.7, where the uncertainty band contains all uncertainties that are evaluated via event weight based variations. Such variations employ re-weighting of the default simulation to evaluate sources of uncertainty without introducing additional uncertainty due to the finite simulation statistic. This approach and the full list of considered uncertainties will be presented in chapter 7. Further, it has to be pointed out that the event normalization is not used in the likelihood fit but the likelihood is build from normalized probability density functions.

The signal purity is predicted to be 92% for μ +jets and 89% for e+jets. The fractions of the different background processes and predicted event counts for μ +jets are listed in table 6.6 and for e+jets in table 6.7.

Jet-parton matching For simulation, the $t\bar{t}$ signal events are categorized according to their jet-parton assignment. The final matching will use the kinematic fit that will be presented in the next section but this does not effect the jet and lepton kinematic presented in the plots of this section. The categories are:

- *correct permutation* ($t\bar{t}$ correct): The four decay quarks are matched to the four leading jets and are assigned to the correct W boson and bottom quarks.
- *wrong permutation* ($t\bar{t}$ wrong): The correct jets from the $t\bar{t}$ decay are selected but the assignment to the partons is wrong, e.g. the bottom quark from the leptonic decaying top quark is switched with the bottom quark from the leptonic decaying one or the light quark and b-quark are interchanged due to b-tag mistagging.
- *unmatched permutation* ($t\bar{t}$ unmatched): At least one of the four leading jets can not be matched to a parton from the $t\bar{t}$ decay. This can be the case when two jets are in the matching radius of a quark from the $t\bar{t}$ decay, the parton decay was not within the detector acceptance or the four leading jets are not the ones out of the $t\bar{t}$ decay due to additional radiations. This category also contains dilepton and alljet $t\bar{t}$ decays that were mis-identified.

The permutation fractions in the simulated signal sample will be listed in table 6.8 together with the permutation fractions after the kinematic fit selection. Without further selection, 72% of the events are categorized as unmatched and for only 20% of the events the jet-parton assignments are fully correct.

6.2.3. Data-simulation comparison

Control plots comparing the p_T , η and ϕ distributions of the muon can be seen in figure 6.8, of the electron in figure 6.9 both combined in figure 6.7. In figure 6.10 control plots for the number of jets, E_T^{miss} and ΔR between the leptons and their nearest³ jets are shown. The p_T distributions of the first six leading jets are presented in figure 6.13. The same distributions split by the lepton decay channel are depicted in the figures 6.11, 6.12, 6.14 and 6.15. As the plots show properties of the lepton and the leading jets sorted by p_T , the permutation type does not matter. The normalized distribution of the background events still in the selection matches approximately the distribution of the signal. At five additional jets (additional to the four from the $t\bar{t}$ decay when normalising the simulation to data) the number of jets starts disagreeing between prediction and data. In addition the tails of the jet p_T distribution are predicted slightly higher than observed in data. The biggest difference between the decay channels can be seen for the η distribution of the lepton, where electrons are more influenced by the structure of the detector, especially at the barrel-endcap transition at $|\eta| \approx 1.5$.

³the one with the smallest ΔR to the lepton

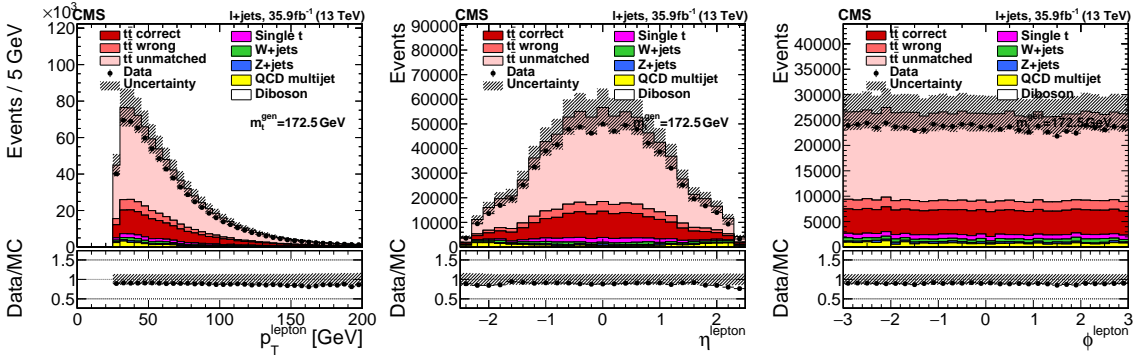


Figure 6.7.: Baseline selection lepton+jets: p_T (left), η (middle) and ϕ (right) distribution of the lepton. The uncertainty band contains simulation statistics, cross section uncertainty and all event weight based uncertainties.

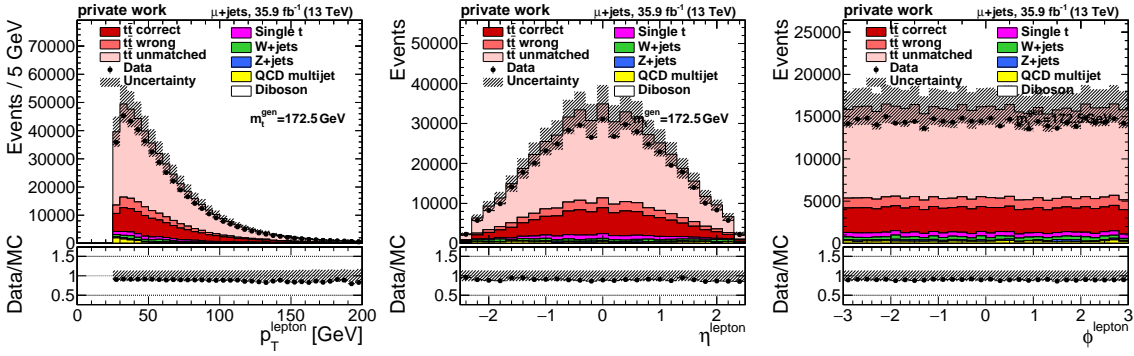


Figure 6.8.: Baseline selection muon+jets: p_T (left), η (middle) and ϕ (right) distribution of the muons. The uncertainty band contains simulation statistics, cross section uncertainty and all event weight based uncertainties.

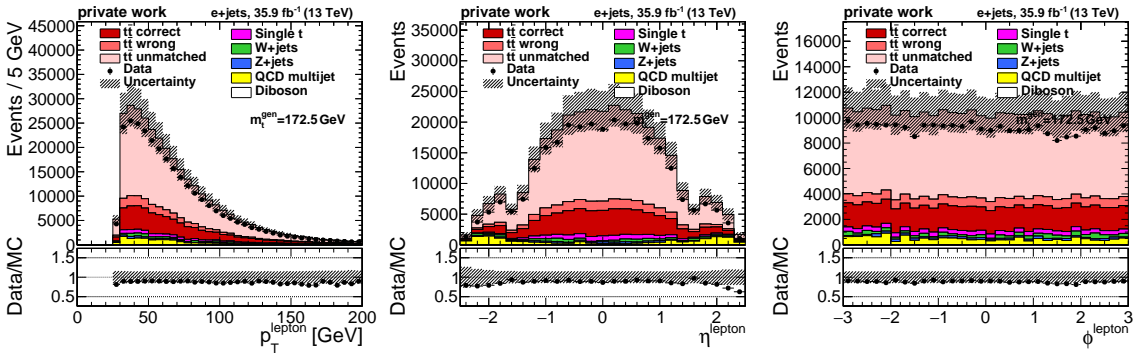


Figure 6.9.: Baseline selection electron+jets: p_T (left), η (middle) and ϕ (right) distribution of the electrons. The uncertainty band contains simulation statistics, cross section uncertainty and all event weight based uncertainties.

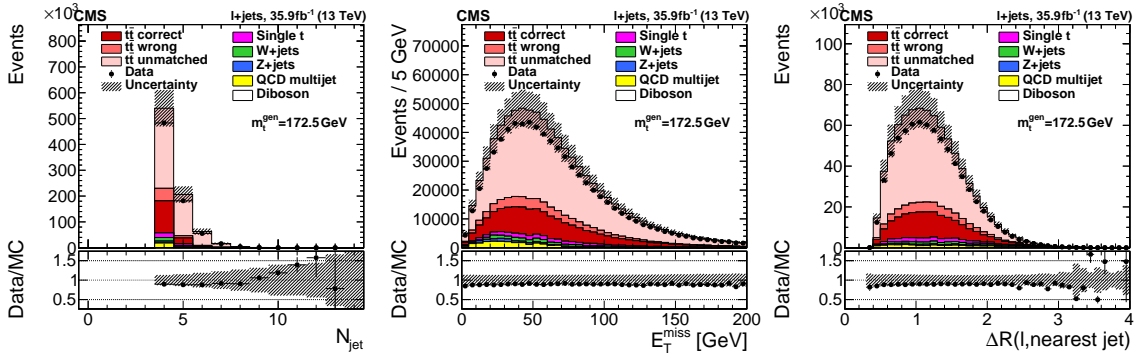


Figure 6.10.: Baseline selection lepton+jets: number of jets (left), E_T^{miss} (middle) and $\Delta R(\text{lepton, nearest jet})$ (right) distributions. The uncertainty band contains simulation statistics, cross section uncertainty and all event weight based uncertainties.

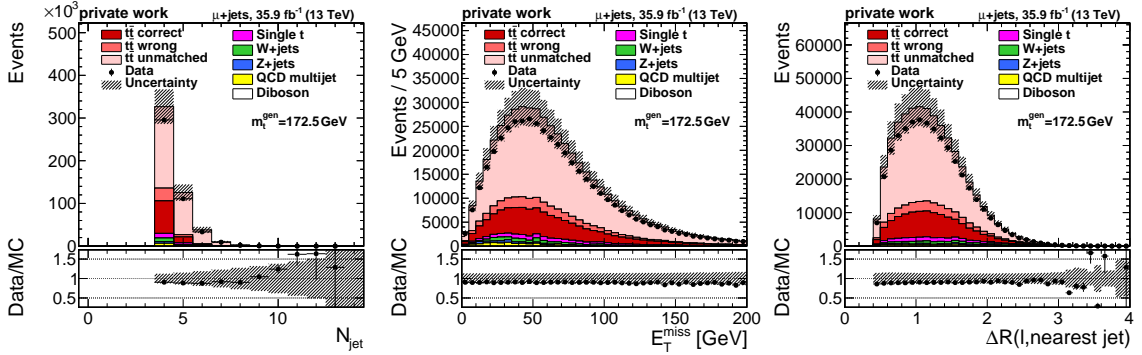


Figure 6.11.: Baseline selection muon+jets: number of jets (left), E_T^{miss} (middle) and $\Delta R(\text{lepton, nearest jet})$ (right) distributions. The uncertainty band contains simulation statistics, cross section uncertainty and all event weight based uncertainties.

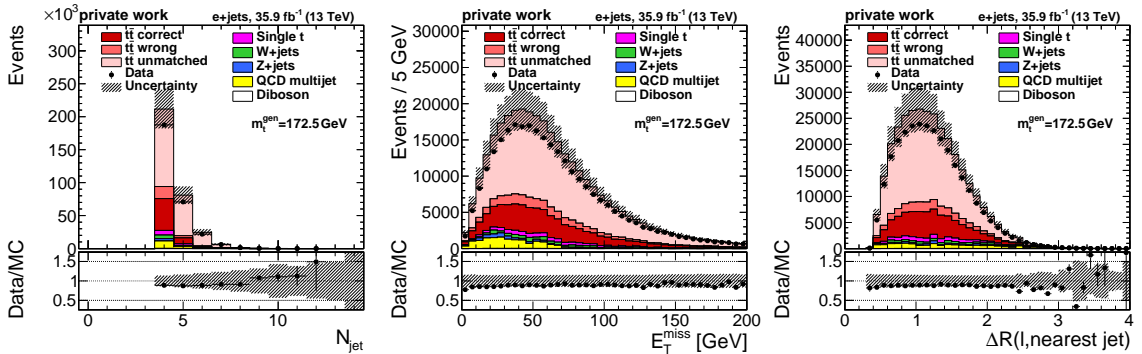


Figure 6.12.: Baseline selection electron+jets: Number of jets (left), E_T^{miss} (middle) and $\Delta R(\text{lepton, nearest jet})$ (right) distributions. The uncertainty band contains simulation statistics, cross section uncertainty and all event weight based uncertainties.

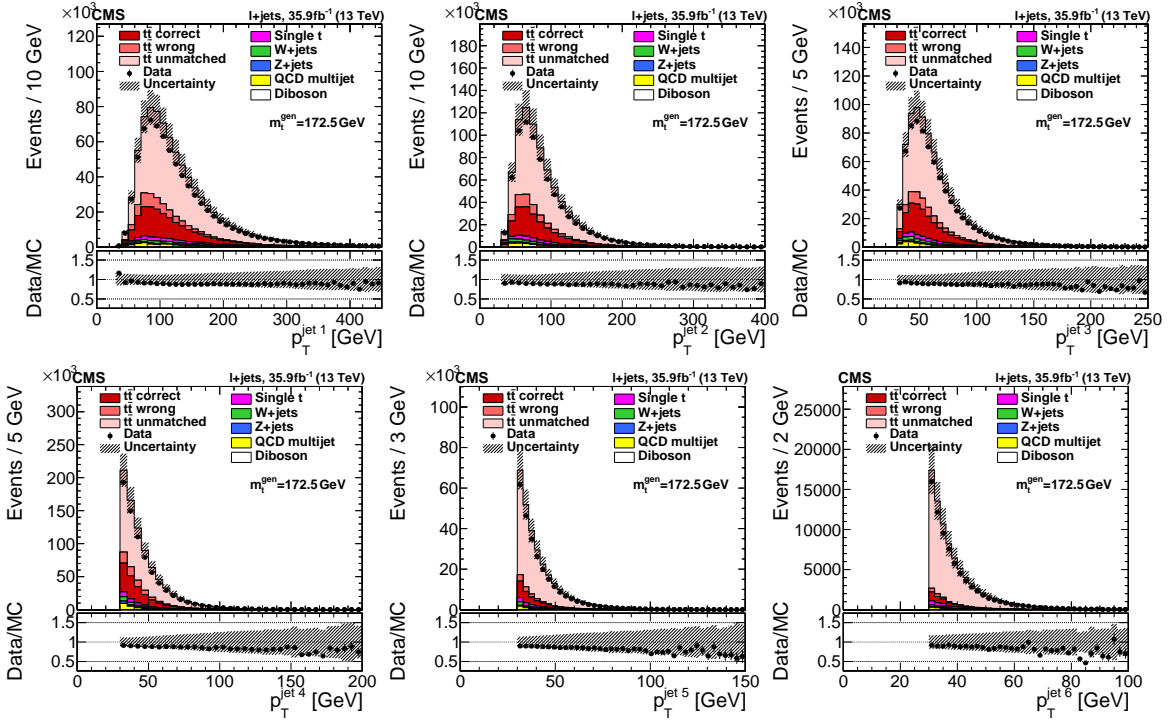


Figure 6.13.: Baseline selection lepton+jets: p_T distributions of the leading six jets. The uncertainty band contains simulation statistics, cross section uncertainty and all event weight based uncertainties.

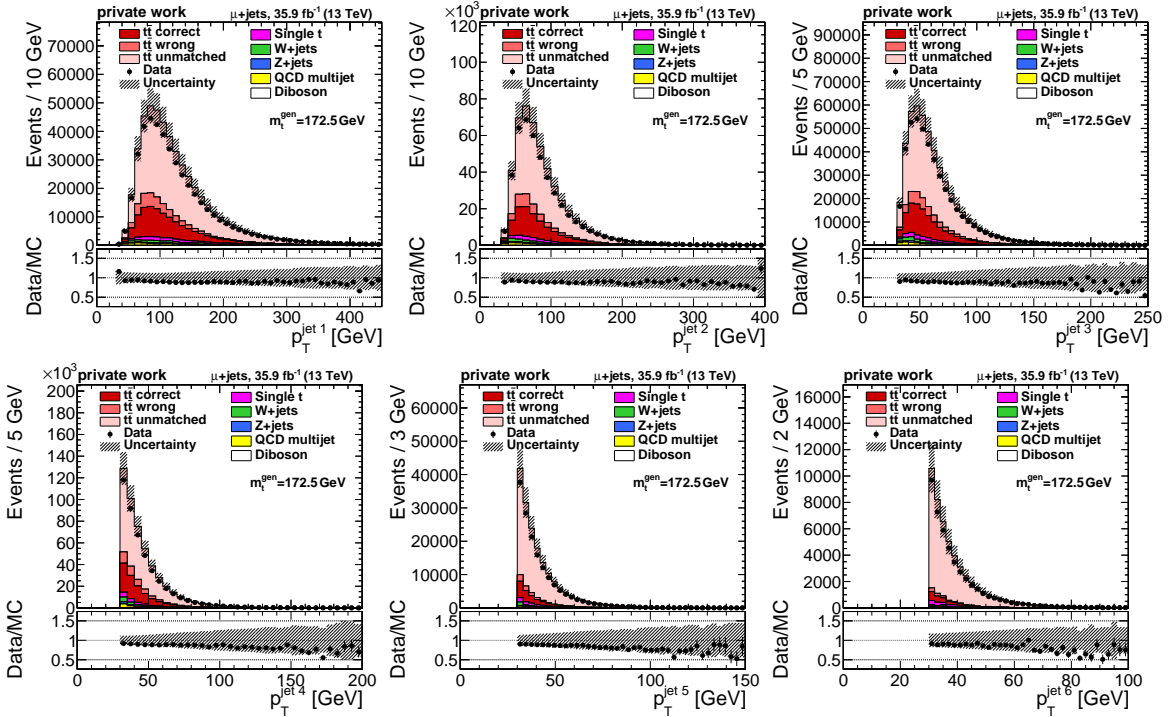


Figure 6.14.: Baseline selection muon+jets: p_T distributions of the leading six jets. The uncertainty band contains simulation statistics, cross section uncertainty and all event weight based uncertainties.

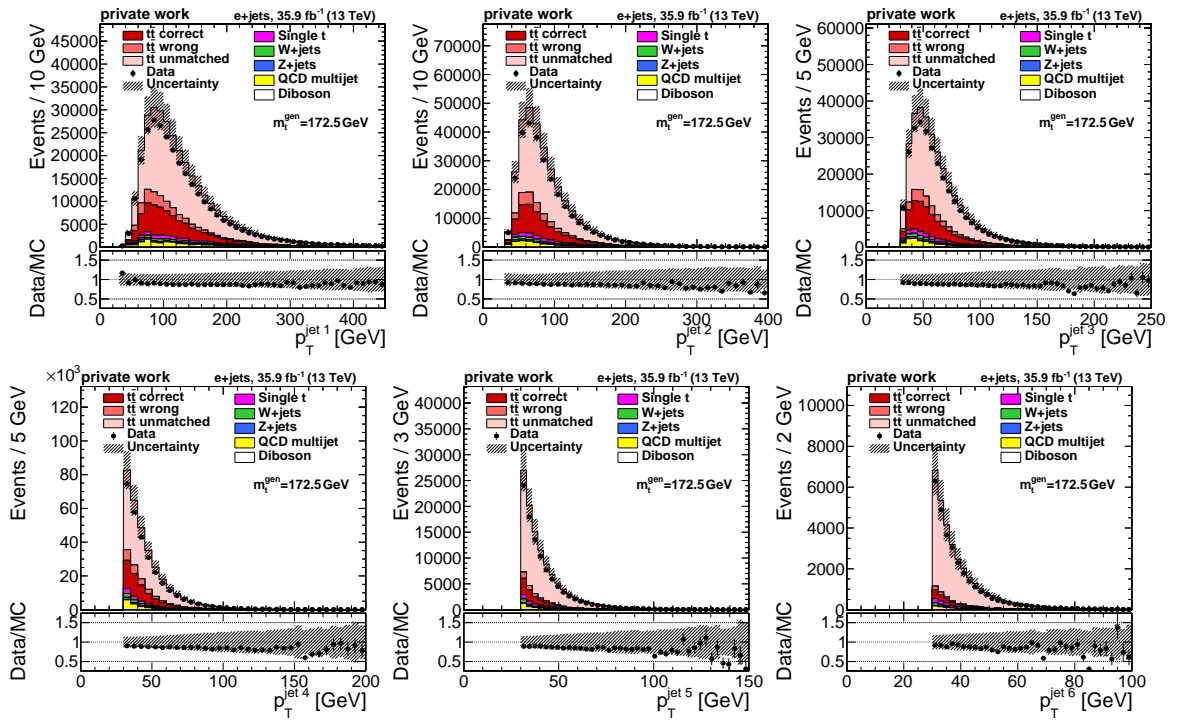


Figure 6.15.: Baseline selection electron+jets: p_T distributions of the leading six jets. The uncertainty band contains simulation statistics, cross section uncertainty and all event weight based uncertainties.

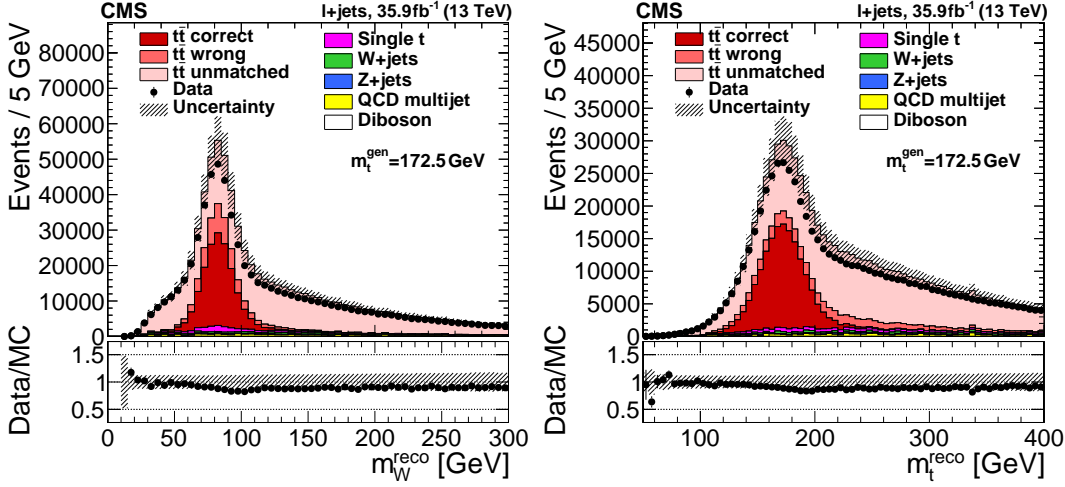


Figure 6.16.: Baseline selection lepton+jets: The mass distributions of the hadronic decaying W-boson candidate (left) and the associated top-quark candidate. Only the jet-parton assignment yielding the highest P_{gof} in the kinematic fit is used. The uncertainty band contains simulation statistics, cross section uncertainty and all event weight based uncertainties.

6.3. Kinematic fit

The invariant masses of top quark candidates are calculated from the sum of the four-vectors of their decay products. A $t\bar{t}$ hypothesis is built by taking the leading two b-tagged jets as candidates for the bottom quarks and the other two of the leading four jets as candidates for the light quarks from the hadronic decaying W boson. This leads to two possible jet-parton assignments per event, which are both considered. The leptonic decaying W boson is reconstructed from the signal lepton and the $E_{\text{T}}^{\text{miss}}$ that corresponds to the neutrino. In addition the z-component of the neutrino momentum has to be estimated. Its sign ambiguity doubles the number of possible permutations. The invariant mass of the systems of one of the W bosons and its associated bottom quark is considered to be the invariant mass of the top quark. The mass distributions of the hadronic decaying W-boson candidate and the associated top-quark candidate are shown in figure 6.16. The shape of the correct permutations is approximately Gaussian around the the simulated masses of $m_{\text{W}} = 80.4\text{ GeV}$ and $m_{\text{t}} = 172.5\text{ GeV}$. The wrong and unmatched permutations have a bigger contribution at higher masses. These distributions and following permutation dependent distributions show the combination that is most likely according to the kinematic fit. The data approximately agrees with the simulation.

For the reconstructed mass, the correct permutation hypothesis is expected to be closest to the leading order parton-level configuration. This classification is not possible for detector data. An optimization of the selection for correct permutation is helpful nonetheless.

To improve the resolution of the reconstructed quantities, to increase the fraction of correct

parton to jet assignments and to decrease background even further, the kinematic variables of the events are fitted to a $t\bar{t} \rightarrow l + \text{jets}$ hypothesis. The fit is the same that was applied in the $\sqrt{s} = 7 \text{ TeV}$, $\sqrt{s} = 8 \text{ TeV}$ and $\sqrt{s} = 13 \text{ TeV}$ analyses and by the DØ experiment [16, 142–144]. It applies 26 constraints on 24 observables. The input observables to this fit are the four-momenta of the four leading jets and the signal lepton, $\vec{k}_T = \vec{E}_T^{\text{miss}} + \vec{p}_{T,\text{lepton}} + \sum_{\text{jets}} \vec{p}_{T,\text{jet}}$, and all their respective resolutions. The constraints of the fit are the measured momenta of the four leading jets and the signal lepton, and the transverse momentum components of the neutrino. Further constraints are that the invariant masses of the top and anti-top quark are equal. The W boson and bottom quark have their known masses of 80.4 GeV and 4.7 GeV, and the masses of the light quarks, the lepton and the neutrino are negligible. The uncertainty on m_W of 0.02% [11] is negligible and is not included.

The fit is executed using the HitFit [28] program and minimizes $\chi^2 = (\mathbf{x} - \mathbf{x}^m)^T G (\mathbf{x} - \mathbf{x}^m)$ with the vector of measured observables \mathbf{x}^m , the vector of fitted observables \mathbf{x} and the inverse error matrix G given by the resolutions of the observables. The invariant mass constraints on $m_W = 80.4 \text{ GeV}$ and $m_t = m_{\bar{t}}$ are added as Lagrange multipliers to the χ^2 functions as

$$\chi^2 = (\mathbf{x} - \mathbf{x}^m)^T G (\mathbf{x} - \mathbf{x}^m) + 2\boldsymbol{\lambda}^T \mathbf{C},$$

with the vector of the Lagrange multiplier $\boldsymbol{\lambda} (\lambda_1, \lambda_2, \lambda_3)$ and the vector of constants $\mathbf{C} (C_1, C_2, C_3)$ with the components

$$\begin{aligned} C_1 &= \frac{(m_{\ell\nu}^{\text{reco}} - m_W)^2}{\Gamma_W^2}, \\ C_2 &= \frac{(m_{q\bar{q}'}^{\text{reco}} - m_W)^2}{\Gamma_W^2} \text{ and} \\ C_3 &= \frac{(m_{bq\bar{q}'}^{\text{reco}} - m_{b\ell\nu}^{\text{reco}})^2}{\Gamma_t^2}. \end{aligned}$$

The decay widths Γ_W and Γ_t are neglected and set to one.

From the χ^2 as goodness-of-fit (gof) measure a p-value $p_n(\chi^2) = \int_{\chi^2}^{\infty} f_n(x) dx$ is derived via the general χ^2 probability function for n-degrees of freedom

$$f_n(\chi^2) = \frac{1}{2^{\frac{n}{2}} \Gamma(\frac{n}{2})} (\chi^2)^{\frac{n}{2}-1} \cdot e^{-\frac{1}{2}\chi^2}.$$

Γ is the gamma function and $f_n(\chi^2)$ is defined for $\chi^2 > 0$.

For two degrees of freedom as in the kinematic fit of this analysis the goodness-of-fit value is $P_{\text{gof}} = e^{-\frac{1}{2}\chi^2}$.

The fit is done for all possible jet-parton assignments of the four leading jets and the two

v solutions as start values. The hypothesis with the highest P_{gof} will be used in all further steps.

$P_{\text{gof}} \geq 0.2$ is used as additional selection criteria on top of the baseline selection. The χ^2 distribution and the resulting P_{gof} distributions are shown in figures 6.18 and 6.19. Most remaining background events get small P_{gof} and events with correct assignment are distributed nearly flat, as expected for the correct hypothesis with properly chosen errors in G . The choice of the P_{gof} threshold follows the previous analysis [8, 145] where it was studied in more depth. The number of events selected in data and the corresponding predictions from simulations for signal and background are listed in tables 6.6 and 6.7, split into the lepton decay channels. The P_{gof} selection has an efficiency of $\sim 30\%$ so that there are 140 362 events selected in the $t\bar{t} \rightarrow \mu + \text{jets}$ channel and 87 265 events for $t\bar{t} \rightarrow e + \text{jets}$ with a predicted purity increased to 95%. The predicted permutation fractions in the signal are listed in table 6.8. The fraction of correct permuted events more than doubles to 47%, with a P_{gof} cut efficiency on correct permuted events of 80% while the cut efficiency on wrong permuted events is 70% and on unmatched 17%. So the P_{gof} selection cut rejects mostly events where not all of the four leading jets originate from leading order $t\bar{t} \rightarrow l + \text{jets}$ decay products. In figures 6.20, 6.21 and 6.22 the top-quark mass distributions before and after the P_{gof} selection are depicted. This selection narrows the resolution of the top-quark candidates mass distribution severely and cuts especially hard on unmatched and background events in the tails.

The simulated $t\bar{t}$ events contain not only events from semi-leptonic but also from dileptonic and hadronic decaying top quark pairs. The fraction of the different decay channel in the baseline and the final selection are listed in table 6.9. The dependence of the decay fraction in the selection to P_{gof} , $m_{\text{W}}^{\text{reco}}$ and $m_{\text{t}}^{\text{fit}}$ are shown in figures 6.23 and 6.24. The fraction of events from dileptonic decaying top quark pairs is about 9% after the baseline cut and gets reduced to about 3% by the kinematic fit cut, with a clear reduction for higher P_{gof} values. The fraction of selected events from fully hadronic decaying $t\bar{t}$ is negligible at 0.1%. For both leptons after the baseline selection no dependency on the decay channel in the used observable distributions was spotted.

Table 6.6.: Muon+Jets final state event yields and fractions for signal and background processes. The uncertainties are the statistics and cross section uncertainty.

	baseline			final ($P_{\text{gof}} \geq 0.2$)		
	events	\pm	[%]	events	\pm	[%]
$t\bar{t} + \text{jets}$	462 436.7	15 076.1	92.0	153 677.2	4 197.4	95.6
Single top	16 310.8	551.7	3.2	3 594.5	198.4	2.2
W+jets	11 233.6	6 815.8	2.2	1 240.5	1 052.1	0.8
Z+jets	4 703.7	3 398.3	0.9	763.8	973.4	0.5
QCD-multijet	7 842.7	5 561.5	1.6	1 434.8	1 047.7	0.9
Diboson	365.5	173.4	0.1	61.9	42.0	<0.01
MC total	502 893.1	17 792.0		160 772.5	4 380.5	
Data	451 618			140 362		

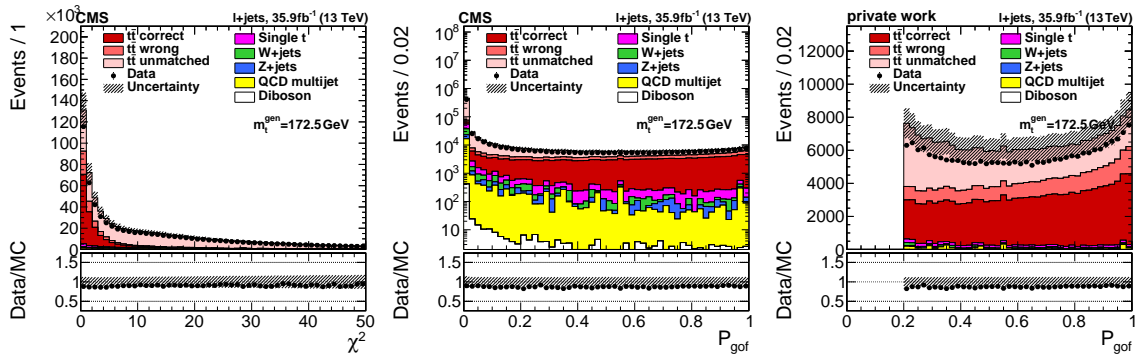


Figure 6.17.: Baseline selection lepton+jets: χ^2 (left) and resulting P_{gof} (middle) distribution before the P_{gof} selection and the P_{gof} distribution afterwards on linear scale (right). The uncertainty band contains simulation statistics, cross section uncertainty and all event weight based uncertainties.

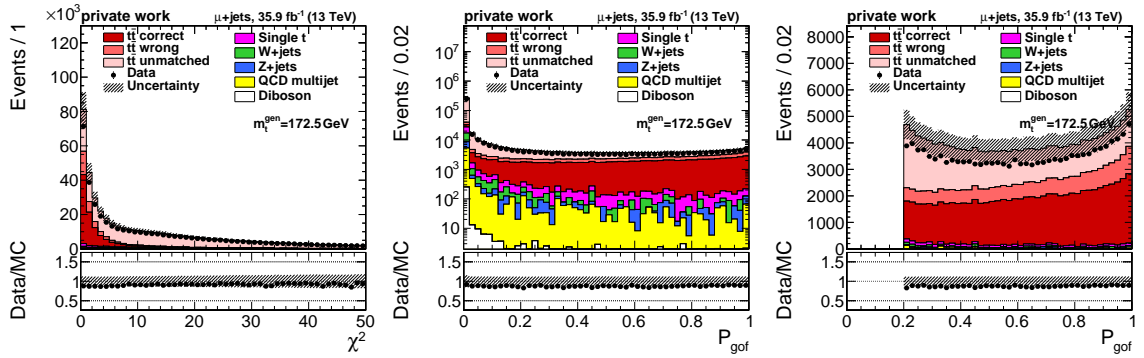


Figure 6.18.: Baseline selection muon+jets: χ^2 (left) and resulting P_{gof} (middle) distribution before the P_{gof} selection and the P_{gof} distribution afterwards on linear scale (right). The uncertainty band contains simulation statistics, cross section uncertainty and all event weight based uncertainties.

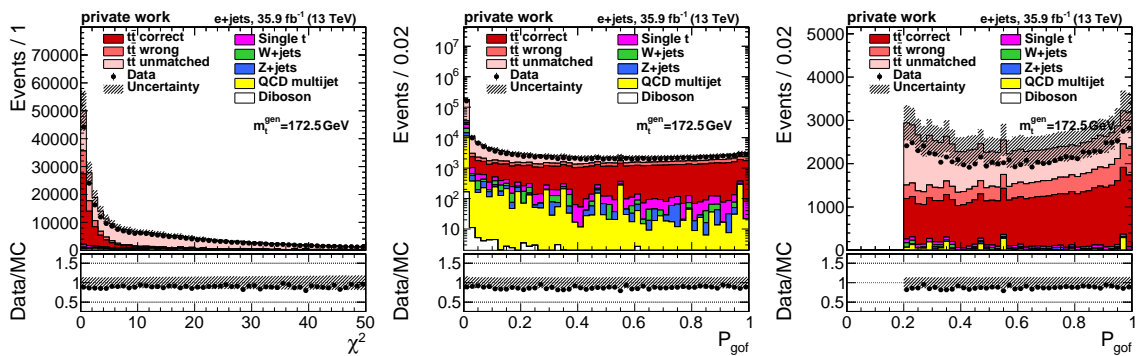


Figure 6.19.: Baseline selection electron+jets: χ^2 (left) and resulting P_{gof} (middle) distribution before the P_{gof} selection and the P_{gof} distribution afterwards on linear scale (right). The uncertainty band contains simulation statistics, cross section uncertainty and all event weight based uncertainties.

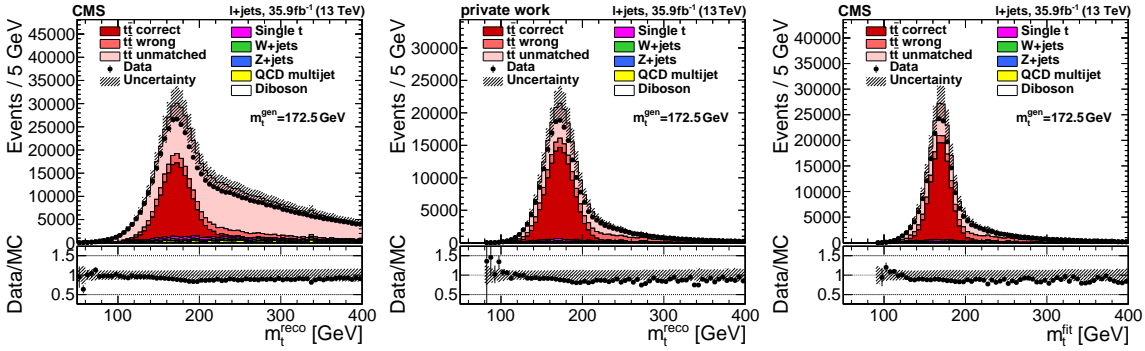


Figure 6.20.: Final selection lepton+jets: The top-quark mass distribution before (left) and after (middle) the P_{gof} selection and the fitted top-quark mass after the P_{gof} selection (right). The uncertainty band contains simulation statistics, cross section uncertainty and all event weight based uncertainties.

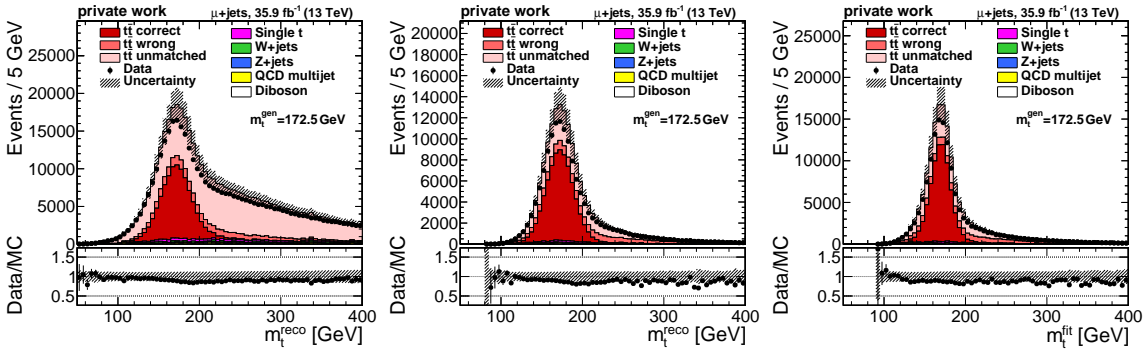


Figure 6.21.: Final selection muon+jets: The top-quark mass distribution before (left) and after (middle) the P_{gof} selection and the fitted top-quark mass after the P_{gof} selection (right). The uncertainty band contains simulation statistics, cross section uncertainty and all event weight based uncertainties.

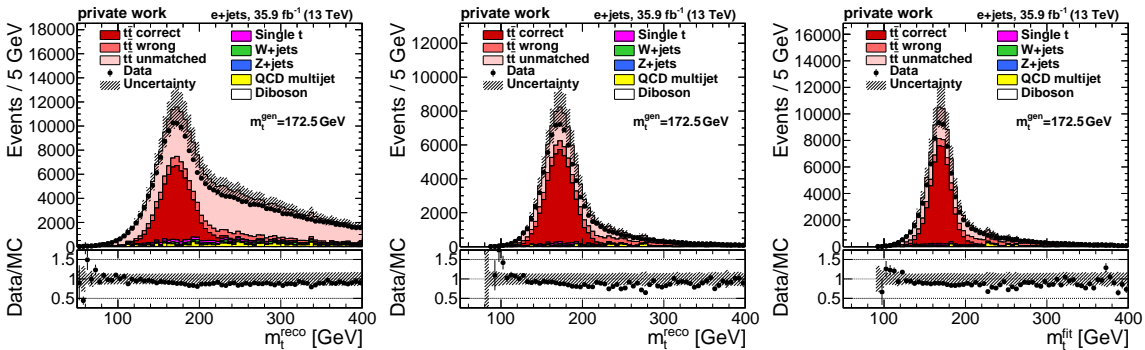


Figure 6.22.: Final selection electron+jets: The top-quark mass distribution before (left) and after (middle) the P_{gof} selection and the fitted top-quark mass after the P_{gof} selection (right). The uncertainty band contains simulation statistics, cross section uncertainty and all event weight based uncertainties.

Table 6.7.: Electron+Jets final state event yields and fractions for signal and background processes. The uncertainties are the statistics and cross section uncertainty.

	baseline			final ($P_{\text{gof}} \geq 0.2$)		
	events	\pm	[%]	events	\pm	[%]
$t\bar{t}$ +jets	288 194.3	18022.8	88.5	94 336.9	4 931.7	95.3
Single top	10 732.5	409.8	3.3	2 313.6	150.5	2.3
W+jets	7 322.5	4782.5	2.2	761.8	730.6	0.8
Z+jets	4 347.4	3085.1	1.3	570.6	872.3	0.6
QCD-multijet	14 770.6	10 494.7	4.5	918.9	704.9	2.1
Diboson	254.7	128.3	0.1	49.5	35.4	<0.1
MC total	325 622.5	21 613.6		100 101.6	5 220.2	
Data	287 842			87 265		

Table 6.8.: Final state permutation fractions.

	muon+jets		electron+jets	
	baseline	final ($P_{\text{gof}} \geq 0.2$)	baseline	final ($P_{\text{gof}} \geq 0.2$)
$t\bar{t}$ correct	19.9%	46.8 %	20.3%	48.2%
$t\bar{t}$ wrong	7.8%	15.6 %	7.8%	15.4%
$t\bar{t}$ unmatched	72.2%	37.7 %	71.9%	36.5%

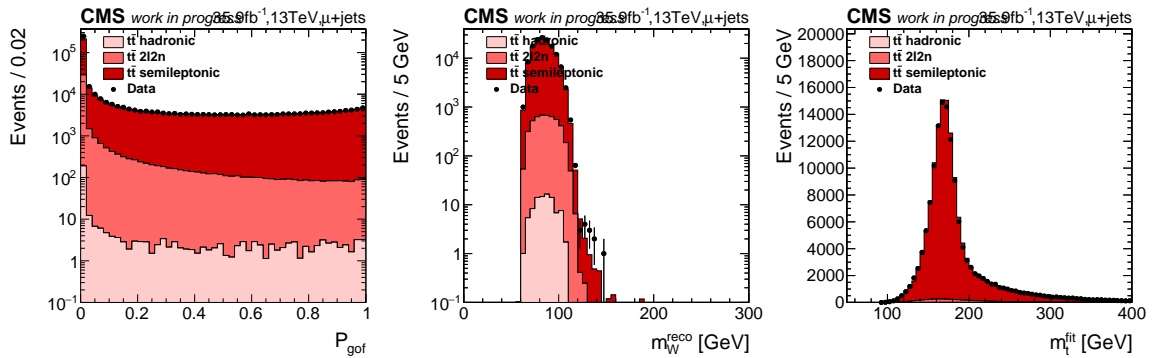


Figure 6.23.: Final selection muon+jets: The P_{gof} distribution (left), the m_W^{reco} (middle) and m_t^{fit} (right) distribution for the final selection split by the top quark decay channels in simulation.

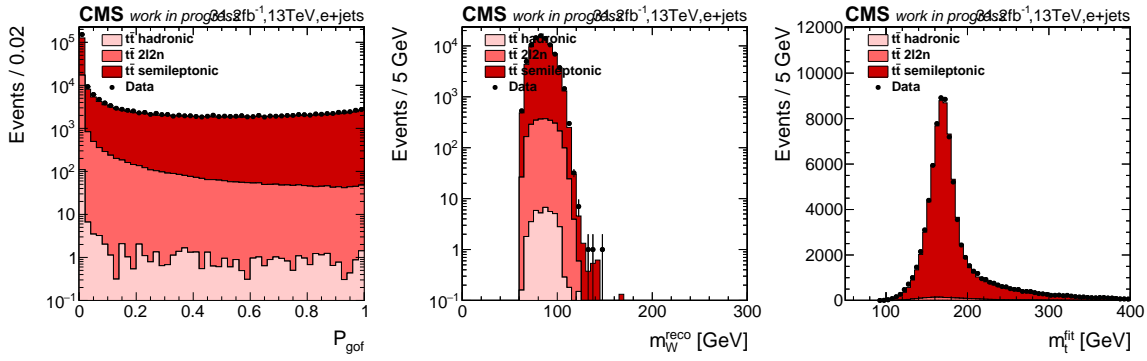


Figure 6.24.: Final selection electron+jets: The P_{gof} distribution (left), the m_W^{reco} (middle) and m_t^{fit} (right) distribution for the final selection split by the top quark decay channels in simulation.

Table 6.9.: Final selection $t\bar{t}$ decay channel fractions.

	muon+jets		electron+jets	
	baseline	final ($P_{\text{gof}} \geq 0.2$)	baseline	final ($P_{\text{gof}} \geq 0.2$)
$t\bar{t}$ semi-leptonic	90.6%	96.6%	90.6%	96.8%
$t\bar{t}$ dileptonic	9.4%	3.3%	9.3%	3.1%
$t\bar{t}$ hadronic	0.1%	0.1%	0.1%	<0.1%

7. Systematic Uncertainties

There are a multitude of effects that can not be determined exactly, that could influence the measurement of the top-quark mass and that are considered as sources of uncertainty. The statistical uncertainty follows directly from the number of selected top quark pair candidate events in the measured data. The systematic uncertainties are caused by shortcomings in the method, limitations of the simulation and uncertainties of the applied corrections on the CMS data. These shortcomings and their predicted effect on the measurement in this analysis will be described and discussed in this chapter.

Typically, effects influencing the measurement are investigated through variations of the simulation. The samples are varied by ± 1 standard deviations (σ) of the expected uncertainty to extract the $\pm 1\sigma$ influence on the observables and thus the measurement. For some uncertainty sources only the variation in one direction can be considered, e.g. for the comparison of different color reconnection models or parton distribution function parameterizations.

The last $t\bar{t} \rightarrow l+jets$ top-quark mass [13, 146] measurement was performed with pseudo-experiments from varied samples and the differences to measurements with pseudo-experiments from the default simulation sample was taken as systematic uncertainty. In this analysis the variations from the same sources are included as nuisance parameter in the likelihood and their impacts are evaluated. This will be described in the next chapter.

The dedicated simulated samples used are listed in table 6.5. For variations evaluated via event based weights on the default sample no additional statistical uncertainty component is considered. The statistical limitations of the default sample are included labeled as *Calibration*. It also includes the statistical uncertainty of the m_t dependence in simulation, fitted from the mass variation samples listed in table 6.3.

7.1. Experimental uncertainties

Jet energy correction (JEC): To evaluate the effect of the uncertainty on the jet energy corrections all jets are scaled p_T , η dependent up/down by their uncertainty [147]. This is done for 23 JEC uncertainty sources independently to give the nuisance fit maximal possibilities for adjustments.¹ These sources are [148]:

¹In former analysis they were bundled into correlation groups, instead of one full JEC uncertainty, to be used for combinations with ATLAS results. The uncertainty source absolute MPF bias corresponds to the

- Absolute statistic, absolute scale, and absolute MPF bias: Constant absolute scale uncertainties from combined photon, $Z \rightarrow ee$ and $Z \rightarrow \mu\mu$ reference scale measurements (absolute scale) and correction for FSR and ISR in the E_T^{miss} projection fraction (MPF bias) and the statistical limitation of the corrections.
- Fragmentation: Impacts of PYTHIA6 Z2 to HERWIG++2.3 based differences in fragmentation and underlying event on the JEC in simulation extrapolation to high p_T . This comparison was not updated to the latest available particle shower versions.
- Single pion ECAL, single pion HCAL: Propagation of $\pm 3\%$ variation in the single particle response in ECAL and HCAL to PF Jets evaluated using FastSim [149] and extrapolation to high p_T .
- Relative JER EC1, relative JER EC2, and relative JER HF: Jet energy resolution (JER) scale factors varied by $\pm 1\sigma$ of their uncertainties, assumed to be fully correlated for the end-cap region inside the tracker (EC1), end-cap region outside the tracker (EC2) and hadronic forward region (HF), evaluated η -dependent.
- Relative p_T BB, relative p_T EC1, relative p_T EC2, and relative p_T HF : Half-difference between log-linear and constant fits versus p_T of the relative MPF method response.
- Relative Balance: Full difference between log-linear fits of the MPF and the p_T -balance method response.
- Relative sample: η -dependent difference between relative residuals observed with di-jet, Z+jets and gamma+jets events.
- Relative FSR : η -dependent impact of uncertainty and JEC due to ISR and FSR differences between MPF log-linear L2 residual corrections from PYTHIA8 and HERWIG++.
- Relative statistic FSR, relative statistic EC, and relative statistic HF: Statistical uncertainty in the determination of η -dependence, calculated from the error matrix of the FSR correction, fitted η dependent and log-linear L2 residuals fitted p_T dependent.
- Pileup data/MC: Used are 5% uncertainty on the data to simulation scale factor for offset correction. This roughly covers the variation seen in the RANDOM CONE method applied on Zero Bias data and neutrino gun simulation.
- Pileup p_T reference, pileup p_T BB, pileup p_T EC1, pileup p_T EC2, and pileup p_T HF: The jet energy is corrected by additional $\pm 1\sigma$ of the pile-up offset dependence on jet p_T . It is estimated from matched simulations events with and without pile-up for the different detector parts BB, EC1, EC2, and HF. Sub-sources are referring to the detector regions $|\eta| < 1.3$ (BB), $1.3 < |\eta| < 2.5$ (EC1), $2.5 < |\eta| < 3.0$ (EC2) and $|\eta| > 3$ (HF).

Jet energy resolution: The jet energy resolution in the simulation is varied by $\pm 1\sigma$ with respect to the degraded resolution taken from [109, 147] with the hybrid method described in subsection 5.2. The uncertainties on the JER scale factors include systematic and statistical components and vary η dependent between 6% and 20%. The JER SFs and uncertainties

correlation group *MPFInSitu*, the relative FSR source corresponds to the correlation group *InterCalibration* and all other uncertainty sources were bundled into the group *Uncorrelated*.

used are listed in table 7.1. The variation is evaluated independent for two $|\eta_{\text{jet}}|$ regions, split at $|\eta_{\text{jet}}| = 1.93$.

Table 7.1.: JER data/simulation scale factors included in MC global tags 80X_mcRun2_asymptotic_2016_TrancheIV_v8 and 94X_mc2017_realistic_v15 (under temporary name "Fall17_25nsV1")

$ \eta $ region	0.000–0.522	0.522 - 0.783	0.783–1.131	1.131-1.305	1.305–1.740	1.740 - 1.930	1.930–2.043
Data/MC SF	1.1595	1.1948	1.1464	1.1609	1.1278	1.1000	1.1426
Stat.Unc	± 0.0052	± 0.0113	± 0.0084	± 0.0161	± 0.0099	± 0.0263	± 0.0512
Syst.Unc	± 0.0642	± 0.0642	± 0.0627	± 0.0982	± 0.0979	± 0.1028	± 0.1099
Total.Unc	± 0.0645	± 0.0652	± 0.0632	± 0.1025	± 0.0986	± 0.1079	± 0.1214
$ \eta $ region	2.043 - 2.322	2.322 - 2.5	2.5–2.853	2.853-2.964	2.964-3.139	3.139-5.191	
Data/MC SF	1.1512	1.2963	1.3418	1.7788	1.1869	1.1922	
Stat.Unc	± 0.0306	± 0.0814	± 0.0619	± 0.0648	± 0.0197	± 0.0386	
Syst.Unc	± 0.1008	± 0.2064	± 0.1559	± 0.1900	± 0.1228	± 0.1437	
Total.Unc	± 0.1140	± 0.2371	± 0.2091	± 0.2008	± 0.1243	± 0.1488	

Muon and electron scale factors: The muon and electron scale factors in simulated events are varied up and down by one standard deviation. The values of the deviations are taken from reference [150–152]. This is done fully correlated for the uncertainties for identification, isolation and trigger scale factor uncertainties.

Lepton momentum correction scales: The lepton energy in simulation is varied up and down by one standard deviation of the energy correction.

Missing transverse momentum: All variations on jet and lepton energies are propagated into the recalculated E_T^{miss} . There is no dedicated nuisance introduced and the impact of this uncertainty is part of the corresponding energy scale uncertainties.

b tagging: The events are weighted to account for $\pm\sigma$ of the p_T , η dependent uncertainties of the b-tag and c-tag efficiencies, correlated with another, and mis-identification rates of the DEEPJET tagger [153, 154]. The uncertainty is evaluated via event based weight variations, reported and studied in [155].

Pileup: The pileup distributions for a $\pm 4.6\%$ variation of the inelastic pp cross section at 69.2 mb were used for the calculation of simulation pileup weights, based on the study in reference [156]. The default and varied distribution is shown in figure 7.1.

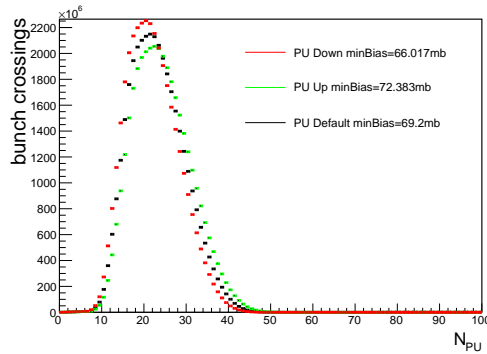


Figure 7.1.: Number of pile up events for the default and varied minimum bias event cross sections (minBias) for the CMS data recorded in 2016.

Non- $t\bar{t}$ background: The background normalization is varied by $\pm 10\%$ for the di-boson [157, 158], Drell-Yang [159] and single top [160, 161], $\pm 30\%$ for W+jets [162] and $^{+100}_{-50}\%$ for the QCD-multijet sample. The top-quark mass dependence on the single top decays is not taken into account explicitly.

Luminosity The impact of the uncertainty on the luminosity of 2.5% [55] is negligible compared to other variations, especially the non- $t\bar{t}$ background. Also the observable templates will be used normalized. Therefore the uncertainty due to the luminosity will not be included.

7.2. Modeling Uncertainties

The uncertainties in the modeling and simulation of the processes in a $t\bar{t}$ decay are categorized in three parts. The modeling of the hadronization of the jets after the $t\bar{t}$ decay, QCD effects in the perturbative regime, and the modeling of soft QCD effects, where perturbation theory does not apply. Most of these uncertainties arise from parameters in components of the simulation chain that are adjusted to measurements and varied to corresponding uncertainty. Some uncertainties are set ad-hoc without direct knowledge of the details of the process in nature.

7.2.1. Modeling of hadronization

Flavor-dependent JEC: The Lund string fragmentation that is implemented in the PYTHIA 6.422 [163] generator was compared to the cluster fragmentation in HER-

WIG++ 2.4 [164]. The relative difference in the jet energy response between these two generators was determined for each jet flavor (split in bottom, charm, lighter quarks and gluon) by the references [103, 165] and is taken as systematic uncertainty.

b jet modeling (bJES): A retuning of the Bowler-Lund fragmentation function for B hadrons to agree with the x_B data measured by the ALEPH [166] and DELPHI [167] collaborations was done. The tuning was redone for the CP5 tuned MC in [168]. As the down variation corresponds to the default setting, the variation is done around the central value between the up and down variation. In addition, further nuisance parameters correspond to the difference between the default setting and the central Bowler-Lund fragmentation, and between the default and the Peterson [169] fragmentation.

Semi-leptonic B hadron decays: The semi-leptonic branching ratio of B hadrons corresponds directly to the abundance of undetected neutrinos inside b flavor jets. The neutrinos lower the response with respect to the original bottom quark. This is taken into account by varying the branching ratio of $(B \rightarrow \ell \nu X)$ by -0.45% and $+0.77\%$ to give an envelope of the measurements from B^0/B^+ decays and their uncertainties [170]. The envelope was evaluated in reference [6].

7.2.2. Modeling of the scattering process

Parton distribution functions (PDF): As the uncertainty due to the choice of parton distribution functions was small in the last analysis (3% of total uncertainty [8]), the full eigenvector variations of different pdf estimations are not used in the full list of impacts. They were evaluated separately and do not effect the final result but will be included when the different uncertainty categories are compared to former analyses. Instead the default NNPDF31_NNLO [73] is compared to the CT14NNLO [171] and MMHT2014NNLO68CL [72] PDFs via event weights. In addition the strong coupling constant $\alpha_s(M_Z) = 0.118$ in the NNPDF31_NNLO extrapolation is varied by ± 0.001 .

Renormalization and factorization scales: Effects of a change of the renormalization and factorization scales in the matrix element calculation were evaluated. The simulated events were weighted to match the shapes of events generated with nominal renormalization scale (μ_R) and factorization scale (μ_F) with $\mu_R^2 = \mu_F^2 = m_t^2 + \sum p_T^2(\text{jet})$, where the sum runs over all additional jets in the event not coming from the $t\bar{t}$ decay and [172]. μ_R and μ_F were scaled simultaneously and independent from each other by factors of 0.5 and 2 of their nominal value. These variations are available as event dependent weights as described in

more detail in [173]. Only the simultaneous change is introduced as a nuisance parameter as it covers the effects of the two other variations.

ISR and FSR: The scales for QCD emission by ISR and FSR used in PYTHIA were varied during the generation of the simulation samples. This varies effectively the value of α_S at Q^2 in the parton shower. The nominal scales are equal to the sum of the absolute transverse momenta of the event and the up/down variations include an additional factor/divident of 2. Weights were generated which are used to reweight the default event samples in order to correspond to other ISR or FSR scales. The weights were derived by evaluating multiple trial functions during the matrix element calculation and assigning weights corresponding to the probability of an event being in the sample given a certain ME generator setting. This method is described in detail in [174, 175]. 32 decorrelated variations are used that each vary the particle shower (PS), renormalization scale (μ_R) and the non-singular terms (cNS) independently for each branching type. The branching types are $q \rightarrow qg$, $g \rightarrow gg$, $g \rightarrow qq$, $X \rightarrow Xg$, where X is a top or bottom quark. In addition to the reduced computational effort this has the additional advantage, compared to the dedicated samples, that no additional statistical uncertainties are introduced. As described in section 8.3 the FSR PS scale variation is the only nuisance in which the likelihood is parameterized quadratically. The motivation and necessity of this special handling will be described and evaluated in section 9.2.1.

ME-PS matching scale (h_{damp}): The POWHEG generator scales the cross section for real emissions by a damping function $h_{\text{damp}}^2 / (p_T^2 + h_{\text{damp}}^2)$, which controls the matrix element to parton shower merging and regulates the high- p_T radiation. The value $h_{\text{damp}} = 1.379 \cdot m_t$ was derived by tuning the distribution of the leading additional jet p_T [82, 83]. Two dedicated variation samples are used where h_{damp} is varied by its uncertainty $\sigma_{h_{\text{damp}}} = {}^{+0.926}_{-0.5052}$.

Top quark p_T : The top quark p_T spectrum is affected by NNLO effects [117] resulting in a slope in the data-to-simulation ratio. The top quark p_T in simulation is varied to match the distribution in data. All simulated signal events are weighted with

$$w_{p_{T_t}} = \sqrt{\exp\left(0.0615 - 0.0005 \cdot p_{T,t,\text{hadr}}^{\text{gen}}\right) \cdot \exp\left(0.0615 - 0.0005 \cdot p_{T,t,\text{lept}}^{\text{gen}}\right)},$$

where $p_{T,t,\text{hadr}}^{\text{gen}}$ is the parton generator level transverse momentum of the hadronically decaying top quark and $p_{T,t,\text{lept}}^{\text{gen}}$ is the leptonically decaying top quark. The scale factor function, derived by comparing CMS data to POWHEG+PYTHIA8, is shown in figure 7.2. The scale factor is not used on the default signal sample but it is included as uncertainty [165, 176–179].

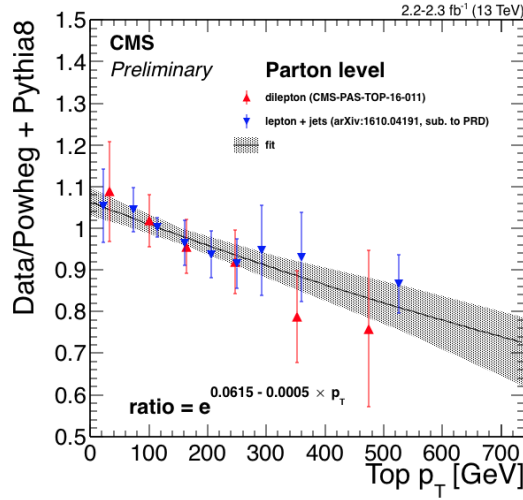


Figure 7.2.: Ratio of the top p_T measured in CMS data recorded in 2016 at parton level with respect to the theory predictions from POWHEG+PYTHIA8 [180].

7.2.3. Modeling of non-perturbative QCD effects

Underlying event (UE): Non-perturbative QCD effects are taken into account by tuning PYTHIA to measurements of the underlying event [181, 182]. Dedicated samples with the CP5 UE tune varied by $\pm 1\sigma$ are used.

Color reconnection (CR) modeling: There are some ambiguities in the modeling of color reconnection effects [183]. Two alternative CR models, GluonMove and QCD based [87] are compared to the default MPI based model. The different models are described in detail in chapter 4. Each model is represented by an individual nuisance parameter. The uncertainties due to the statistical limitation of the additional models are included in the nuisance parameter fit.

Early resonance decay (ERD): In addition to comparing different color reconnection models a simulation sample including additional early resonance decays in PYTHIA 8 is compared to the default sample with the ERD option turned off.

In contrast to the former 2016 $t\bar{t} \rightarrow \text{lepton} + \text{jets}$ top-quark mass analysis, no uncertainty due to the choice of matrix element generator is included as the available alternative samples use a different UE tune and have major deviations in the jet p_T spectrum compared to data. This will be discussed further when comparing this thesis to former analyses in section 9.4.

8. Methodology

In this analysis a maximum likelihood (ML) fit on data is used to measure the value of the top quark mass. The likelihood is parameterized in m_t and also includes nuisance parameters for all considered uncertainty sources. This way, not only the impact of the different uncertainty sources are evaluated but they can also potentially be reduced by the fit, thereby improving the precision on m_t .

In former top quark mass precision measurements in the semi-leptonic $t\bar{t}$ decay channel, templates of the m_t^{fit} and m_W^{reco} distributions were built dependent on m_t and a jet energy scale factor (JSF), to reduce the uncertainty from jet energy corrections. m_t and JSF were measured by fitting the m_t and JSF dependent probability densities derived from simulation to the m_t^{fit} and m_W^{reco} distributions of collision data. An additional improvement of the systematic uncertainty was achieved by combining measurements with and without the in-situ measurement of the JSF, therefore combining the measured jet scale factors with prior corrections.

In this thesis the likelihood ratio, $\lambda(m_t, \vec{\theta}, \vec{\beta}, \vec{\omega} | \text{data})$, is used which depends in addition to m_t also on the nuisance parameters $\vec{\theta}$, including systematic effects, and statistical nuisance parameters $\vec{\beta}$ and $\vec{\omega}$ that handle limitations from simulation statistics.

Independent observables will be chosen, so that their combined probability density function, $P(\text{data} | m_t, \vec{\theta}, \vec{\beta}, \vec{\omega})$, can be simplified to

$$P(\text{data} | m_t, \vec{\theta}, \vec{\beta}, \vec{\omega}) = \prod_i P_i(x_i | m_t, \vec{\theta}, \vec{\beta}, \vec{\omega}),$$

where x_i iterates over up to ten histograms of observables.

8.1. Pseudo-experiments

This analysis is developed and calibrated with pseudo-data, also called pseudo-experiments or toy data. The total number of events in one pseudo-data set is determined by a Poisson distribution with the number of selected events in data as mean. Simulated signal and background events are selected randomly according to the predicted signal fraction. The event based weights (see chapter 6) of the simulation are used in all distributions. Negative weights of events are considered by including an additional event for every selected event with negative weight, so if an event with negative weight is selected the number of effectively selected

events is decreased instead of increased. This is mostly relevant for the events generated with the AMC@NLO generator as background candidates. Every pseudo-data set generated this way is treated like the full selected data of this analysis. The drawing of pseudo-data is performed a few hundred times to yield statistically significant results, which will be checked via their pull distributions. Compared to generating pseudo-distributions this approach has the benefit that all correlations are taken into account.

8.2. Observables

Similar to the method that was used in previous top quark mass precision measurements, templates from multiple observables are created. Considered as observables are:

- m_t^{fit} , the invariant mass of top quark candidate after the kinematic fit, for $P_{\text{gof}} \geq 0.2$
- m_W^{reco} , the invariant mass of the hadronically decaying W-boson, for $P_{\text{gof}} \geq 0.2$
- $m_{\ell b}^{\text{reco}}|_{P_{\text{gof}} < 0.2}$, the invariant mass of the lepton-bottom quark system from the leptonically decayed top quark candidate, with

$$m_{\ell b}^{\text{reco}} = \sqrt{\left(P_{\ell}^{\text{reco}} + P_b^{\text{reco}}\right)^2},$$

where P_{ℓ}^{reco} and P_b^{reco} are the four-vectors of the lepton and the b jet associated with the same top quark before the kinematic fit, for the events rejected by the P_{gof} cut

- $m_{\ell b}^{\text{reco}}/m_t^{\text{fit}}$, for $P_{\text{gof}} \geq 0.2$
- $R_{\text{bq}}^{\text{reco}}$, the ratio between the transverse momentum of the bottom and light quark jet candidates, with

$$R_{\text{bq}}^{\text{reco}} = \frac{p_{\text{T},\text{b1}} + p_{\text{T},\text{b2}}}{p_{\text{T},\text{q1}} + p_{\text{T},\text{q2}}},$$

for $P_{\text{gof}} \geq 0.2$.

The observable combinations used are labeled the following:

- 1D: m_t^{fit}
- 2D: 1D with addition of m_W^{reco}
- 3D: 2D with addition of $m_{\ell b}^{\text{reco}}|_{P_{\text{gof}} < 0.2}$
- 4D: 3D with addition of $m_{\ell b}^{\text{reco}}/m_t^{\text{fit}}$
- 5D: 4D with addition of $R_{\text{bq}}^{\text{reco}}$

The 5D observable setting is used as default and will yield the final result.

As in previous analyses, the m_W^{reco} distribution is not added mainly for its information on the top-quark mass but to reduce its dependency on the jet energy scale and corresponding

uncertainties. In addition it introduces a handle to reduce uncertainties due to additional radiations that influence the energy of light quarks, like for example from final state radiation (FSR). It is expected that the m_W^{reco} depends least on the top quark mass value.

The observable $m_{\ell b}^{\text{reco}}$ was used to measure the top-quark mass in the dilepton channel [184]. In that case the b-jet-to-lepton combinatorics were solved by first matching each of the two b jets with the lepton that produces the lower $m_{\ell b}^{\text{reco}}$ value and then matching each of the two leptons with the b jet that produces the lower $m_{\ell b}^{\text{reco}}$ value. This results in two or three values of $m_{\ell b}^{\text{reco}}$ where each of the two b jets and the two leptons is used at least once and guarantees that the true value of $m_{\ell b}^{\text{reco}}$ is the same or higher, preserving the theoretical maximum. In the muon+jets channel of the data analyzed in this thesis this method would result for $P_{\text{gof}} \geq 0.2$ ($P_{\text{gof}} < 0.2$) in only 47% (49%) correct b-jet-to-lepton assignment. With the parton assignment from the kinematic fit a much higher correct assigned fraction is achieved, at the cost of not conserving the cut-off to higher values of $m_{\ell b}^{\text{reco}}$ that was utilized in the dilepton analysis to extract m_t . As a template from the full distribution is used in the analysis, the loss of the clear cut-off is not a problem.

In events with $P_{\text{gof}} < 0.2$ the parton-jet assignment of the bottom quark from the leptonically decayed top-quark candidate is still correct in 60.8% of the events. In 34.45 % of the events where the parton-jet assignment is not fully correct the two bottom quark candidates are switched. The $m_{\ell b}^{\text{reco}}|_{P_{\text{gof}} < 0.2}$ is a useful distribution to extract the top-quark mass dependency of these events. In addition it could help to reduce the uncertainty from lepton scale factors and bottom flavor related uncertainties. For all other observables the selection criterion $P_{\text{gof}} \geq 0.2$ is used.

The addition of $R_{\text{bq}}^{\text{reco}}$ could further decrease the uncertainty by introducing a dependency on the difference in jet response between light and bottom quark jets to the likelihood. This could reduce the uncertainty from b-jet energy and tagging scale uncertainties as well as top- p_T and color reconnection related uncertainties.

With pseudo-experiments (see section 8.1), using one of the observables at a time, further of sources systematic uncertainties that could be reduced significantly by the additional observables were identified. In fig. 8.1 the expected error on nuisance parameters in the case where only the parameter itself is free in the likelihood maximization, is shown. The nuisance parameter definition and the fit procedure will be explained in detail in section 8.3 and the uncertainty sources are defined in chapter 7. A mean error of unity corresponds to the pre-fit (before the likelihood fit) error with no reduction of the impact from the corresponding uncertainty source by the likelihood fit. Nuisances with an error greater than 0.95 are not included in the plot. Errors that are much smaller than unity indicate the potential of reducing the corresponding uncertainty source by the inclusion of the observable. In addition to the expected effects described before, m_W^{reco} could reduce the effect of the early resonance decay uncertainty, $m_{\ell b}^{\text{reco}}$ potentially reduces the effect from background normalization and PDF extrapolation uncertainties, and $R_{\text{bq}}^{\text{reco}}$ could reduce the uncertainty due to choice of color reconnection scheme and PDF extrapolation uncertainties.

For the $P_{\text{gof}} \geq 0.2$ region, $m_{\ell b}^{\text{reco}}$ needs to be de-correlated from m_t^{fit} . This can be achieved by

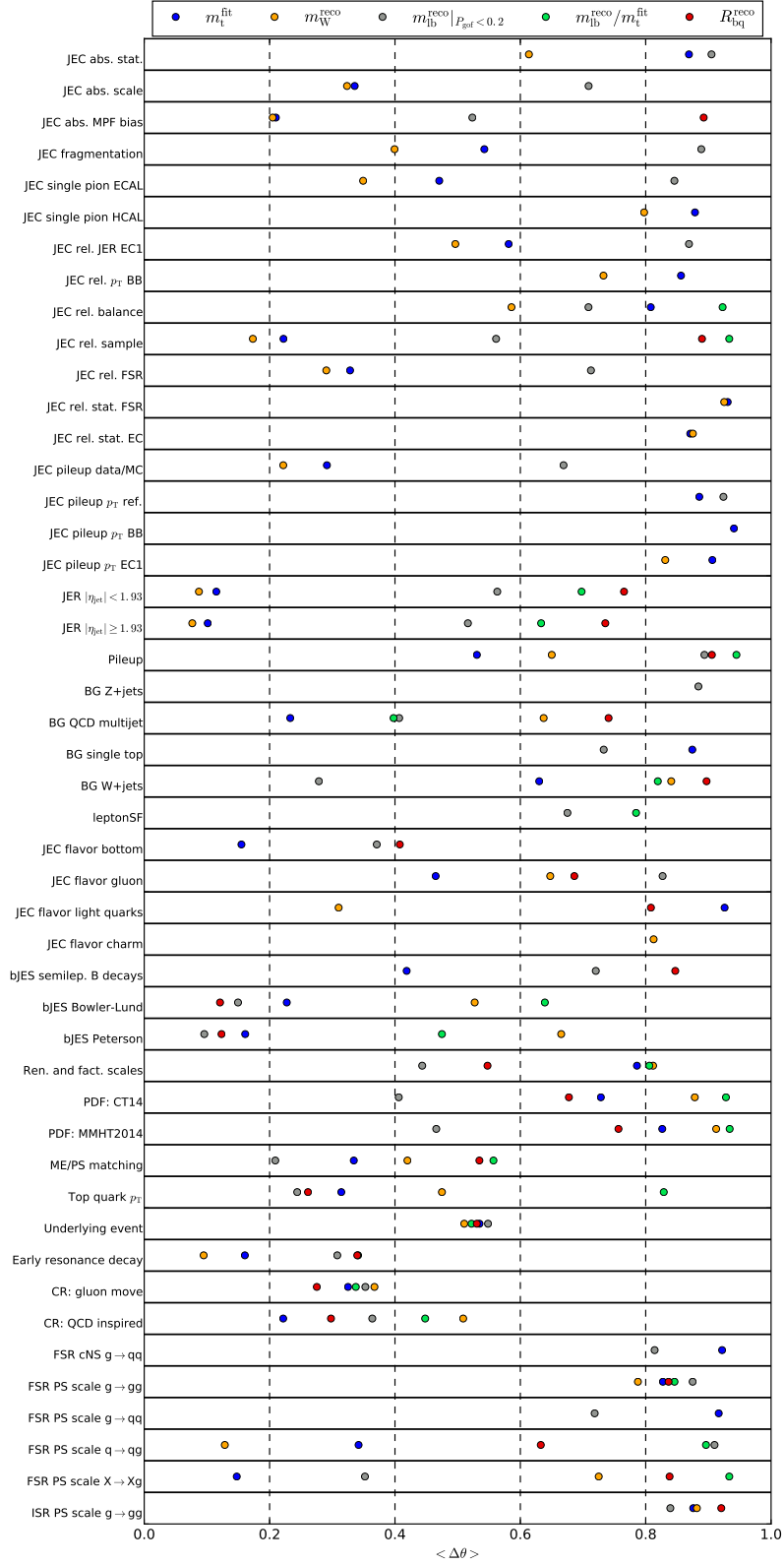


Figure 8.1.: Lepton+jets: Mean error of nuisance parameters when doing pseudo-experiments with single observables with one free nuisance parameter at a time and fixed m_t . Nuisances where the mean error is greater than 0.95 are not shown. A mean error of unity corresponds to the pre-fit error where the nuisance error is not reduced by the likelihood fit.

dividing by m_t^{fit} as was investigated in ref. [185]. The correlation between $m_{\ell b}^{\text{reco}}$ and m_t^{fit} with and without the reduction of $m_{\ell b}^{\text{reco}}$ are shown in figure 8.2. The correlation factor between $m_{\ell b}^{\text{reco}}$ and m_t^{fit} is about 30%. When dividing $m_{\ell b}^{\text{reco}}$ by m_t^{fit} to obtain $m_{\ell b}^{\text{reco}}/m_t^{\text{fit}}$ the correlation factor gets reduced to -4.9%. The correlation between all used observables in data and the different jet-parton permutation types are shown in the appendix figure A.1. All correlation factors between the observables are listed in table 8.1. The biggest correlation factor is 13% between $R_{\text{bq}}^{\text{reco}}$ and $m_t^{\text{fit}} \cdot m_{\ell b}^{\text{reco}} |_{P_{\text{gof}} < 0.2}$ is uncorrelated from all other observables by construction since $P_{\text{gof}} \geq 0.2$ is required for them. The small correlation factors are not sufficient to show that the usage of multiple observables on the same events does not introduce a bias. Therefore the independence of these observables is evaluated. The mathematical definition of independence is

$$P(A, B) = P(A) \cdot P(B)$$

with the combined probability density $P(A, B)$ of two observables A and B and their independent probability densities $P(A)$ and $P(B)$. One way to justify the independency of observables is to plot them in bins of one another. The normalized distributions should not depend on the selected bin. In the upper row of figure 8.3 this is shown for m_W^{reco} and $R_{\text{bq}}^{\text{reco}}$. For small m_W^{reco} the distributions differ considerably. In the lower row of figure 8.3 the 2D distributions between m_W^{reco} and $R_{\text{bq}}^{\text{reco}}$ is shown on the left. Normalized to unity it is an estimation of the combined probability density, $P(m_W^{\text{reco}}, R_{\text{bq}}^{\text{reco}})$. The independence criterion is tested using the ratio of the combined and multiplied independent probability densities, $P(m_W^{\text{reco}}, R_{\text{bq}}^{\text{reco}})/(P(m_W^{\text{reco}}) \cdot P(R_{\text{bq}}^{\text{reco}}))$, shown in the bottom center of figure 8.3. With the exception of a region at small m_W^{reco} , it is constant with values around one. The region with a higher ratio does not include many events. To evaluate this the ratio values are weighted with the number of events in the corresponding bin. This is shown in the histogram in the lower right of figure 8.3. The entries in the histogram look reasonably distributed with only a small number of effective entries outside a Gaussian profile with a mean of one. For all other combinations of observables such plots are included in appendix section A.

To be sure that the residual correlations and dependencies are no problem toy studies will be used to validate the likelihood parameterization approach in section 8.3.1.

Table 8.1.: Lepton+jets: Correlation factor between all one-on-one combinations of the observable.

	$R_{\text{bq}}^{\text{reco}}$	$m_{\ell b}^{\text{reco}}/m_t^{\text{fit}}$	m_W^{reco}
m_t	0.13	0.01	0.04
m_W^{reco}	-0.03	-0.04	
$m_{\ell b}^{\text{reco}}/m_t^{\text{fit}}$	-0.09		

The distributions of the observable are displayed in figures 8.5, 8.6 and 8.4 for μ +jets, e+jets and both decay channels combined. The dependency of these observables on the top-quark mass values in simulation is shown in figures 8.9 and 8.10.

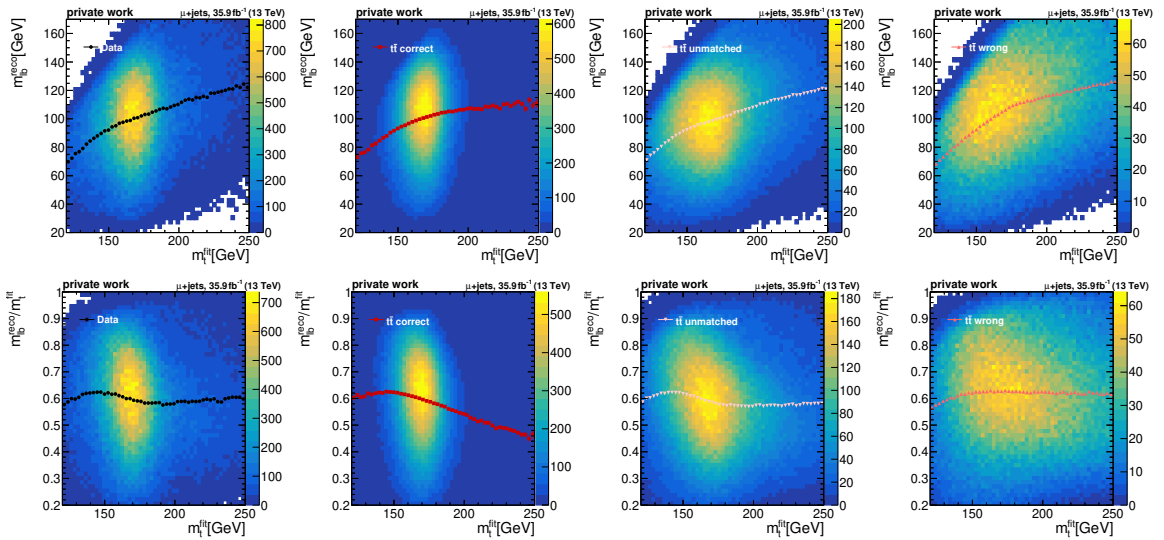


Figure 8.2.: Muon+jets: Correlations and profiles between $m_{\ell b}^{\text{reco}}$ and m_t^{fit} (top row) and the reduced $m_{\ell b}^{\text{reco}}$ and m_t^{fit} (bottom row) for data (left column) and the different permutation types (correct, wrong, unmatched) in simulation.

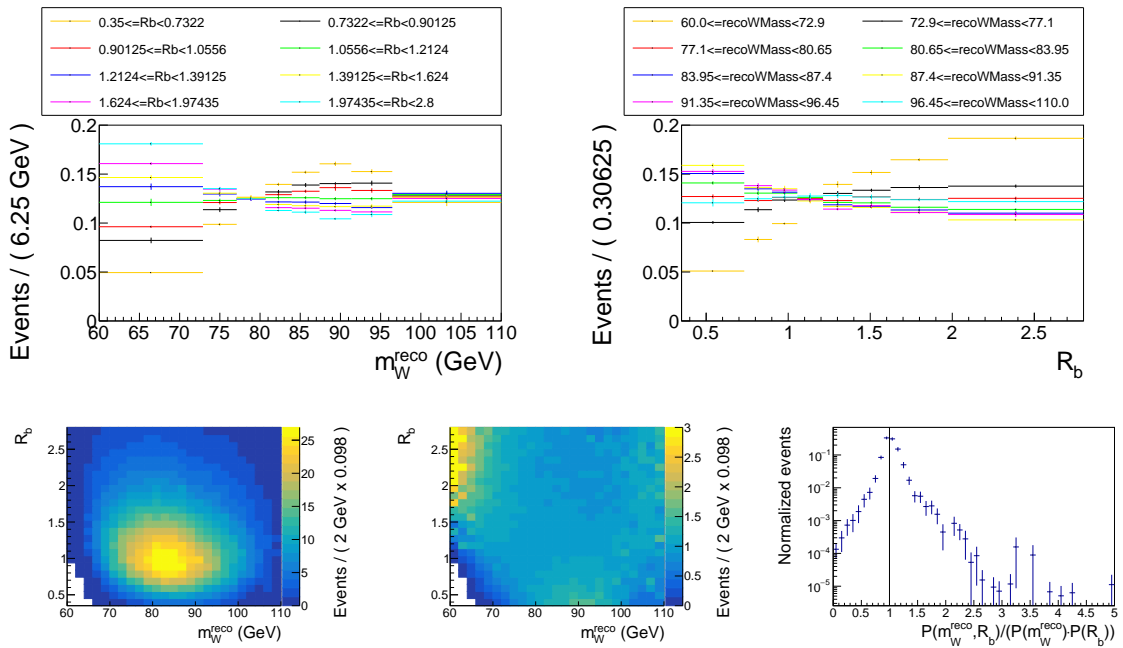


Figure 8.3.: Muon+jets simulation: Upper row: The m_W^{reco} distribution in bins of R_b^{reco} (left) and the R_b^{reco} distributions in bins of m_W^{reco} . Lower row: Correlation between m_W^{reco} and R_b^{reco} (left) and the ratio of the combined probability distribution of m_W^{reco} and R_b^{reco} to the multiplied probability distribution of m_W^{reco} and R_b^{reco} , $P(m_W^{\text{reco}}, R_b^{\text{reco}}) / (P(m_W^{\text{reco}}) \cdot P(R_b^{\text{reco}}))$ with all values limited to 3 (center). The value of $P(m_W^{\text{reco}}, R_b^{\text{reco}}) / (P(m_W^{\text{reco}}) \cdot P(R_b^{\text{reco}}))$ weighted by the number of events in the corresponding bin. The rightmost bin contains the overflow (right).

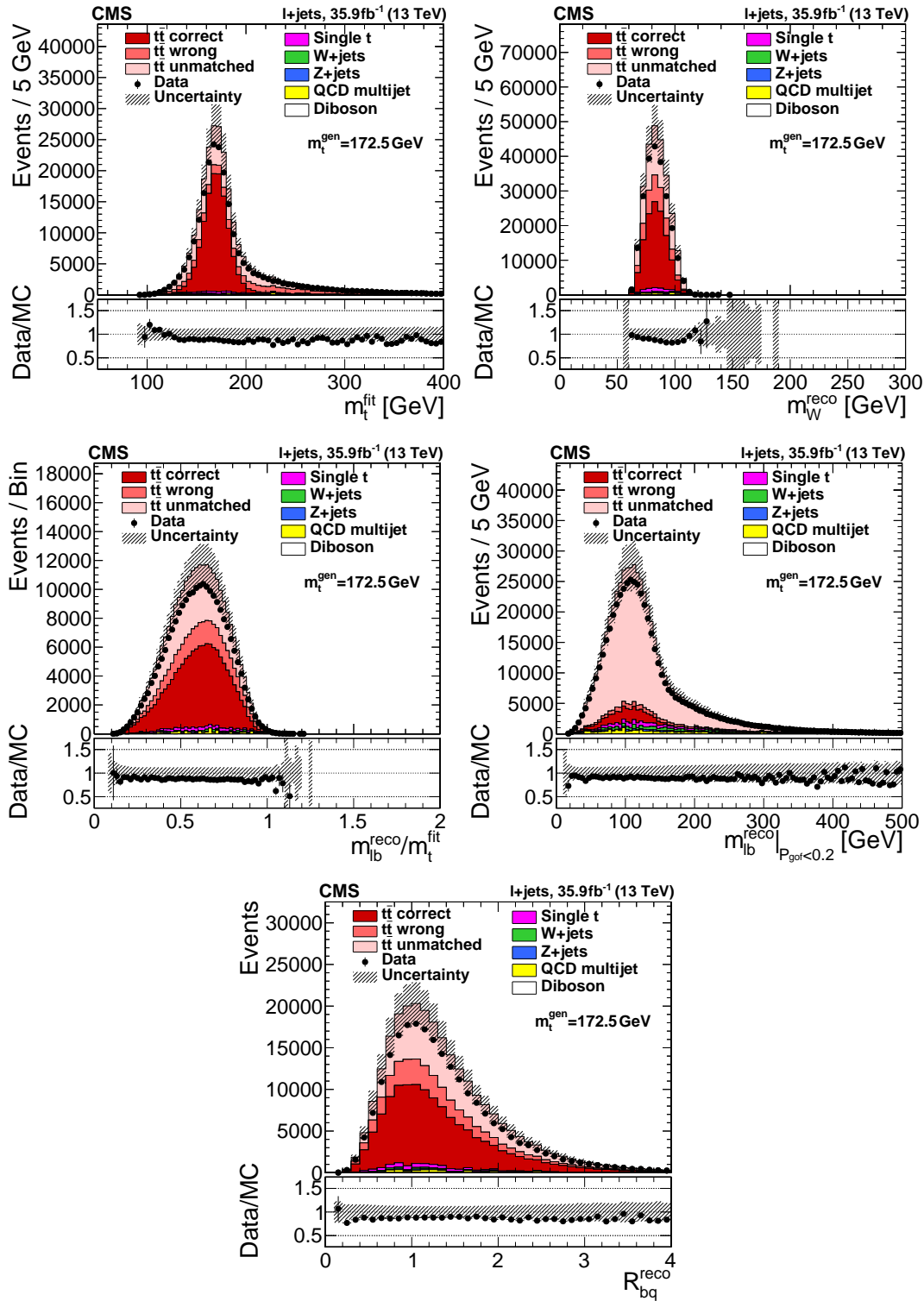


Figure 8.4.: Final selection lepton+jets: Distributions of the used observables. Fitted top-quark mass for $P_{\text{gof}} \geq 0.2$ (upper left), reconstructed mass of the W bosons candidate that decays hadronic for $P_{\text{gof}} \geq 0.2$ (upper right), the mass of the lepton-b system from the leptonic decayed top divided by m_t^{fit} ($m_{lb}^{\text{reco}}/m_t^{\text{fit}}$) for $P_{\text{gof}} \geq 0.2$ (middle left) and m_{lb}^{reco} for $P_{\text{gof}} < 0.2$ (middle right) and the ratio of bottom to light tagged jet p_T (bottom). The uncertainty band contains simulation statistic, cross section uncertainty and all event weight based uncertainties.

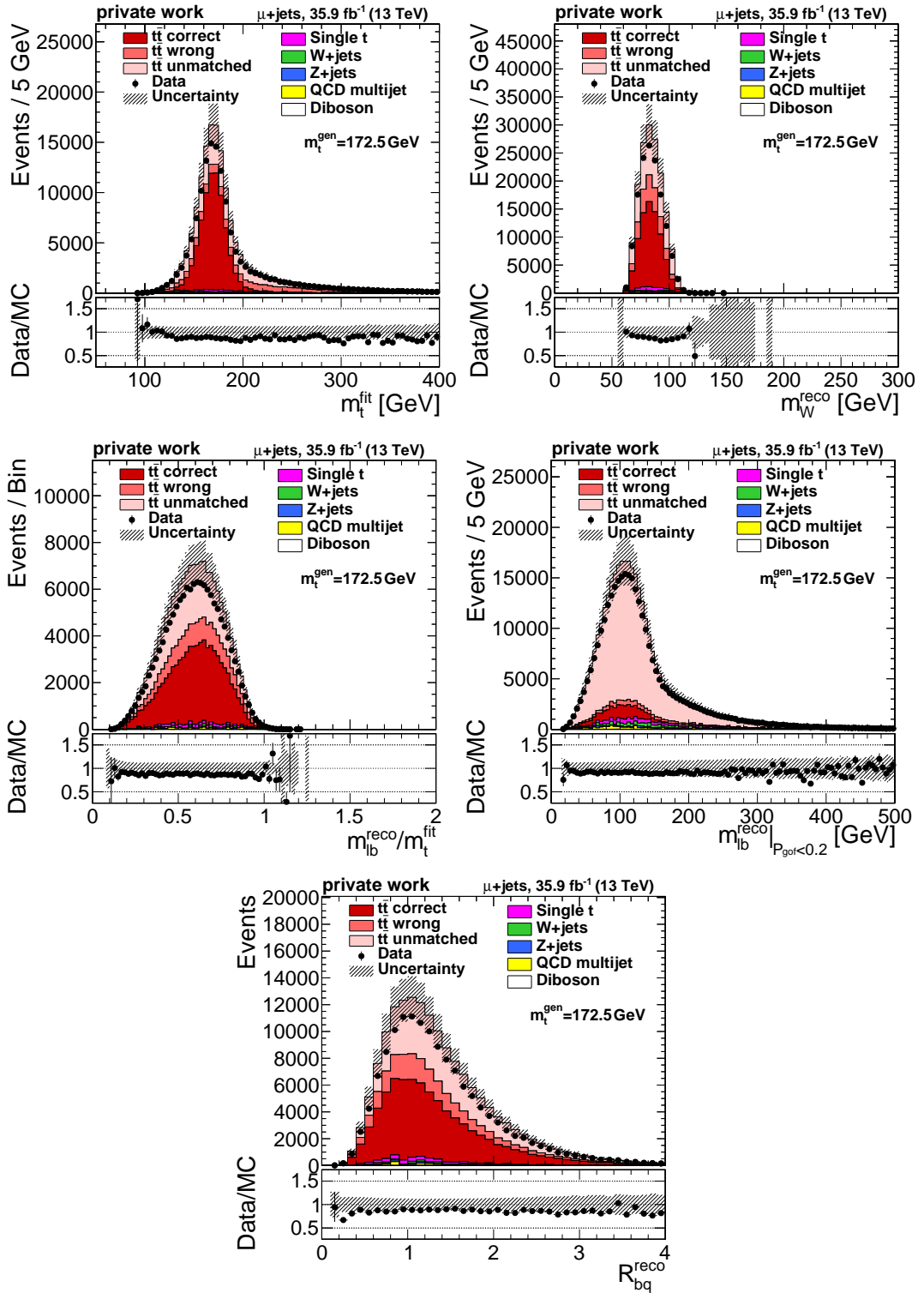


Figure 8.5.: Final selection muon+jets: Distributions of the used observables: Distributions of the used observables: Fitted top-quark mass for $P_{\text{gof}} \geq 0.2$ (upper left), reconstructed mass of the W bosons candidate that decays hadronic for $P_{\text{gof}} \geq 0.2$ (upper right), the mass of the lepton-b system from the leptonic decayed top divided by m_t^{fit} ($m_{lb}^{\text{reco}}/m_t^{\text{fit}}$) for $P_{\text{gof}} \geq 0.2$ (middle left) and m_{lb}^{reco} for $P_{\text{gof}} < 0.2$ (middle right) and the ratio of bottom to light tagged jet p_T (bottom). The uncertainty band contains simulation statistics, cross section uncertainty and all event weight based uncertainties.

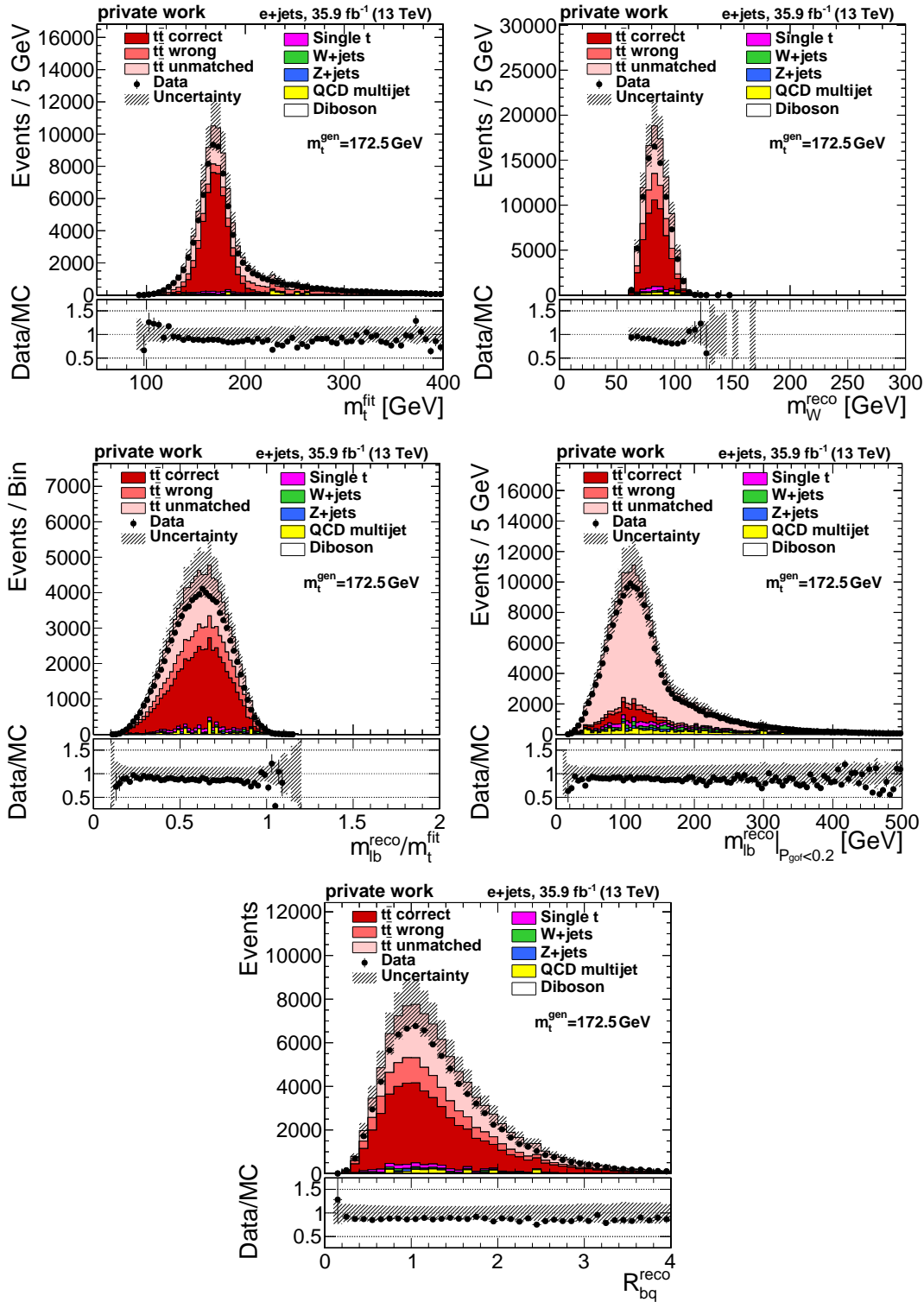


Figure 8.6.: Final selection electron+jets: Distributions of the used observables. Distributions of the used observables: Fitted top-quark mass for $P_{\text{gof}} \geq 0.2$ (upper left), reconstructed mass of the W bosons candidate that decays hadronic for $P_{\text{gof}} \geq 0.2$ (upper right), the mass of the lepton-b system from the leptonic decayed top divided by m_t^{fit} ($m_{lb}^{\text{reco}}/m_t^{\text{fit}}$) for $P_{\text{gof}} \geq 0.2$ (middle left) and m_{lb}^{reco} for $P_{\text{gof}} < 0.2$ (middle right) and the ratio of bottom to light tagged jet p_T (bottom). The uncertainty band contains simulation statistic, cross section uncertainty and all event weight based uncertainties.

8.3. Templates, nuisance parameterization and fit

From the distribution of the observables in simulation probability density functions are constructed. The m_t^{fit} distribution is described with

$$P\left(m_t^{\text{fit}}\right) = f_{\text{sig}} V\left(m_t^{\text{fit}}|\mu, \sigma\right) + \sum_{n=0}^4 p_n T_n\left(m_t^{\text{fit}}\right), \quad (8.1)$$

where the Voigt profile

$$V(x|\mu, \sigma) = \int_{-\infty}^{\infty} G(x', \sigma) L(x - x', \mu) dx'$$

is a convolution of a Gaussian G with a Lorentz function L and Chebyshev polynomials T_n , up to the order $n = 4$, defined as

$$\begin{aligned} T_{n+1}(x) &= 2xT_n(x) - T_{n-1}(x) \\ \text{with } T_0(x) &= 1 \text{ and } T_1(x) = x. \end{aligned}$$

The Voigt profile describes the signal part of the distribution and the Chebyshev polynomials the background. Chebyshev polynomials are used because its functional form can be evaluated faster than the Crystal Ball function used for this distribution in former analyses and the inner product of the T_n is orthogonal. The signal fraction f_{sig} is left free during the fit as well as the parameters μ , σ and p_n . The decay width Γ in the Lorentz function is fixed to 1.5 GeV, close to the theoretical decay width. That the extracted m_t is unbiased, also by the choice of the parameterization, will be checked in section 8.3.1 and section 8.3.3. This parameterization will be fit to histograms of m_t^{fit} from 130 GeV to 350 GeV with 55 bins.

The other observables are all parameterized with eight bins of equal depth each. This results in seven free parameters each, as the probability density functions are normalized. Equal depth means that the bin width is chosen in a way that the number of events in each bin is approximately the same. This way there is no big variation due to low statistics in the highest and lowest bin and the peak is described by more bins. The bin widths are estimated from the default signal simulation and kept the same for all variations. Because the probability density functions are normalized there are seven free parameters from the eight bins. All bin edges are listed in table 8.2. The probability density function is build by multiplying the Poisson probabilities of all bins.

The n 'th parameter of the probability density functions of the observable $obs \in \left\{m_t^{\text{fit}}, m_W^{\text{reco}}, m_{\ell b}^{\text{reco}}/m_t^{\text{fit}}, m_{\ell b}^{\text{reco}}|_{P_{\text{got}} < 0.2}, R_{\text{bq}}^{\text{reco}}\right\}$ is labeled α_k and parameterized linear, factorized with m_t and the vector of nuisance parameters $\vec{\theta}$. So for each free parameter k , for all observables, it is

$$\alpha_k(m_t, \vec{\theta}) = C_k \cdot \left(1 + d_k \cdot \left(\alpha_k^0 + s_k^0 \cdot (m_t - 172.5 \text{ GeV})\right) \prod_i \left(1 + d_k \cdot s_k^i \theta_i\right)\right),$$

Table 8.2.: Bin Edges of the binned templates.

μ +jets m_W^{reco}	60	72.9	77.1	80.7	84	87.4	91.4	96.5	110
e+jets m_W^{reco}	60	73.1	77.3	80.8	84.1	87.5	91.4	96.7	110
μ +jets $m_{\ell b}^{\text{reco}}/m_t^{\text{fit}}$	0.2	0.39	0.48	0.54	0.6	0.65	0.71	0.79	1
e+jets $m_{\ell b}^{\text{reco}}/m_t^{\text{fit}}$	0.2	0.42	0.5	0.56	0.62	0.67	0.73	0.8	1.0
μ +jets $m_{\ell b}^{\text{reco}} _{p_{\text{gof}} < 0.2}$	0	70.5	87.3	100.5	112.8	126.0	143.1	181.5	300
e+jets $m_{\ell b}^{\text{reco}} _{p_{\text{gof}} < 0.2}$	0	73.8	90.9	104.1	116.4	129.9	149.1	191.4	300
μ +jets $R_{\text{bq}}^{\text{reco}}$	0.35	0.73	0.90	1.06	1.21	1.39	1.62	1.97	2.8
e+jets $R_{\text{bq}}^{\text{reco}}$	0.35	0.718	0.89	1.05	1.21	1.39	1.62	1.97	2.8

where the arbitrary constants C_k and d_k are fixed by the default simulation such that α_k^0 is in the order of 1.0. The variables indexed $i > 0$ correspond to different nuisances while $i = 0$ indicates the base offset and slope from a parameterization without additional nuisances. The used values of C_k and d_k used for the m_t^{fit} distributions described with eq. 8.1 are listed in the tab. 8.3. The same values are used for both lepton channels. For the binned distributions the $C_k = n_{\text{bin}}/n_{\text{hist}}/w_{\text{bin}}$ values are the number of events in the corresponding bin n_{bin} divided by the number of events in the corresponding histogram and the bin width w_{bin} . Their $d_k = 1/\sqrt{n_{\text{bin}}}$ is calculated from the number of events predicted from the default simulation in the corresponding bin, n_{bin} .

This parameterization should lead to all fitted parameters being of similar size and uncertainty. This will improve the numerical stability of the likelihood evaluations later.

An exception is made for the dependence of the nuisance parameters corresponding to the FSR uncertainty through μ_R . Their dependence is parameterized quadratically, so instead of the ' $s_k^i \theta_i$ ' part of the α_k parameterization the dependence

$$s_{Lk}^i \cdot \frac{(-\theta_i) \cdot (\theta_i - 1)}{2} + s_{Rk}^i \cdot \frac{\theta_i \cdot (\theta_i + 1)}{2} = \frac{s_{Rk}^i - s_{Lk}^i}{2} \theta_i^2 + \frac{s_{Rk}^i + s_{Lk}^i}{2} \theta_i$$

with the two slope parameters s_{Lk}^i and s_{Rk}^i , is inserted. This will be motivated and evaluated in sec. 9.2.1.

 Table 8.3.: Used fixed arbitrary constants C_k and d_k for numerical stability of the fit in the description of the m_t^{fit} distributions. The same numbers are used for both lepton channels.

k	m_t^{fit}, μ	m_t^{fit}, σ	m_t^{fit}, p_0	m_t^{fit}, p_1	m_t^{fit}, p_2	m_t^{fit}, p_3	m_t^{fit}, p_4	$m_t^{\text{fit}}, f_{\text{sig}}$
d_k	0.001	0.1	0.02	0.1	0.1	0.1	0.1	0.03
C_k	170.6	11.9	-0.95	-0.2	0.39	-0.3	0.2	0.55

α_k^0 is fitted first to the default simulation sample to guarantee that it results in $m_t = 172.5 \text{ GeV}$ and $\vec{\theta} = \vec{0}$. Afterwards the slopes s_k^i are derived on the mass and uncertainty variations. The $i > 0$ correspond to different nuisances while $i = 0$ is the base offset from a parameterization

without additional nuisances. The slopes from all nuisances i including the offset at $i = 0$ are gathered in the vector \vec{s}_k . To later include also the statistical uncertainties on α_k^0 and \vec{s}_k , additional nuisance parameters β_k and $\vec{\omega}_k$ are added. This is done for all nuisances that correspond to variations evaluated with dedicated simulation samples. The final functional form is:

$$\alpha_k(m_t, \vec{\theta}, \beta_k, \vec{\omega}_k) = C_k \cdot \left(1 + d_k \cdot \left(\alpha_k^0 + \beta_k + s_k^0 \cdot (m_t - 172.5 \text{ GeV}) + \omega_k^0 \cdot 1 \text{ GeV} \right) \right) \quad (8.2)$$

$$\times \prod_i \left(1 + d_k \cdot \left(s_k^i \theta_i + \omega_k^i \cdot 1.0 \right) \right)$$

The factors of 1.0 GeV and 1.0 represent the expected magnitude from prior knowledge on m_t and $\vec{\theta}$.

In the final fit $\vec{\theta}$ is constrained by adding to the likelihood standard normal functions of mean 0 and width 1. $\vec{\beta}$ and ω are constrained by multi-dimensional Gaussian functions centered on zero with a variance equal to their covariance matrix obtained in the fit of the corresponding slopes. The $\vec{\beta}$ or ω from the same observable and nuisances are treated as correlated. This method is basically the Barlow-Beeston approach for finite MC samples [186]. The $\vec{\beta}$ and the ω corresponding to nuisances that are not evaluated from dedicated samples but by varying the default sample are fixed to 0.

The probability density functions for all observables and the constraints are stored in a ROOFIT [89] model along with the selection for each observable. Therefore the addition of new observables and categories in this setup is straight forward. For the likelihood fit to (pseudo-)data sets the events are converted into a ROOFIT data sample and histograms are constructed for each observable. For the measurement and the evaluation of the impact from the nuisance parameters on it, a negative binned log-likelihood fit using the MINUIT2 package is performed.

To estimate the impact of one uncertainty source i on the measurement (σ_i) the corresponding nuisance parameter θ_i is fixed in the fit to its post-fit value $\theta_i^{\text{post-fit}}$ plus/minus its post-fit uncertainty $\Delta\theta_i^{\text{post-fit}}$. Then for both cases the likelihood maximization is performed again. The difference in m_t between the fit with all parameters and the fit with the fixed nuisance is interpreted as the up/down impact of the nuisance as

$$\sigma_i^{\text{up/down}} = m_t - m_t |_{\theta_i = \theta_i^{\text{post-fit}} \pm \Delta\theta_i^{\text{post-fit}}} .$$

For nuisances that reflect the limited simulation sample sizes, different procedures are applied.

For the uncertainties of the default simulation and the m_t dependence, the fit is once performed with only m_t as a free parameter, so with $\vec{\theta} = \vec{\theta}^{\text{post-fit}}$ and all β_k and $\vec{\omega}_k$ fixed to their post-fit values. This gives the statistical uncertainty of the measurement

$$\sigma_{\text{stat}} = \sigma_{m_t} |_{\vec{\theta} = \vec{\theta}^{\text{post-fit}}, \beta_k = \beta_k^{\text{post-fit}}, \vec{\omega}_k = \vec{\omega}_k^{\text{post-fit}}} .$$

Then all nuisances related to the default simulation and the m_t dependence (β_k and ω_k^0) are set free as well in a second fit. The quadratic difference between the error on m_t from this

two fits is interpreted as the calibration uncertainty

$$\sigma_{\text{calibration}} = \sqrt{\sigma_{m_t} |_{\vec{\theta}=\vec{\theta}^{\text{post-fit}}, \omega_k^i |_{i>0}=0}^2 - \sigma_{\text{stat}}^2}.$$

This collects the uncertainty from constraints of β_k and ω_k^0 corresponding to uncertainties from the fit of α_k on the default signal simulation and s_k^0 from the default signal simulation and the m_t variation samples.

For the nuisances related to the finite size of the same independent and systematically varied sample, the fit is once performed with all these nuisances (θ_i) and the nuisance of the corresponding systematic effect (ω_k^i) fixed to their post-fit values. The quadratic difference between the m_t error in the full fit and this fit is interpreted as the overall impact of the systematic effect and the sample size as

$$\sigma_i^{\text{up/down}} = \sqrt{\sigma_{m_t}^2 - \sigma_{m_t} |_{\theta_i=\theta_i^{\text{post-fit}} \pm \Delta\theta_i^{\text{post-fit}}, \omega_k^i=\omega_k^{i,\text{post-fit}}}^2}.$$

The impact of the sample size alone (σ_i^{stat}) is inferred by quadratically subtracting the mean of the up and down impacts found for the systematic effect from the overall impact as

$$\sigma_i^{\text{stat}} = \sqrt{\left(\frac{\sigma_i^{\text{up}} + \sigma_i^{\text{down}}}{2}\right)^2 - \sigma_{m_t} |_{\theta_i=\theta_i^{\text{post-fit}}, \omega_k^i=0}^2}.$$

The parameterization and the extraction of the fit results are further illustrated by a walk-through with an example nuisance in appendix chapter B.

The effect of different top-quark mass values on the distributions of observables and parameterizations is shown in figure 8.9 for the μ +jets channel and in figure 8.10 for e+jets. The same is shown for all variations in appendix D.2. For variations from a dedicated simulation sample an uncertainty band corresponding to the statistical uncertainty is shown. If no explicit P_{gof} selection is given then the $P_{\text{gof}} \geq 0.2$ selection is applied.

For a full $t\bar{t} \rightarrow \text{lepton+jets}$ measurement the likelihoods from the μ +jets and e+jets templates are added. The $m_{\text{W}}^{\text{reco}}$ distribution, which is included to constrain jet energy dependencies, does not change significantly with m_t . Especially noteworthy is a significant m_t dependency in the $m_{\ell b}^{\text{reco}} |_{P_{\text{gof}} < 0.2}$ distribution. This is information on the top quark mass that was not included in former $t\bar{t} \rightarrow \text{l+jets}$ analyses. If slopes s_k^i of the mass dependence and a nuisance dependence have opposite components this can help to reduce the uncertainty from that nuisance parameter on the top quark mass measurements via the likelihood fit. The slopes s_k^0 of the top mass dependence and the slopes for two example nuisances (multiplied with d_k) are presented in figure 8.7 and figure 8.8 for the muon and the electron channel. These examples help to explain how the nuisance parameters are able to reduce the uncertainty on the m_t measurement. The chosen example nuisances correspond to the uncertainty due to choice of color reconnection (CR) scheme and jet energy resolution uncertainty (JER) of jets with

$|\eta| < 1.93$]. Slopes of zero indicate that the parameter does not depend on the nuisance. For mean (sigma) of the m_t parameterization, the slopes for m_t and JER differ significantly from zero, as expected. The estimation of the uncertainty due to the CR scheme is limited by the size of the simulation sample that is available. This results in large uncertainties on the slopes of the parameterization of the corresponding nuisance parameter. The effect can be seen in the slopes of the m_t^{fit} template, where the values of slopes for the CR gluonmove nuisance are in the same order of magnitude as for m_t and the other example nuisance, but the uncertainties on the slope values are so big that they are compatible with zero. This means that no CR dependency of the m_t^{fit} distribution can be seen within the available statistical uncertainty of the simulation. This is a case where an additional nuisance parameter $\vec{\omega}$ is needed to account for the limited simulation sample size.

A prominent feature that is visible when comparing the three variations, is that the mean parameter of the Voigtian profile depends on m_t , but not on the two example nuisance parameters. Looking at m_W^{reco} it can be seen that the highest bin depends on JER, but not on m_t and the CR scheme. This could potentially reduce the impact from the uncertainty on JER. In the $R_{\text{bq}}^{\text{reco}}$ bins no such prominent feature is visible, but the slope derived for the CR gluonmove nuisance parameter is clearly higher than for the m_t and JER dependence. The m_t slope values for the $m_{\ell\text{b}}^{\text{reco}}/m_t^{\text{fit}}$ bins get higher for higher bins but the slope values of the example nuisances get lower. This is more prominent for the muon+jets case than for the electron+jets. A part of this difference could be caused by the smaller relative uncertainties on simulation statistic in the muon case. For $m_{\ell\text{b}}^{\text{reco}}|_{P_{\text{gof}} < 0.2}$ the m_t slope is dependent on the bin but the slopes for the example nuisances are small.

8.3.1. Toy consistency checks of the parameterization

Different tests for the likelihood parameterization were performed. For them toy pseudo-data sets were generated, different from the pseudo-experiments described before. Toy sets are derived from the probability densities described by the likelihood model. All checks are performed using the final five observables and both decay channels. In addition to the checks presented here, closure plots were produced where the nuisance values are measured on the corresponding variation in simulation. They are presented in appendix D.1. For all nuisance parameters the different systematic uncertainty variations are within the error of the extracted values. So for variations that none of the included observables depend on, the prior error is extracted.

Alternative statistical uncertainty An alternative parameterization of the nuisance parameters corresponding to the uncertainty from the finite simulation sample size is tested and

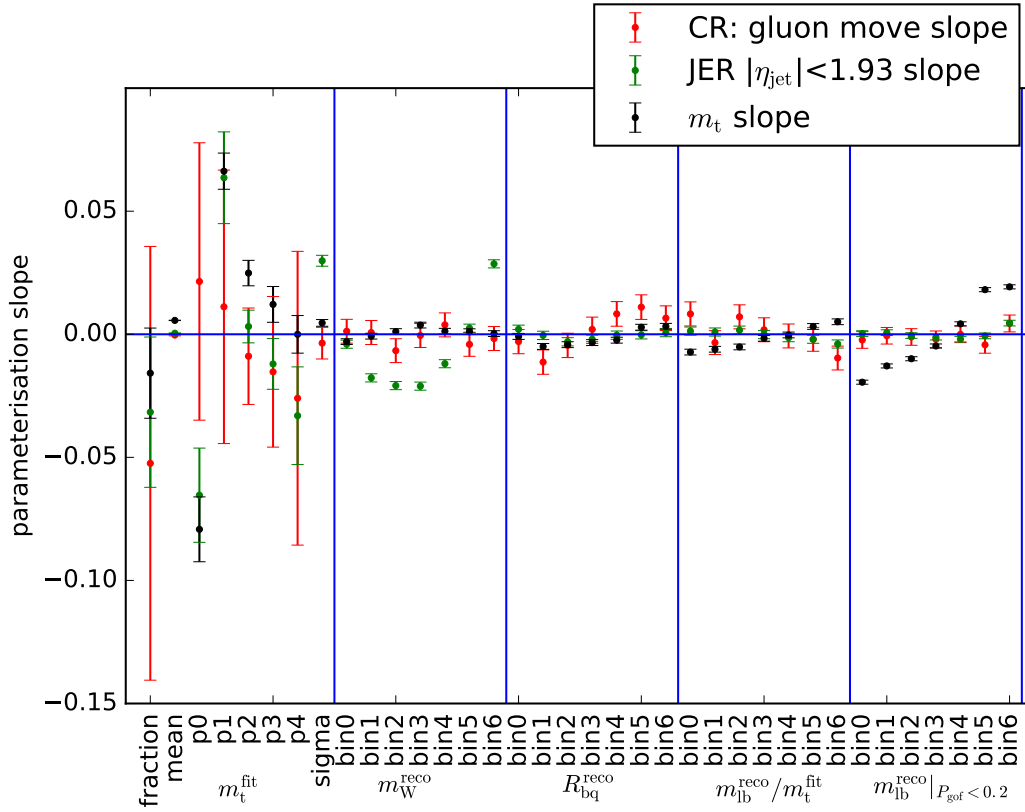


Figure 8.7.: Muon+Jets: Slopes in the template parameterization for the top quark mass and two example nuisances.

compared to the default model. The alternative model uses the parameterization of

$$\alpha_k(m_t, \vec{\theta}, \beta_k, \vec{\omega}_k) = C_k \cdot \left(\alpha_k^0 + \beta_k + d_k \left(s_k^0 \cdot (m_t - 172.5 \text{ GeV}) + \omega_k^0 \cdot 1 \text{ GeV} \right) \right) \quad (8.3)$$

$$\times \prod_i \left(1 + d_k \cdot (s_k^i \theta_i + \omega_k^i \cdot \theta_i) \right),$$

where, compared to the default (eq. 8.2), the nuisances accounting for the statistical uncertainty on a slope parameter s_i are scaled by θ_i . This alternative model is labelled V2 in the following.

To evaluate model V2 its parameterization is derived from simulation as is done for the default model. Pseudo-data is generated from the model. A value for m_t is picked from a uniform distribution between $172.5 - \sqrt{3}$ and $172.5 + \sqrt{3}$ GeV and all nuisance values $\vec{\theta}$ are picked from Gaussian distributions with zero mean and unity width. As examples the nuisance corresponding to the FlavorPureBottom JEC is taken, as it is a leading uncertainty source not evaluated via a dedicated sample, and CR_GluonMove as an important uncertainty limited by simulation statistics will be shown in the following. The generated values for these two example nuisances and m_t are shown in figure 8.11.

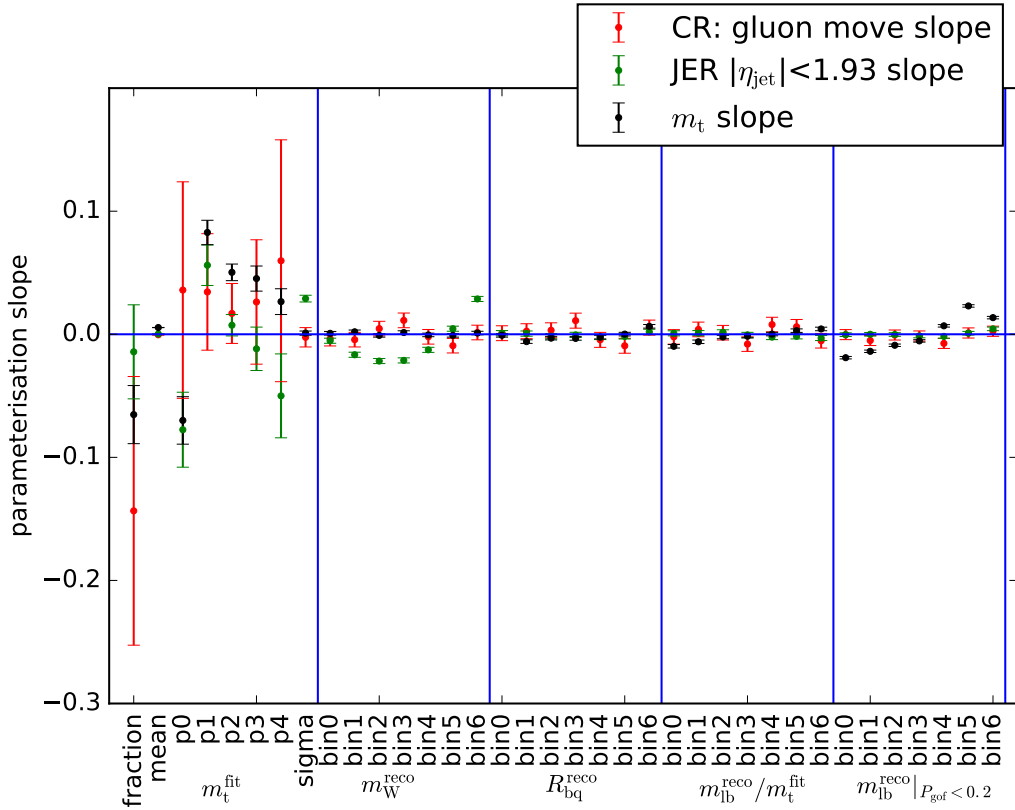


Figure 8.8.: Electron+Jets: Slopes in the template parameterization for the top quark mass and two example nuisances.

For the parameters α_k , derived from dedicated simulation samples, the slope s_k^i are smeared within their statistical uncertainty. From these model settings the expected number of entries per bin is computed and picked from a Poisson distribution around this expectation. After the pseudo-data set is generated the model parameters are reset to their default values. Then the likelihood is maximized on the pseudo-data and the pre- and post-fit values of all fit parameters and their uncertainties are stored.

The maximization is done with and without the ω_k accounting for the statistical uncertainties on the s_k^i for 1000 toys for each combination. The m_t and all nuisance pulls are evaluated.

The pull distributions of the example nuisance FlavorPureBottom for the cases without and with ω_k for the default model and model V2 are depicted in figure 8.12. There is no difference between the models visible. The pull distributions of the example nuisance CR_GluonMove for the cases without and with ω_k for the default model and model V2 are depicted in figure 8.13. Without nuisances ω_k accounting for the sample statistics, both models underestimate the uncertainty. With ω_k the pull for the default model has a width of one around zero, but is much too wide for the alternative model V2. This had to be expected as the toy is generated with a Gaussian prior but two Gaussian uncertainties are multiplied in the model V2.

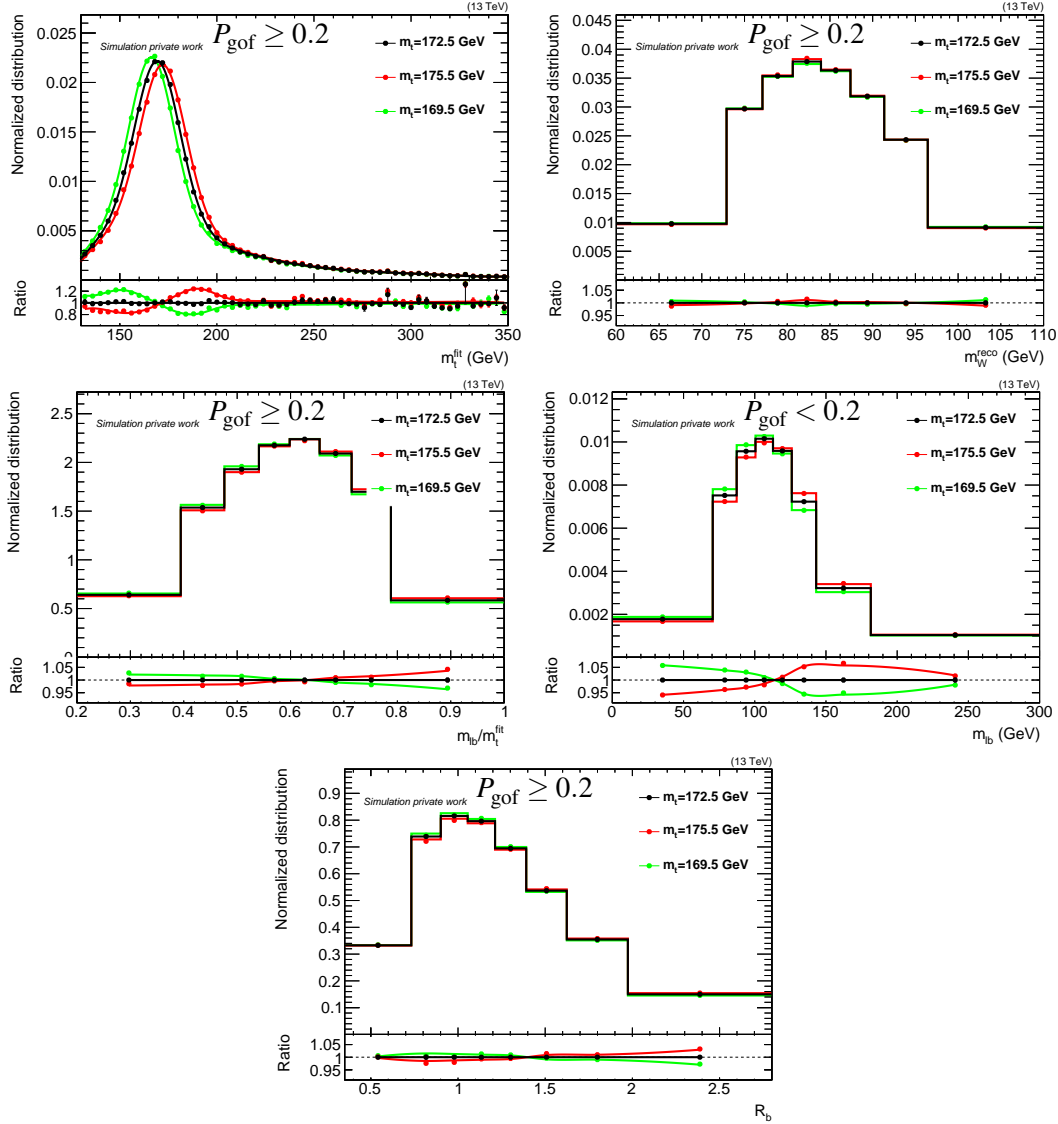


Figure 8.9.: Muon+jets: The distributions of observables and their parameterization for different top-quark mass values in simulation: m_t^{fit} (upper left), m_W^{reco} (upper right), $m_{\ell b}^{\text{reco}}/m_t^{\text{fit}}$ (middle left), $m_{\ell b}^{\text{reco}}$ for events with $P_{\text{gof}} < 0.2$ (middle right) and R_b^{reco} (bottom right). For the binned templates the bins are divided by their width to maintain the form of the distribution.

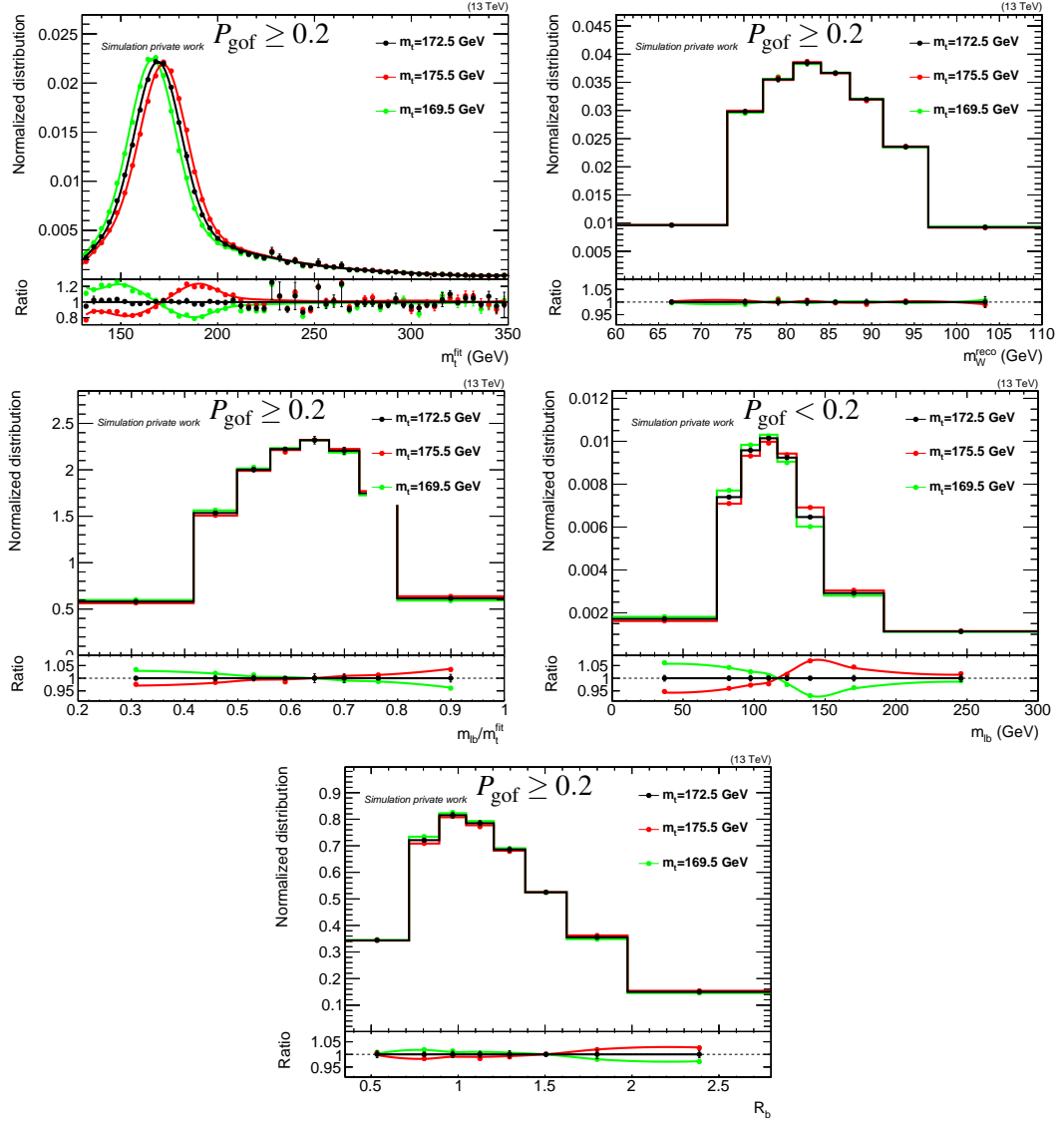


Figure 8.10.: Electron+jets: The distributions of observables and parameterization for different top-quark mass values in simulation: m_t^{fit} (upper left), m_W^{reco} (upper right), $m_{\ell b}^{\text{reco}}/m_t^{\text{fit}}$ (middle left), $m_{\ell b}^{\text{reco}}$ for events with $P_{\text{gof}} < 0.2$ (middle right) and R_b^{reco} (bottom right). For the binned templates the bins are divided by their width to maintain the form of the distribution.

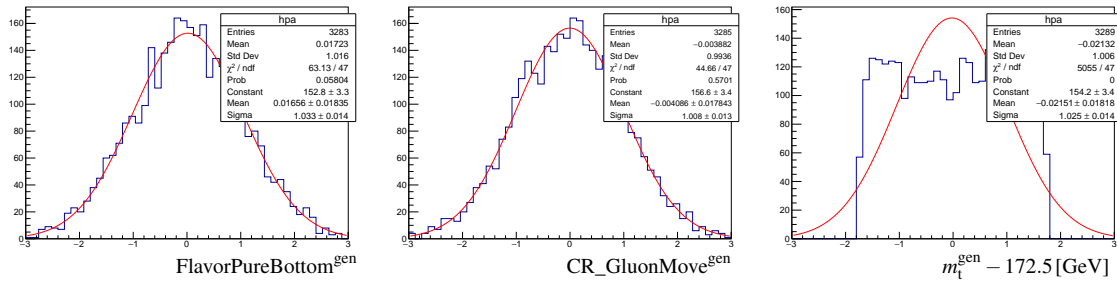


Figure 8.11.: Generated values for the three important example parameters.

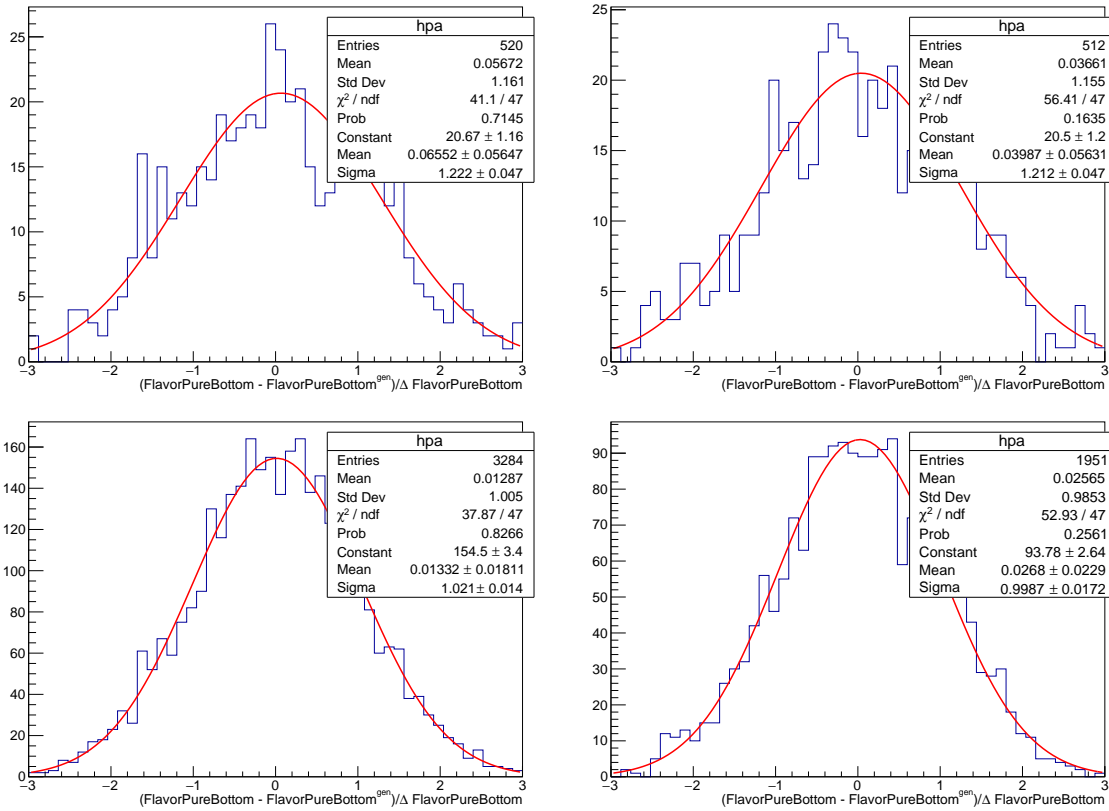


Figure 8.12.: Pull distributions $\frac{\theta - \theta^{\text{gen}}}{\Delta\theta}$ for the FlavorPureBottom nuisance. The top row shows the results for the fit with the additional nuisances ω_k fixed to 0 in the fit, the bottom row the results with the additional nuisances ω_k as additional fit parameters. The left column shows the results for the *default* model and the right column the results for the alternative model V2. [187]

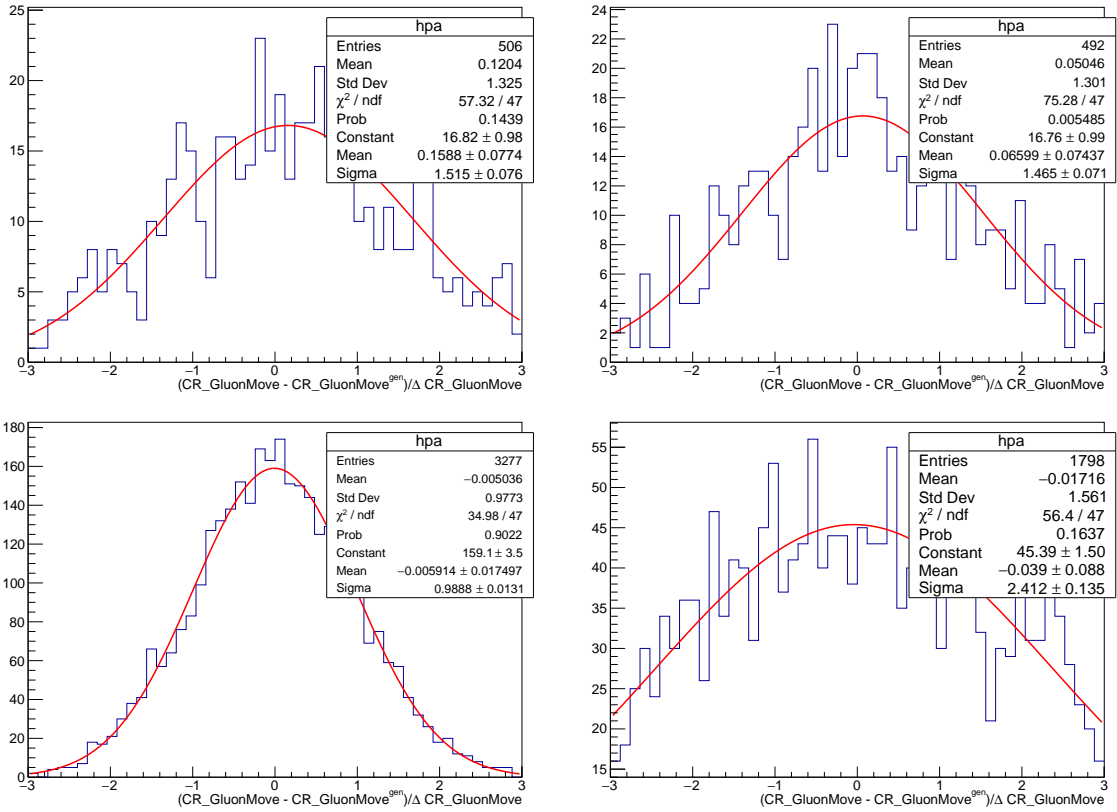


Figure 8.13.: Pull distributions $\frac{\theta - \theta^{gen}}{\Delta\theta}$ for the CR_GluonMove nuisance. The top row shows the results for the fit with the additional nuisances ω_k fixed to 0 in the fit, the bottom row the results with the additional nuisances ω_k as additional fit parameters. The left column shows the results for the *default* model and the right column the results for the alternative model *V2*.

The pull widths for m_t are shown in figure 8.14. Without ω_k they are too wide, illustrating that the additional parameter for the simulation statistic is needed. With ω_k the pulls for both models look good with a possible bias for the alternative model.

Toys from statistically fluctuated input To further verify the handling of the simulated statistics 'fluctuated' model parameterizations are derived.

The content of the input histograms is varied. For independent simulation samples Poisson distributions around the original number of entries per bin are used. For histograms correlated to the default simulation the relative changes for the histograms are propagated. From the varied histograms, a model is derived. This model is called a 'fluctuated' model. About 1000 of such models are derived. From these models pseudo-data sets with Gaussian priors for all nuisance values and a uniform prior between $172.5 - \sqrt{3}$ and $172.5 + \sqrt{3}$ GeV for m_t are generated as was described in the last subsection. The default likelihood is then fitted to these pseudo-data sets and the results are analyzed for possible biases. The resulting differ-

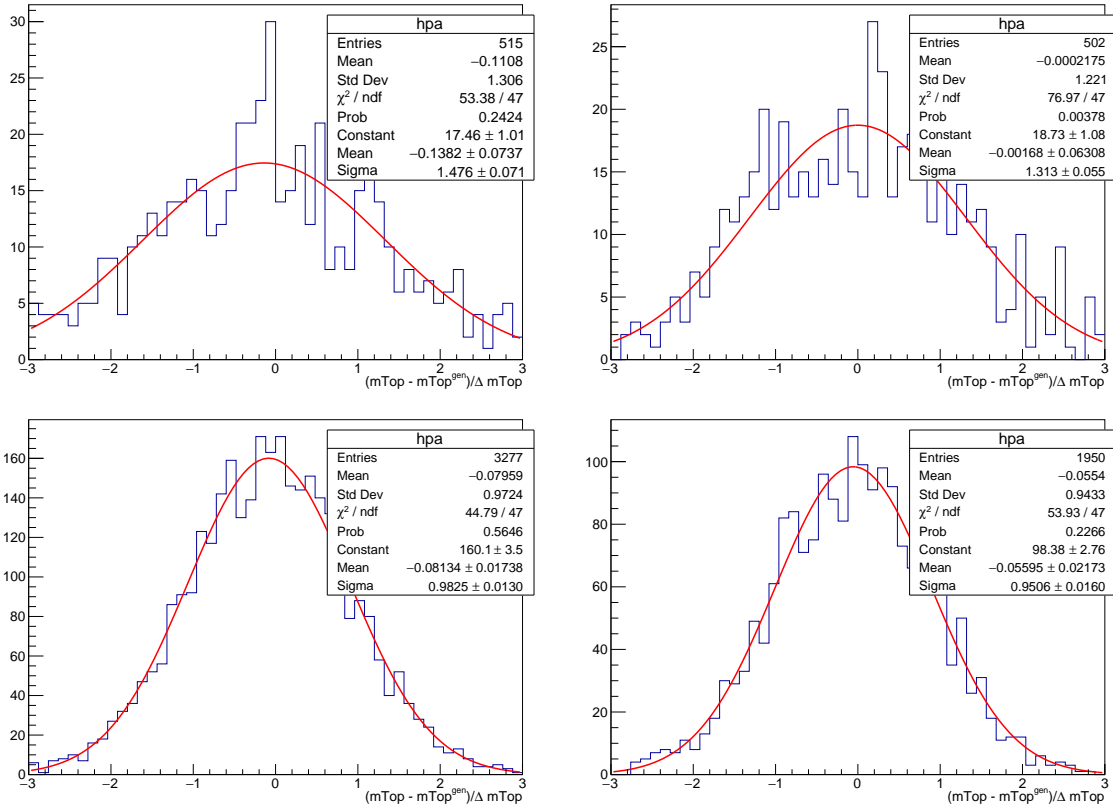


Figure 8.14.: Pull distributions $\frac{\theta - \theta^{gen}}{\Delta\theta}$ for m_t . The top row shows the results for the fit with the additional nuisances ω_k fixed to 0 in the fit, the bottom row the results with the additional nuisances ω_k as additional fit parameters. The left column shows the results for the *default* model and the right column the results for the alternative model V2.

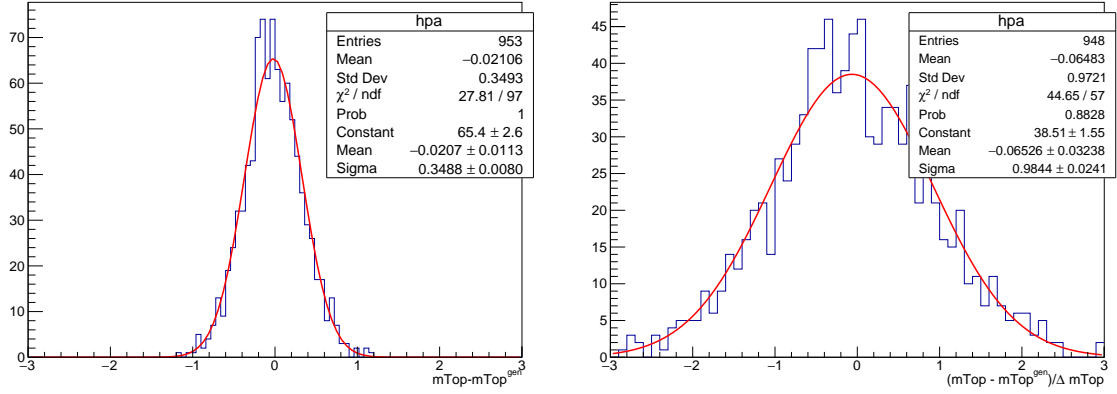


Figure 8.15.: Validation of the overall mass extraction method: (left) the difference between generated and estimated m_t , (right) the pull distribution on m_t .

ence and pull between pseudo-data and fit result are displayed in fig. 8.15. The pull with a mean of zero and width of one shows that the treatment of the uncertainty due to simulation statistics works well.

8.3.2. Double counting between FSR and JEC

In the context of the nuisance parameter method the chosen uncertainty sources are evaluated further. To estimate the uncertainty due to the choice of the renormalization scale, the FSR modelling is varied. This changes the out-of-cone hard emission and inside cone emission probability of the jets and therefore the momentum spectrum of the particles in jets. The observable effect would be a change in the number of additional jets and in the jet energy response. As the variation is done independently for the different branching types this may affect the response jet flavor dependently similar to the flavor dependent part of the jet energy correction uncertainties and might lead to double counting of uncertainties. In table 8.4 the response difference from the different uncertainty sources is presented. They were extracted via the width of Gaussians that were fitted to the response distributions from all jets with particle level $30 < p_T < 200 \text{ GeV}$ and $|\eta| < 2.4$ and the corresponding flavor. The biggest response difference can be seen by varying the gluon flavor dependent JEC uncertainty for all jets (+0.56) and the bottom flavor part for bottom flavored jets (-0.38). The branching type specific FSR scale variations change the response for bottom jets by 16%–26% of the assumed flavor-dependent JEC uncertainty, for light jets by 35%–65%.

Another approach to estimate the effect of this dependence is to fit the nuisance value of the flavor dependent JEC uncertainties to the response distribution from other variations. The results are shown in table 8.5. With the $X \rightarrow Xg$ FSR PS scale variation the bottom flavor JEC nuisance is evaluated via the jet response to be ${}_{+0.25}^{-0.14}$ and the light quark nuisance when varying the $q \rightarrow qg$ FSR PS scale nuisance to be ${}_{+0.73}^{-0.42}$. This is up to 30% of the effect from real bottom flavor and 71% of the effect from the light quark flavor JEC variation

Table 8.4.: Response difference for different flavored jets caused by a $\pm 1\sigma$ variation of different uncertainties.

uncertainty source	$\Delta R(\text{all})$ [%]	$\Delta R(\text{b-jets})$ [%]	$\Delta R(\text{uds-jets})$ [%]
JEC flavor bottom	0	-0.38	0
JEC flavor light quarks	-0.10	0	-0.20
JEC flavor gluon	+0.56	0	+0.02
JEC abs. scale	+0.15	+0.15	+0.15
FSR PS scale $g \rightarrow gg$	+0.08/+0.04	+0.04/+0.02	+0.06/+0.03
FSR PS scale $g \rightarrow qq$	-0.04/-0.03	0/0	-0.01/0
FSR PS scale $q \rightarrow qg$	+0.09/+0.05	0/0	+0.13/+0.07
FSR PS scale $X \rightarrow Xg$	+0.01/0	+0.10/+0.06	0/0

Table 8.5.: Estimation of the nuisance values for $\pm 1\sigma$ variation of different uncertainties using the response distributions.

uncertainty source	value of nuisance for					
	JEC abs. scale		JEC flavor bottom		JEC flavor light quarks	
	up	down	up	down	up	down
JEC flavor bottom	-	-	1.13	-0.86	-	-
JEC flavor light quarks	-0.71	0.85	-	-	0.98	-1.03
FSR PS scale $X \rightarrow Xg$	0.05	-0.08	-0.14	0.25	-0.02	0.04
FSR PS scale $q \rightarrow qg$	0.40	-0.67	-0.01	0.02	-0.42	0.73

respectively. When the FSR and JEC variation are assumed to be uncorrelated in the top quark mass measurement this puts the upper bound of overestimating from double counting a part of the flavor dependent jet response uncertainty to 23%. This would not change the final result. But this interplay could also be part of the dependencies that reduce the impact of the corresponding uncertainty sources.

8.3.3. Single nuisance closure

A closure test that uses all nuisance parameters independently is performed. For each uncertainty source the likelihood is minimized on pseudo-experiments derived from the sample where this uncertainty is varied up or down corresponding to a nuisance value of ± 1 . These are the same samples that were used to derive the model. For this test only the corresponding nuisance parameter is left free and its value is extracted with the default model. Example results are presented in fig. 8.16. Each point in the graphs is the mean extracted nuisance value from >3000 pseudo-experiment sets (each corresponding to the statistics expected in data) and its error bar is the predicted mean error on the nuisance value. The red line is a fitted line through these points and the red band is the 1σ confidence interval of the fit as returned by the `Root TVirtualFitter` (therefore scaled by χ^2/N_{df}). The extracted and generated

values are the same on the dotted line, so if the method works fine it should lie within the confidence band.

The presented examples are for the 5D observable selection in the muon+jets channel. For the top quark mass and the JEC flavor bottom (FlavorPureBottom) variations this check shows excellent closure. The JEC flavor bottom uncertainty is of special interest as it will be the leading uncertainty source. The JEC relative p_T uncertainty in the HF detector region is an example of an uncertainty source on which the selected observable distributions do not depend, because events with one of the four leading jets or a lepton in this region were rejected in the selection. The generator values are still within the uncertainty of the extracted values, indicating that this case can be handled well with the parameterization too. The top quark p_T (topPt) and gluonmove CR model nuisances are examples where one-sided alternatives are used to estimate the effect of the uncertainty source with and without the use of a dedicated sample. Both cases close as well, giving us even more confidence in the parameterization.

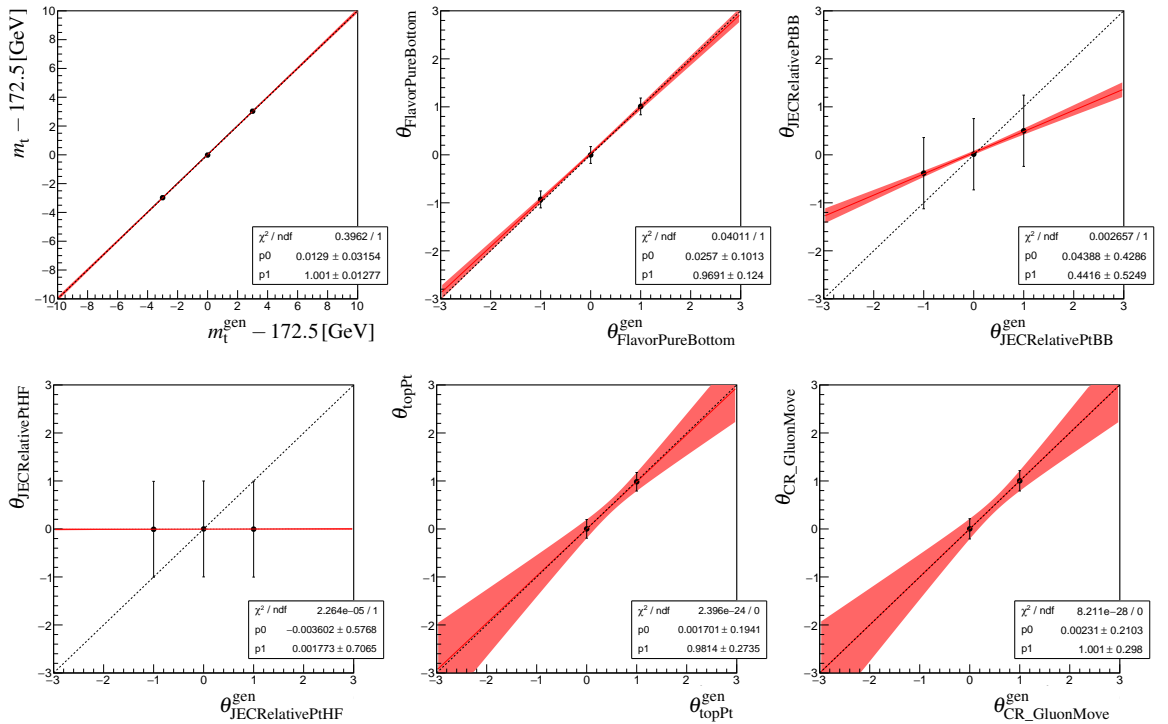


Figure 8.16.: Closure test in muon+jets simulation of the variation of one nuisance at the time while leaving only the corresponding nuisance free. All five observables are used. The presented example nuisances are from left to right in the upper row: m_t , JEC flavor bottom, JEC relative p_T BB and in the lower row: JEC relative p_T HF, top quark p_T , CR scheme: GluonMove.

8.3.4. Nuisance correlation

The correlation matrices between the nuisance parameters with the highest impacts in the 5D uncertainty prediction are presented in the figures 8.17 and 8.18. They indicate which nuisance could be effected by shifts in other nuisances in the likelihood fit and potentially help explaining nuisance values that can not be explained by their isolated physical behaviour. The correlations when fitting all observables on data are shown in fig. 8.17. The same fit was performed for simulation and no significant difference could be seen. Most correlations are expected. For example, the bJES fragmentation nuisance has a high (absolute) correlation factor to the bJES fragmentation model comparison of -55% and color reconnection model related nuisances, that are correlated by -40%. Other correlation factors can not be explained so straight forward, like the correlation factor of -27% between the relative sample JEC and the PS scale variation for $q \rightarrow qg$ FSR. The interpretation of the final measured nuisance values is also made more complex by parameters that are correlated to multiple other parameters by about 30%. An example is the top quark p_T nuisance that is correlated to the alternative ERD setting and bJES model as well as to the ME renomalization and factorization scale. Fig. 8.18 shows the correlation for the different observables separately. This helps to identify which distribution mediates the different correlation. For example the correlation factor between the top quark p_T variation and bJES fragmentation model comparison of 37% is mainly visible in $m_{\ell b}^{\text{reco}} |_{P_{\text{gof}} < 0.2}$ and the connection between the top quark p_T variation and ERD setting of 26% in R_{bq}^{reco} . All correlations look reasonable. Four nuisance parameter stand out as they are correlated to the m_t parameter at more than 20% in the 5D case. These are corresponding to the uncertainties due to the bottom flavor JEC, the FSR PS scale for the $q \rightarrow qg$ and $X \rightarrow Xg$ and the W+jets background. The correlation of the bottom flavor JEC and $X \rightarrow Xg$ FSR PS scale is mediated by m_t^{fit} and $m_{\ell b}^{\text{reco}} |_{P_{\text{gof}} < 0.2}$ distributions. This can be explained as they all depend highly on the energy in jets from bottom quarks that in turn depend highly on the actual mass of the decaying top quark. The correlation of the W+jets background variation of -22% cannot be tracked to a specific observable and as the variation effect of this uncertainty source is dominated by its sample statistics no clear physics interpretation can be made. The correlation between m_t and the $q \rightarrow qg$ FSR PS scale is 40% bigger and switches its sign when combining all observables compared to the single observable case. This showcases that not all dependencies in the combination of the 10 distributions in a parameterization with over 75 nuisance parameter are directly evident. The $q \rightarrow qg$ FSR PS scale nuisance will stay important and will be investigated more after partial unblinding in section 9.2.1.

nuisance correlation 5D

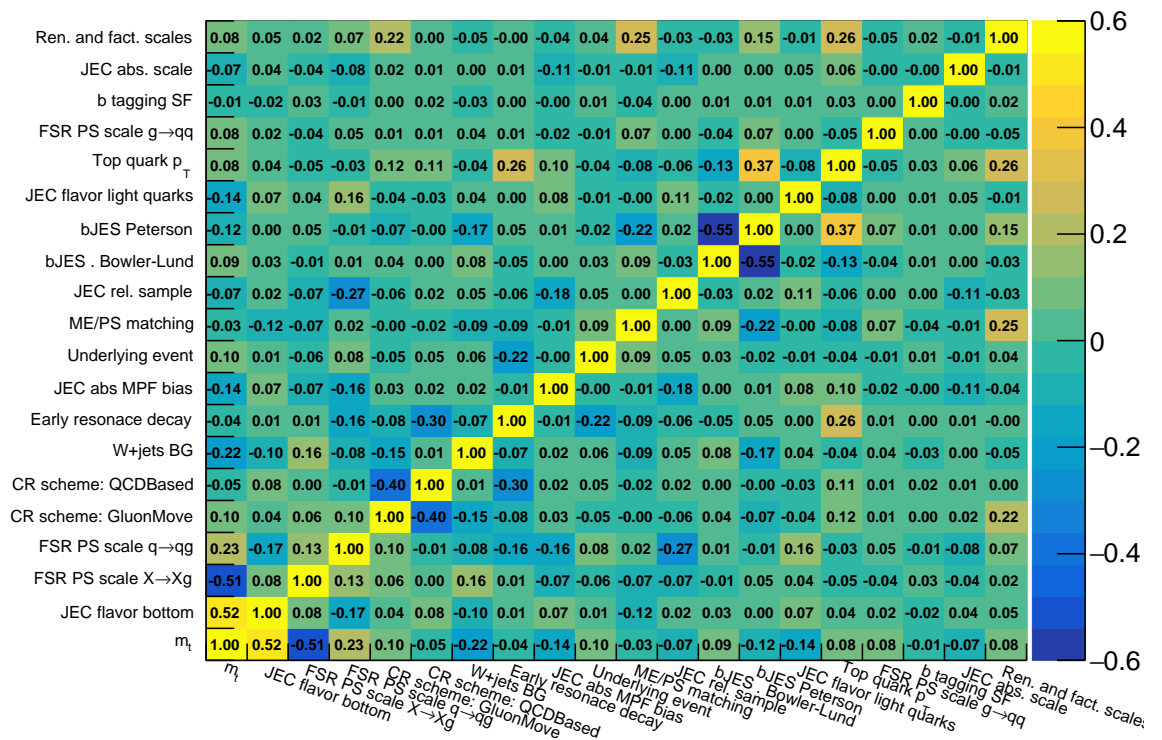


Figure 8.17.: Lepton+jets: Correlation matrix between the leading impacts nuisance parameters when fitting all observables on data.

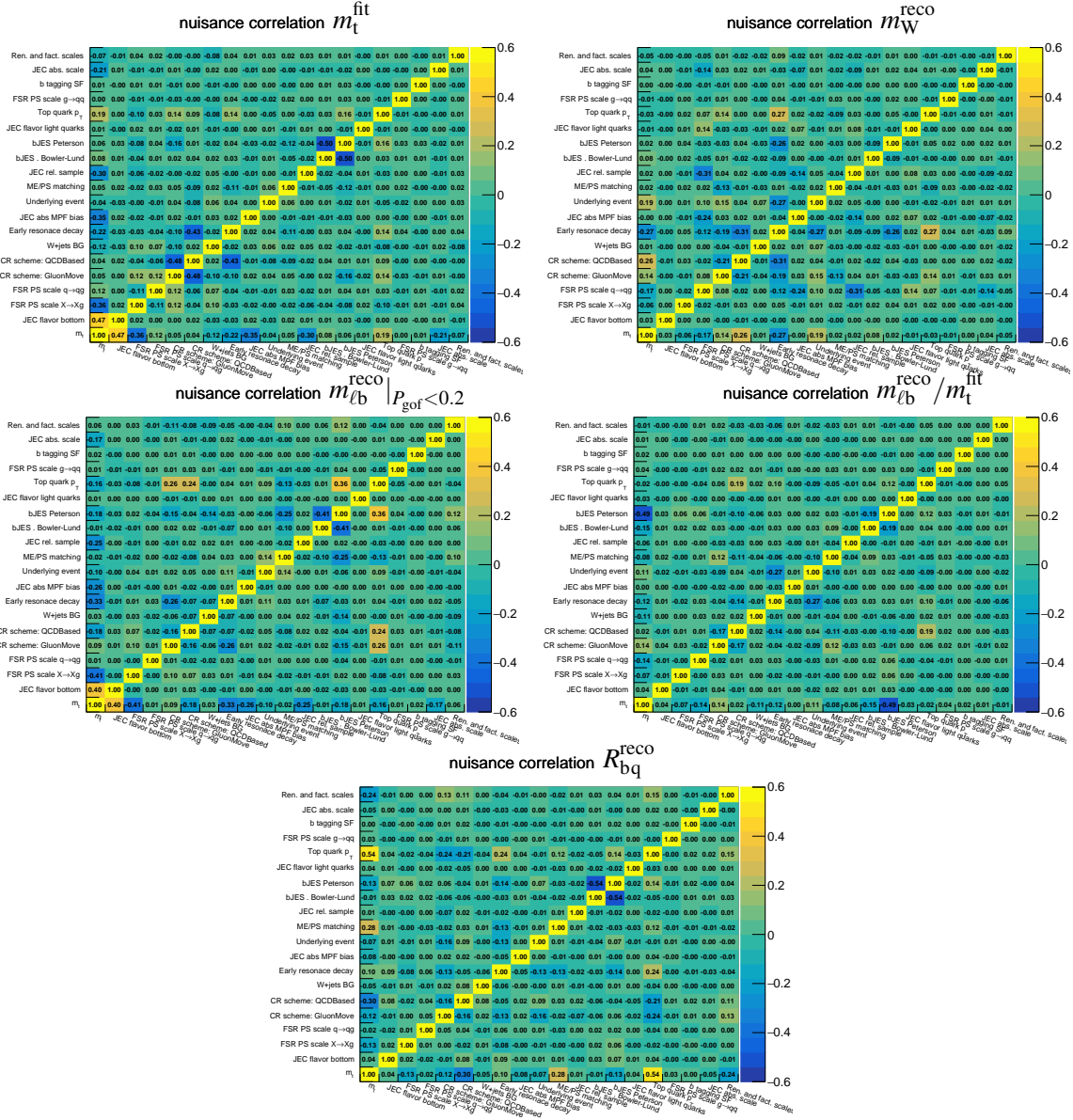


Figure 8.18.: Lepton+jets: Correlation matrix between the leading impacts nuisance parameters when fitting only one observable on data. The used observable is in the upper row left: m_t^{fit} , upper row right: m_W^{reco} , middle row left: $m_{lb}^{\text{reco}} |_{P_{\text{gof}} < 0.2}$, middle row right: $m_{lb}^{\text{reco}} / m_t^{\text{fit}}$ and lower row: R_{bq}^{reco} .

9. Results of the measurement

In order not to bias the result in an unconcious manner the data was blinded (not used) in all steps described so far, except for control distributions in section 6 and section 8. The unblinding of the measurement is performed step-wise. First the full uncertainty and the impacts of the different uncertainty sources are predicted from simulation. In a second step, the negative log-likelihood is minimized for the data while the top quark mass value is kept unknown. In this state multiple additional checks are performed to verify the method further. Only after that the full measurement is performed.

9.1. Nuisance impact predictions

The full uncertainty and the impact of the different uncertainty sources are predicted by performing the maximum likelihood fit on thousands of pseudo-data sets. The pseudo-data sets are generated as described in section 8.1. The distributions of the predicted total uncertainty from multiple pseudo-data sets for different observable settings are shown in figure 9.1. A clear improvement from including the additional observables and both leptons is visible, but the distributions overlap and have widths of about 0.01 GeV. This is in the order of the predicted difference in the uncertainty between some of the observable combinations. The predicted total uncertainty with three observables in the lepton+jets case is already smaller than the 5D electron+jets prediction and of a similar size that the 4D muon+jets prediction. The total predicted uncertainty when using both leptons and all observables is 0.37 GeV. In the context of the measured uncertainties it will be discussed in more detail to which degree the uncertainties get more precise with the inclusion of additional observables.

The impact (estimated effect of an uncertainty source on m_t) of a single uncertainty source is derived by fixing the corresponding nuisance to its $\pm 1\sigma$ values as derived by the likelihood fit ('post-fit') and then repeating the fit. The difference in the m_t result between this and the full fit is the impact of the corresponding uncertainty source. This method was described in more detail in section 8.3. The quoted impacts on m_t are the mean of the impacts from about 200 pseudo-data sets.

In figure 9.2 a comparison of the impacts (left) and errors after the fit (right) of a few example nuisance parameters are shown for different observable combinations and lepton channels. An error of unity on a nuisance parameter value corresponds to their constraint before the fit. The combination of all observables as well as the two lepton channels reduce

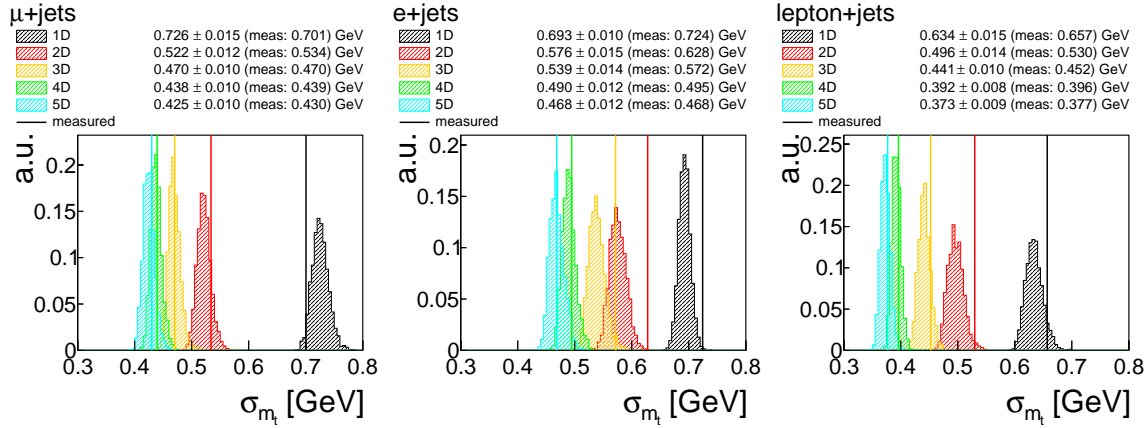


Figure 9.1.: The predicted (filled histograms) and measured (vertical lines) total uncertainty on m_t with different observable selections for μ +jets (left), e +jets (center) and lepton+jets (right). The legend includes the mean and standard deviation of the predictions.

the total predicted uncertainty down to 0.37 GeV for the 5D setting. Also most impacts get decreased by the inclusion of the additional observables.

But it can be seen that for a lower total uncertainty not all single nuisance impacts are lower. For the comparison of different lepton channels this is clear, but it is also true within one lepton channel or combination. For example the predicted impact due to the $X \rightarrow Xg$ FSR PS scale uncertainty is larger for the final 5D setting, that uses all observables and both leptons, than for the 4D case, that does not include the R_{bq}^{reco} observable. This could be caused by the reduction of the impact of other b-flavor jet p_T related nuisance parameters through the inclusion of the bottom-to-light-quark- p_T ratio at the cost of a higher impact from this source. This illustrates the non-trivial correlation between all the free parameters in the fit. Another example of an impact that does not just get smaller by the inclusion of more observables is the effect from the color reconnection scheme. But as this impact is just driven by simulation statistics no physical reason can be attributed to this effect. For a lower total uncertainty the error of the nuisance parameter get smaller. This corresponds to the uncertainty of the corresponding systematic effect getting smaller compared to prior of the fit. Nevertheless, a smaller nuisance error does not necessary yield smaller impacts. An example of this is again the $X \rightarrow Xg$ FSR PS scale variation as can be seen when comparing the 4D and 5D lepton+jets settings. A prominent nuisance with a highly reduced impact and small error, compared to its prior, is the jet energy resolution uncertainty. In former analyses a major reason to include the m_W^{reco} observable was to reduce this uncertainty. This analysis predicts that the error on the leading JER nuisance parameter already gets reduced below 60% without the inclusion of any additional observable and gets further decreased to 31% for the final setting. This strong constraint will be further checked in section 9.2.1 after the partial unblinding. Another nuisance parameter with a strong constraint is the color reconnection scheme. This effect has no further consequence on the uncertainty in m_t as the simulation statistics part of

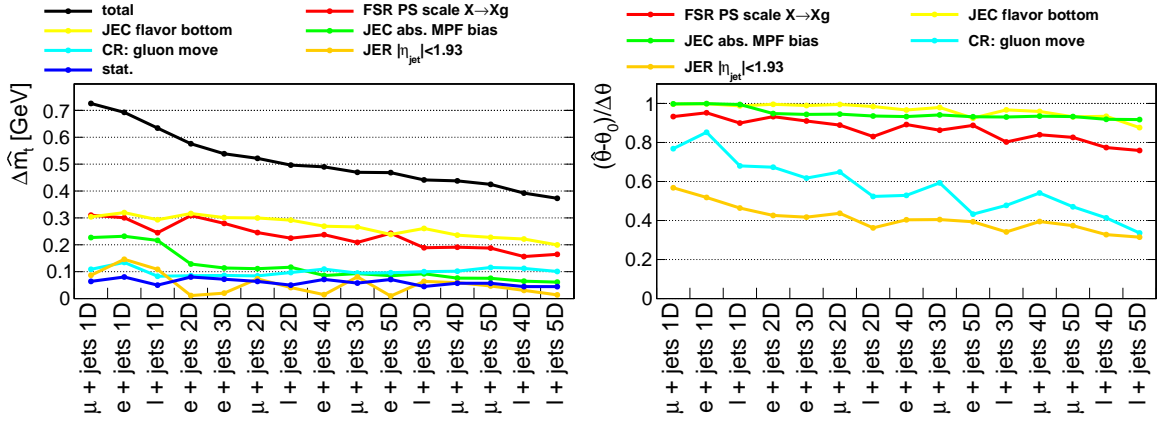


Figure 9.2.: Comparison of the predicted nuisance impacts (left) and nuisance errors (right) for example uncertainty sources in the different observable settings (1D to 5D, see definitions in section 8.2) for the μ +jets, e+jets and combined lepton+jets case.

the impact can not be reduced in this manner.

The predicted mean and width of the nuisance values and the pre- and post-fit impacts are extracted from pseudo-experiments. The pre-fit impacts assume no further constraint on the corresponding nuisance parameter by the fit while it is included in the post-fit impacts. For the 25 leading uncertainty sources in the final setting with five observables this is shown in figure 9.3 for the combined $t\bar{t} \rightarrow$ lepton+jets channel, in figure 9.4 for the $t\bar{t} \rightarrow \mu$ +jets case and in figure 9.5 for $t\bar{t} \rightarrow e$ +jets. All nuisance impacts for this and reduced sets of observables are included in the appendix C.2. It was checked that all pull distributions are Gaussian. For the prediction from simulation the pull mean is zero by design, within the variance from the finite number of performed fits on pseudo-data sets. On data this will correspond to the measured value of the nuisance parameter and can be understood, within its uncertainty, as the value of a variation observed in the phase-space of this analysis. For example the values of the JEC nuisance parameters indicate how much additional residual jet energy corrections are needed in addition to the default simulation in order to best describe what can be seen in the selected events.

The pre-fit impacts are an estimate of the effect of the corresponding uncertainty source without the inclusion of the nuisances as parameters in the likelihood fit. So the difference to the post-fit impact is the predicted improvement by the nuisance parameter method. The total predicted uncertainty in the 5D lepton+jets channel of ± 0.37 GeV includes ± 0.04 GeV predicted data statistical uncertainty and ± 0.03 GeV of calibration uncertainty. The calibration uncertainty is the residual uncertainty on m_t due to the choice of parameterization and simulation statistics, further described in chapter 7. The total predicted uncertainty for the muon+jets channel is ± 0.42 GeV including ± 0.06 GeV predicted data statistical uncertainty. For the electron+jets channel slightly larger values of ± 0.47 GeV including ± 0.07 GeV predicted data statistical uncertainty are obtained.

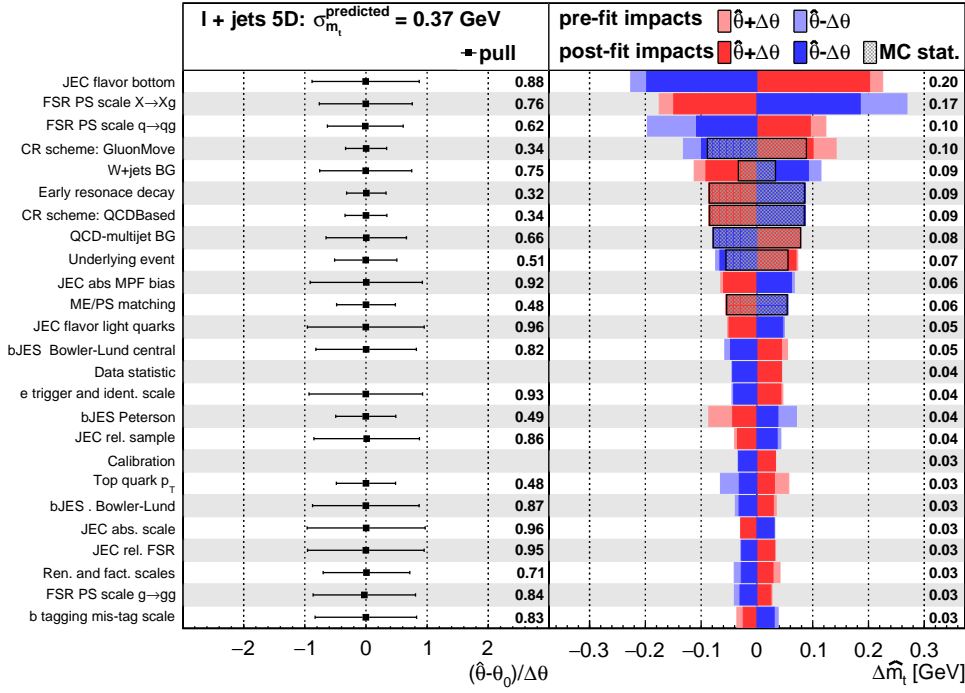


Figure 9.3.: Lepton+jets simulation: Biggest predicted uncertainty nuisance impacts and pulls when using all five observables m_t^{fit} , m_W^{reco} , $m_{\ell b}^{\text{reco}}/m_t^{\text{fit}}$, $m_{\ell b}^{\text{reco}}|_{P_{\text{gof}} < 0.2}$ and $R_{\text{bq}}^{\text{reco}}$ as observable. The left plot shows the postfit pulls on the most important nuisances and the numbers quote the postfit uncertainty on the nuisance parameter. The right plot shows their pre-fit and postfit impacts. The postfit impacts include the contribution from the nuisances accounting for the limited size of simulation samples (MC stat.). The average of these postfit impacts is printed on the right. The rows are sorted by the size of the postfit impact.

The biggest single nuisance impact is predicted to be the bottom flavor JEC uncertainty with an impact of ± 0.20 GeV. At about 54% of the total predicted uncertainty it is expected to dominate the measurements uncertainty. The next-to-leading impact is predicted to be the $X \rightarrow Xg$ FSR PS scale uncertainty at 0.17 GeV, that is 46% of the total predicted uncertainty. The next biggest five impacts (0.09 to 0.10 GeV) are the $q \rightarrow qg$ FSR PS scale variation, the W+jets background and the ERD and color reconnection alternative simulation settings. The last four are all limited by the number of events in their simulated samples.

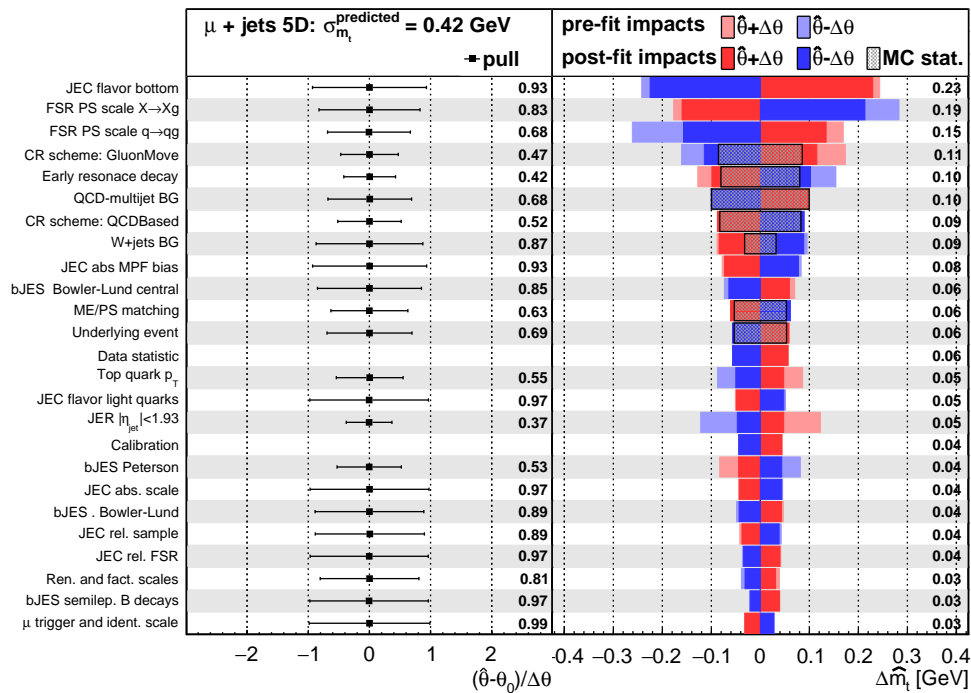


Figure 9.4.: Muon+jets simulation: Biggest predicted uncertainty nuisance impacts and pulls when using all five observables m_t^{fit} , m_W^{reco} , $m_{\ell b}^{\text{reco}}/m_t^{\text{fit}}$, $m_{\ell b}^{\text{reco}}|_{P_{\text{gof}}<0.2}$ and $R_{\text{bq}}^{\text{reco}}$ as observable. The left plot shows the postfit pulls on the most important nuisances and the numbers quote the postfit uncertainty on the nuisance parameter. The right plot shows their pre-fit and postfit impacts. The postfit impacts include the contribution from the nuisances accounting for the limited size of simulation samples (MC stat.). The average of these postfit impacts is printed on the right. The rows are sorted by the size of the postfit impact.

9.2. Partial unblinding

The likelihood is maximized on the selected data events, while the value of the measured top quark mass is kept blind. The measured values of the nuisance parameters will be checked and the measured uncertainties and nuisance impacts and pulls compared to their predictions from simulation.

The post-fit templates and their comparison with the data histograms are shown in fig. 9.6. Overall they agree quite well for all observables and for all bins. For the m_t^{fit} distribution there are limits in the description of the data with the chosen template parameterization visible. The post-fit curve and data points differ within a few percent in the left flank of the Voigt-peak and in the tail that is mainly parameterized by the Chebyshev polynomials. The difference between the data and the fit curve in the tail are presumably due to statistical

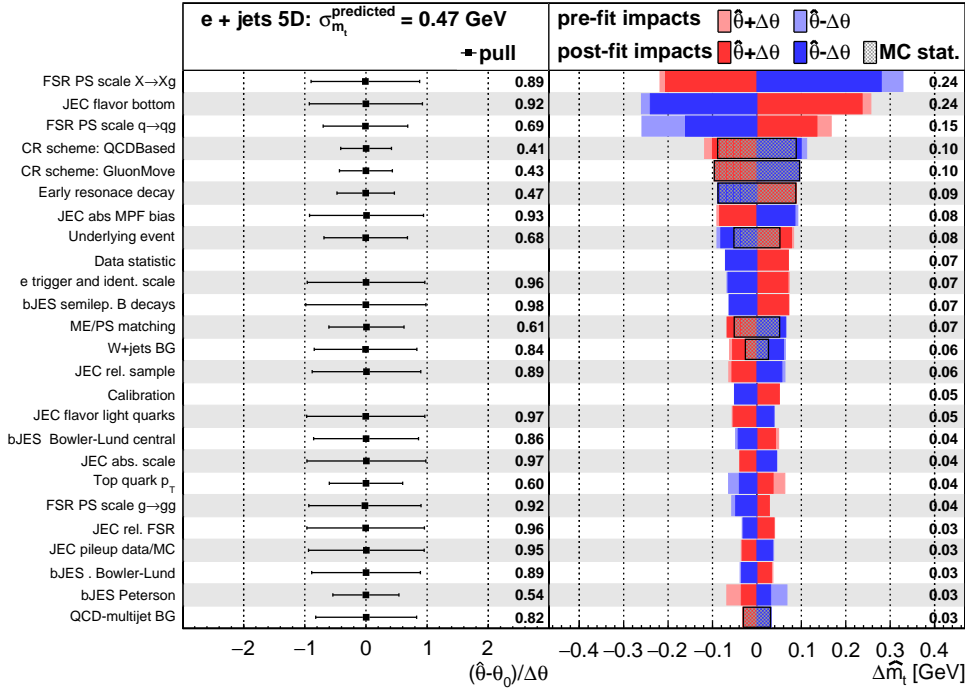


Figure 9.5.: Electron+jets simulation: Biggest predicted uncertainty nuisance impacts and pulls when using all five observables m_t^{fit} , m_W^{reco} , $m_{\ell b}^{\text{reco}}/m_t^{\text{fit}}$, $m_{\ell b}^{\text{reco}}|_{P_{\text{gof}} < 0.2}$ and $R_{\text{bq}}^{\text{reco}}$ as observable. The left plot shows the postfit pulls on the most important nuisances and the numbers quote the postfit uncertainty on the nuisance parameter. The right plot shows their pre-fit and postfit impacts. The postfit impacts include the contribution from the nuisances accounting for the limited size of simulation samples (MC stat.). The average of these postfit impacts is printed on the right. The rows are sorted by the size of the postfit impact.

uncertainties, but both lepton channels have a similar region around $m_t^{\text{fit}} = 250\text{GeV}$ with a positive, and around $m_t^{\text{fit}} = 300\text{GeV}$ with a negative data-histogram-to-fit-curve ratio. When the template was fit to simulation a similar effect was visible around $m_t^{\text{fit}} = 250\text{GeV}$, but with a smaller ratio value, as can be seen in figure 8.9 and 8.10. The difference at the left flank of the peak can not be seen for simulation. It is not a problem for this analysis but could be a point to consider for future analyses looking to improve this method of top quark mass measurement even more.

For the binned template distributions the fit matches the data points very well with only one data point outside the $\pm 1\sigma$ range of the curve at a data to fit-curve ratio of about 1%.

The total predicted and total measured uncertainties on m_t , σ_{m_t} , when using only either m_W^{reco} , $m_{\ell b}^{\text{reco}}|_{P_{\text{gof}} < 0.2}$, $m_{\ell b}^{\text{reco}}/m_t^{\text{fit}}$ or $R_{\text{bq}}^{\text{reco}}$ as observable, are shown in fig. 9.7. The same when only

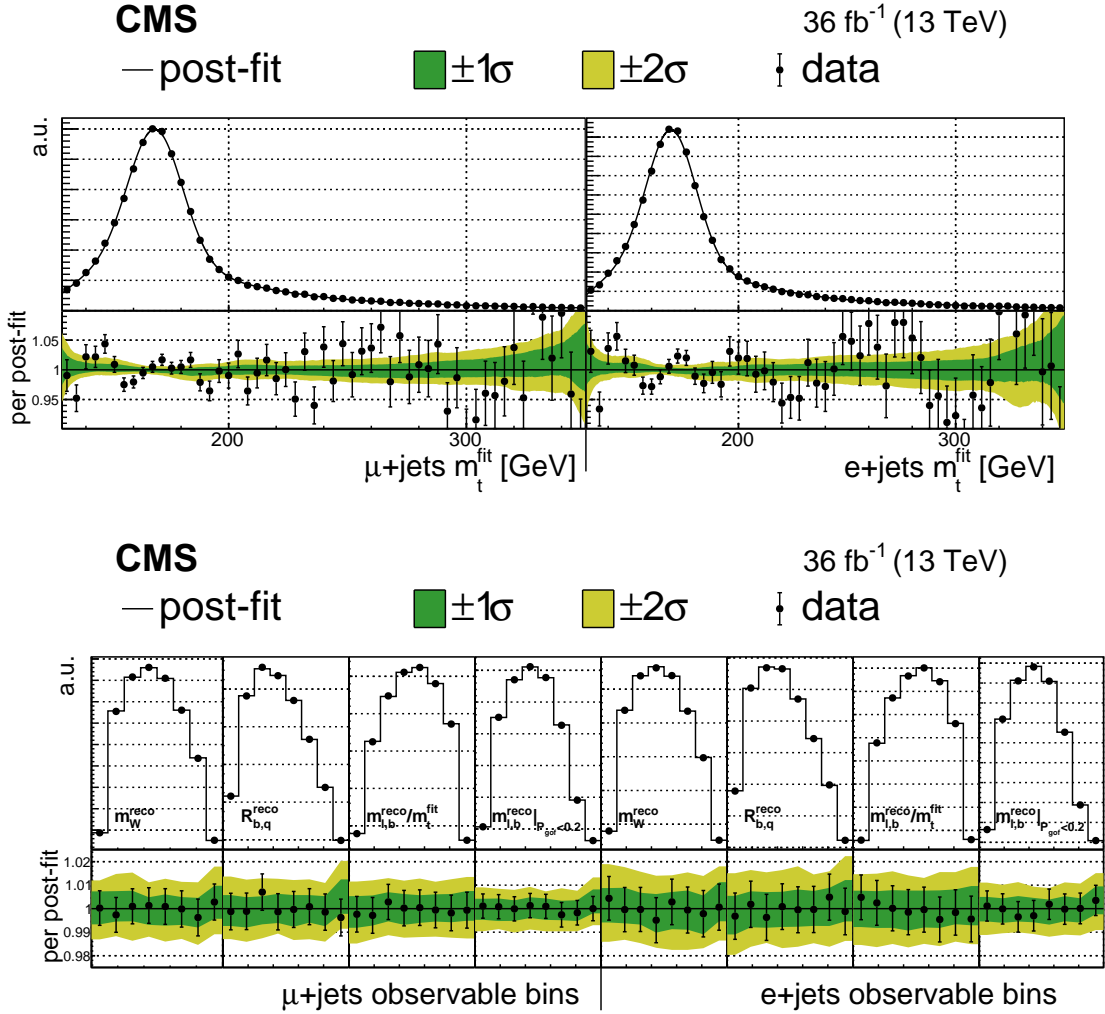


Figure 9.6.: Post-fit templates and distributions with error band of the observables compared to data. The bin edges of the binned templates (bottom plot) are listed in table 8.2

m_t^{fit} is used as observable is labeled as '1D' in fig. 9.1. They agree reasonably with one another. The differences are not driven by a single uncertainty source but the combination of small differences in multiple nuisances. The measured σ_{m_t} ranges from above ± 5 GeV, when using only m_W^{reco} , down to ± 0.67 GeV, when $m_{l,b}^{\text{reco}}|_{p_{\text{got}} < 0.2}$ from both lepton channels is used. The latter uncertainty is already in the order of the uncertainty on the former m_t measurement on the CMS data from the same data taking period in the lepton+jets channel [8], while using a phase-space excluded in that analysis. For the muon+jets and lepton+jets channels the uncertainty when only m_W^{reco} is used is higher and outside the predicted range. As the uncertainty is bigger than the simulated m_t variation from which the templates are derived, it is outside of the calibration range and not well defined. This further illustrates the

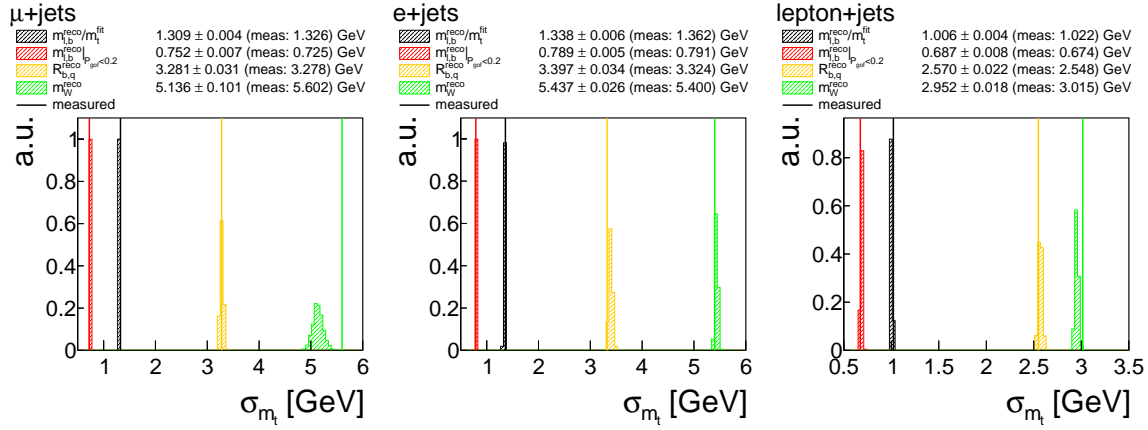


Figure 9.7.: The predicted (filled histogram) and measured (vertical lines) total uncertainty on m_t from single observables for μ +jets (left), e +jets (center) and lepton+jets (right). The legend includes the mean and standard deviation of the predictions.

statements on the m_t dependency of the different additional observables that were made in section 8.

The predicted and measured nuisance values, nuisance pull widths and impacts from the ML fit are compared, first with each of the additional observables only. The full results can be seen in the appendix figures C.1–C.12. Most nuisance values are measured close to zero with their predicted uncertainties. Notable deviations of that will be discussed in the following.

When using only m_W^{reco} as observable the nuisance parameters corresponding to the $q \rightarrow qg$ FSR PS scale variation is measured at -1σ . This will be discussed as part of the checks after the partial unblinding in section 9.2.1.

For the measurement with only R_{bq}^{reco} as observable the nuisance values from dedicated samples vary up to 0.5σ . This is expected as their nuisance parameterization is limited by the size of the simulation samples. Another notable nuisance value corresponds to the top quark p_T variation that is measured at $+1\sigma$. This indicates that the top quark p_T scale function, that is used here as alternative, is actually needed for simulation to match data.

With only $m_{\ell b}^{\text{reco}}/m_t^{\text{fit}}$ as observable some nuisance values are measured at about $(\pm)0.5\sigma$. They are corresponding to the comparison to the *gluon-move* color reconnection scheme and the QCD-multijet background that are both limited by simulation statistics. In the case with $m_{\ell b}^{\text{reco}}|_{P_{\text{gof}} < 0.2}$ as only observable, no nuisance value is measured outside of $\pm 0.5\sigma$.

The total predicted uncertainties on m_t , from about 1000 pseudo-experiments each, are compared to the uncertainty on the measurement for different observable selections in fig. 9.1. The measured uncertainties are within the predicted range. For the 5D e +jets and lepton+jets settings the measured uncertainty is 0.01 GeV bigger as the mean prediction. This is within one standard deviation of it.

When using only the m_t^{fit} distributions as observable (1D), the uncertainty on the top quark mass in the $t\bar{t} \rightarrow \mu(e)+\text{jets}$ case is measured to be $\pm 0.70(0.72)$ GeV. This is about 0.02 GeV more precise than predicted in the muon case, but 0.02 GeV worse for electrons. When both lepton channels are combined the measured uncertainty with only the m_t^{fit} observable is with $\sigma_{m_t} = 0.66$ GeV already at a similar precision than the former analysis [8]. In the $\mu(e)+\text{jets}$ case the biggest improvement step to $\pm 0.53(0.63)$ GeV is the inclusion of the m_W^{reco} distribution to improve the jet energy corrections. The difference between the mean predicted and measured uncertainty in the electron+jets case is, at 0.05 GeV, even higher here. Therefore the inclusion of the electron decay channel in the 2D lepton+jets selection does not improve the measurement. With the inclusion of more additional observables this difference in the predicted and measured uncertainty gets smaller and is not relevant for the 4D and 5D settings. The observables $m_{\ell b}^{\text{reco}}/m_t^{\text{fit}}$ and $m_{\ell b}^{\text{reco}}|_{P_{\text{gof}} < 0.2}$ include information from the leptonically decaying top quark, which was only included indirectly via the kinematic fit, and events that were not included in the 2D approach. With the inclusion of $m_{\ell b}^{\text{reco}}|_{P_{\text{gof}} < 0.2}$ the measurement uncertainty is $\pm 0.47(0.57)$ GeV with $t\bar{t} \rightarrow \mu(e)+\text{jets}$ events and ± 0.45 GeV when combining both. In this settings the inclusion of electron+jets results in an improvement of 0.02 GeV of the precision compared to just the muon decay channel. So with the additional $m_{\ell b}^{\text{reco}}/m_t^{\text{fit}}$ distribution the uncertainty in the muon (electron) case is $\pm 0.44(0.50)$ GeV combining to ± 0.40 GeV. As last additional observable $R_{\text{bq}}^{\text{reco}}$ is included for the final 5D setting. This reduced the uncertainties even further to 0.43(0.47) GeV for $t\bar{t} \rightarrow \mu(e)+\text{jets}$ events that are combined to the final measured uncertainty of $\sigma_{m_t} = 0.377$ GeV. The final measured uncertainty is within its predicted range of 0.373 ± 0.008 GeV.

The predicted and measured values of the nuisance parameters, the pulls widths, the uncertainty of the m_t measurement, and the impacts of the different uncertainty sources when using all five observables are shown in figure 9.8 for muon+jets, figure 9.9 for electron+jets and figure 9.10 for lepton+jets, for sources of uncertainty that result in impacts bigger than 0.01 GeV. The pull widths and impacts agree, with small differences. The final measured uncertainty on m_t includes ± 0.04 GeV statistical uncertainty and ± 0.03 GeV from the calibration. The leading uncertainty sources match the prediction. The major differences is the impact due to the $X \rightarrow Xg$ FSR PS scale uncertainty that is 0.03 GeV smaller while the impact from the $q \rightarrow qg$ FSR PS scale is 0.4 GeV bigger. The full nuisance and impacts measurements for other observable selections are presented in appendix C.2.

When just the m_t^{fit} observable is used the measured values of all nuisance parameters are compatible with zero. Starting with the inclusion of the m_W^{reco} observable the $q \rightarrow qg$ FSR PS scale variation nuisance is measured below minus one and the value of the nuisance parameter corresponding to the JER for jets with $|\eta| < 1.93$ at about -0.5, with a pull width of 0.39. Both differ from zero at more than one standard deviation. With the inclusion if $m_{\ell b}^{\text{reco}}|_{P_{\text{gof}} < 0.2}$ the nuisance parameter of the matrix element renormalization and factorization scale gets measured close to minus one. In the 3D observable setting this uncertainty source has only a 0.02 GeV impact on the mass measurement, but it is, at ${}_{+11\%}^{-12\%}$, the leading uncertainty on the number of predicted events. A nuisance value of minus one roughly corresponds to the difference in predicted and measured number of events in the selection

of this analysis. Here it is measured from normalized probability density functions of the observables, so without a direct inclusion of the number of events. The ratio of measured to predicted events is 91% without and 87% with the $P_{\text{gof}} > 0.2$ selection as can be seen in the tables 6.6 and 6.7 in chapter 6. The fact that the simulation with the measured values of the nuisances parameters better matches the selected number of events further increases the confidence in the method and measurement.

No additional similar feature can be seen with the inclusion of $m_{\text{fb}}^{\text{reco}}/m_t^{\text{fit}}$. As fifth observable $R_{\text{bq}}^{\text{reco}}$ is added. With this observable setting the impact from the top quark p_T variation increases by 0.02 GeV and the value of its nuisance parameter gets measured at 0.5 in the muon+jets case and at zero in the electron+jets case. This is the nuisance value with the most pronounced lepton flavor dependency. Other non-zero values of nuisances in the final setting, which were already discussed for a few observables, are the following: The nuisance value corresponding to the $q \rightarrow qg$ FSR PS scale variation is measured at -1.5 and with a pull width of 0.46 of its pre-fit variation, is stronger constrained than predicted. The nuisance parameters corresponding to the JER for jets with $|\eta| < 1.93$ is measured to be 0.75 of its down variation. The nuisance value corresponding to the correlated renormalization and factorization scales of the matrix element is measured at -1.6 of its pre-fit uncertainty. The impacts will be combined in groups for simpler comparison and combinations with other analyses in section 9.4.

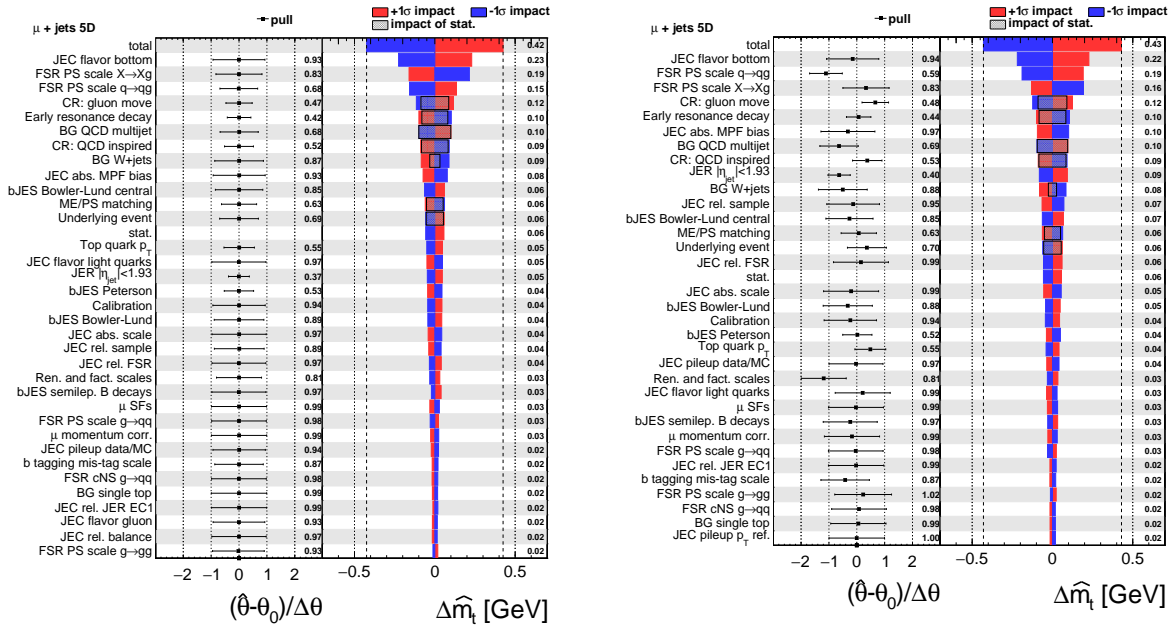


Figure 9.8.: Muon+jets: The pull mean and width and impacts predicted from pseudo-data (left) and measured (right) when using all observables (5D).

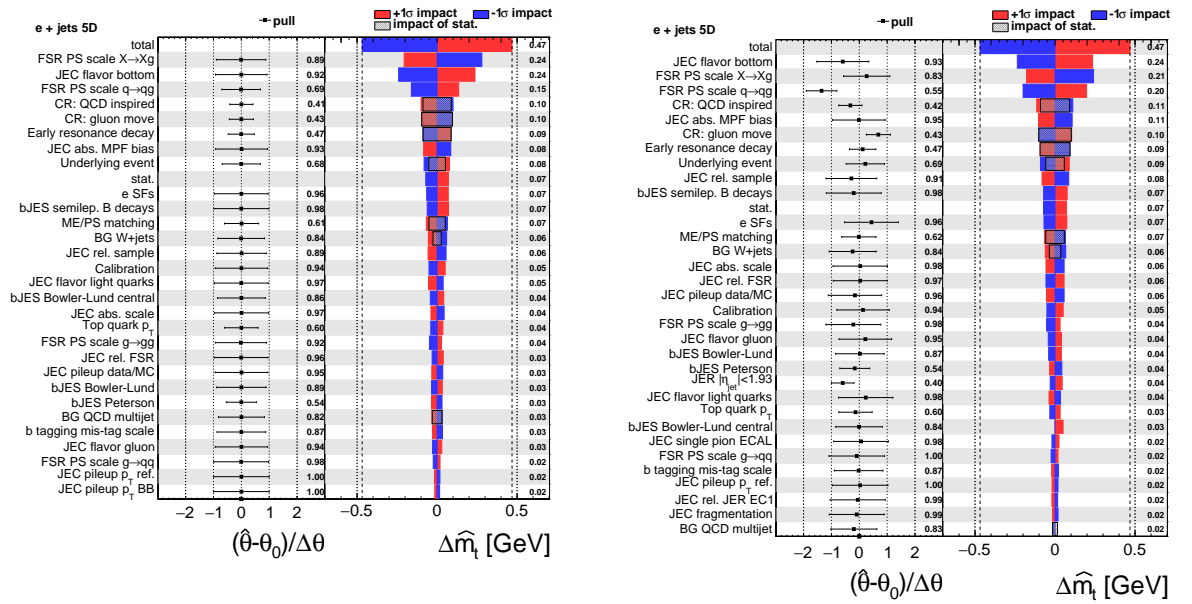


Figure 9.9.: Electron+jets: The pull mean and width and impacts predicted from pseudo-data (left) and measured (right) when using all observables (5D).

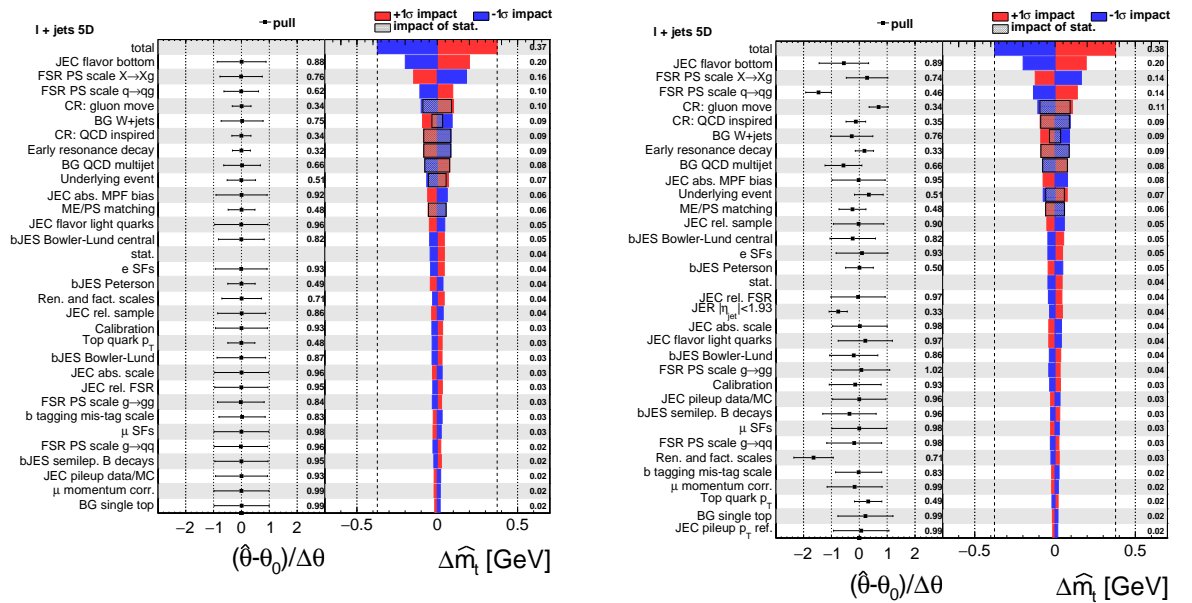


Figure 9.10.: Lepton+jets: The pull mean and width and impacts predicted from pseudo-data (left) and measured (right) when using all observables (5D).

9.2.1. Cross-checks after partial unblinding

Some of the nuisance parameters were considerably constrained beyond their pre-fit uncertainty by the fit on data and some are measured beyond ± 1 of their pre-fit standard deviation. This may change the value and uncertainty of the final m_t measurement. A few cross-checks were performed to further validate the modeling in use. The following checks were performed on an older state of the analysis so its numbers do not line up with the final results. The changes done afterwards do not change the validity of the checks and some, like the decisions to use statistical nuisance components for the QCD-multijet and W+jets background variations and a quadratic parameterization in the FSR PS scale nuisances, are result of their outcome.

Minimum Likelihood values As a check that the model with linear m_t and nuisance parameterization matched physics reasonably well, the likelihood values of the NLL fit for pseudo-data and blinded data are listed in table 9.1. The quoted error are the root-mean-square variations from 2000 pseudo-data sets. The likelihoods increase slightly with the inclusion of additional observables and are about 20% bigger when using both leptons compared to the single lepton channels. When the fit is performed on measured data the likelihood value is about 9% smaller for all observable settings. This suggests that the measured data set is described better by the parameterization than the pseudo-data sets. One reason for this could be the limited event count after the selection in the QCD-multijet and W+jets background. For this sample some histogram bins are dominated by a few events with high weights increasing the χ^2 and likelihood values.

Table 9.1.: Minimum likelihood values. Mean and variation from prediction on pseudo-data sets and measured in data.

Obs.	μ +jets		e+jets		lept.+jets	
	sim.	data	sim.	data	sim.	data
1D	137 \pm 10	122	135 \pm 9	127	172 \pm 13	151
2D	137 \pm 10	125	135 \pm 9	129	174 \pm 13	155
3D	138 \pm 10	127	136 \pm 9	131	175 \pm 13	158
4D	138 \pm 10	128	137 \pm 9	133	177 \pm 15	160
5D	140 \pm 10	130	138 \pm 9	135	179 \pm 13	165

Background sample statistic After the event selection the QCD-multijet and W+jets background simulation samples contain only a small number of unique events. Therefore the corresponding uncertainties have a large pre-fit uncertainty that gets strongly constrained by the ML fit on data. To ensure that the uncertainties do not get over-constrained additional statistical uncertainty parameters, like the ones used for variation from dedicated samples,

are added for the QCD-multijets and W+jets background uncertainties. This results in an increase of the total uncertainty by 0.02 GeV to 0.37 GeV and shifts the observed mass value up by 0.05 GeV as nuisance parameters get less constrained and move slightly towards their prior.

Jet energy resolution The pull width of the nuisance corresponding to the uncertainty on the jet energy resolution for jets with $|\eta| < 1.93$ gets strongly constrained by including the m_W^{reco} observable. While m_W^{reco} is very sensitive to the resolution of light flavor jets, m_t^{fit} and the other observables depend also mainly on the resolution of bottom jets. Most sources of the resolution degradation should affect the light flavor and bottom flavor jets identically but the assumption that different observables are fully correlated in the JER nuisance parameters might be too strong. To estimate this effect an alternative model is constructed where the JER nuisances are separated for m_W^{reco} from all the other observables. This results in a 0.06 GeV higher extracted m_t with an uncertainty of ± 0.40 GeV where both separated JER nuisance parameters are measured at similar values, implying a strong correlation. The check was performed with dedicated nuisance parameters and a combined model but the effect is also visible when the measurement with only m_W^{reco} as observable (appendix fig. C.3) is compared to only using m_t^{fit} (appendix fig. C.13) or $m_{\ell b}^{\text{reco}}|_{p_{\text{gof}} < 0.2}$ (appendix fig. C.12). The impacts of the separated nuisance parameters on m_t are anti-correlated. This explains the low impact of JER on the final measurement when full correlation is assumed.

Scale in $q \rightarrow qg$ splittings in the final state parton shower As the nuisance parameter corresponding to the μ_R scale in the $q \rightarrow qg$ splittings of FSR (fsr_Q2QG_muR) stands out by getting highly constrained and its value is measured below minus one value of its standard deviation it is checked in more detail. The numbers and plots in this section were derived using a linear α_k parameterization for the FSR nuisance parameters if not stated otherwise. The default parameterization was changed as result of the following evaluation. In figure 9.11 the effect of the default nuisance parameter setting is compared to not using the fsr_Q2QG_muR nuisance parameter. All points in that plot are measurements of m_t that are offset by the same random number for blinding. When comparing the default measurement (black) with the measurement with all nuisance parameters fixed to their prior values (red) the difference in m_t corresponds to the shift of m_t by including the sources of uncertainty as nuisance parameters in the likelihood. The sign and magnitude of this difference depends on the included observables and lepton channels. For the 5D lepton+jets setting the difference is 0.36 GeV. So m_t is measured $0.74\sigma_{m_t}^{\text{pre-fit}}$ lower when nuisance parameters are included in the likelihood. $\sigma_{m_t}^{\text{pre-fit}}$ is the measured uncertainty when the nuisance parameters are not constrained by the fit but set to their 'pre-fit' values. When the fsr_Q2QG_muR nuisance parameter is not used (fixed at zero), m_t gets measured 0.23 GeV higher for the 5D lepton+jets selection. This difference becomes relevant and has roughly the same order of magnitude for all settings that include the m_W^{reco} observable. When fixing the fsr_Q2QG_muR nuisance the biggest effect that is visible on the other nuisances is on the FlavorPureBottom parameter

that corresponds to the bottom flavor part of flavor dependent jet energy correction uncertainty. It gets shifted by -0.48σ , increasing its impact by 17%. This is not surprising as the effect on the m_W^{reco} from the `fsr_Q2QG_muR` variation is a peak shift that looks similar to some jet energy correction effects and the minimization has a bigger effect on uncertainty sources with bigger impacts. The m_W^{reco} PDF before and after the likelihood fit and for simulation with $\theta_{\text{fsr_Q2QG_muR}} = \pm 1$ is shown in figure 9.12. This further illustrates why its nuisance parameter gets shifted below one. Similar PDFs of all variations are included in appendix D.2.

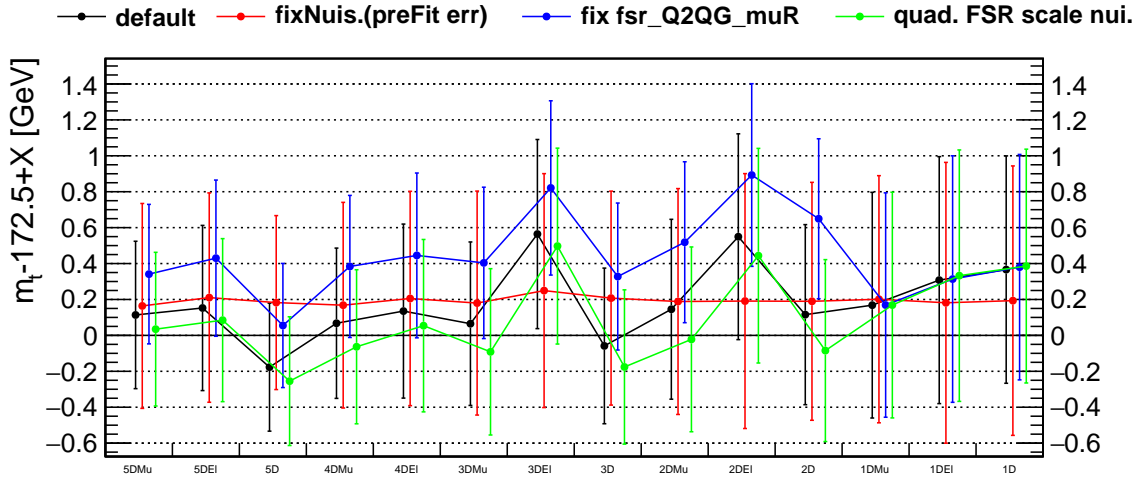


Figure 9.11.: Blinded measured top quark mass (all points have the same random offset) for different observable selections when using all nuisance parameter (black), using no additional nuisance parameter (red), when the `fsr_Q2QG_muR` nuisance parameter is fixed at zero (blue) and when using quadratic parameterized `fsr_*_muR` nuisances.

To investigate this even further and check how well FSR variations greater than $\pm 1\sigma$ from event based weights work, the centrally provided reduced ($\pm 0.5\sigma$) and conservative ($\pm 2\sigma$) variation of the combined FSR weights are used. The measured FSR nuisance parameters from these six variations is shown in the left plot of figure 9.13. With a perfect calibration all points should be on the dotted line with unity slope. This does work for $\theta_{\text{FSR}_{\text{gen}}} = \pm 0.5$ but further away from zero the extracted FSR nuisance values get measured too high, for $\theta_{\text{FSR}_{\text{gen}}} = 2$ more than 50%. For the right plot in figure 9.13 the FSR nuisance is parameterized quadratically instead of linearly, so a variable for an additional quadratic dependency is included for the θ_i corresponding to the FSR uncertainty variation in equation 8.2. With this, the calibration closes for $\theta_{\text{FSR}_{\text{gen}}} = \pm 1$ and is only slightly off for $\theta_{\text{FSR}_{\text{gen}}} = 2$. The calibration closure for linear (left plot) and quadratic (right plot) parameterization of $\theta_{\text{fsr_Q2QG_muR}}$ is shown in figure 9.14. For the linear parameterization a similar calibration as in the combined FSR case is visible. Note that the direction of the variation is inverted when comparing vari-

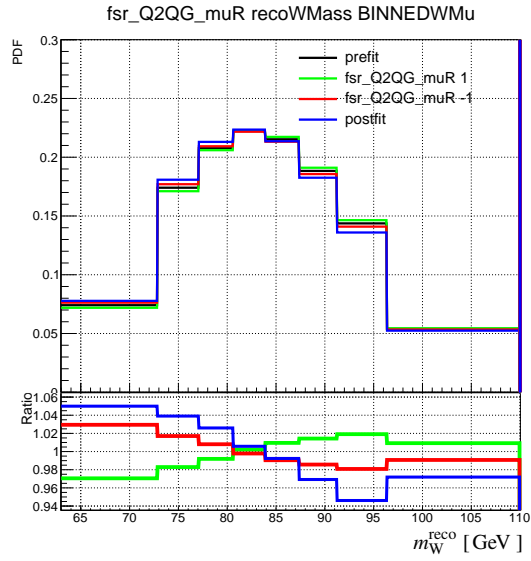


Figure 9.12.: m_W^{reco} PDF for muon+jets for the default simulation (black), $\theta_{\text{fsr_Q2QG_muR}} = \pm 1$ (green, red) and after the likelihood fit on data (blue).

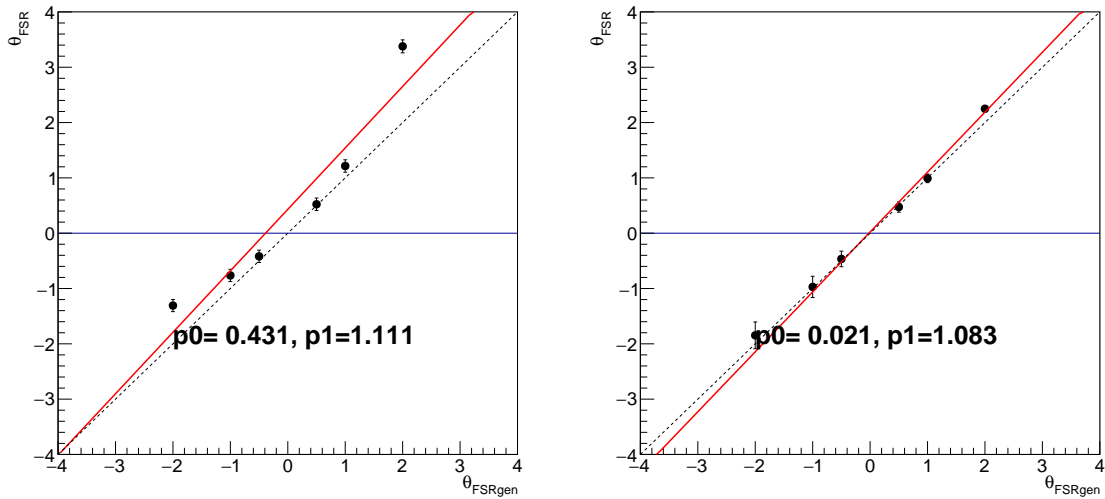


Figure 9.13.: The measured FSR on muon+jets simulation using all observables (5D) with FSR varied up and down by 0.5 , 1 and 2σ when using linear FSR nuisance parameterization (left) and quadratic parameterization (right). The red line is the fitted slope, the dotted line is the target unity slope.

ations from the combined variation to the FSR weights split into branching types. With the quadratic parameterization the calibration closes well.

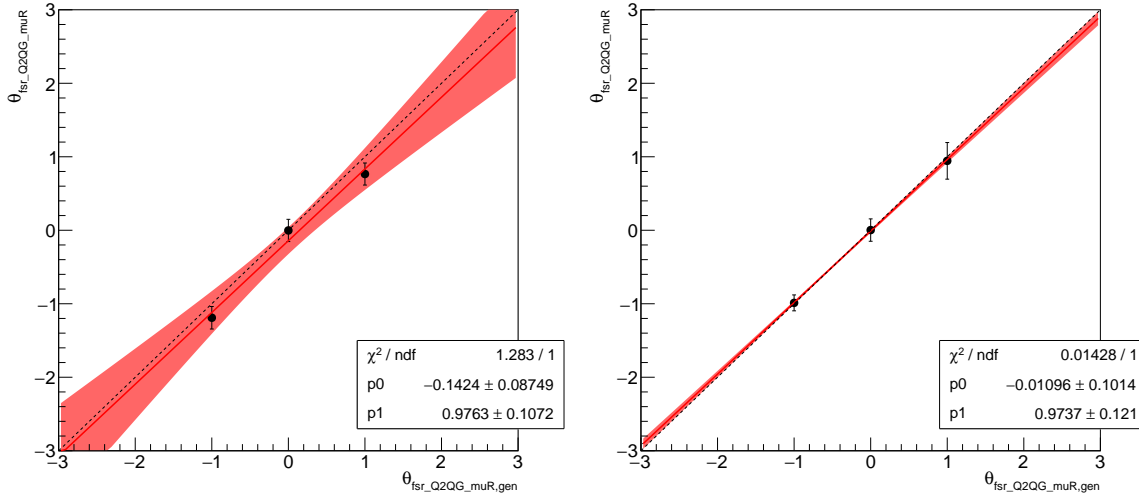


Figure 9.14.: The measured fsr_Q2QG_muR on muon+jets simulation using all observables (5D) with fsr_Q2QG_muR varied up and down by 1σ when using linear fsr_Q2QG_muR nuisance parameterization (left) and quadratic parameterization (right). The red line is the fitted slope, the dotted line is the target unity slope.

The effect of using a quadratic parameterization for the μ_R variation parts of FSR is investigated further. In figure 9.15 the measured value of the fsr_Q2QG_muR nuisance parameter for linear (black) and quadratic (red) parameterization is shown. For most observable and lepton channel settings the difference is minor. When using all observables and both lepton channels the fsr_Q2QG_muR nuisance parameter gets measured about 0.1σ closer to zero. The effect on the m_t measurement can be seen in figure 9.11. When comparing the 5D observable lepton+jets setting, the measured m_t value gets 0.08GeV smaller while the uncertainty on it does not change.

The differences on the impacts of the different sources of uncertainty when using this quadratic parameterization in a full 5D measurement are minor. The most interesting change is that the pull width of the fsr_Q2QG_muR nuisance parameter gets decreased by additional 0.18 to 0.43 (0.46 in the final setting).

Going further this quadratic parameterization will be used.

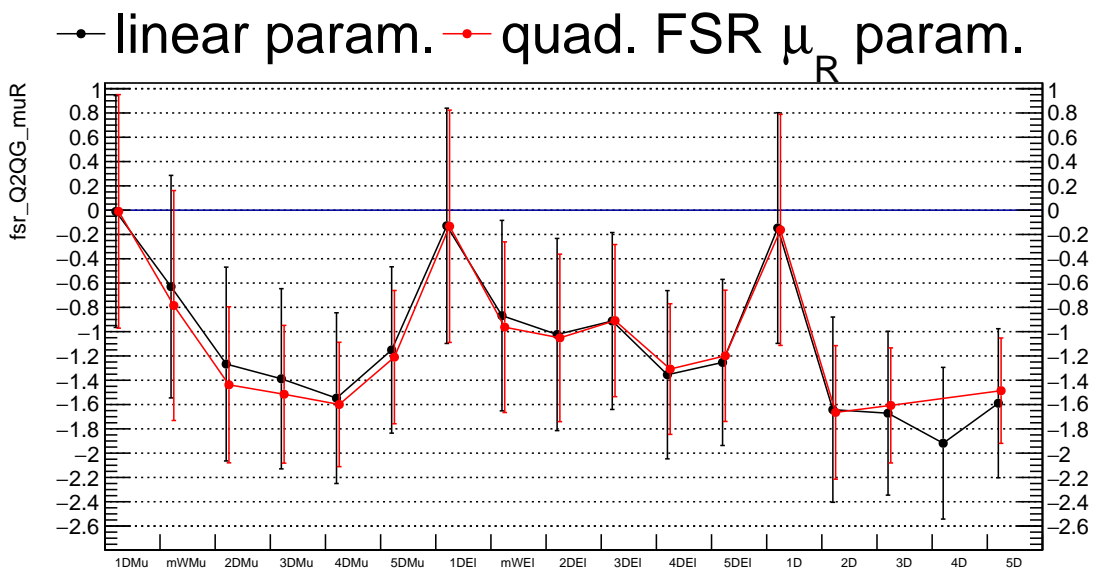


Figure 9.15.: Measurement of $\text{fsr_Q2QG_}\mu_R$ with different observable selections with linear (black) and quadratic (red) parameterization of the $\text{fsr_}\mu_R$ nuisances. The fit of the 4D lepton+jets setting with quadratic $\text{fsr_}\mu_R$ nuisance parameterization in the example setting used here did not converge. (This problem is not present in the final setting.)

9.3. Fully unblinded results

The fully unblinded results of the profile likelihood fits to data are shown in figure 9.16 (left) for the electron+jets, muon+jets, and lepton+jets channels for the different combinations of observables 1D to 5D as introduced in section 8.2. The constraints on the different nuisance parameters from the additional observables reduce the uncertainty on m_t . They also change the measured m_t value as they effectively alter the parameters of the reference $t\bar{t}$ simulation. The measured values of m_t are consistent for the different settings. With the exception of the 1D case, the measured m_t value is smaller in the combined lepton+jets channel than in the single lepton case. This happens as the combination of the channels pulls the nuisance parameter values further from their prior, while the correlations between the nuisance parameters and m_t are not trivial. The measured m_t values range from $172.29(\pm 0.63)$ GeV for the 2D e+jets case to $171.62(\pm 0.40)$ GeV for the 4D l+jets combination. The l+jets 5D result is quoted as the final result.

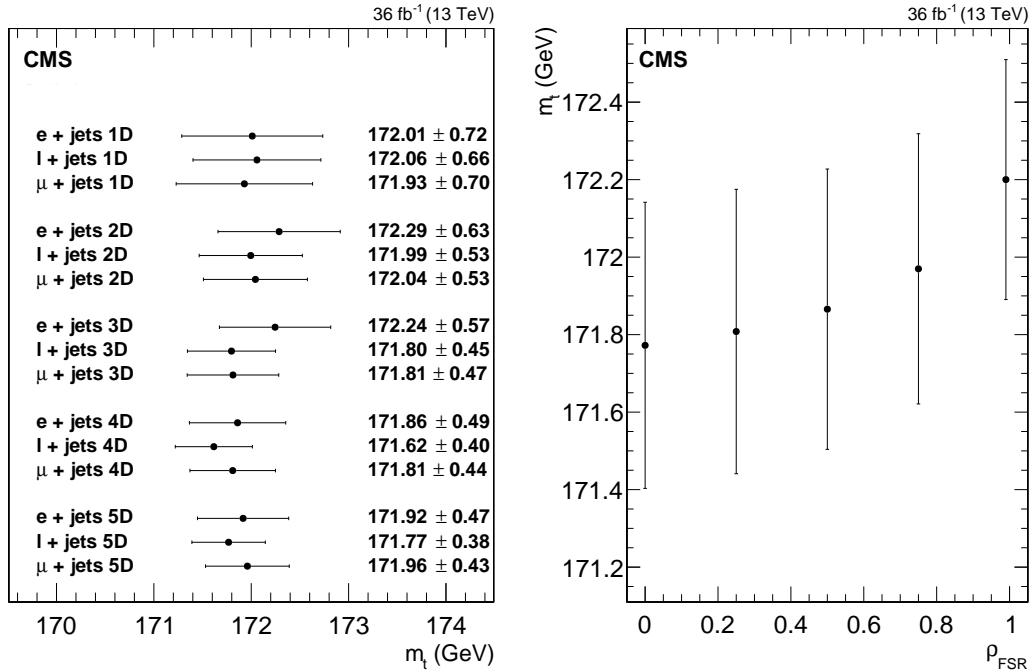


Figure 9.16.: Left: Measurement of m_t in the three different channels for the different sets of observables and categories. Right: Dependence of the 5D result on the assumed correlation between the FSR PS scales for different branchings in the lepton + jets channel.

The ML fit of the templates from the five observables to the selected events in the respective

channels yields:

$$\begin{aligned}
\text{electron+jets: } m_t^{\text{e+jets } 5D} &= 171.92 \pm 0.47 \text{ GeV}, \\
\text{muon+jets: } m_t^{\text{\mu+jets } 5D} &= 171.96 \pm 0.43 \text{ GeV}, \\
\text{lepton+jets: } m_t^{5D} &= 171.77 \pm 0.38 \text{ GeV}.
\end{aligned}$$

The top quark mass values extracted in this thesis are conceptually slightly different to former direct measurements. The value is extracted via templates parameterized in the top quark mass parameter of simulation, as in former direct measurements, but in this analysis the templates are modified by nuisance parameters that are allowed to vary. The fit to data changes some of the simulation settings and correction values compared to the nominal values they would be set to in former analysis methods. Therefore the quoted mass value corresponds not to a single simulation setting, like in former analyses, but to the mass parameters in the full set of contained simulation settings that are used as nuisance parameters. This difference should be included in the uncertainties of former direct top quark mass measurements. If all nuisance parameters are set to their prior knowledge ($\vec{\theta} = \vec{0}$) the top quark mass value is measured to be 172.01 GeV with an estimated uncertainty of ± 0.60 GeV in the 5D l+jets setting. The higher uncertainty is mainly driven by the overestimated JER uncertainty and the uncertainty due to the $q \rightarrow qg$ FSR PS scale. It still surpasses the precision of the former analysis on the same data slightly.

The final result of the nuisance values, and the pulls and impacts of the leading sources of systematic uncertainty are shown in figure 9.17. The bars in lighter colors show the estimated pre-fit impacts, so the difference between the light and dark colored parts of the impact bars indicate the improvement by the inclusion of the nuisance parameters in the likelihood. For uncertainty sources that are not limited by simulation statistics this improvement corresponds to the constraints visible in the pull widths. The biggest impact decrease can be seen for the FSR PS scale of the $q \rightarrow qg$ branching and JER for jets with $|\eta_{\text{jet}}| < 1.93$. Both decrease by more than 0.1 GeV. For the JER impact this is 2/3 of the effect, matching the 0.33σ pull width (compared to its prior) of the corresponding nuisance parameter after the fit.

Dependency on the correlation of the FSR PS scale branchings The only remaining nuisance parameter with a strong pull and an impact above 0.05 GeV is the FSR PS scale of the $q \rightarrow qg$ branching. As already discussed in paragraph 9.2.1, the pull is caused by the difference in the peak position of m_W^{reco} . It would behave different for FSR PS scales that are fully correlated to each other, as was used in the previous measurements in this channel. In that case the lower peak position in the m_W^{reco} distribution would not cause the same shift of the $q \rightarrow qg$ part of the FSR PS scale and result in a higher m_t value. A ML fit to data including all five observables and both lepton channels and assuming fully correlated FSR PS scale choices returns $m_t = 172.14 \pm 0.31$ GeV. This value is in good agreement with the previous measurement on the same data of $m_t = 172.25 \pm 0.08$ (stat+JSF) ± 0.62 (syst) GeV, taking

into account the changes in the event reconstruction and selection and in the simulation. The assumption of fully correlated FSR PS scales would also reduce the overall uncertainty significantly as parts of the impacts from the scale choice for gluon radiation from b quarks ($X \rightarrow Xg$) and light quarks ($q \rightarrow qg$) cancel.

Because of the deviation of the FSR PS scale nuisance result of the $q \rightarrow qg$ branching from the default simulation, the final result strongly depends on the choice of the correlation between the FSR PS scales. The measurement was repeated for different correlation coefficients between the different FSR PS scale nuisances in the pre-fit covariance matrix. The result of this study is shown in the right half of figure. 9.16. As the splitting of different particle types occur at different scales fully correlated FSR PS scales are not physical. Also the difference in the nuisance parameter values for the FSR PS scales per branching do support a full correlation. For low correlation coefficients ($\rho_{\text{FSR}} < 0.5$) only a small dependence on FSR PS scale correlations is found. Therefore the FSR PS scale nuisance parameters are kept uncorrelated.

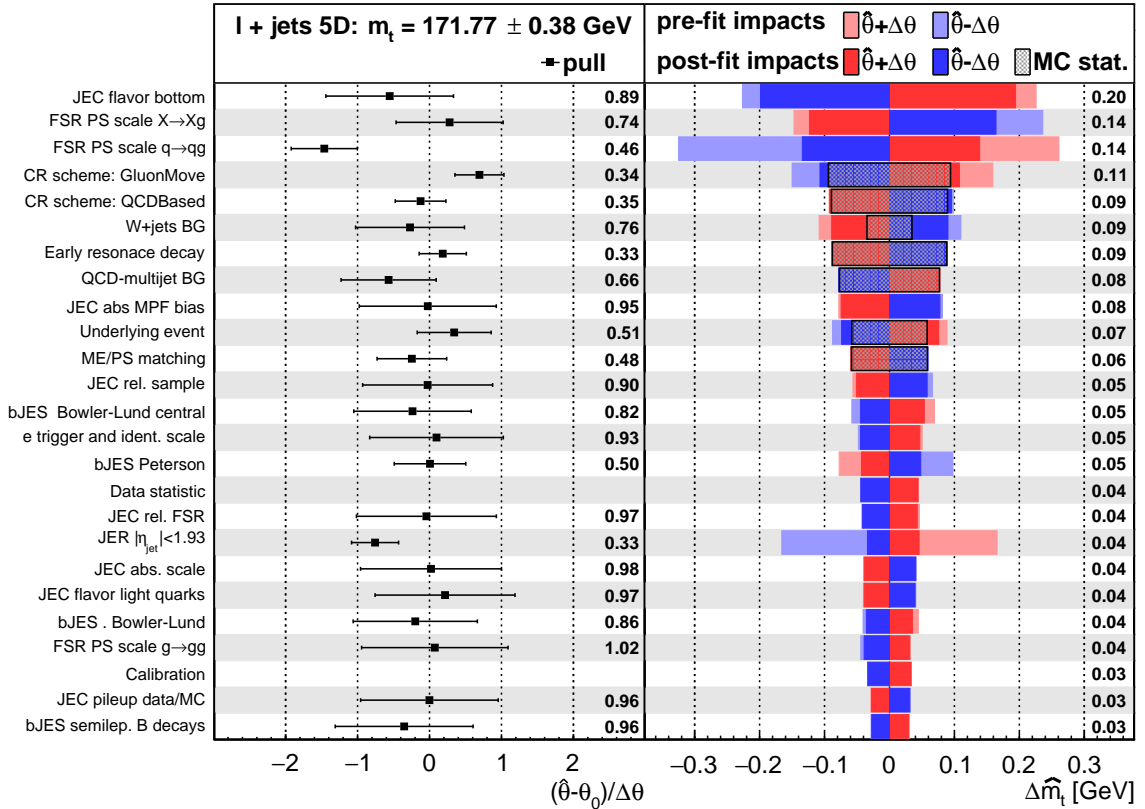


Figure 9.17.: Lepton+jets: Measurement of m_t in the combined lepton+jets channel using the 5D set of observables. The left plot shows the postfit pulls on the most important nuisances and the numbers quote the postfit uncertainty on the nuisance parameter. The right plot shows their pre-fit and postfit impacts. The postfit impacts include the contribution from the nuisances accounting for the limited size of simulation samples (MC stat.). The average of these postfit impacts is printed on the right. The rows are sorted by the size of the postfit impact.

9.4. Comparison to former measurements

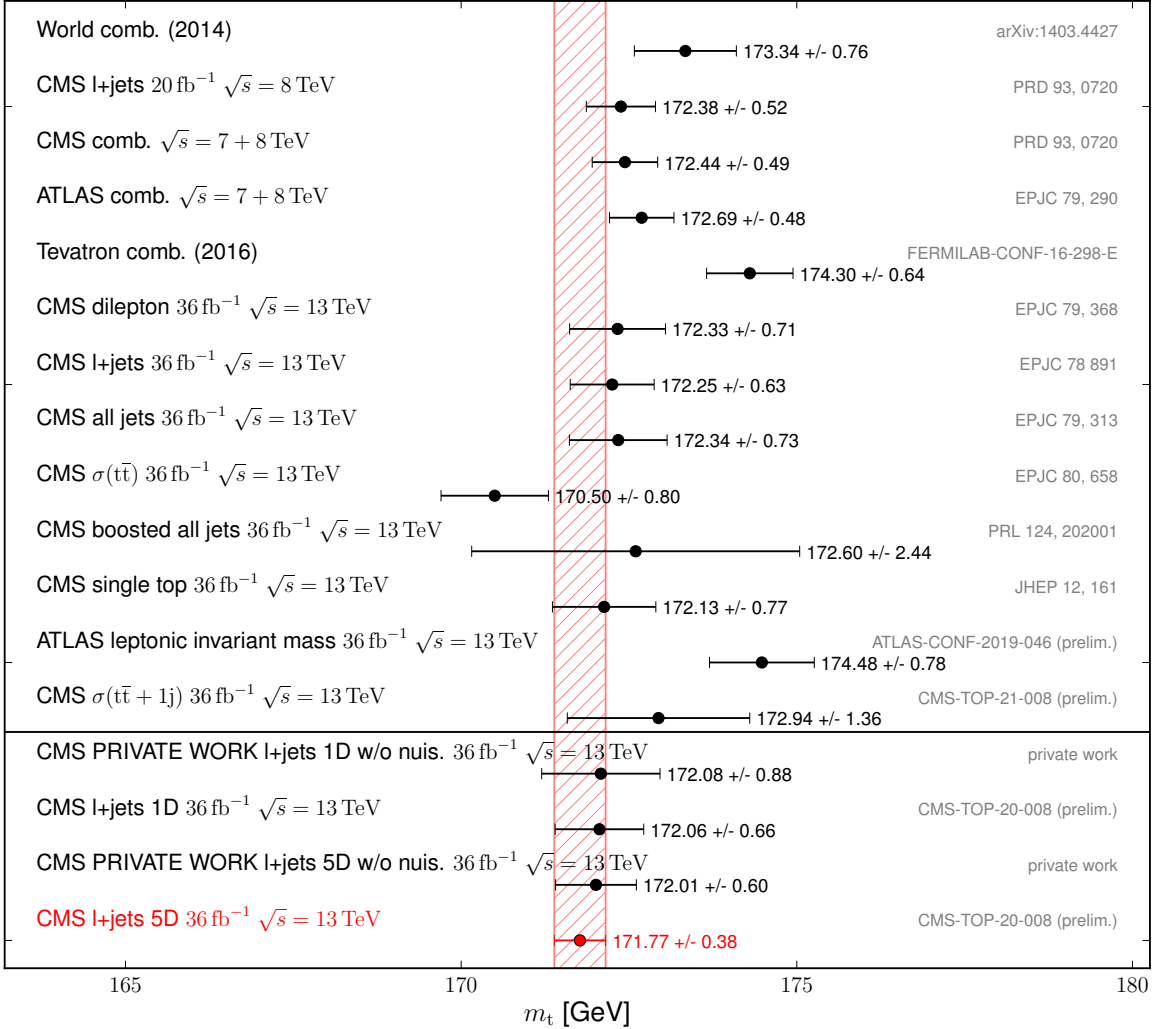


Figure 9.18.: Comparison of the result of this analysis to other top quark mass measurements. The result of this thesis is shown in red. The shaded error corresponds to its error.

The final result is put into the context of former top quark mass measurements in figure 9.18. Further details on the former measurements were presented in section 2.2.3. The analysis presented in this thesis is not only the most precise top quark mass measurement, but even more precise than any combination published by the CMS and ATLAS collaborations to date. The red area in the plot indicates the $\pm 1\sigma$ interval of the final result of this analysis. The m_t value that is measured when only the m_t^{fit} distribution is used as observable and all nuisance parameters are fixed to their prior values is included as ‘l+jets 1D w/o nuis.’. The difference to the final result of a 0.31 GeV higher top quark mass value illustrates the effect

of allowing the uncertainty source settings to be different from their prior assumptions. The m_t that is measured on the 5D observable set with all nuisance parameters are fixed to their prior values is included as ‘l+jets 5D w/o nuis.’

When comparing the different measurements presented in the plot, one has to keep in mind that different mass definitions are compared. The difference of the pole-mass from cross-section unfolding and the Monte-Carlo mass from direct measurements was described in section 2.2.3.

The final result is smaller than, but compatible with, the former direct top quark mass measurements by the CMS and ATLAS collaborations, but there is some tension to the 2014 world combination [3]. The higher value in the combination is driven by the $D\bar{0}$ result of $174.94 \pm 0.83(\text{stat}) \pm 1.25(\text{syst})$ GeV [188]. A difference in the other direction is visible when comparing the result to analyses that are extracting the top quark pole mass through unfolding of its cross-section or similar observables. Their results lead to a smaller mass values but as they measure the mass in a different definition a comparison is not straight forward.

A more than two σ deviation is also visible to a novel top quark mass measurement method performed with the ATLAS experiment that measured $m_t = 174.48 \pm 0.78$ GeV. That analysis uses the invariant mass of the two leptons from 36 fb^{-1} of $t\bar{t} \rightarrow l+jets$, where one of the b-hadrons decays into an additional muon, with an ML fit that also includes the sources of uncertainty as nuisance parameters. This leads to higher uncertainties due to branching uncertainties of the B meson but reduces the effect of JEC related uncertainties. Its result is in some tension with the combinations from the LHC experiments but in agreement with the combination of the Tevatron measurements [17].

Comparison to previous analysis on the same data As this analysis was done on the same data used by ref. [7] before, its results will be compared to the result of that analysis in more detail.

For this the impacts of different groups of uncertainties are estimated. To preserve all correlations, the combined uncertainty for each group X is calculated from the partial covariance matrix of the ML fit, $\text{cov}(X, X)$. The uncertainty on m_t from a set of nuisances is $\sqrt{\text{cov}(m_t, X) \text{cov}(X, X)^{-1} \text{cov}(X, m_t)}$. For uncertainty sources containing (simulation) statistic limitations the square root of the difference between the full and partial impact on m_t from all other sources is taken as combined uncertainty. The impacts of the uncertainty groups are presented in table 9.2. As this does not display the correlations between these groups, the quadratic sum of these groups is larger than the uncertainty from the ML fit. Unlike the former list of impacts, the PDF group in this table contains the full eigenvector variations. The former top quark mass measurement on 36 fb^{-1} of $t\bar{t} \rightarrow l+jets$ CMS data recorded in 2016 measured $m_t = 172.25 \pm 0.63$ GeV. The analysis included m_W^{reco} as additional observable for an in-situ measurement of a jet scale factor that is combined with the prior JEC. This analysis measures the top quark mass 0.48 GeV lighter and 0.25 GeV more precise. The higher precision can not be tracked down to a small set of uncertainty sources. Most of the important sources of uncertainty in this analysis have impacts that are smaller than the

Table 9.2.: Comparison of the mass uncertainty sources in the previous measurement [7] (TOP-17-007), the most precise measurement at $\sqrt{s} = 8\text{TeV}$ [4] (TOP-14-002) and the new 2D and 5D results in the lepton+jets channel.

	$\delta m_t [\text{GeV}]$			
	TOP-14-002	TOP-17-007	2D	5D
<i>Experimental uncertainties</i>				
Method calibration	0.04	0.05	0.04	0.03
JEC	0.16	0.18	0.31	0.16
E_T^{miss} -scale	0.03	-	-	-
Jet energy resolution	0.03	0.12	0.11	0.05
b tagging	0.06	0.03	0.01	0.02
lepton trigger/reco. scales	0.01	-	0.01	0.06
Pileup	0.04	0.05	0.01	0.01
Non- $t\bar{t}$ background	0.03	0.02	0.07	0.13
<i>Modeling uncertainties</i>				
JEC flavor	0.34	0.39	0.30	0.21
b jet modeling	0.16	0.12	0.14	0.13
PDF	0.04	0.02	0.02	0.02
Ren. and fact. scales	0.09 (incl. FSR/ISR)	0.01	0.05	0.03
ME/PS matching	0.07	0.07	0.08	0.06
ME generator	0.12	0.20	-	-
ISR PS scale	-	0.07	0.01	0.01
FSR PS scale	-	0.13	0.37	0.22
Top quark p_T	0.02	0.01	0.06	0.02
Underlying event	0.11	0.07	0.09	0.05
Early resonance decays	-	0.07	0.11	0.09
CR modeling	0.09	0.31	0.18	0.15
<hr/>				
Total systematic (quad. sum)	0.48	0.62	0.66	0.48
Statistical	0.16	0.08	0.05	0.04
<hr/>				
Total	0.51	0.63	0.53	0.38

uncertainties reported before.

With the use of a more efficient b-tagging algorithm and a lower threshold of the isolated electron HLT this analysis selects 47% more events with $P_{\text{gof}} \geq 0.2$ than the former one. In the former analysis electrons were selected with $p_T > 34\text{GeV}$, in this analysis with $p_T > 29\text{GeV}$. In addition information from the events with $P_{\text{gof}} < 0.2$ is included in this analysis via the $m_{\ell b}^{\text{reco}} |_{P_{\text{gof}} < 0.2}$ distribution. This leads to a reduction of the statistical uncertainty. The leading uncertainty in both analyses is due to the bottom flavor JEC uncertainty. In the former analysis it is 0.32 GeV and its total effect is reduced slightly as the JEC flavor bottom uncertainties are used fully correlated. In this analysis the impact of the JEC flavor bottom

nuisance parameter is 0.31 GeV in the 1D case and gets further decreased to 0.2 GeV, mainly by the inclusion of the $m_{\ell b}^{\text{reco}}/m_t^{\text{fit}}$ observable. The JEC flavor nuisance parameters are used without explicit correlation and the light quark, gluon and charm parts yield much smaller impacts than the one due to the bottom flavor.

The next important sources of uncertainty are due to the FSR PS scales. In the former analysis they were used fully correlated via dedicated samples, estimating an uncertainty of 0.13 GeV with a statistical uncertainty due to the sample size of 0.05 GeV that was not included in the full uncertainty. For this measurement event based weights are employed for this variation and the $X \rightarrow Xg$ and $q \rightarrow qg$ FSR PS scale splits yield impacts of about 0.14 GeV each. The $X \rightarrow Xg$ parts impact is reduced from 0.27 GeV in the 1D case by the inclusion of the additional observables. The impact of the $q \rightarrow qg$ split gets increased by the shift of its nuisance parameter from the deviation of the peak position in the m_W^{reco} distribution. The effects on m_t of these two leading FSR PS scale uncertainties have opposite directions. The combination of all FSR related uncertainties is 0.22 GeV, that is about 70% bigger than in the former analysis.

In the former analysis the quoted uncertainty due to the choice of color reconnection scheme is $0.31(\pm 0.08)$ GeV. It is the maximum difference between the two alternative CR models to the default simulation. The uncertainty on this difference from the limited size of the simulation sample is not included if it is smaller than the difference. In this analysis the effects of the comparisons to both CR schemes are used and both are, when their effect is reduced by the fit of their nuisance parameters, limited by sample statistics to roughly 0.1 GeV. This is approximately matching the sample statistics uncertainty in the former analysis. Both CR impacts combine to 0.18 GeV in the 2D case and this decreases to 0.15 GeV for the final result.

In this analysis the uncertainty due to the non- $t\bar{t}$ background is limited by the sample statistics of the W+jets and QCD-multijet simulation to 0.09 GeV and 0.08 GeV. Their impact was increased by the inclusion of events with $P_{\text{gof}} < 0.2$ that match the $t\bar{t}$ -hypothesis of the kinematic fit less and have a 5% worse signal ratio. The combined non- $t\bar{t}$ background impact is estimated to be 0.13 GeV. The former analysis was less sensitive to variations in the background as it did not include events with $P_{\text{gof}} < 0.2$. The quoted uncertainty of 0.02 GeV from non- $t\bar{t}$ background events was negligible.

The impact due to the usage of ERD is slightly higher at 0.09 GeV compared to 0.07 GeV in the former analysis. Both are limited by the size of the simulation sample.

In the former analysis the JEC uncertainty sources were bundled in correlation groups, depending on the correlation between the CMS and ATLAS experiments. The first group, 'MPFInSitu', is identical with the JEC abs. MPF bias source in this thesis. The uncertainty on the top quark mass is estimated to be 0.23 GeV when only m_t^{fit} is used in this and in the former analysis and is reduced to 0.08 GeV for this and to 0.07 GeV for the former analysis. With the new method the inclusion of the R_{bq}^{reco} observable is needed to reach the same uncertainty on this source as the former analysis.

The second JEC correlation group is called 'InterCalibration' and is identical to the JEC rel. FSR source. This uncertainty stayed at 0.04 GeV for all observable settings. This matches the uncertainty in the former analysis.

A bigger difference can be seen for the other JEC uncertainty sources. In the former analysis

they were combined to the 'Uncorrelated' group, resulting in an uncertainty of 0.16 GeV. For the measurement in this thesis all JEC uncertainty sources are represented by independent nuisance parameters. This gives the ML fit the most possibilities to find the best minimum and potentially further constrain the effects of individual sources of uncertainty. The leading JEC uncertainties in this group have impacts of 0.05 GeV (JEC rel. sample), 0.04 GeV (JEC abs. scale) and 0.03 GeV (JEC pileup data/MC). For the different sources the observables that lead to the main impact reduction vary. For example the JEC rel. sample impact is reduced mainly via the m_W^{reco} and $m_{\ell b}^{\text{reco}}|_{p_{\text{gof}} < 0.2}$ observable while the $m_{\ell b}^{\text{reco}}/m_t^{\text{fit}}$ observable has a big effect on the JEC abs. sample impact. When the JEC impacts are combined the additional observables are needed to reduce their uncertainty below the uncertainty that was quoted in the former analysis.

Two further examples of variations with a reduced effect in this analysis are the semileptonic B-hadron decay fragmentation and the JEC flavor gluon uncertainty. In the former analysis their uncertainty was estimated to be 0.08 GeV and 0.02 GeV when only m_t^{fit} is used as observables but increased to 0.10 GeV and 0.15 GeV in the final setting. With the new method their impact in the 1D case is slightly higher at 0.09 GeV and 0.03 GeV but gets reduced, mainly by the inclusion of m_W^{reco} , to 0.03 GeV and 0.01 GeV.

The quoted experimental calibration uncertainty of 0.03 GeV is slightly smaller than the 0.05 GeV of the former analysis. The slightly more stable calibration could be caused by the differences in the template parameterizations. Major differences are that no dedicated jet energy scale factor dependency is used in this thesis and that the m_W^{reco} distribution is parameterized in eight bins of nearly equal integral while the former measurement used an asymmetric Gauss function.

In the former analysis an uncertainty due to the choice of the matrix element generator of 0.22 GeV, from comparing samples generated with AMC@NLO v2.2.2 FxFX to the default from POWHEG v2, was included. As the available alternative samples were not tuned to the $\sqrt{s} = 13\text{ TeV}$ CMS data and have major deviations in the jet p_T spectrum a dedicated comparison to alternative ME generators was not feasible in this thesis. The decision to omit this as source of uncertainty was also taken in the latest direct top quark mass measurements in the all-jets $t\bar{t}$ decay channel [13]. Compared to former approaches the measured value of m_t does depend less on the choice of simulation settings as the nuisance parameters allow the likelihood to differ from the default.

Comparison to the former most precise m_t measurement The most precise top quark mass measurement up to the measurement presented in this thesis uses the same $t\bar{t}$ decay channel and approach as the former analysis on the 2016 CMS data but with events from $\sqrt{s} = 8\text{ TeV}$ collisions [4]. It measured the top quark mass at $172.35 \pm 0.51\text{ GeV}$ and has some differences in the evaluation and inclusion of uncertainty sources.

It did not evaluate the effect of additional early resonance decays and of the lepton isolation and identification scale uncertainties. The uncertainty it quoted for the color reconnection modelling is a comparison to simulation without color reconnection instead of the com-

parison between different color reconnection scheme that is employed in this thesis. Also the FSR/ISR PS scale variations were not evaluated in dedicated variations but as part of the renormalization and factorization scale uncertainty. It included the difference between samples generated with the MADGRAPH and the POWHEG matrix element generator as uncertainty source and used a dedicated variation to evaluate the uncertainty due to unclustered energy. The effect of the variation of the unclustered energy uncertainty was only 0.03 GeV, much smaller than the other differences discussed here.

The biggest improvements in the systematic uncertainties compared to the 8 TeV analysis can be seen in the impacts of JEC flavor uncertainties. When including all considered observables the JEC flavor uncertainties are in combination 0.13 GeV smaller. Also the uncertainty due to data statistics is 0.12 GeV smaller with the higher number of events that were recorded at the higher center-of-mass energy of the later LHC run. On the other hand some uncertainty source groups are bigger in this analysis. For example the uncertainty due to non- $t\bar{t}$ background, that is 0.1 GeV larger, and CR modeling, that is 0.05 GeV larger. Both are driven by simulation statistic that was evaluated differently in the $\sqrt{s} = 8$ TeV analysis.

With the combination of, among others, the NLO ME generators, a better underlying event tune, and the reduction of the JEC flavor uncertainties from the additional observables this measurement was able to surpass the precision of the $\sqrt{s} = 8$ TeV analysis significantly.

10. Summary

In this thesis the top quark mass was measured in 36fb^{-1} of data from proton-proton collisions at $\sqrt{s} = 13\text{TeV}$, collected with the CMS detector. The measurement uses $t\bar{t}$ events containing one isolated muon or electron and at least four jets, with two jets identified as bottom flavored, in the final state. Compared to the former analyses on the same data, more events were selected, by using a different high level trigger for isolated electrons and a b-tagging algorithm with a higher efficiency. For each event, the invariant mass of the top quark candidates is reconstructed with a kinematic fit of the decay products to a $t\bar{t}$ hypothesis. A likelihood method is applied to up to five observables, m_t^{fit} , m_W^{reco} , $m_{\ell b}^{\text{reco}}|_{P_{\text{gof}} < 0.2}$, $m_{\ell b}^{\text{reco}}/m_t^{\text{fit}}$ and $R_{\text{bq}}^{\text{reco}}$, per lepton channel. These observables were not only used to extract the top quark mass, but also to constrain all known sources of systematic uncertainties. Most observables include a cut on the P_{gof} of the kinematic fit at 0.2. Unlike former analyses, in this measurement events with $P_{\text{gof}} < 0.2$ are also included via the $m_{\ell b}^{\text{reco}}|_{P_{\text{gof}} < 0.2}$ observable. The correlation and independence between the observables was evaluated on simulation and data. All considered sources of uncertainties are included as nuisance parameters in the likelihood. The linear parameterizations of distributions of these observables are derived from simulation. Its stability, dependencies on m_t and other nuisance parameters, and closure was investigated using pseudo-data sets. Dedicated parameters were included to handle the statistic errors from the simulated samples. These statistic nuisance parameters were validated using toys generated from the parameterization with non-nominal nuisance distributions. When the likelihood was fit to data, consistent results were obtained for measurements with different sets of the observables. The handling of the FSR PS scales was changed compared to former analyses and nuisance values outside the variation range were measured for one of them. Therefore, multiple dedicated checks were performed to validate that they are handled correctly. The top quark mass was measured to be

$$m_t = 171.77 \pm 0.38 \text{ GeV} ,$$

including 0.04GeV statistical uncertainty. The value of m_t depends on the measured nuisance values and thus their definitions and correlations. This makes the measured m_t value more independent from the matrix element generators and parton shower algorithm on which the simulation, and thus the parameterization of the likelihood, is based. This result denotes a considerable improvement compared to all previously published top quark mass measurements and also surpasses the precision of the previously published measurement in this channel on the same data set. The analysis presented in this thesis showcases the precision that is achievable from direct measurements of the top quark mass.

10.1. Outlook

Although this measurement surpasses the precision of all former top quark mass measurements it still contains areas where analyses with similar approaches could achieve improvements.

With the employed method higher data statistics would not improve the result, as its impact is already only 0.04 GeV, but there could be improvements from higher statistics in the simulation. Because the event selection yields a rather high background rejection, the uncertainty on the few simulated background events that are selected can be rather large. This results not only in large impacts for the corresponding sources of uncertainty, but also causes fits to the histograms of the combined signal and background simulation to be less stable.

In the final observable setting, three among the seven impacts that are larger than 0.1 GeV are limited by simulation statistics. The additional precision that could be gained from very high simulation statistics is estimated to be 0.07 GeV. If the mean effect on the distributions would not change, the nuisance parameters would shift the measured value by additional 0.17 GeV towards smaller top quark mass values.

Another possible point of improvement is the parameterization of the invariant top quark mass distribution. The combination of a Voigt profile and Chebyshev polynomials describes it reasonably well while being not too computationally intensive. However, in fits to data and simulation, it can be seen that its description of the width of the peak and of the tail to high values are not perfect. It is not clear if a better description would really increase the precision of the measurement, as the calibration uncertainty, covering this limitation, is only 0.03 GeV.

Furthermore, even more accurate jet energy corrections could improve this type of top quark mass measurement. The impacts of the bottom flavor dependent JEC uncertainty was only slightly reduced by the addition of nuisance parameters to the likelihood and new observables. It is still the leading uncertainty source. As it is derived from the comparison of different simulations, a better understanding of these differences could help to choose a more precise correction for the default simulation.

Other uncertainty sources, that could be decreased by additional investigations, are the uncertainties due to choice of the color reconnection scheme and of early resonance decays. As no single color reconnection algorithm seems to correspond to what is observed in data in all kinematic regions, maybe a mixing of simulated events produced with different approaches could describe the measurements more precisely.

A way to investigate this and other nuisance parameters in an even more thorough manner, could be a differential study. When measurements are performed separately in different kinematic regions, the difference in the behaviour of nuisance parameters could give hints to other points of improvement.

For such studies, the higher instantaneous luminosity of the upgraded LHC could yield further improvements.

Impact on particle physics In the context of vacuum stability predictions of the standard model of particle physics, like that presented in section 2.2.5, the result of this thesis is, compared to former combinations, closer to the stability boarder. Although the measured result is not the pole mass it should be similar to it. If it would be identified as the pole mass, and assuming the mass of the Higgs boson $m_{\text{H}} = 125.09 \text{ GeV}$ and the strong coupling scale $\alpha_s(M_Z) = 0.1181$ without considering uncertainties, the stability border, according to eq. 2.1, would be within two standard deviations of the result of this analysis.

A global electroweak fit of the SM including this result and the latest W boson mass measurement [21] was performed by [189]. As m_t value a combination of the 2016 Tevatron combination [17], the CMS combination of 7 TeV and 8 TeV results [42], the combination of 7 TeV and 8 TeV results from ATLAS [43], the CMS $\sqrt{s} = 13 \text{ TeV}$ measurements in dilepton [31], lepton+jets (this analysis), all-jets [44] and single-top [45] channels and the $\sqrt{s} = 13 \text{ TeV}$ lepton+jets measurement by ATLAS was used. Assuming linear correlation coefficients between the systematic uncertainties these results combine to $m_t = 171.79 \pm 0.38 \text{ GeV}$. This is dominated by the result of this thesis. Since there is some tension between the individual measurements, especially between this result and the measurement from $D\emptyset$, also a conservative average with the error inflated to 1 GeV was considered.

The W boson mass was averaged from all existing measurements from LEP 2 [190], the Tevatron [21] and the LHC [191, 192] to $m_W = 80.4133 \pm 0.0080 \text{ GeV}$. Since there is significant tension between the new CDF measurement and the other measurements also a conservative average with the error inflated to 0.015 GeV was considered. Before the new m_W and m_t measurement the overall consistency fit of the SM resulted in a p-value of 0.45 at 1σ [193]. With the new measurements the p-value is 2.5×10^{-5} and 0.1 when conservative errors are used. The biggest difference is caused by the new CDF m_W measurement which is impossible to reconcile with the SM within reasonable values of m_t , but the result of this thesis also pushes the SM predictions away from data.

In the near future, a combination of the result presented in this thesis with measurements on data recorded by the CMS experiment in 2017 and 2018 and results from the ATLAS collaboration will even further decrease the uncertainty on the top quark mass and make the difference to the SM in electroweak fits clearer. As the uncertainty on the relation of the direct measurements from simulation templates to a theoretically well defined top quark mass is currently of similar size as the uncertainty of this analysis, as was discussed in section 2.2.2, it should fuel further theoretical studies on the topic.

In the future, experiments at high energy electron-positron colliders could scan the $e^+e^- \rightarrow t\bar{t}$ cross-section turn-on-curve around 350 GeV center of mass. With a simultaneous measurement of the top quark decay width this is predicted to result in an uncertainty below 40 MeV [194]. That is ten times more precise than the presented measurement. But as of now, no e^+e^- collider that could reach this center-of-mass energy has been built.

Appendices

A. Observable Correlations and Independency

Fig.A.1 shows the correlation 2D maps and profile of all one on one combinations of the observables used in this analysis in data and the different permutation types in simulation. Further the independence of the observables that use the same events is evaluated. All possible one on one combinations of the observable distribution that use events with $P_{\text{gof}} \geq 0.2$ are shown binned in the other. In addition the compatibility with the mathematical definition of independence is checked. So if the combined probability distribution is the same as the multiplied single probability distributions ($P(A,B) = P(A) \cdot P(B)$), is checked. For muon+jets simulation this is shown in figures A.2 – A.7 and for electron+jets simulation in figures A.8 – A.13. The bins where the ratio of the combined and multiplied single probability distribution is not close to one contain only few events.

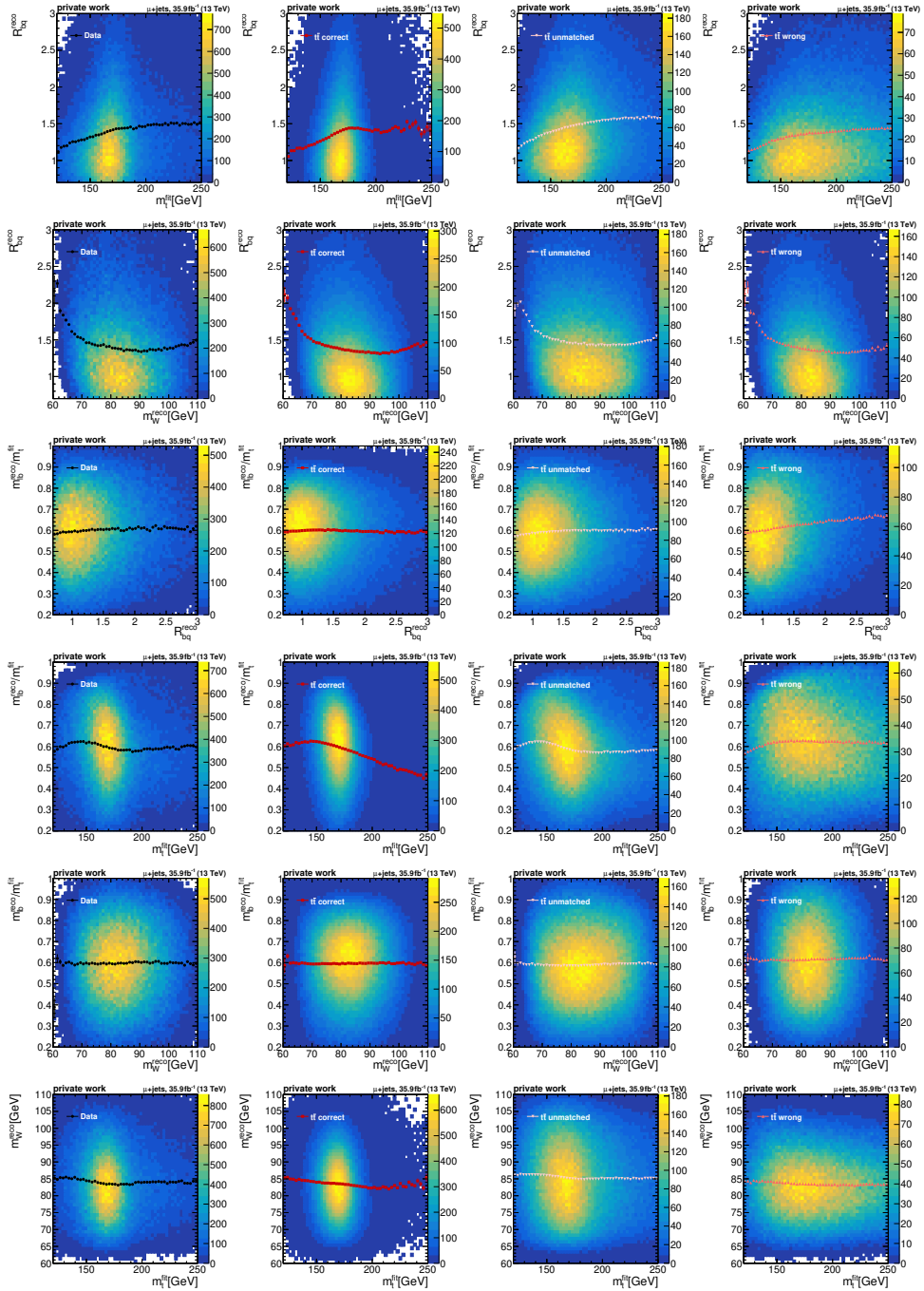


Figure A.1.: Muon+jets: Correlations distributions and profiles between different observable candidates for data and the different permutation types in simulation.

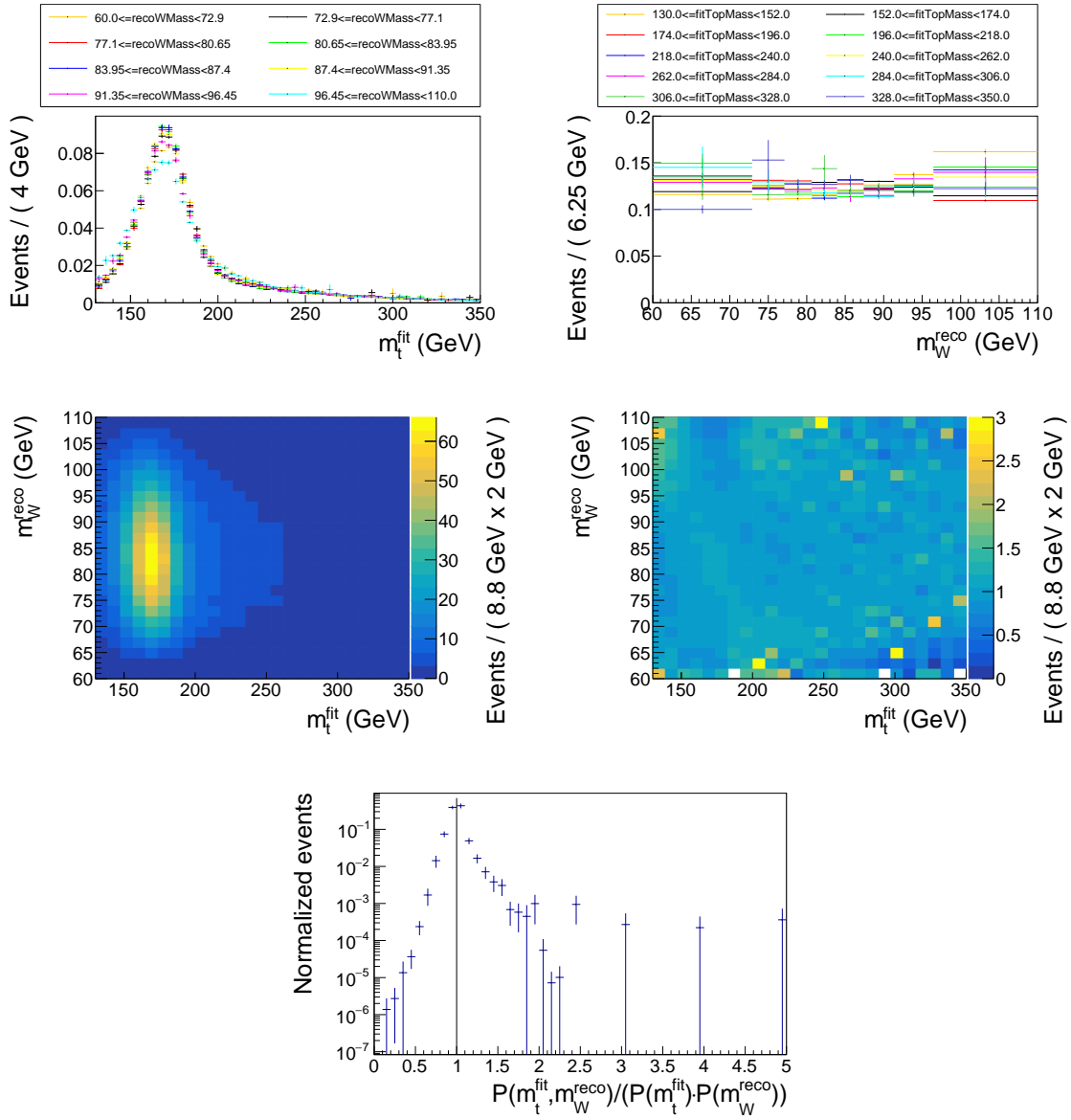


Figure A.2.: Muon+jets simulation: Upper row: The m_t^{fit} in bins of m_W^{reco} (left) and the m_W^{reco} distributions in bins of m_t^{fit} . Middle row: m_t^{fit} to m_W^{reco} (left) and the ratio of the combined probability of m_t^{fit} and m_W^{reco} to the multiplied probability of m_t^{fit} and m_W^{reco} $P(m_t^{\text{fit}}, m_W^{\text{reco}}) / (P(m_t^{\text{fit}}) \cdot P(m_W^{\text{reco}}))$ (right). The z-axis is limited to three. Lower row: The value of $P(m_t^{\text{fit}}, m_W^{\text{reco}}) / (P(m_t^{\text{fit}}) \cdot P(m_W^{\text{reco}}))$ weighted by the number of events in the corresponding bin. The rightmost bin contains the overflow.

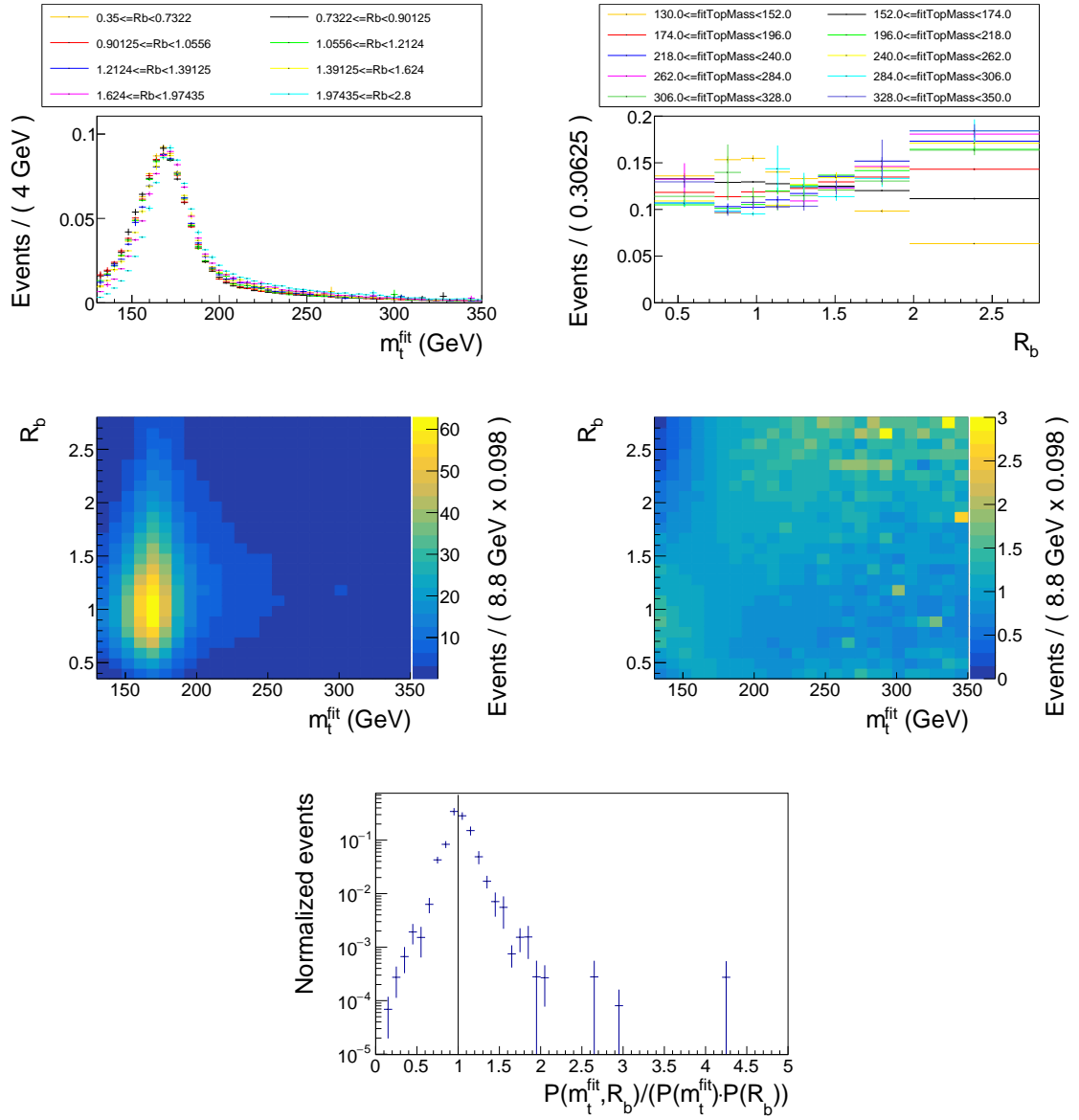


Figure A.3.: Muon+jets simulation: Upper row: The m_t^{fit} in bins of R_{bq}^{reco} (left) and the R_{bq}^{reco} distributions in bins of m_t^{fit} . Middle row: m_t^{fit} to R_{bq}^{reco} (left) and the ratio of the combined probability of m_t^{fit} and R_{bq}^{reco} to the multiplied probability of m_t^{fit} and R_{bq}^{reco} $P(m_t^{\text{fit}}, R_{bq}^{\text{reco}}) / (P(m_t^{\text{fit}}) \cdot P(R_{bq}^{\text{reco}}))$ (right). The z-axis is limited to three. Lower row: The value of $P(m_t^{\text{fit}}, R_{bq}^{\text{reco}}) / (P(m_t^{\text{fit}}) \cdot P(R_{bq}^{\text{reco}}))$ weighted by the number of events in the corresponding bin. The rightmost bin contains the overflow.

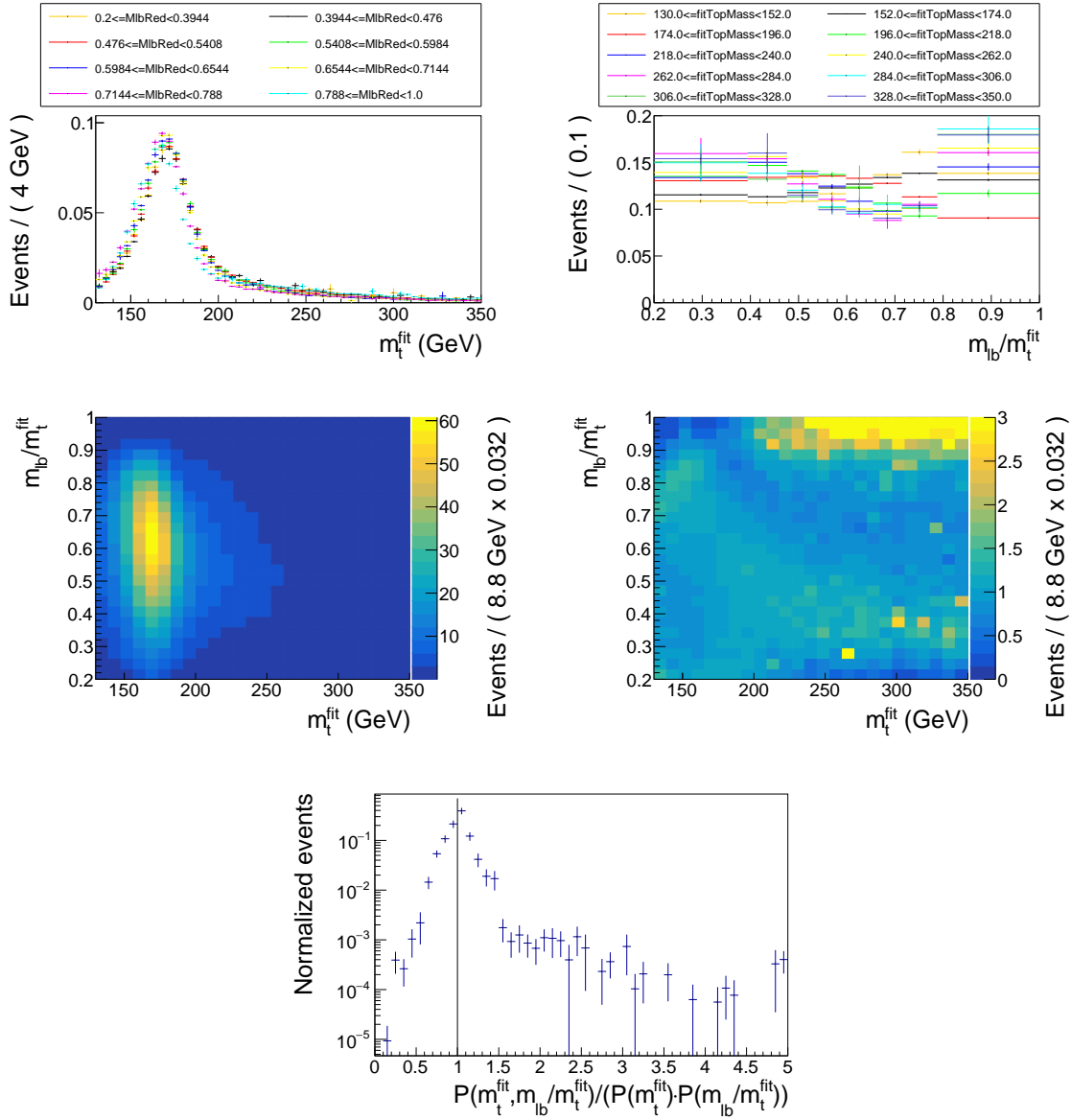


Figure A.4.: Muon+jets simulation: Upper row: The m_t^{fit} in bins of $m_{\ell b}^{\text{reco}}/m_t^{\text{fit}}$ (left) and the $m_{\ell b}^{\text{reco}}/m_t^{\text{fit}}$ distributions in bins of m_t^{fit} . Middle row: m_t^{fit} to $m_{\ell b}^{\text{reco}}/m_t^{\text{fit}}$ (left) and the ratio of the combined probability of m_t^{fit} and $m_{\ell b}^{\text{reco}}/m_t^{\text{fit}}$ to the multiplied probability of m_t^{fit} and $m_{\ell b}^{\text{reco}}/m_t^{\text{fit}}$ $P(m_t^{\text{fit}}, m_{\ell b}^{\text{reco}}/m_t^{\text{fit}})/(P(m_t^{\text{fit}}) \cdot P(m_{\ell b}^{\text{reco}}/m_t^{\text{fit}}))$ (right). The z-axis is limited to three. Lower row: The value of $P(m_t^{\text{fit}}, m_{\ell b}^{\text{reco}}/m_t^{\text{fit}})/(P(m_t^{\text{fit}}) \cdot P(m_{\ell b}^{\text{reco}}/m_t^{\text{fit}}))$ weighted by the number of events in the corresponding bin. The rightmost bin contains the overflow.

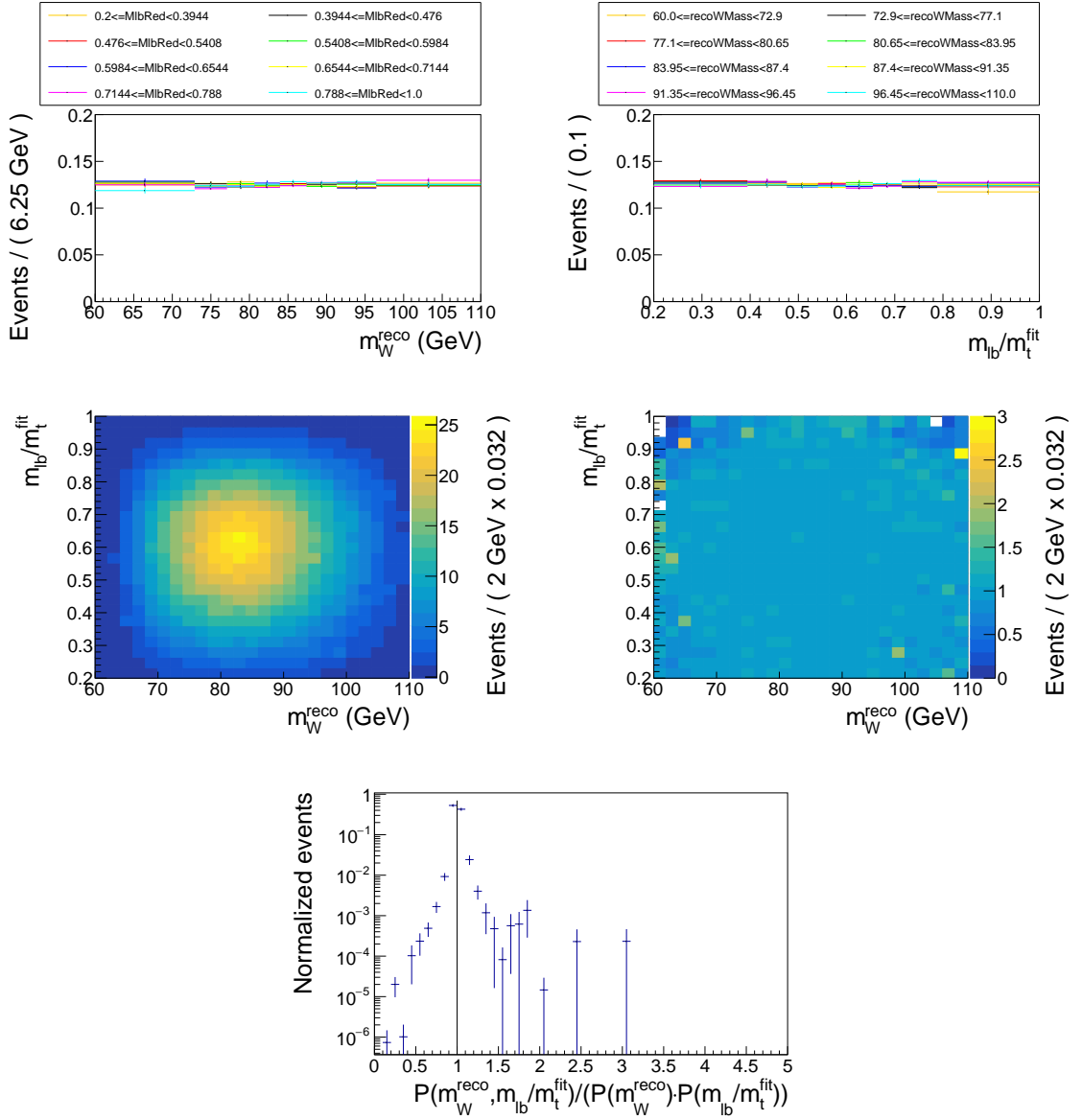


Figure A.5.: Muon+jets simulation: Upper row: The m_W^{reco} in bins of $m_{\ell b}^{\text{reco}}/m_t^{\text{fit}}$ (left) and the $m_{\ell b}^{\text{reco}}/m_t^{\text{fit}}$ distributions in bins of m_W^{reco} . Middle row: m_W^{reco} to $m_{\ell b}^{\text{reco}}/m_t^{\text{fit}}$ (left) and the ratio of the combined probability of m_W^{reco} and $m_{\ell b}^{\text{reco}}/m_t^{\text{fit}}$ to the multiplied probability of m_W^{reco} and $m_{\ell b}^{\text{reco}}/m_t^{\text{fit}}$ $P(m_W^{\text{reco}}, m_{\ell b}^{\text{reco}}/m_t^{\text{fit}})/(P(m_W^{\text{reco}}) \cdot P(m_{\ell b}^{\text{reco}}/m_t^{\text{fit}}))$ (right). The z-axis is limited to three. Lower row: The value of $P(m_W^{\text{reco}}, m_{\ell b}^{\text{reco}}/m_t^{\text{fit}})/(P(m_W^{\text{reco}}) \cdot P(m_{\ell b}^{\text{reco}}/m_t^{\text{fit}}))$ weighted by the number of events in the corresponding bin. The rightmost bin contains the overflow.

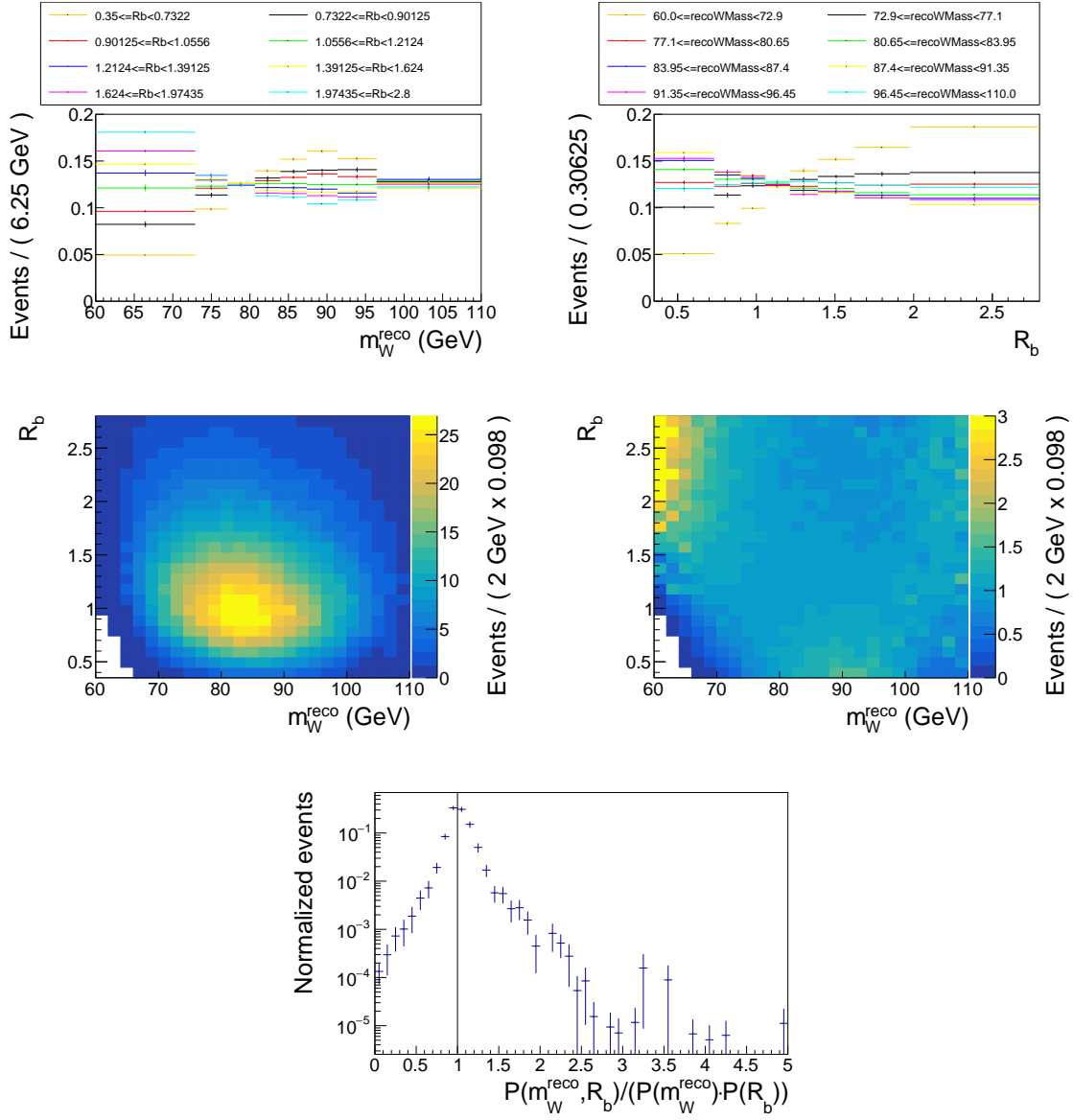


Figure A.6.: Muon+jets simulation: Upper row: The m_W^{reco} in bins of $R_{\text{bq}}^{\text{reco}}$ (left) and the $R_{\text{bq}}^{\text{reco}}$ distributions in bins of m_W^{reco} . Middle row: m_W^{reco} to $R_{\text{bq}}^{\text{reco}}$ (left) and the ratio of the combined probability of m_W^{reco} and $R_{\text{bq}}^{\text{reco}}$ to the multiplied probability of m_W^{reco} and $R_{\text{bq}}^{\text{reco}}$ $P(m_W^{\text{reco}}, R_{\text{bq}}^{\text{reco}}) / (P(m_W^{\text{reco}}) \cdot P(R_{\text{bq}}^{\text{reco}}))$ (right). The z-axis is limited to three. Lower row: The value of $P(m_W^{\text{reco}}, R_{\text{bq}}^{\text{reco}}) / (P(m_W^{\text{reco}}) \cdot P(R_{\text{bq}}^{\text{reco}}))$ weighted by the number of events in the corresponding bin. The rightmost bin contains the overflow.

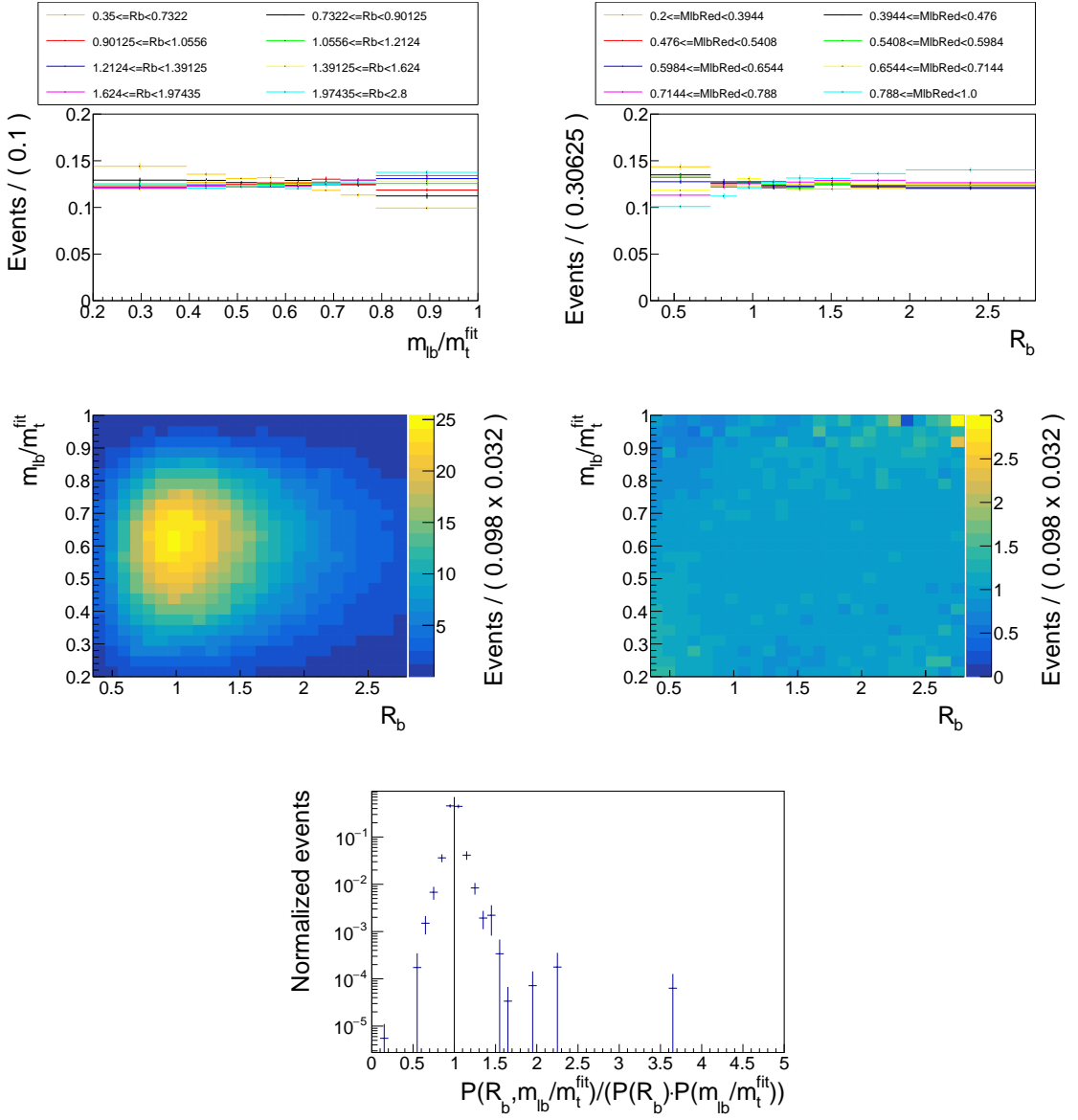


Figure A.7.: Muon+jets simulation: Upper row: The m_{lb}^{reco}/m_t^{fit} in bins of R_{bq}^{reco} (left) and the R_{bq}^{reco} distributions in bins of m_{lb}^{reco}/m_t^{fit} . Middle row: m_{lb}^{reco}/m_t^{fit} to R_{bq}^{reco} and the ratio of the combined probability of m_{lb}^{reco}/m_t^{fit} and R_{bq}^{reco} to the multiplied probability of m_{lb}^{reco}/m_t^{fit} and R_{bq}^{reco} $P(m_{lb}^{reco}/m_t^{fit}, R_{bq}^{reco}) / (P(m_{lb}^{reco}/m_t^{fit}) \cdot P(R_{bq}^{reco}))$ (right). The z-axis is limited to three. Lower row: The value of $P(m_{lb}^{reco}/m_t^{fit}, R_{bq}^{reco}) / (P(m_{lb}^{reco}/m_t^{fit}) \cdot P(R_{bq}^{reco}))$ weighted by the number of events in the corresponding bin. The rightmost bin contains the overflow.

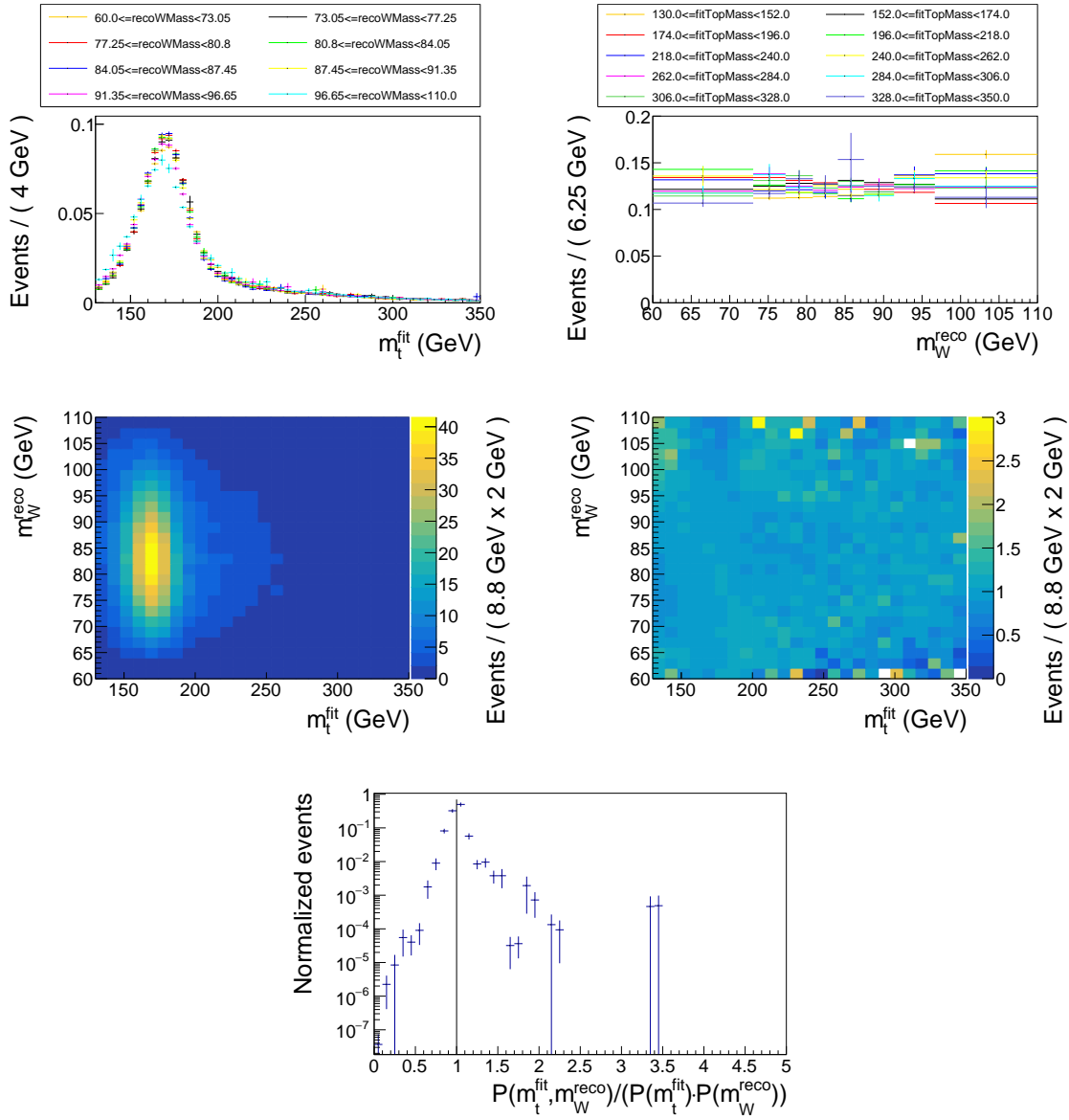


Figure A.8.: Electron+jets simulation: Upper row: The m_t^{fit} in bins of m_W^{reco} (left) and the m_W^{reco} distributions in bins of m_t^{fit} . Middle row: m_t^{fit} to m_W^{reco} (left) and the ratio of the combined probability of m_t^{fit} and m_W^{reco} to the multiplied probability of m_t^{fit} and m_W^{reco} $P(m_t^{fit}, m_W^{reco}) / (P(m_t^{fit}) \cdot P(m_W^{reco}))$ (right). The z-axis is limited to three. Lower row: The value of $P(m_t^{fit}, m_W^{reco}) / (P(m_t^{fit}) \cdot P(m_W^{reco}))$ weighted by the number of events in the corresponding bin. The rightmost bin contains the overflow.

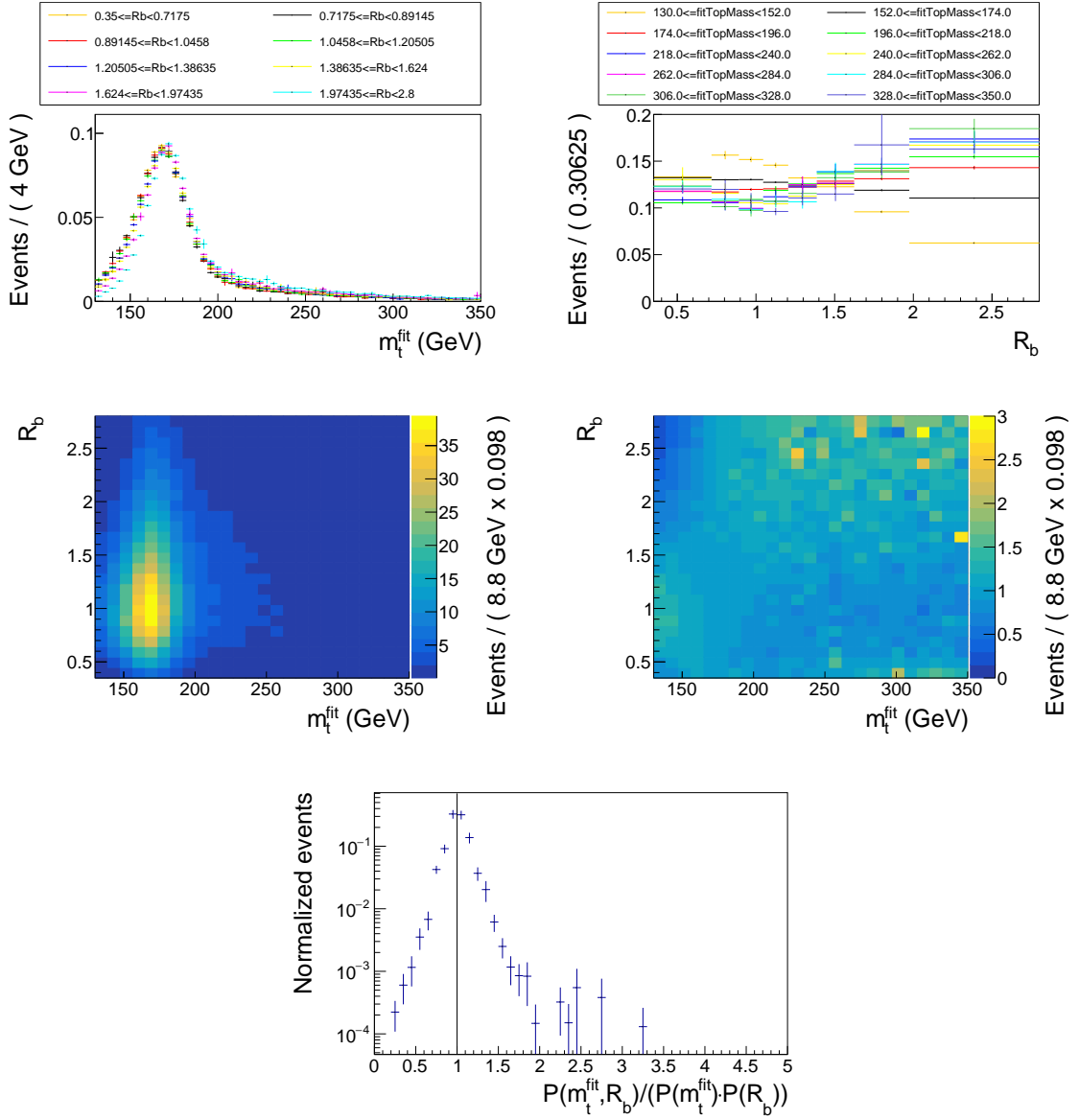


Figure A.9.: Electron+jets simulation: Upper row: The m_t^{fit} in bins of R_{bq}^{reco} (left) and the R_{bq}^{reco} distributions in bins of m_t^{fit} . Middle row: m_t^{fit} to R_{bq}^{reco} (left) and the ratio of the combined probability of m_t^{fit} and R_{bq}^{reco} to the multiplied probability of m_t^{fit} and R_{bq}^{reco} $P(m_t^{fit}, R_{bq}^{reco}) / (P(m_t^{fit}) \cdot P(R_{bq}^{reco}))$ (right). The z-axis is limited to three. Lower row: The value of $P(m_t^{fit}, R_{bq}^{reco}) / (P(m_t^{fit}) \cdot P(R_{bq}^{reco}))$ weighted by the number of events in the corresponding bin. The rightmost bin contains the overflow.

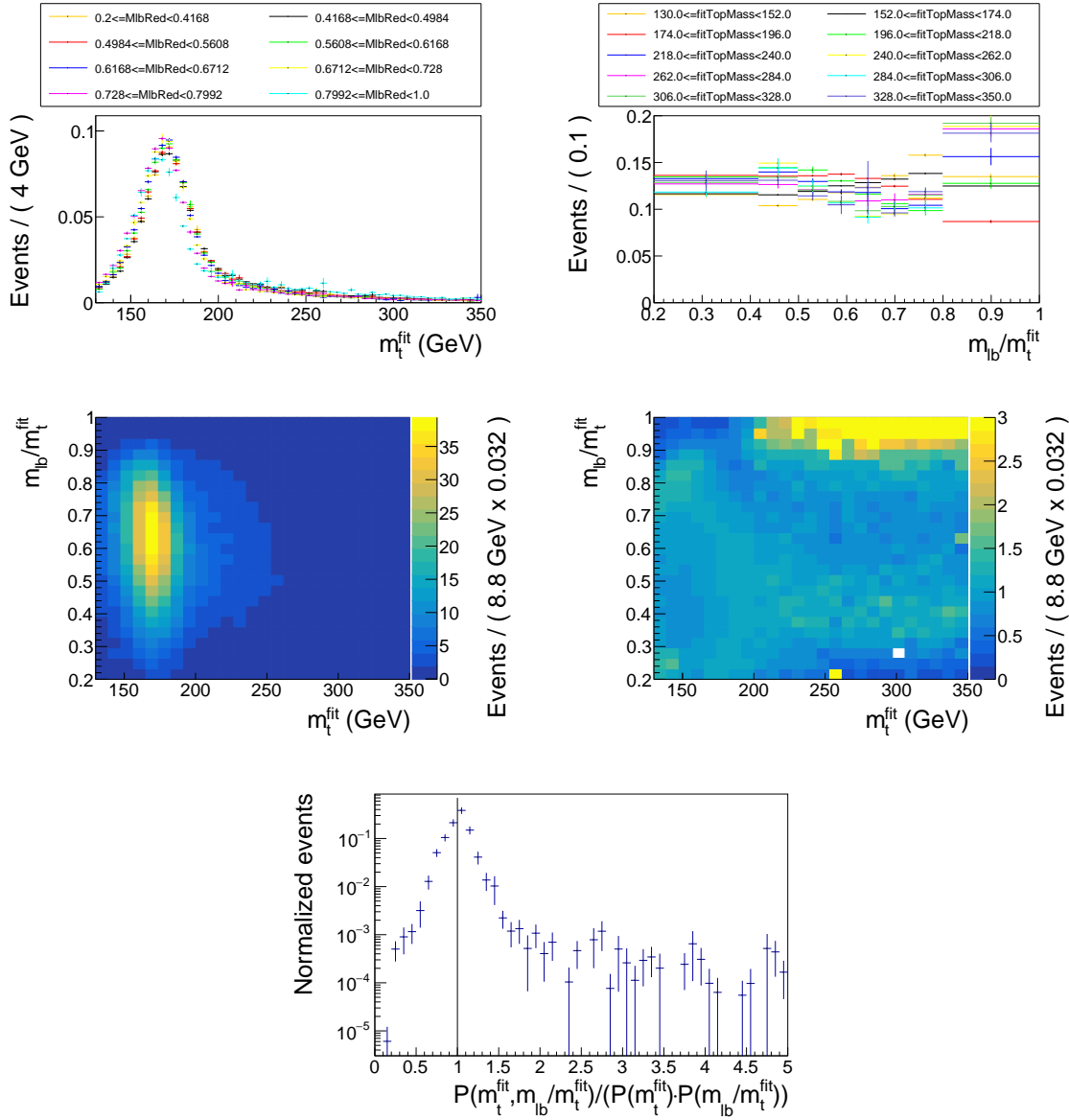


Figure A.10.: Electron+jets simulation: Upper row: The m_t^{fit} in bins of $m_{\ell b}^{\text{reco}}/m_t^{\text{fit}}$ (left) and the $m_{\ell b}^{\text{reco}}/m_t^{\text{fit}}$ distributions in bins of m_t^{fit} . Middle row: m_t^{fit} to $m_{\ell b}^{\text{reco}}/m_t^{\text{fit}}$ (left) and the ratio of the combined probability of m_t^{fit} and $m_{\ell b}^{\text{reco}}/m_t^{\text{fit}}$ to the multiplied probability of m_t^{fit} and $m_{\ell b}^{\text{reco}}/m_t^{\text{fit}}$ $P(m_t^{\text{fit}}, m_{\ell b}^{\text{reco}}/m_t^{\text{fit}})/(P(m_t^{\text{fit}}) \cdot P(m_{\ell b}^{\text{reco}}/m_t^{\text{fit}}))$ (right). The z-axis is limited to three. Lower row: The value of $P(m_t^{\text{fit}}, m_{\ell b}^{\text{reco}}/m_t^{\text{fit}})/(P(m_t^{\text{fit}}) \cdot P(m_{\ell b}^{\text{reco}}/m_t^{\text{fit}}))$ weighted by the number of events in the corresponding bin. The rightmost bin contains the overflow.

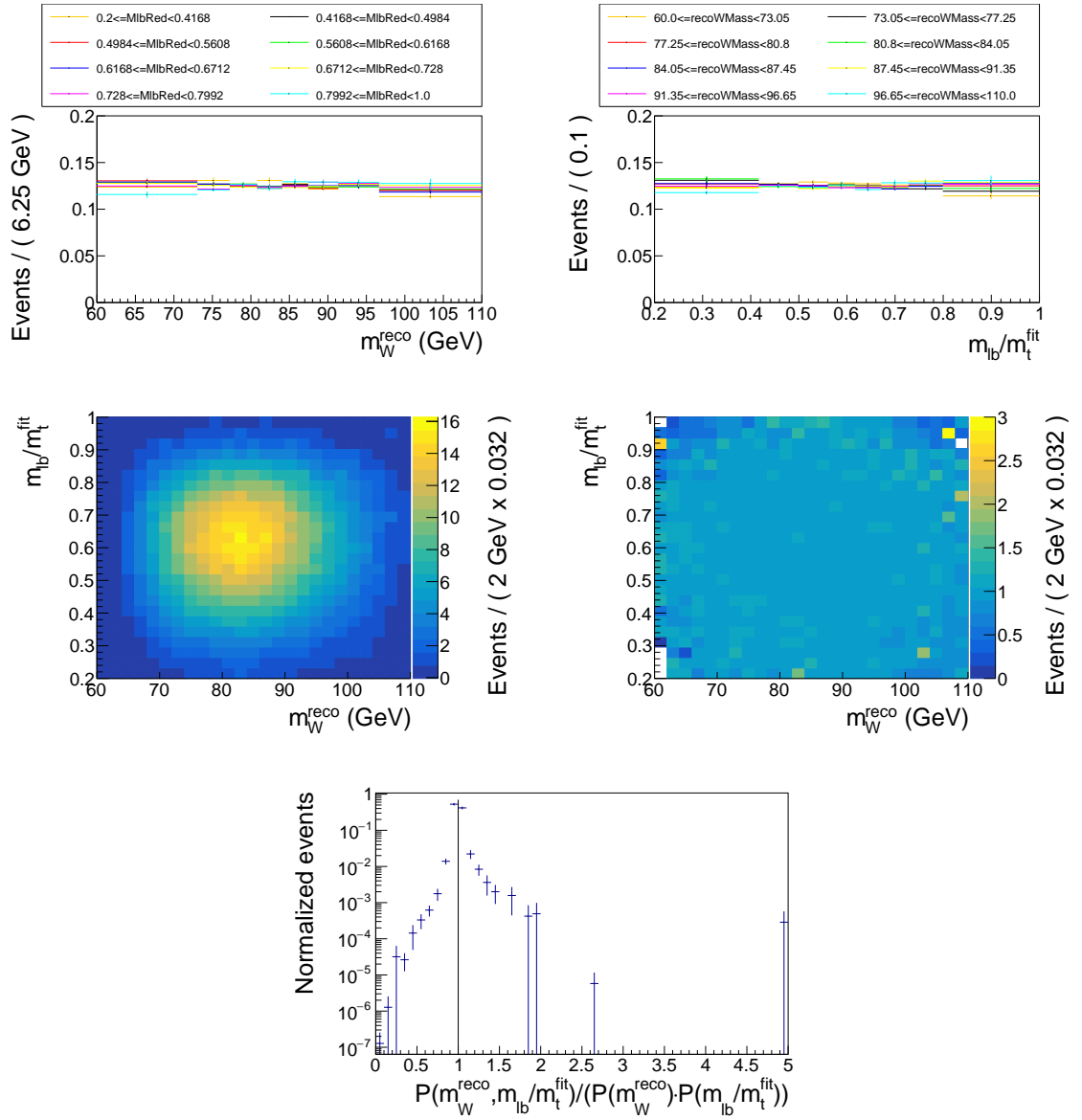


Figure A.11.: Electron+jets simulation: Upper row: The m_W^{reco} in bins of $m_{lb}^{\text{reco}}/m_t^{\text{fit}}$ (left) and the $m_{lb}^{\text{reco}}/m_t^{\text{fit}}$ distributions in bins of m_W^{reco} . Middle row: m_W^{reco} to $m_{lb}^{\text{reco}}/m_t^{\text{fit}}$ (left) and the ratio of the combined probability of m_W^{reco} and $m_{lb}^{\text{reco}}/m_t^{\text{fit}}$ to the multiplied probability of m_W^{reco} and $m_{lb}^{\text{reco}}/m_t^{\text{fit}}$ ($P(m_W^{\text{reco}}, m_{lb}^{\text{reco}}/m_t^{\text{fit}}) / (P(m_W^{\text{reco}}) \cdot P(m_{lb}^{\text{reco}}/m_t^{\text{fit}}))$) (right). The z-axis is limited to three. Lower row: The value of $P(m_W^{\text{reco}}, m_{lb}^{\text{reco}}/m_t^{\text{fit}}) / (P(m_W^{\text{reco}}) \cdot P(m_{lb}^{\text{reco}}/m_t^{\text{fit}}))$ weighted by the number of events in the corresponding bin. The rightmost bin contains the overflow.

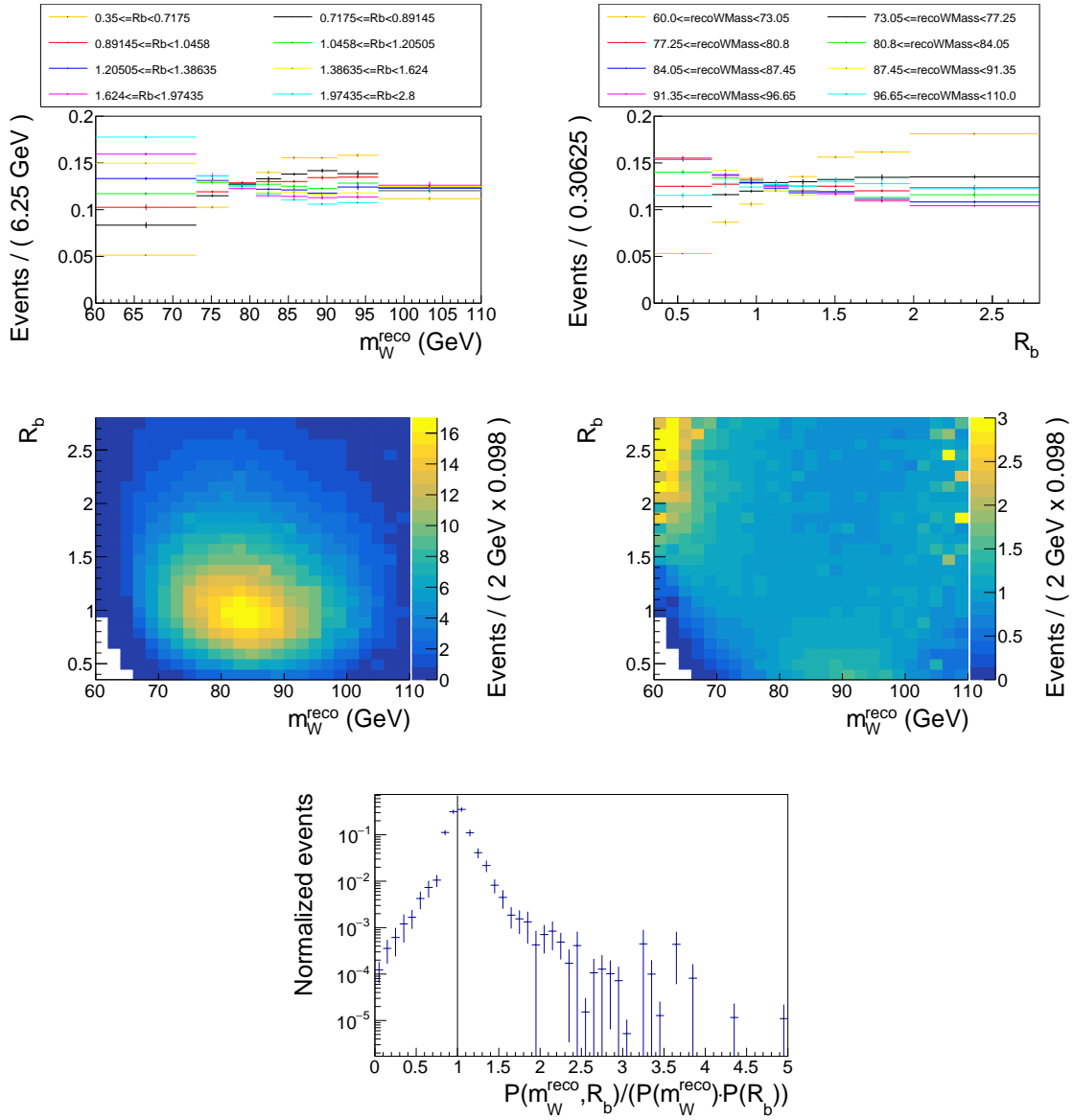


Figure A.12.: Electron+jets simulation: Upper row: The m_W^{reco} in bins of R_{bq}^{reco} (left) and the R_{bq}^{reco} distributions in bins of m_W^{reco} . Middle row: m_W^{reco} to R_{bq}^{reco} (left) and the ratio of the combined probability of m_W^{reco} and R_{bq}^{reco} to the multiplied probability of m_W^{reco} and R_{bq}^{reco} $P(m_W^{\text{reco}}, R_{bq}^{\text{reco}}) / (P(m_W^{\text{reco}}) \cdot P(R_{bq}^{\text{reco}}))$ (right). The z-axis is limited to three. Lower row: The value of $P(m_W^{\text{reco}}, R_{bq}^{\text{reco}}) / (P(m_W^{\text{reco}}) \cdot P(R_{bq}^{\text{reco}}))$ weighted by the number of events in the corresponding bin. The rightmost bin contains the overflow.

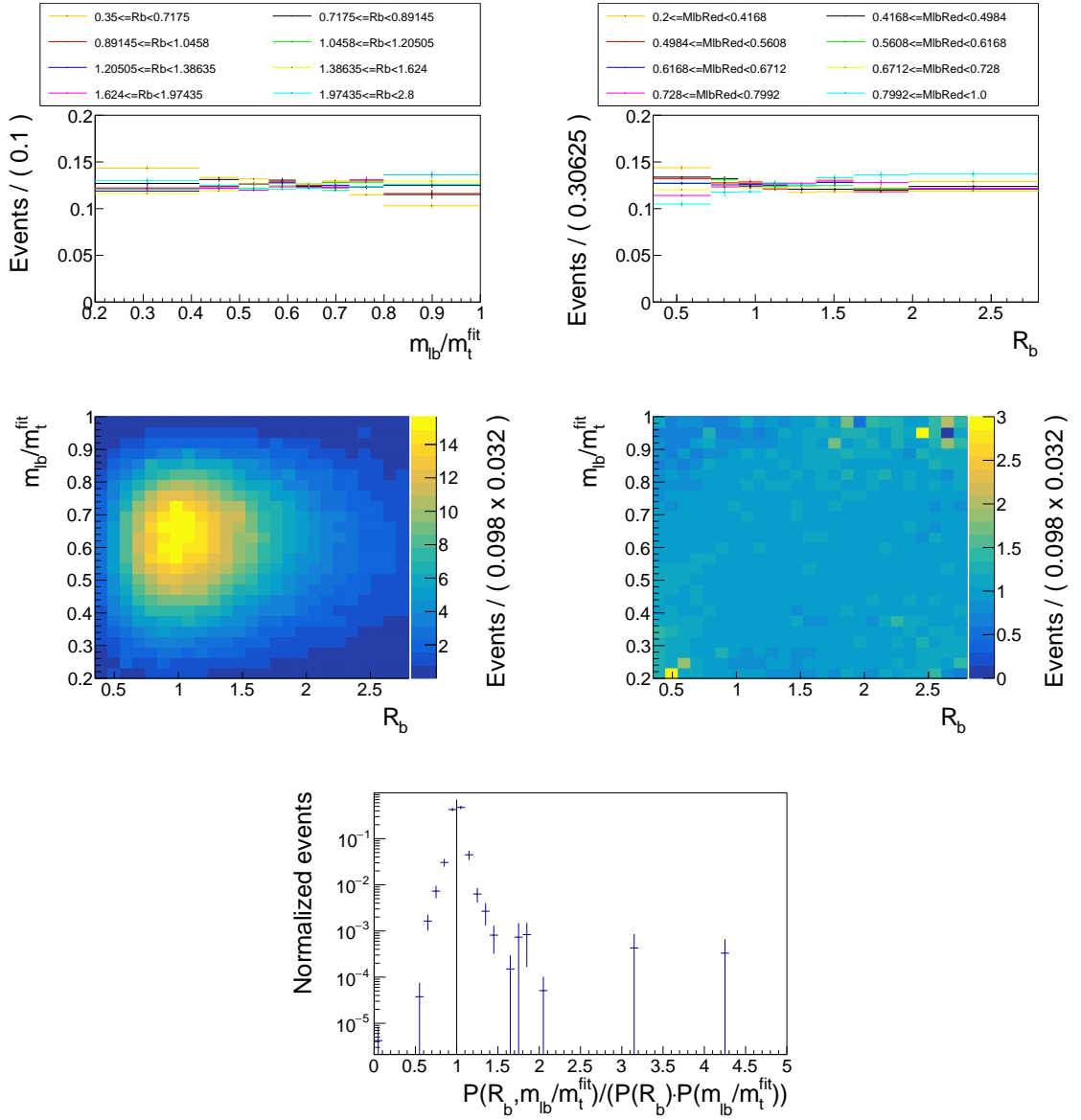


Figure A.13.: Electron+jets simulation: Upper row: The $m_{\ell_b}^{\text{reco}}/m_t^{\text{fit}}$ in bins of R_{bq}^{reco} (left) and the R_{bq}^{reco} distributions in bins of $m_{\ell_b}^{\text{reco}}/m_t^{\text{fit}}$. Middle row: $m_{\ell_b}^{\text{reco}}/m_t^{\text{fit}}$ to R_{bq}^{reco} (left) and the ratio of the combined probability of $m_{\ell_b}^{\text{reco}}/m_t^{\text{fit}}$ and R_{bq}^{reco} to the multiplied probability of $m_{\ell_b}^{\text{reco}}/m_t^{\text{fit}}$ and R_{bq}^{reco} $P(m_{\ell_b}^{\text{reco}}/m_t^{\text{fit}}, R_{bq}^{\text{reco}})/(P(m_{\ell_b}^{\text{reco}}/m_t^{\text{fit}}) \cdot P(R_{bq}^{\text{reco}}))$ (right). The z-axis is limited to three. Lower row: The value of $P(m_{\ell_b}^{\text{reco}}/m_t^{\text{fit}}, R_{bq}^{\text{reco}})/(P(m_{\ell_b}^{\text{reco}}/m_t^{\text{fit}}) \cdot P(R_{bq}^{\text{reco}}))$ weighted by the number of events in the corresponding bin. The rightmost bin contains the overflow.

B. Example model build and measurement

B.1. Example model build

To better illustrate the details of the method a walk-through through the modelling and fit algorithms with example numbers will be presented. The example numbers are not from the final state of this analysis, but still illustrate their typical magnitude. As example parameter the mean, μ , of the Voigtian describing the m_t^{fit} distribution for the $t\bar{t} \rightarrow \mu + \text{jets}$ channel is used. Step for step it will be described how the parameters of its parameterization $\alpha_{m_t^{\text{fit}}, \mu}$ following eq. 8.2 are derived and how the result, error and single nuisance impact predictions are extracted from (pseudo-)data.

Before any fit the scales C_k is set so that the magnitude of the parameter α_k is 1, in this case $C_{m_t^{\text{fit}}, \mu} = 170.6$. In addition $d_{m_t^{\text{fit}}, \mu} = 0.001$ is taken from prior examination of the m_t^{fit} distribution. The parameters of the α 's are determined from simulation samples including the background samples and one of the signal variations.

First the offset α_k^0 is fitted using the default signal sample with $m_t = 172.5$ GeV. For the example parameter this results in $\alpha_{m_t^{\text{fit}}, \mu}^0 = 0.9927 \pm 0.0001$. α_k^0 close to 1 shows that C_k was chosen sensible.

Next the m_t slopes s_k^0 are derived by fitting to samples with $m_t \in \{169.5 \text{ GeV}, 172.5 \text{ GeV}, 175.5 \text{ GeV}\}$ resulting in $s_{m_t^{\text{fit}}, \mu}^0 = 5.69 \pm 0.07 \text{ GeV}^{-1}$ for the example parameter. The real effective slope of the top-quark mass dependencies is $C_{m_t^{\text{fit}}, \mu} \cdot d_{m_t^{\text{fit}}, \mu} \cdot s_{m_t^{\text{fit}}, \mu}^0 = 0.97 \text{ GeV}^{-1}$. This matches the expectation that the mean of the Voigtian profile, μ , is fully correlated (slope of one) to the value of the top-quark mass.

With the m_t dependent parameters fixed, the slopes of the nuisances are derived independent of each other. As example the nuisance corresponding to the systematic uncertainty from the comparison of the default (MPI based) to the gluonmove color reconnection scheme, CRgm, is chosen. The change of the color reconnection scheme is interpreted as $\theta_{\text{CRgm}} = 1\sigma$ variation and the slopes s_k^{CRgm} are fitted to this. The slope in the example parameter is $s_{m_t^{\text{fit}}, \mu}^{\text{CRgm}} = -0.34 \pm 0.29$.

Further variables corresponding to the statistical uncertainty from the simulation samples, β for the offset and $\vec{\omega}$ for the slopes, are added.

For all nuisances constraints are added. The systematic variation nuisances $\vec{\theta}$ are constrained by Gaussian profiles centered on 0 with a width of 1, corresponding to $\pm 1\sigma$ variations. The nuisances β and $\vec{\omega}$ are each constrained with one multivariate Gaussian per nuisance per observable. For example the 8 $\omega_{m_t^{\text{fit}}, X}^{\text{CRgm}}$ in the 8 parameters of the Voigt+Chebyshev description of the m_t^{fit} distribution are constrained by one 8 dimensional multivariate Gaussian. The mean of the multivariate Gaussian profiles are 0 (in all dimensions) and its covariance matrix is set to the correlation matrix between the corresponding slopes $s_{m_t^{\text{fit}}, X}^{\text{CRgm}}$. Values of the maximum and minimum correlations from the used example parameter are listed in table B.1. The β and ω 's are in addition multiplied by the error on the corresponding α or s to get the correlation constraint scaled to the covariance.

After this step the model that will be fit to data is built. A part of the concrete pa-

Table B.1.: Example correlation values between different template parameters. μ , p_1 and p_2 are parameters of the m_t^{fit} parameterization.

parameter	min(corr)	max(corr)
$\alpha_{m_t^{\text{fit}}, \mu}^0$	$\text{corr}(\mu, p_2) = 0.06$	$\text{corr}(\mu, p_1) = -0.36$
$s_{m_t^{\text{fit}}, \mu}^0$	$\text{corr}(\mu, p_2) = -0.01$	$\text{corr}(\mu, p_1) = -0.36$
$s_{m_t^{\text{fit}}, \mu}^{\text{CRgm}}$	$\text{corr}(\mu, p_2) = 0.054$	$\text{corr}(\mu, p_1) = -0.35$

parameterization of the parameter μ in the m_t^{fit} probability density function for example is

$$\begin{aligned}
\alpha_{m_t^{\text{fit}}, \mu} \left(m_t, \vec{\theta} \right) = & 170.6 \cdot (0.99 + 0.00014 \cdot \beta_{m_t^{\text{fit}}, \mu} \\
& + 0.001 \cdot \left(5.69 \text{ GeV}^{-1} \cdot (m_t - 172.5 \text{ GeV}) + \omega_{m_t^{\text{fit}}, \mu}^0 \cdot 0.068 \text{ GeV} \right)) \\
& \times \left(1 + 0.001 \cdot \left(-0.34 \cdot \theta_{\text{CRgm}} + 0.29 \cdot \omega_{m_t^{\text{fit}}, \mu}^{\text{CRgm}} \right) \right) \\
& \times \prod_{i \neq \text{CRgm}} \left(1 + d_{m_t^{\text{fit}}, \mu} \cdot \left(s_{m_t^{\text{fit}}, \mu}^i \theta_i + \omega_{m_t^{\text{fit}}, \mu}^i \right) \right).
\end{aligned}$$

B.2. Example fit results

The m_t and $\vec{\theta}$ values are determined by a negative log-likelihood fit of the model on (pseudo-) data. In the following the estimation of the result and their uncertainty on one pseudo-data set will be described. The number of events in the pseudo-data set is pulled randomly from a Poisson distribution around the number of selected data events. For the $t\bar{t} \rightarrow \mu + \text{jets}$ channel this is $n_{\text{data}, \mu} = 451\,618$. In this example 462\,032 events were drawn from the default signal

plus background simulation. This selection includes 5 659 events with negative weights (mostly from AMC@NLOFFFX samples used for the Drell-Yang background) resulting in 450 714 effective events with a signal fraction of 0.92. A log-likelihood fit of the model with free variable m_t , $\vec{\theta}$, β and $\vec{\omega}$, constrained as described above, found the minimum at $m_t = -0.03 \pm 0.63$ GeV (remember the 172.5 GeV offset in the parameterization), $\theta_{\text{CRgm}} = 0.01 \pm 0.85$, $\beta_{m_t^{\text{fit}}, \mu} = 0.014 \pm 0.989$, $\omega_{m_t^{\text{fit}}, \mu}^0 = 0.006 \pm 0.998$, $\omega_{m_t^{\text{fit}}, \mu}^{\text{CRgm}} = 0.028 \pm 0.953$, and similar values for the other nuisances that will not be listed in this example. The error on θ_{CRgm} smaller than 1 indicates that the influence of CRgm variation can be reduced. For the example pseudo-data set the top quark mass $m_t = 172.5 \pm 0.6$ GeV is measured. When performing the measurement on 200 pseudo-data sets the mean of the measured top quark mass closes at $\langle m_t \rangle = -0.01$ GeV with a predicted total uncertainty of $\langle \sigma_{m_t} \rangle = 0.63$ GeV. In addition the color reconnection is determined to be 1% in the direction of the gluonmove scheme.

To estimate the impact of the individual uncertainty sources the minimisation is repeated for all uncertainty sources with the corresponding nuisance fixed to their variations from the full fit where all parameters are fitted simultaneously. For the CRgm nuisance this means that it is fixed to its post-fit result $\theta_{\text{CRgm}} = -0.02 \pm 0.85$ (for both directions independent) and the fit is repeated with all other variables (m_t , β , $\theta_{i \neq \text{CRgm}}$, $\vec{\omega}$) free. With this the negative log-likelihood minimisation is repeated yielding $m_t^{\text{CRgm Up}} = -0.0124 \pm 0.6281$ GeV and $m_t^{\text{CRgm Down}} = -0.0158 \pm 0.6073$ GeV. The difference of $m_t^{\text{CRgm Up/Down}}$ to $m_t = -0.01414$ GeV from the full fit is the impact of the CRgm uncertainty on the top quark mass measurement, so for this example pseudo-data set $\Delta m_t^{\text{CRgm}} = m_t^{\text{CRgm Down}} - m_t = -0.002$ GeV. After each impact determination all parameters are reset to the result of the full fit.

To determine the impact of the statistic uncertainty from the pseudo-data set (not the simulation statistic) all variables except m_t are fixed to their full fit results and the minimisation is repeated. The uncertainty on m_t in this setting, the uncertainty from pseudo-data statistic, is for this example $\sigma_{m_t}^{(\text{stat})} = 0.06$ GeV.

To determine the impact of the default and m_t variation simulation statistic the fit is repeated with all variables fixed except m_t , β_k and ω_k^0 . The quadratic difference of the error on the resulting m_t to the data statistic is the *calibration* impact. For the example pseudo-data set this is $\sigma_{m_t}^{\text{calibration}} = 0.02$.

To determine the statistic impact of other uncertainty sources the minimisation is repeated with the corresponding nuisance and the corresponding statistic uncertainty nuisances fixed to their results from the full fit. For the pseudo-data set used as example θ_{CRgm} is set to -0.02 and its statistic nuisance $\omega_{m_t^{\text{fit}}, \mu}^{\text{CRgm}}$ to 0.028. This minimisation of this setting results in a error on m_t of $\sigma_{m_t} |_{\theta_{\text{CRgm}} \text{ and } \omega_{m_t^{\text{fit}}, \mu}^{\text{CRgm}} \text{ fixed}} = 0.63$ GeV. The impact of the statistical limitation of the

CRgm sample is the quadratic difference of this error to the m_t error from a minimisation where $\omega_{m_t, \mu}^{\text{CRgm}}$ is left free. No dedicated minimisation is performed for only θ_{CRgm} fixed to its value after the full fit but it is estimated from the mean of the error on m_t from the previous fit where CRgm was fixed to its up/down variation. So the impacts of the CRgm sample statistic in this example is

$$\sqrt{\left(\frac{\sigma_{m_t}^{\text{CRgm Up}} + \sigma_{m_t}^{\text{CRgm Down}}}{2}\right)^2 - \sigma_{m_t}^2 \Big|_{\theta_{\text{CRgm}} \text{ and } \omega_{m_t, \mu}^{\text{CRgm}} \text{ fixed}}} \text{ GeV} = 0.10 \text{ GeV}.$$

C. Predicted and measured nuisance values and impacts for different observable selections

C.1. Partial unblinded impacts from single observables

In this section the full lists of predicted impacts from pseudo-experiments (left plots) and measured nuisance parameters and impacts with blinded m_t value (right plots) for different single observables and lepton inclusions are shown. The nuisances are sorted by their predicted impact. If no impact value is shown the value is below 0.005 GeV. Each prediction is averaged from more than 200 pseudo-experiment sets, each corresponding to the full expected data statistic.

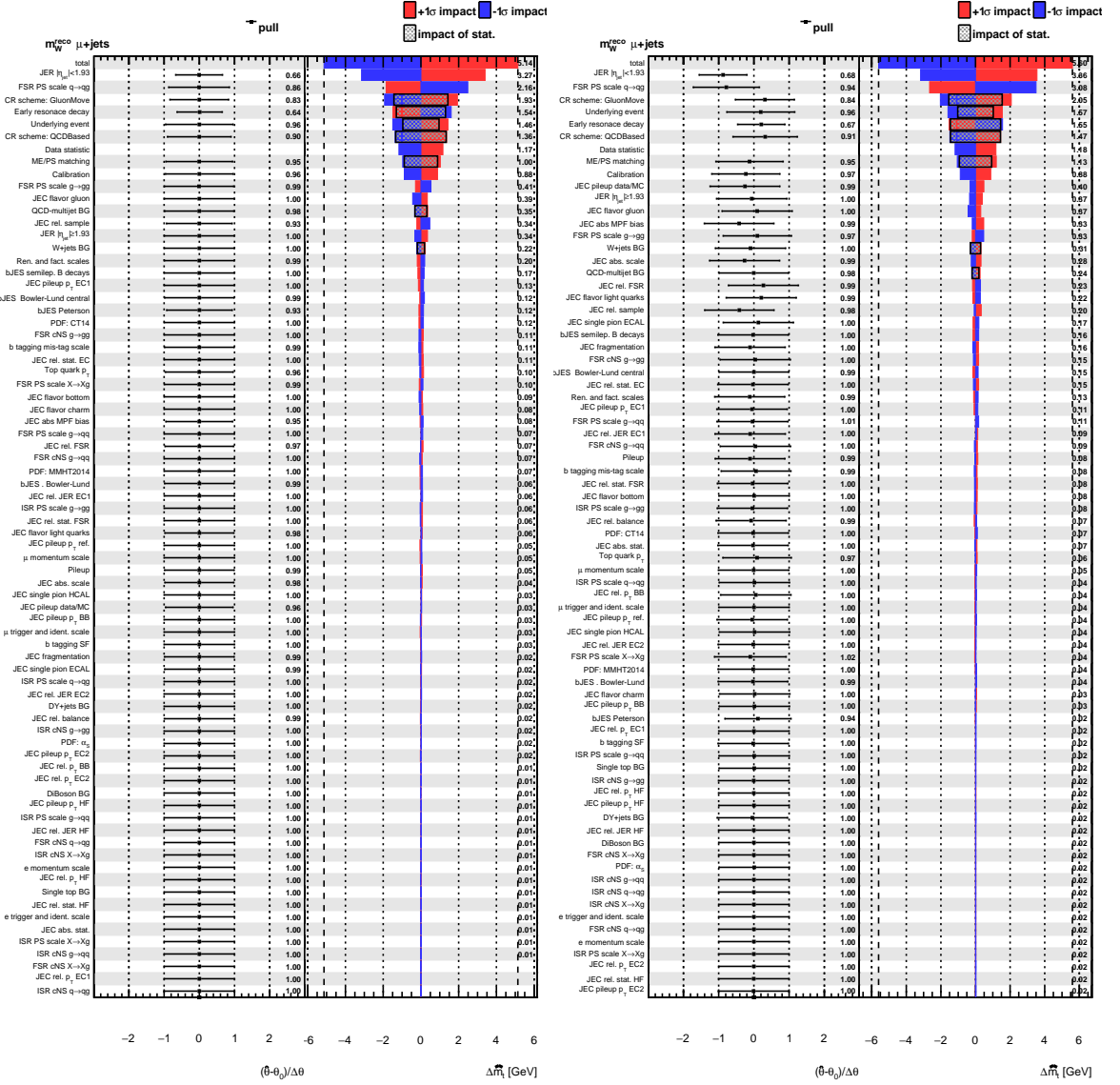


Figure C.1.: Muon+jets: The pull mean and width and impacts from pseudo-data (left) and measured (right) when using only m_W^{reco} as observable.

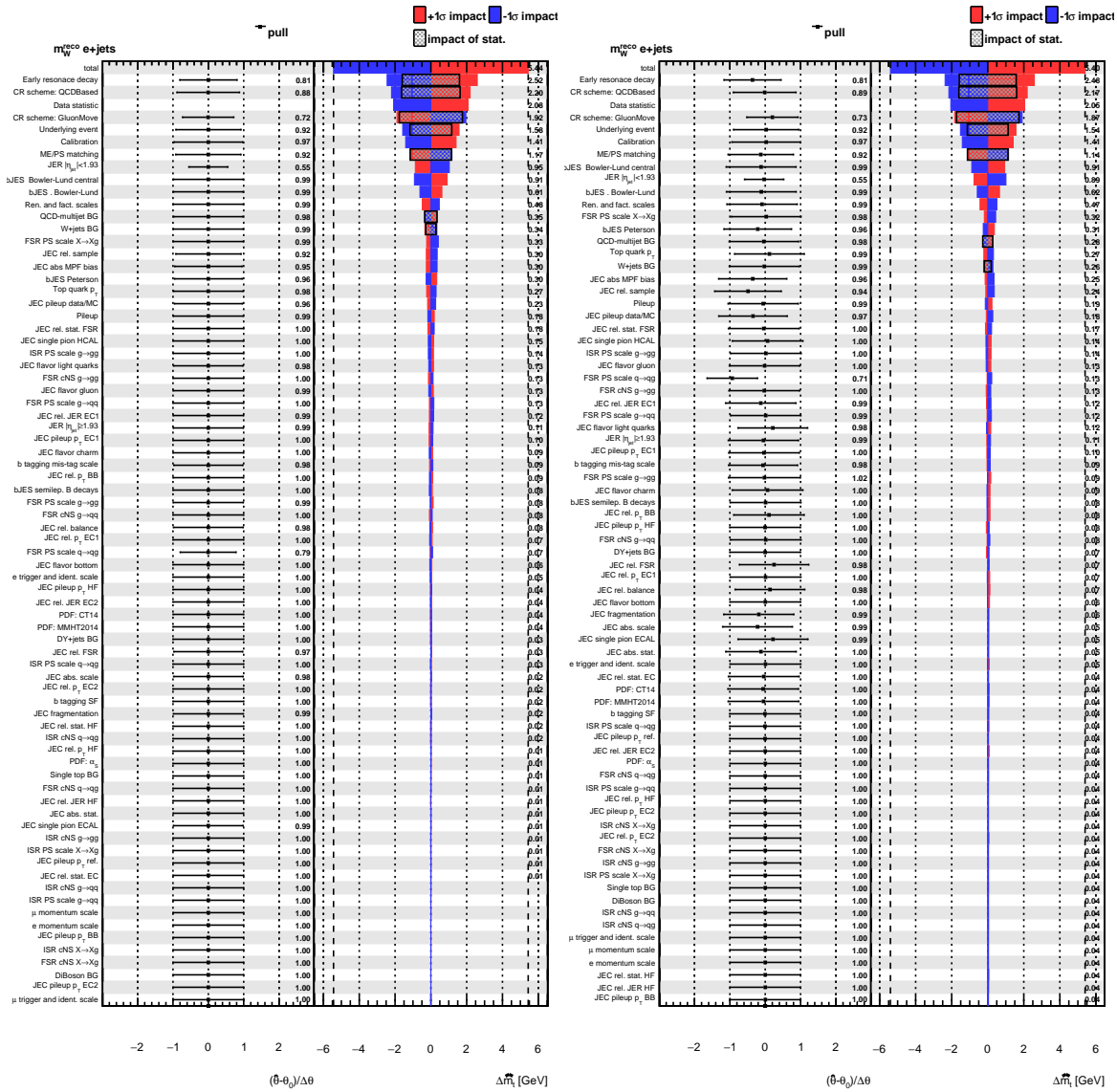


Figure C.2.: Electron+jets: The pull mean and width and impacts from pseudo-data (left) and measured (right) when using only m_W^{reco} as observable.

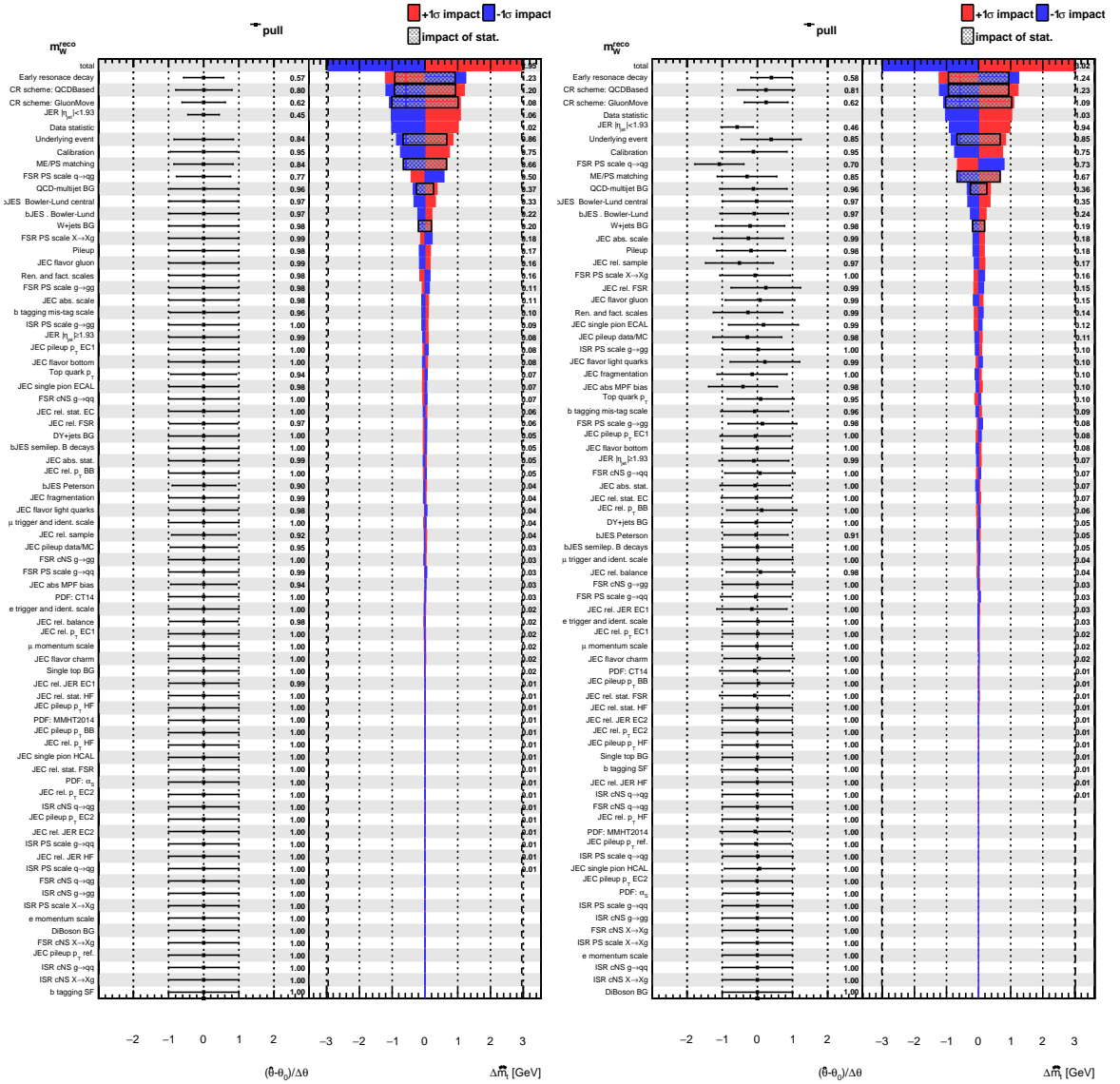


Figure C.3.: Lepton+jets: The pull mean and width and impacts from pseudo-data (left) and measured (right) when using only m_W^{reco} as observable.

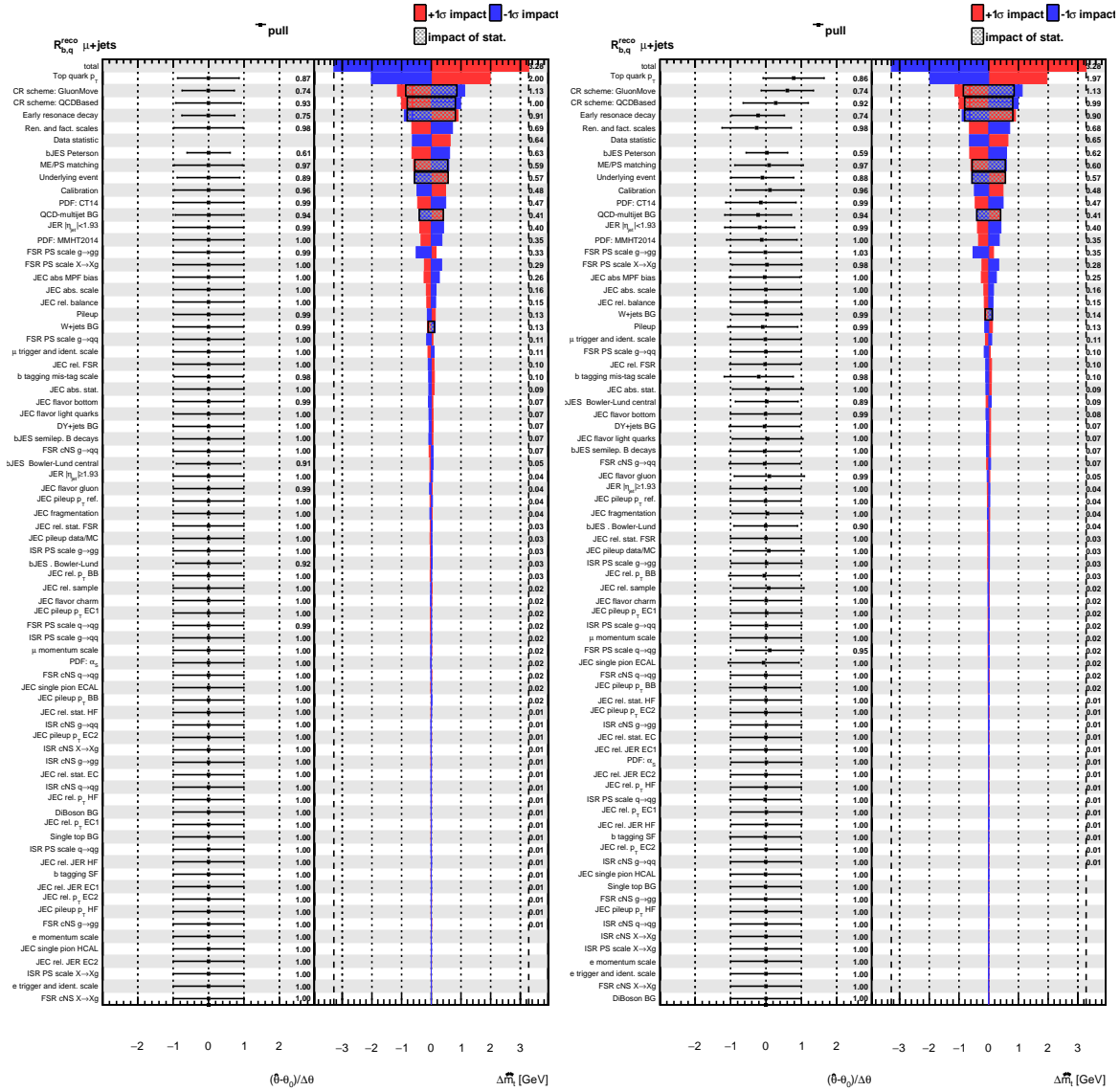


Figure C.4.: Muon+jets: The pull mean and width and impacts from pseudo-data (left) and measured (right) when using only R_{bq}^{reco} as observable.

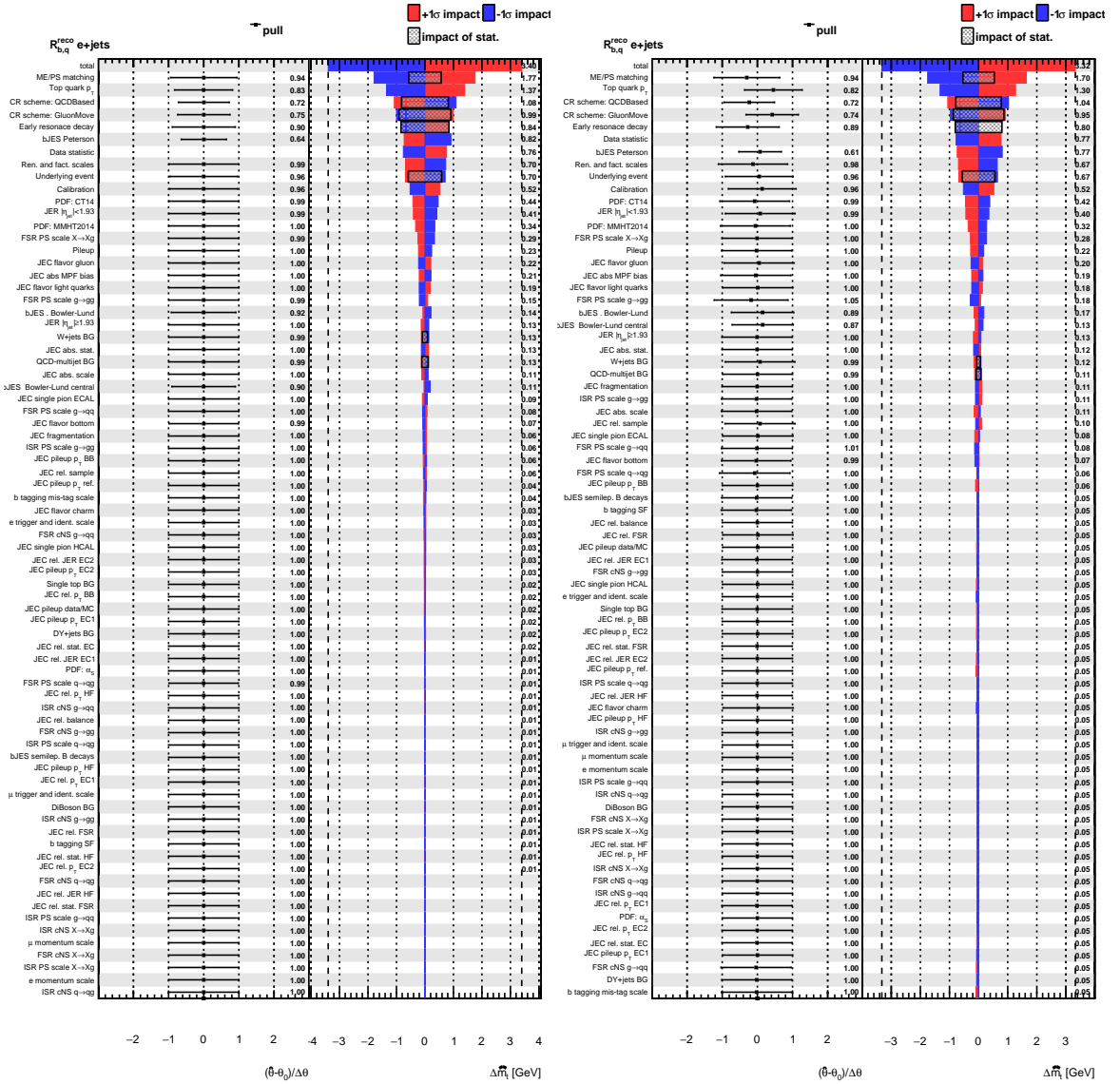


Figure C.5.: Electron+jets: The pull mean and width and impacts from pseudo-data (left) and measured (right) when using only R_{bq}^{reco} as observable.

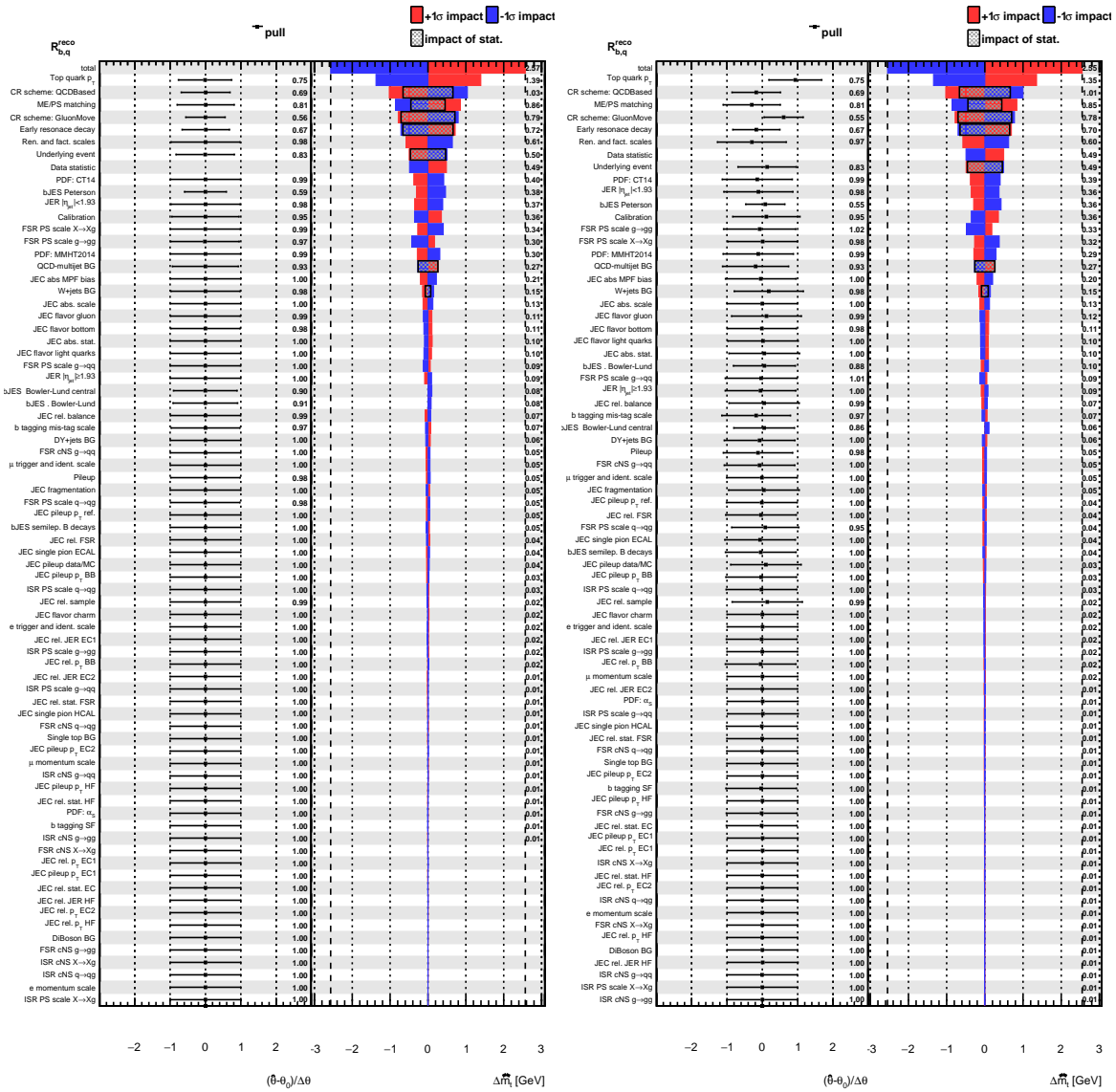


Figure C.6.: Lepton+jets: The pull mean and width and impacts from pseudo-data (left) and measured (right) when using only K_{bq}^{reco} as observable.

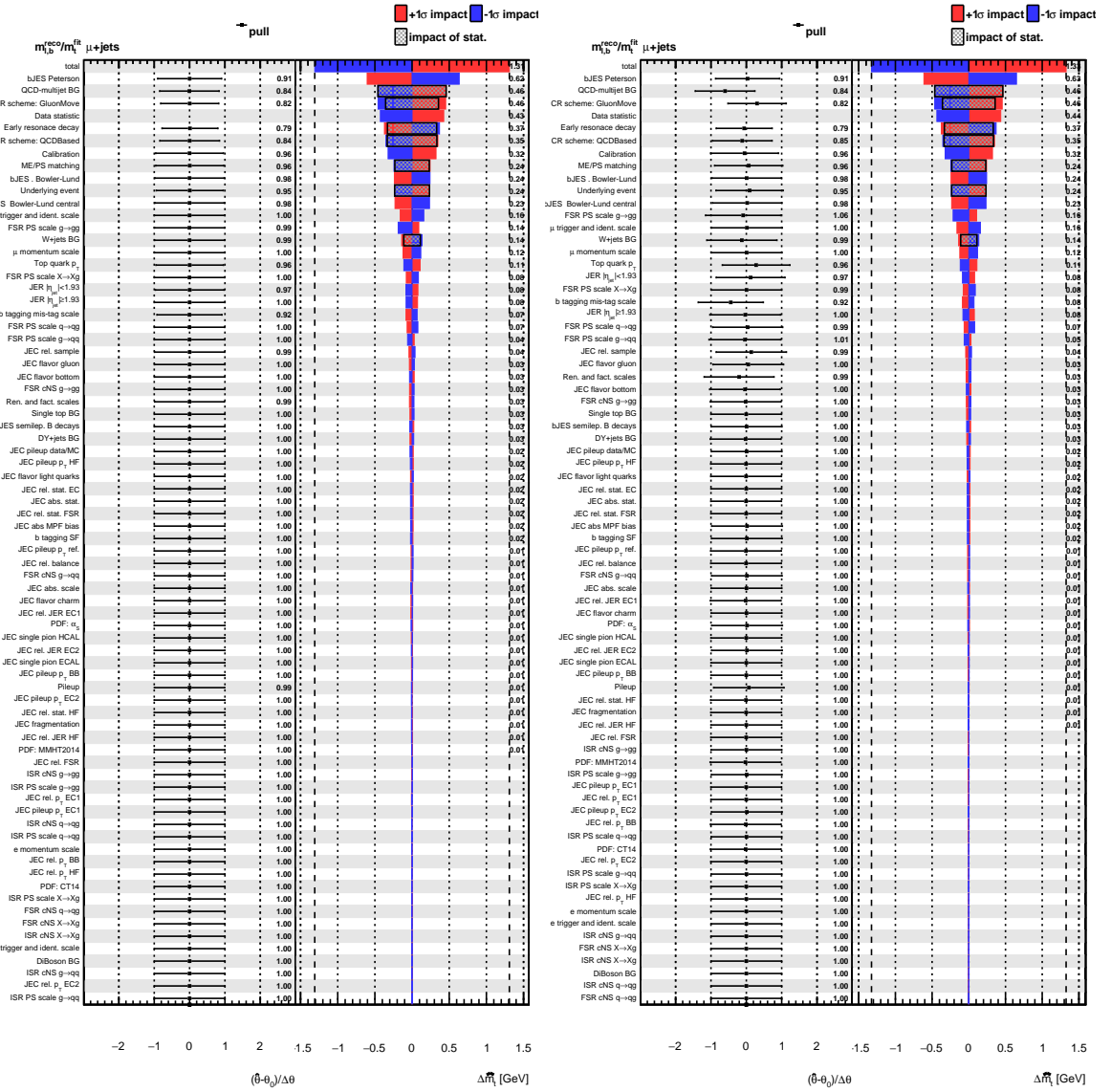


Figure C.7.: Muon+jets: The pull mean and width and impacts from pseudo-data (left) and measured (right) when using only $m_{lb}^{\text{reco}}/m_t^{\text{fit}}$ as observable.

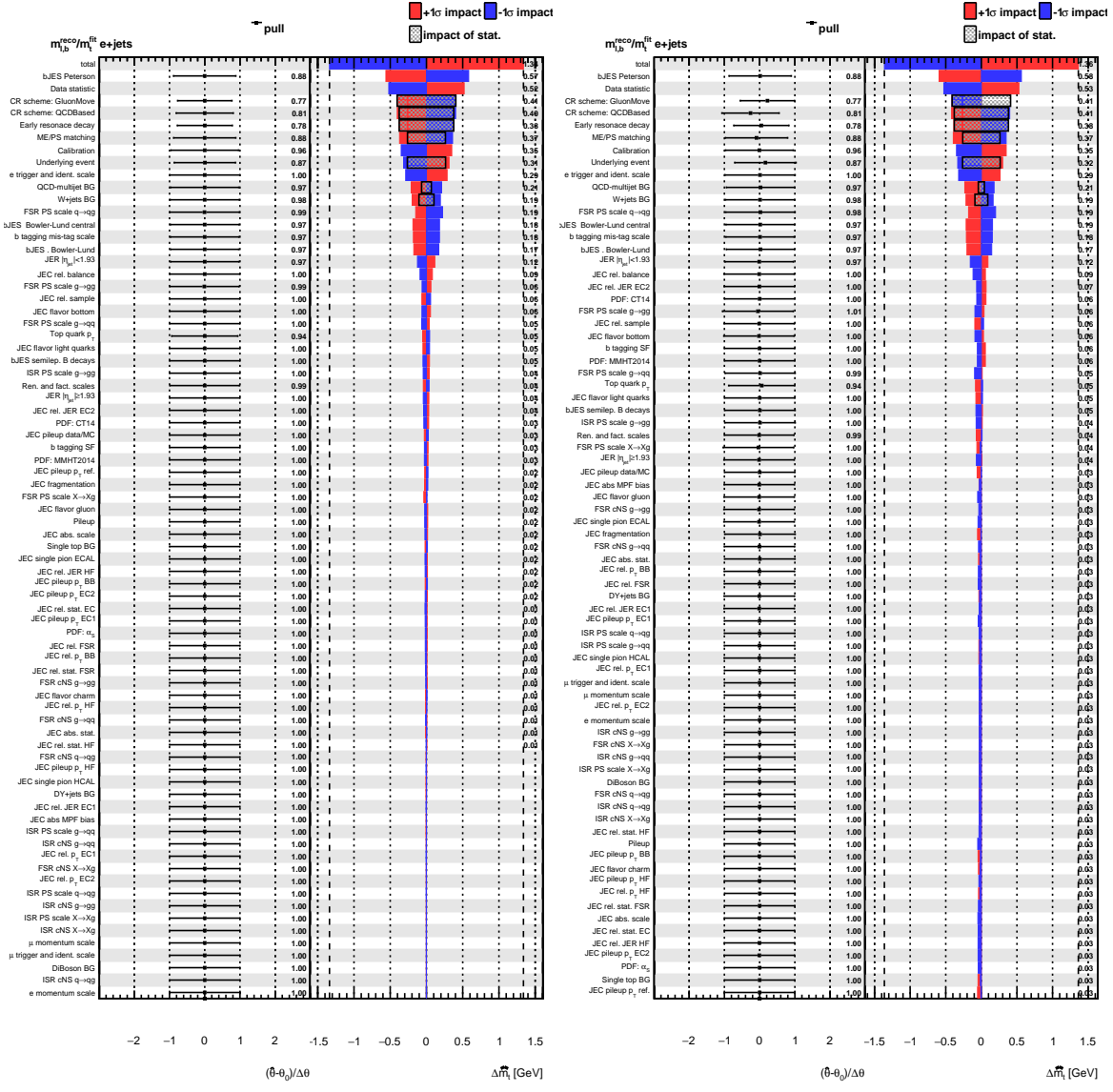


Figure C.8.: Electron+jets: The pull mean and width and impacts from pseudo-data (left) and measured (right) when using only m_{lbred} as observable.

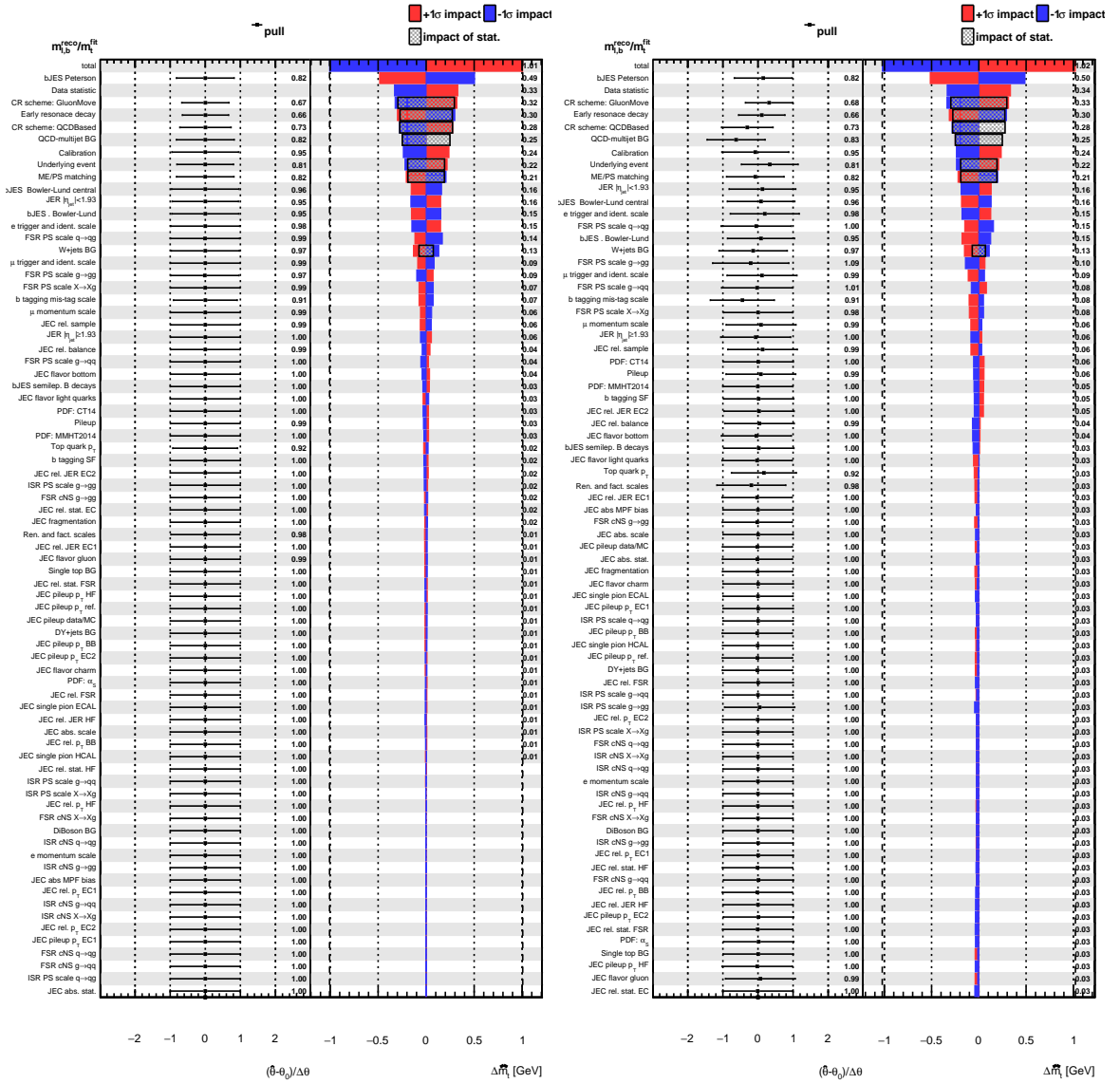


Figure C.9.: Lepton+jets: The pull mean and width and impacts from pseudo-data (left) and measured (right) when using only m_{lb}^{reco}/m_t^{fit} as observable.

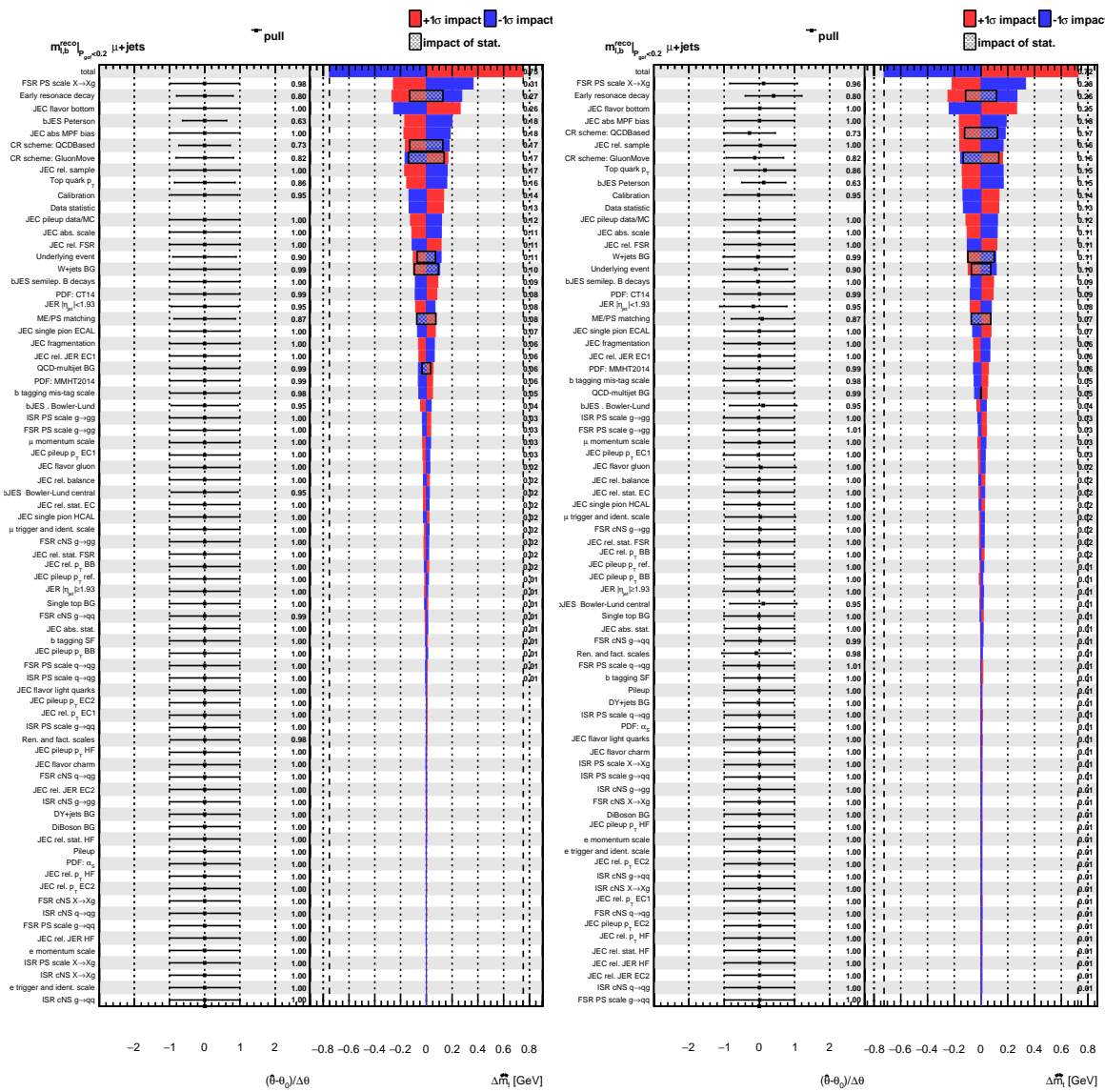


Figure C.10.: Muon+jets: The pull mean and width and impacts from pseudo-data (left) and measured (right) when using only $m_{lb}^{reco} |_{P_{tot} < 0.2}$ as observable.

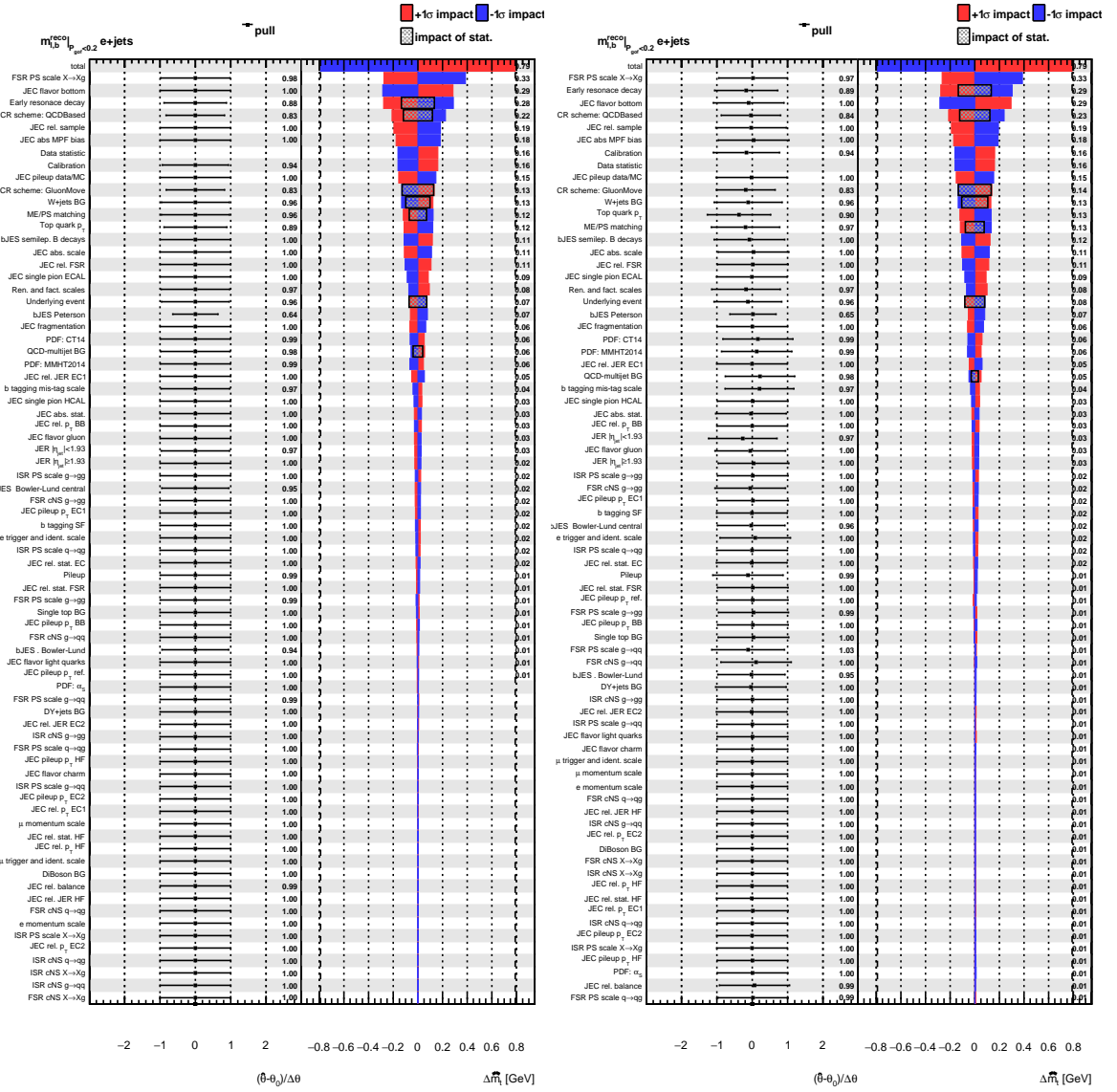


Figure C.11.: Electron+jets: The pull mean and width and impacts from pseudo-data (left) and measured (right) when using only $m_{lb}^{reco} |_{P_{gof} < 0.2}$ as observable.

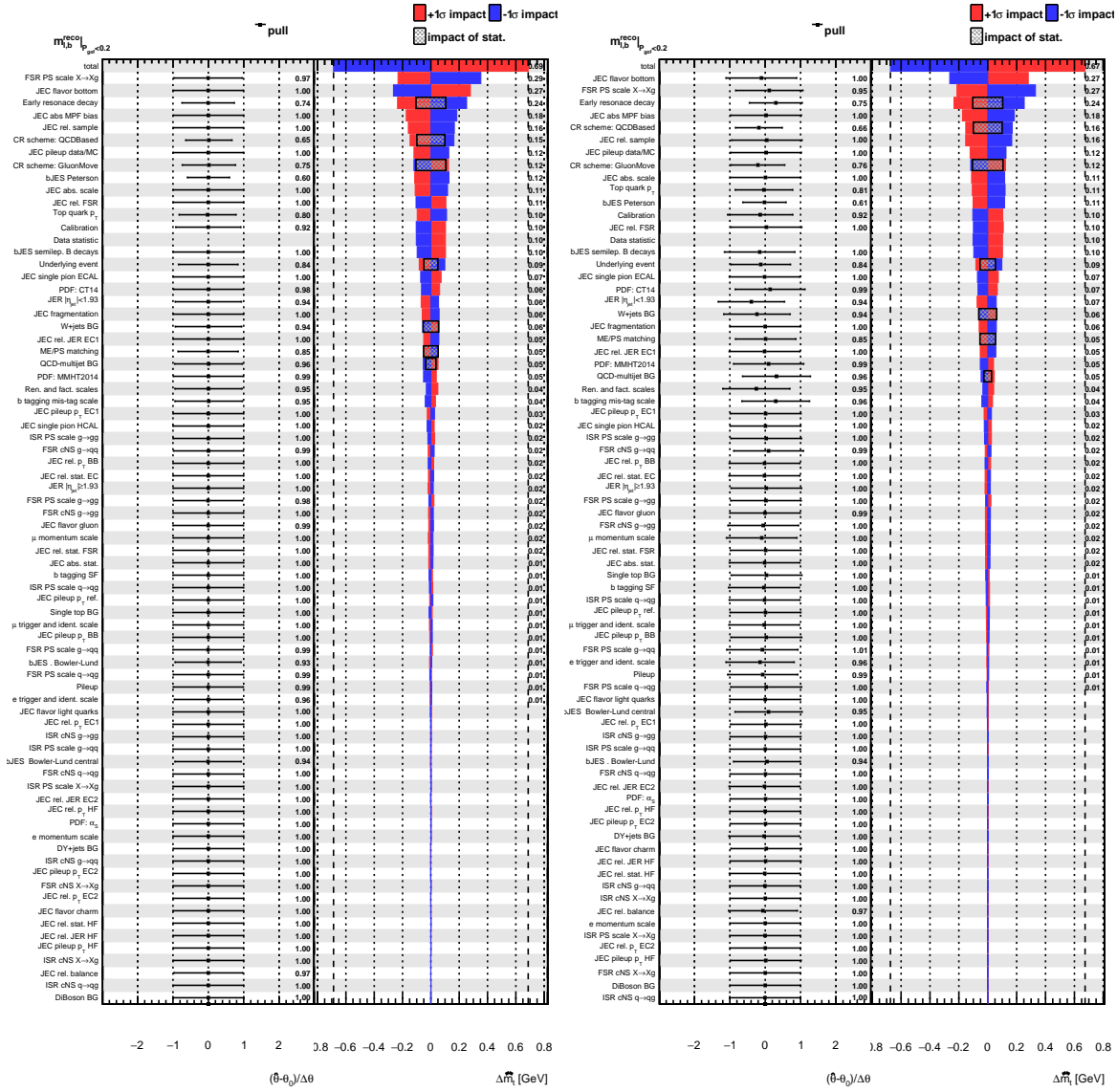


Figure C.12.: Lepton+jets: The pull mean and width and impacts from pseudo-data (left) and measured (right) when using only $m_{lb}^{reco}|_{P_{gof}<0.2}$ as observable.

C.2. Full nuisance impacts for different observable selections

In this section the full lists of predicted impacts from pseudo-experiments (left plots) and measured nuisance parameters and impacts with blinded m_t value (right plots) for different observable and lepton inclusions are shown. The full final predicted uncertainty and its impacts from the all considered uncertainty sources is shown in fig.C.25. The nuisances are sorted by their predicted impact. If no impact value is shown the value is below 0.005 GeV. Each prediction is averaged from more than 200 pseudo-experiment sets, each corresponding to the full expected data statistic.

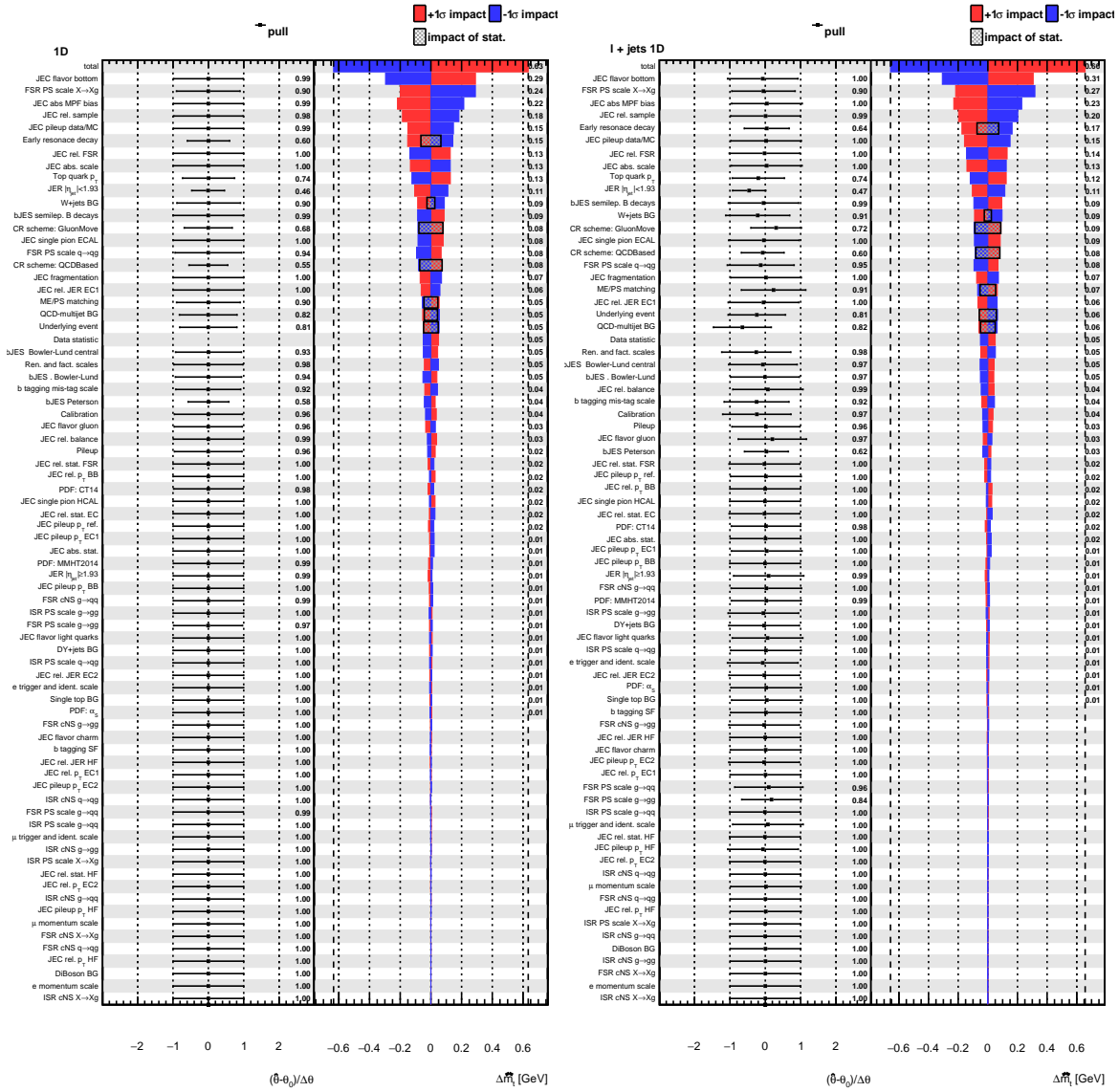


Figure C.13.: Lepton+jets: Uncertainty nuisance impacts and pulls when using m_t^{fit} as observable from pseudo-data (left) and measured (right).

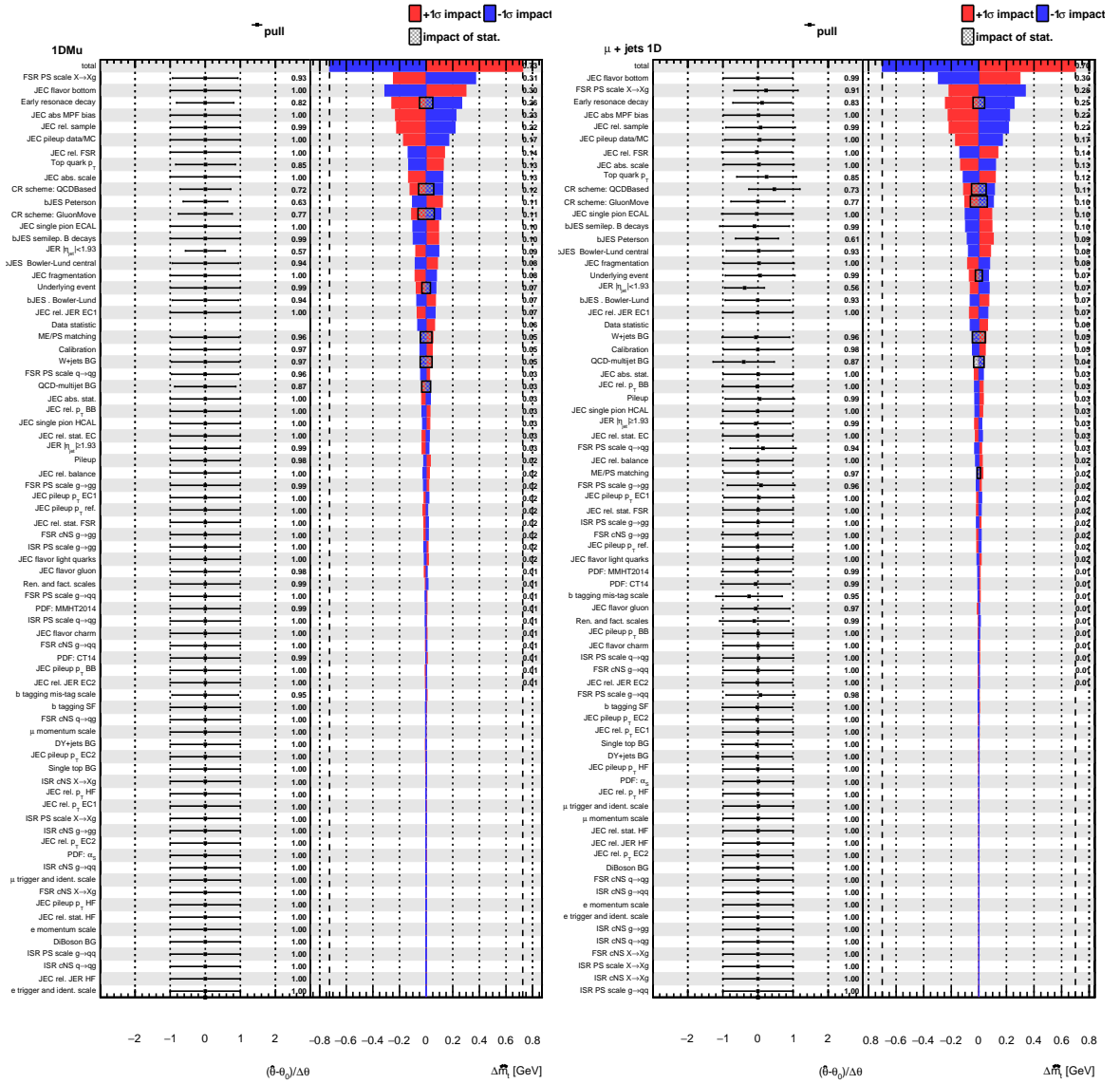


Figure C.14.: Muon+jets: Uncertainty nuisance impacts and pulls when using m_t^{fit} as observable from pseudo-data (left) and measured (right).

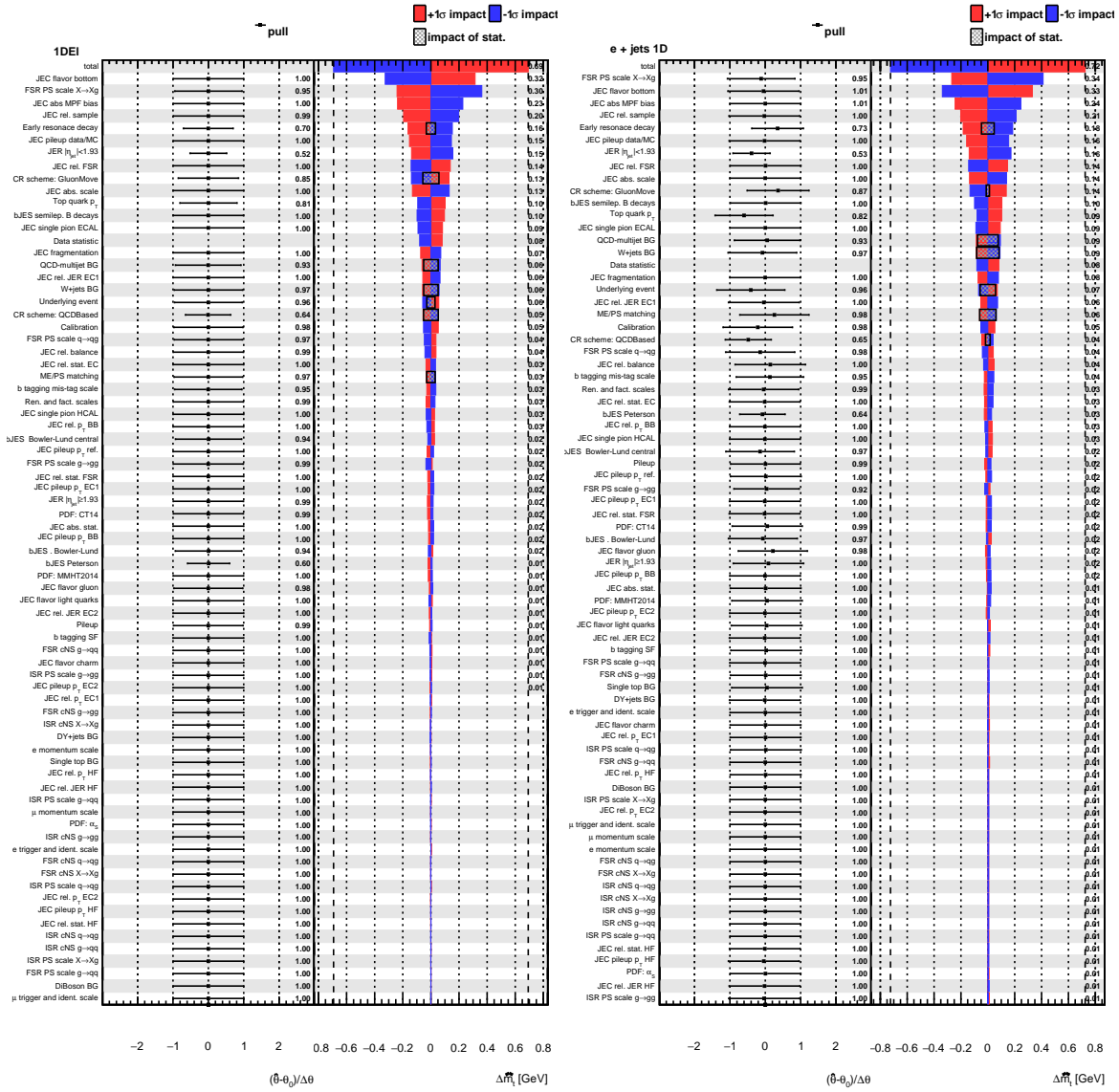


Figure C.15.: Electron+jets: Uncertainty nuisance impacts and pulls when using m_t^{fit} as observable from pseudo-data (left) and measured (right).

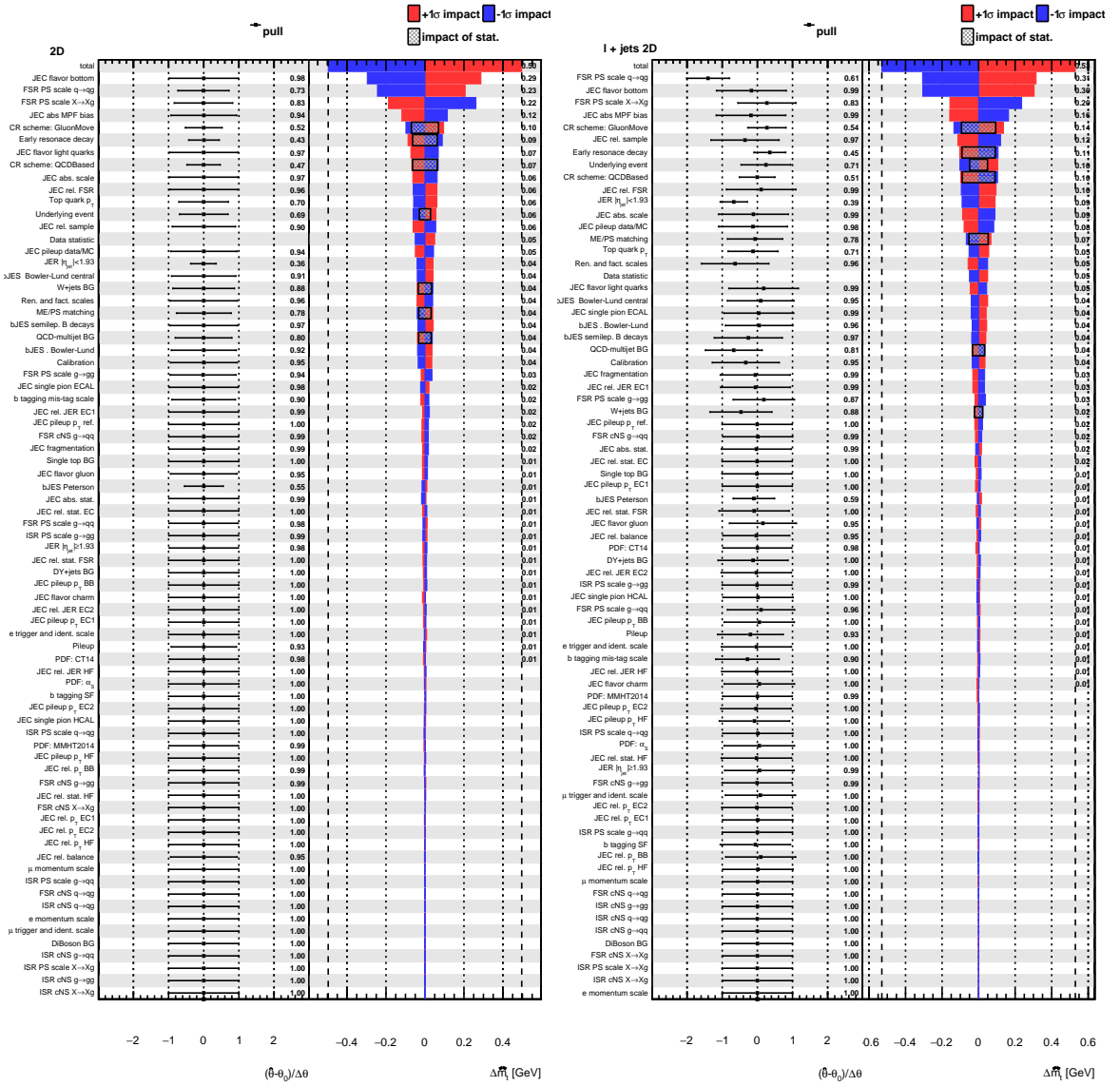


Figure C.16.: Lepton+jets: Uncertainty nuisance impacts and pulls when using m_t^{fit} and m_W^{reco} as observable from pseudo-data (left) and measured (right).

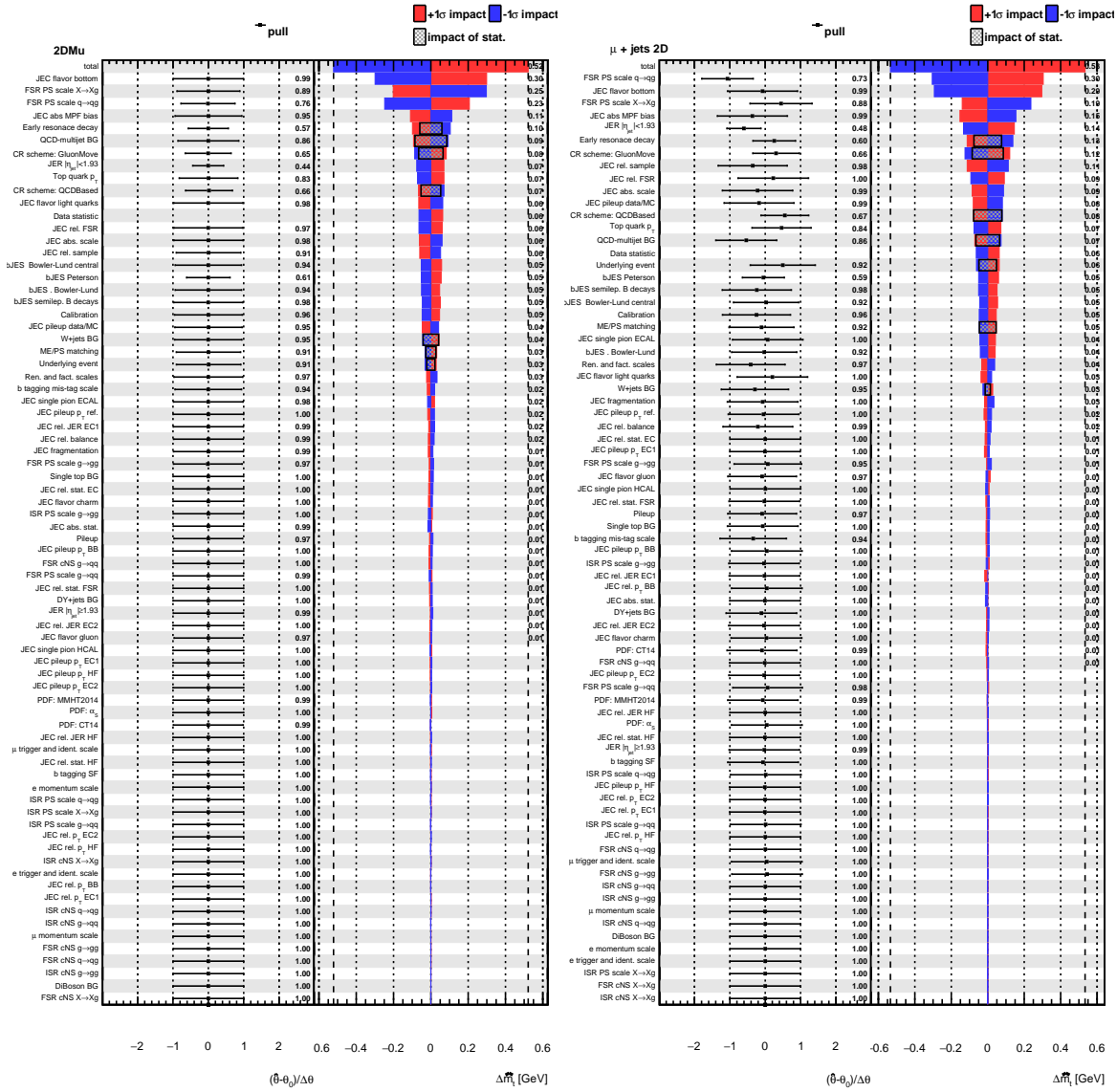


Figure C.17.: Muon+jets: Uncertainty nuisance impacts and pulls when using m_t^{fit} and m_W^{reco} as observable from pseudo-data (left) and measured (right).

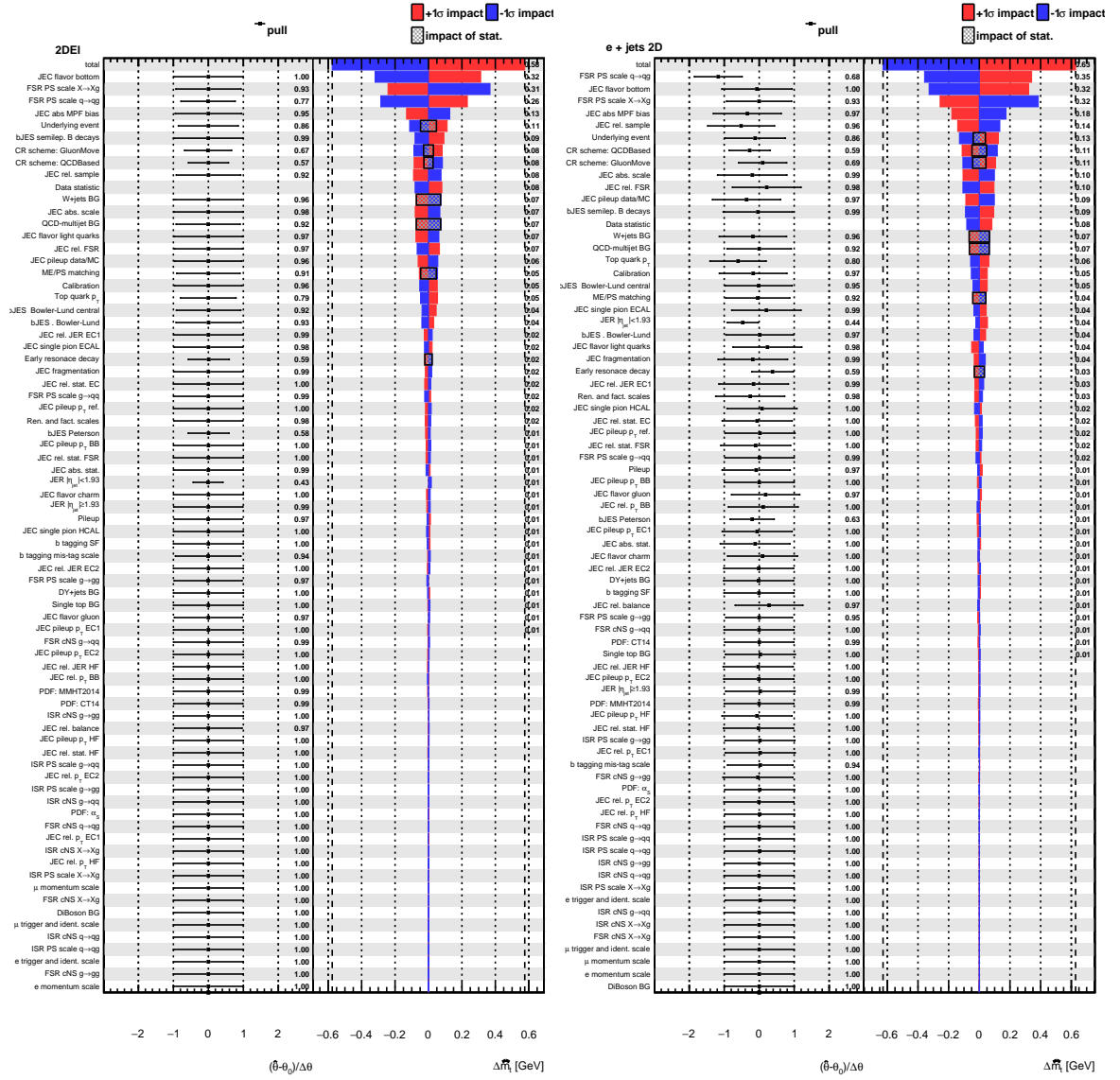


Figure C.18.: Electron+jets: Uncertainty nuisance impacts and pulls when using m_t^{fit} and m_W^{reco} as observable from pseudo-data (left) and measured (right).

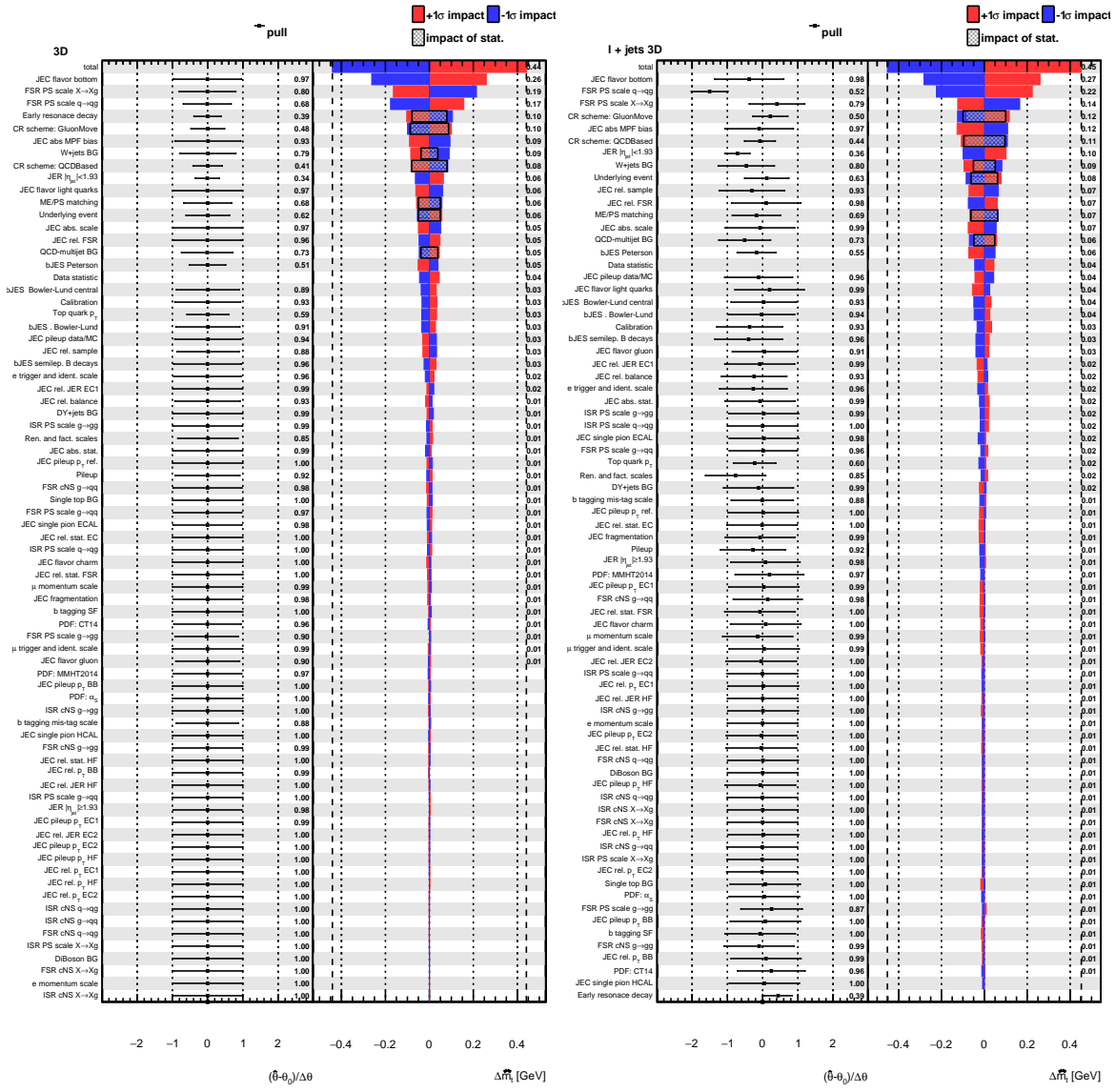


Figure C.19.: Lepton+jets: Uncertainty nuisance impacts and pulls when using m_t^{fit} , m_W^{reco} and $m_{cb}^{\text{reco}} |_{P_{\text{gof}} < 0.2}$ as observable from pseudo-data (left) and measured (right).

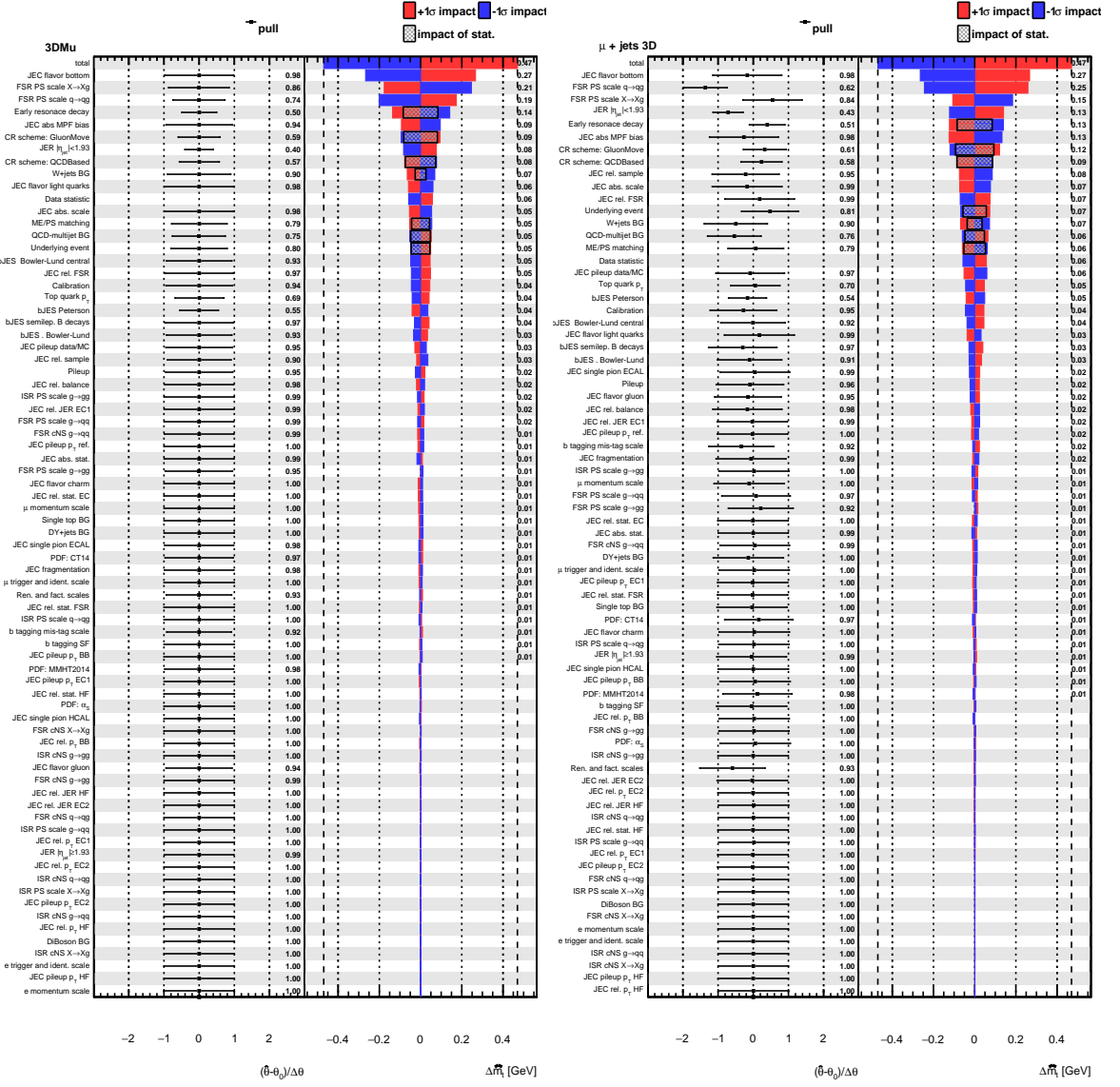


Figure C.20.: Muon+jets: Uncertainty nuisance impacts and pulls when using m_t^{fit} , m_W^{reco} and $m_{\text{lb}}^{\text{reco}} |_{P_{\text{gof}} < 0.2}$ as observable from pseudo-data (left) and measured (right).

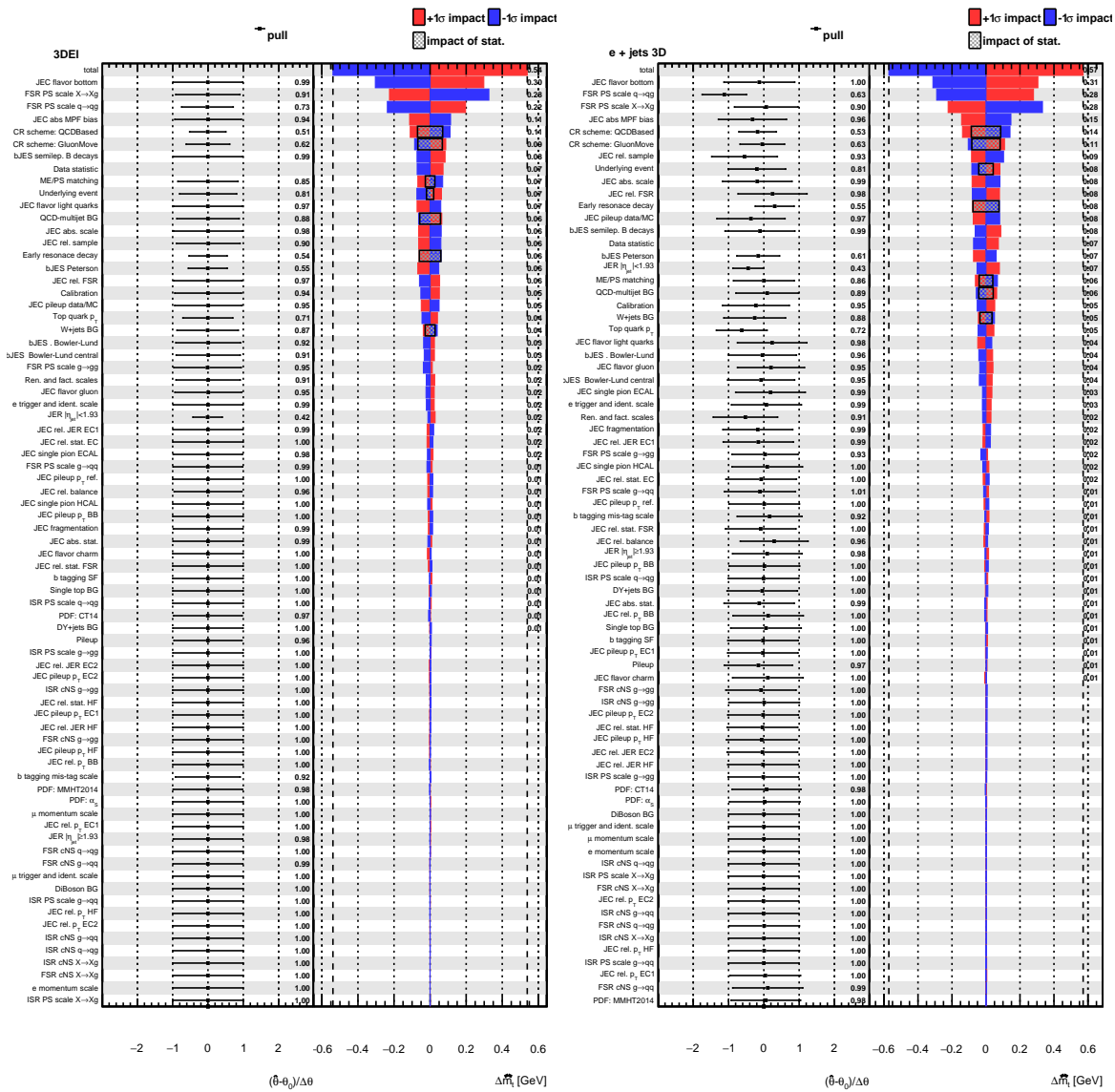


Figure C.21.: Electron+jets: Uncertainty nuisance impacts and pulls when using m_t^{fit} , m_W^{reco} and $m_{cb}^{\text{reco}}|_{P_{\text{gof}} < 0.2}$ as observable from pseudo-data (left) and measured (right).

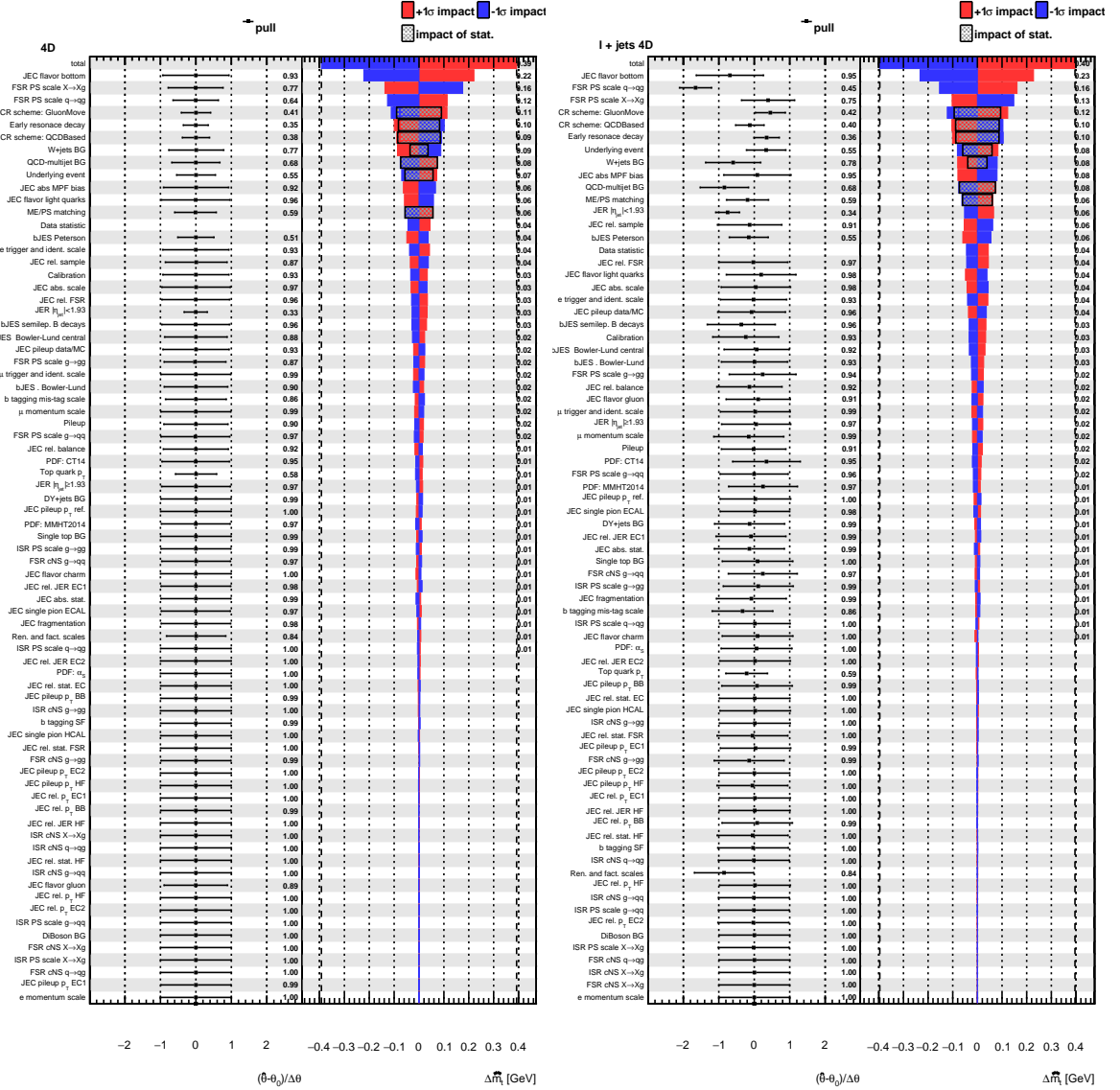


Figure C.22.: Lepton+jets: Uncertainty nuisance impacts and pulls when using m_{ℓ}^{fit} , $m_{\text{W}}^{\text{reco}}$, $m_{\ell, \text{b}}^{\text{red}}$ and $m_{\ell, \text{b}}^{\text{reco}} |_{P_{\text{gof}} < 0.2}$ as observable from pseudo-data (left) and measured (right).

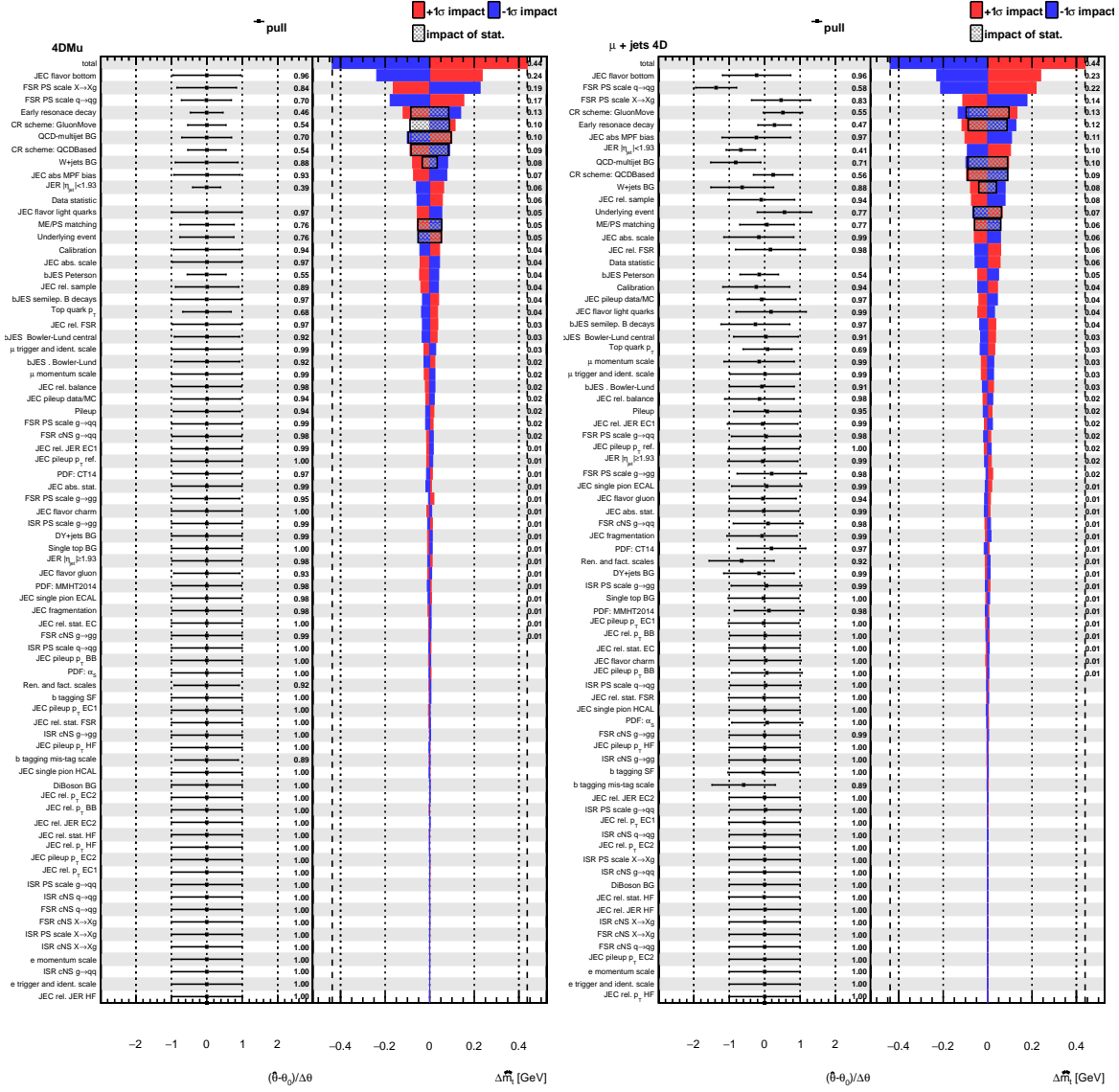


Figure C.23.: Muon+jets: Uncertainty nuisance impacts and pulls when using m_t^{fit} , m_W^{reco} , $m_{l,b}^{\text{red}}$ and $m_{lb}^{\text{reco}}|_{P_{\text{gof}} < 0.2}$ as observable from pseudo-data (left) and measured (right).

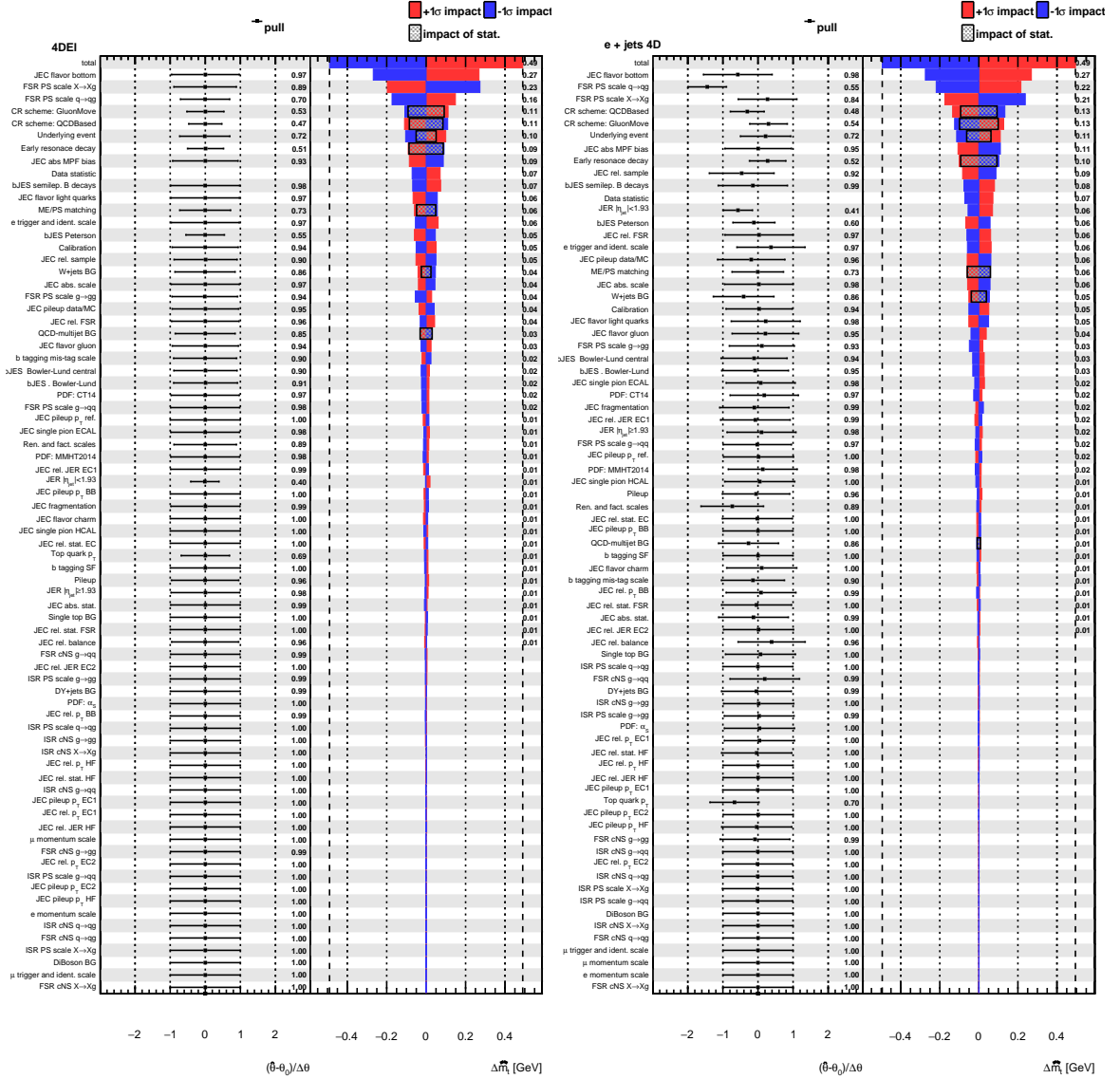


Figure C.24.: Electron+jets: Uncertainty nuisance impacts and pulls when using m_t^{fit} , m_W^{reco} , $m_{cb}^{\text{reco}}/m_t^{\text{fit}}$ and $m_{cb}^{\text{reco}}|_{P_{\text{gof}} < 0.2}$ as observable from pseudo-data (left) and measured (right).

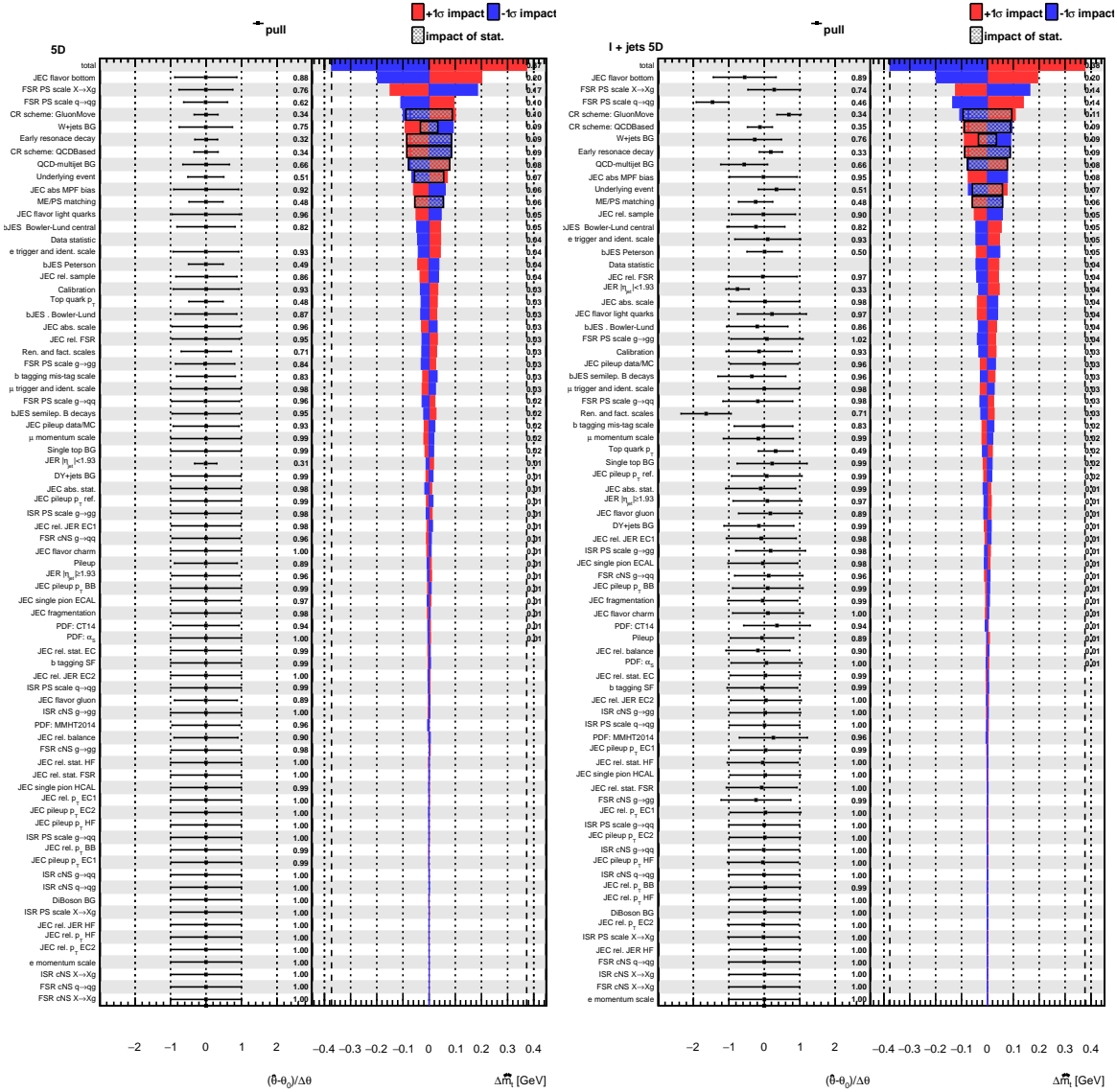


Figure C.25.: Lepton+jets: Uncertainty nuisance impacts and pulls when using m_t^{fit} , m_W^{reco} , $m_{\ell b}^{\text{reco}}/m_t^{\text{fit}}$, $m_{\ell b}^{\text{reco}}|_{P_{\text{gof}} < 0.2}$ and $R_{\text{bq}}^{\text{reco}}$ as observable from pseudo-data (left) and measured (right).

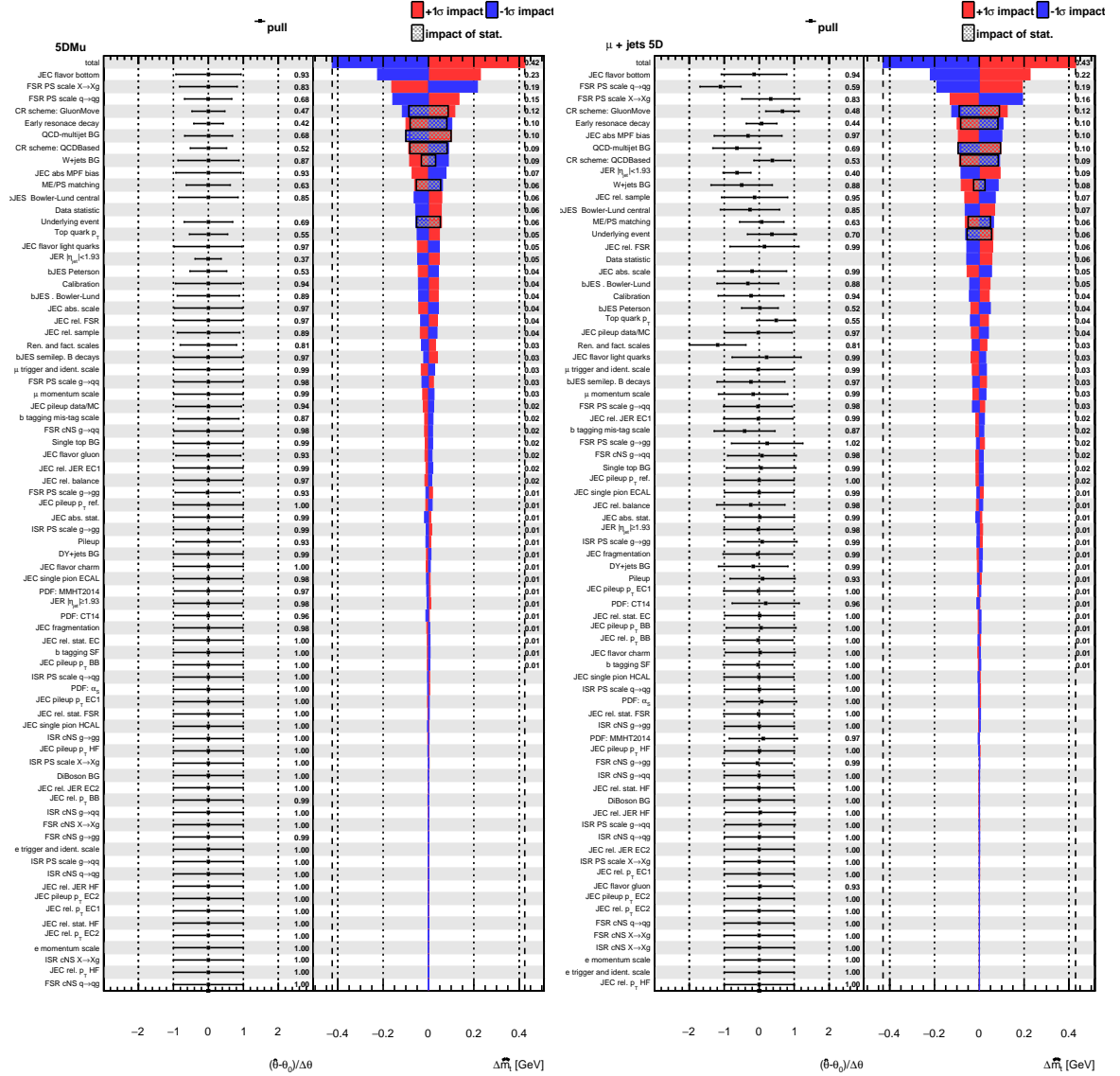


Figure C.26.: Muon+jets: Uncertainty nuisance impacts and pulls when using m_t^{fit} , m_W^{reco} , $m_{\ell b}^{\text{reco}}/m_t^{\text{fit}}$, $m_{\ell b}^{\text{reco}}|_{P_{\text{gof}} < 0.2}$ and $R_{\text{bq}}^{\text{reco}}$ as observable from pseudo-data (left) and measured (right).

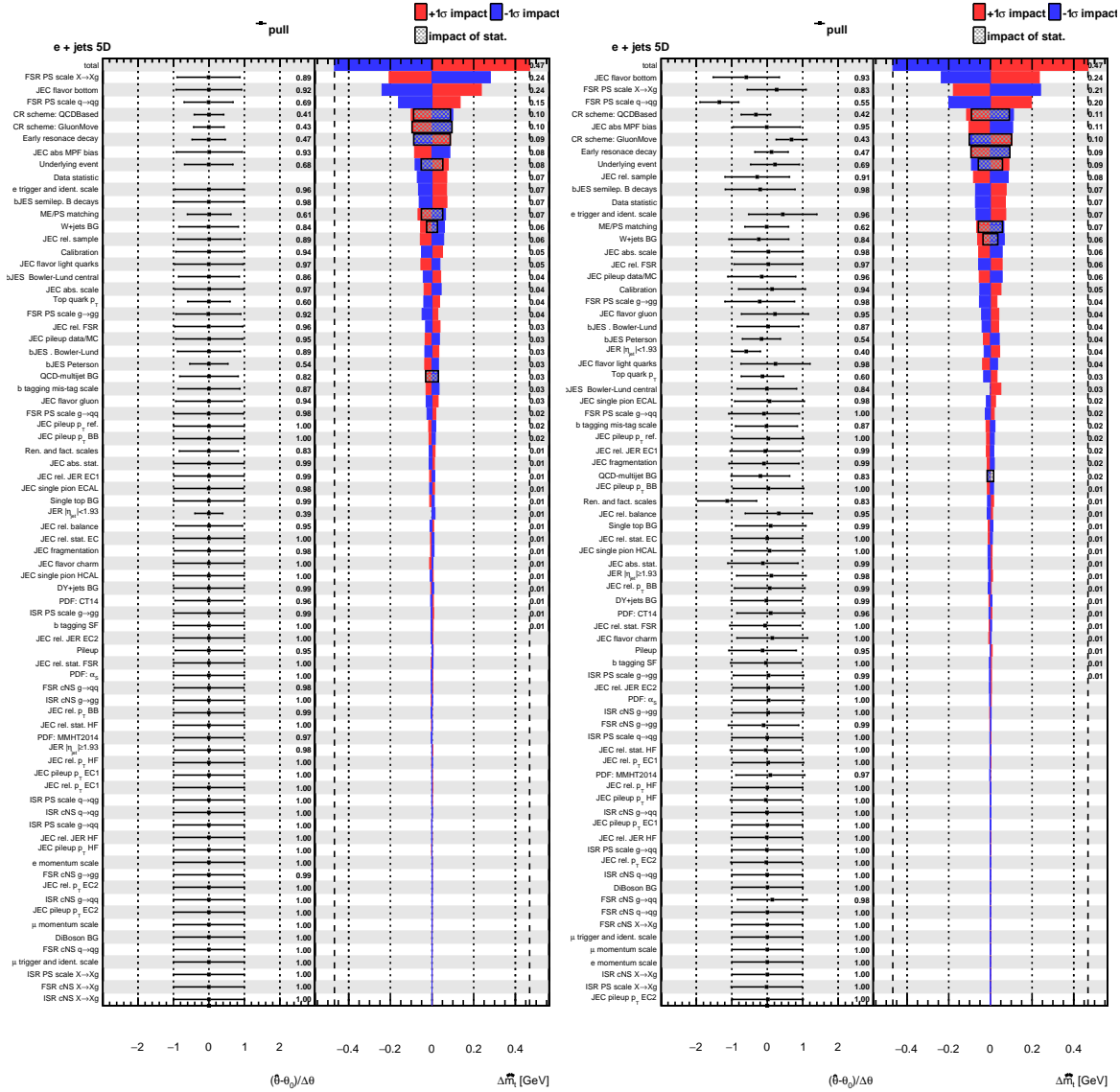


Figure C.27.: Electron+jets: Uncertainty nuisance impacts and pulls when using m_t^{fit} , m_W^{reco} , $m_{\ell b}^{\text{reco}} / m_t^{\text{fit}}$, $m_{\ell b}^{\text{reco}} |_{P_{\text{gof}} < 0.2}$ and $R_{\text{bq}}^{\text{reco}}$ as observable from pseudo-data (left) and measured (right).

D. Additional model controlplots

D.1. Single Nuisance Closure

In this section the closure for single nuisances is checked. For each uncertainty source the likelihood is fit to pseudo-experiments where the corresponding uncertainty is varied up or down corresponding to a nuisance value of ± 1 . For this fit only this nuisance is left free and it can be seen that its value can be reproduced by the parameterization of the observable distributions. Each point is the mean extracted nuisance value from >3000 pseudo-experiment sets (each corresponding to the statistic expected in data) and the plotted error bar is the predicted mean error on the nuisance value. The red line are is a fitted line through this points and the red band is the 1σ confidence interval of the fit as returned by the Root `TVirtualFitter` (therefore scaled by χ^2/ndof). The upper row of each figures shows this check when including all observables, the lower rows show the check for the same nuisances when only using m_{τ}^{fit} as observables. All figures are for the muon+jets case.

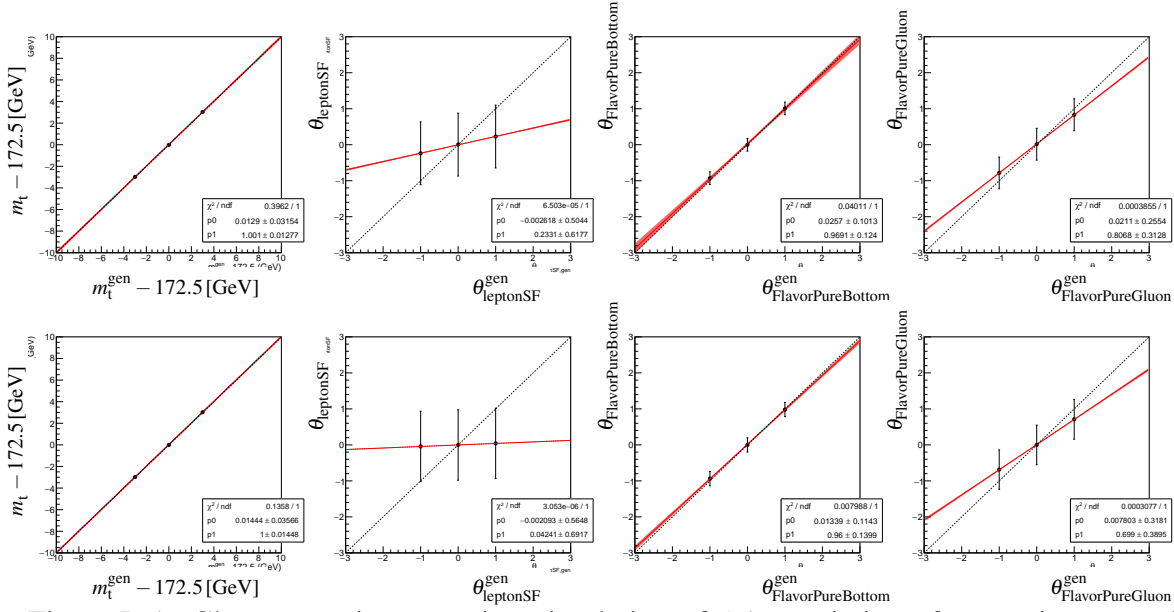


Figure D.1.: Closure test in muon+jets simulation of $\pm 1\sigma$ variation of one nuisance at the time while leaving only the corresponding nuisance free. The observable settings are upper row: 5D, lower row: 1D.

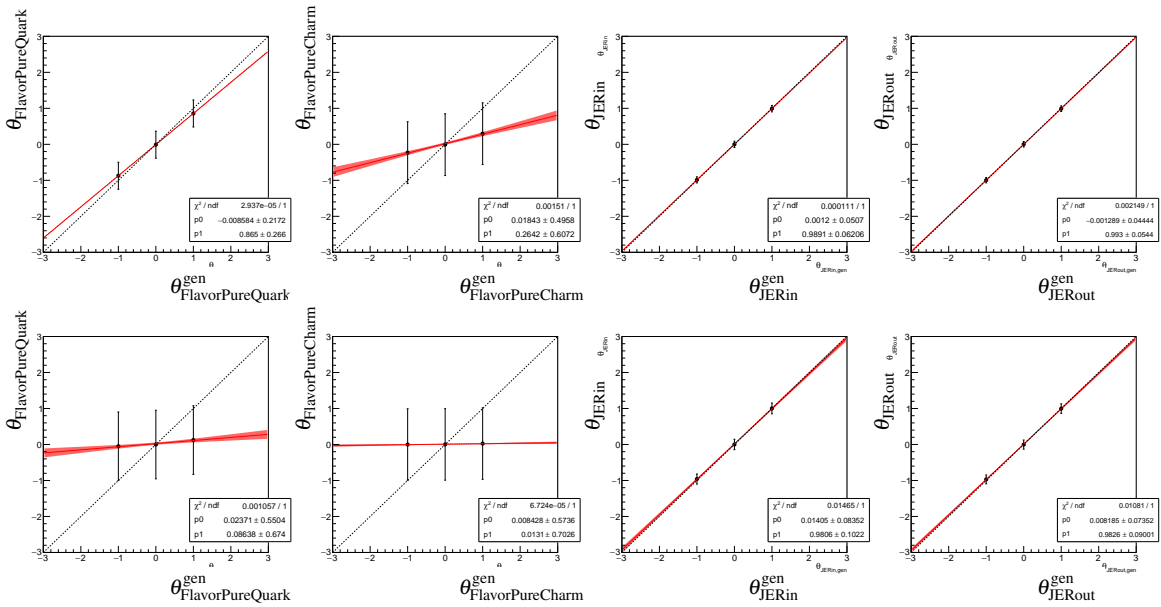


Figure D.2.: Closure test in muon+jets simulation of $\pm 1\sigma$ variation of one nuisance at the time while leaving only the corresponding nuisance free. The observable settings are upper row: 5D, lower row: 1D.

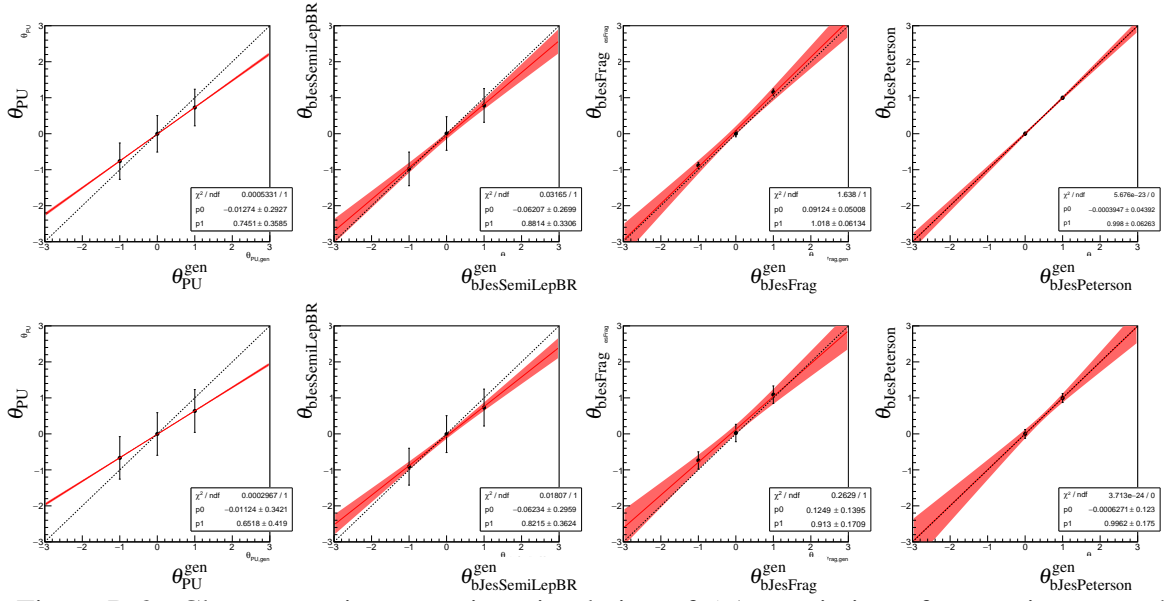


Figure D.3.: Closure test in muon+jets simulation of $\pm 1\sigma$ variation of one nuisance at the time while leaving only the corresponding nuisance free. The observable settings are upper row: 5D, lower row: 1D.

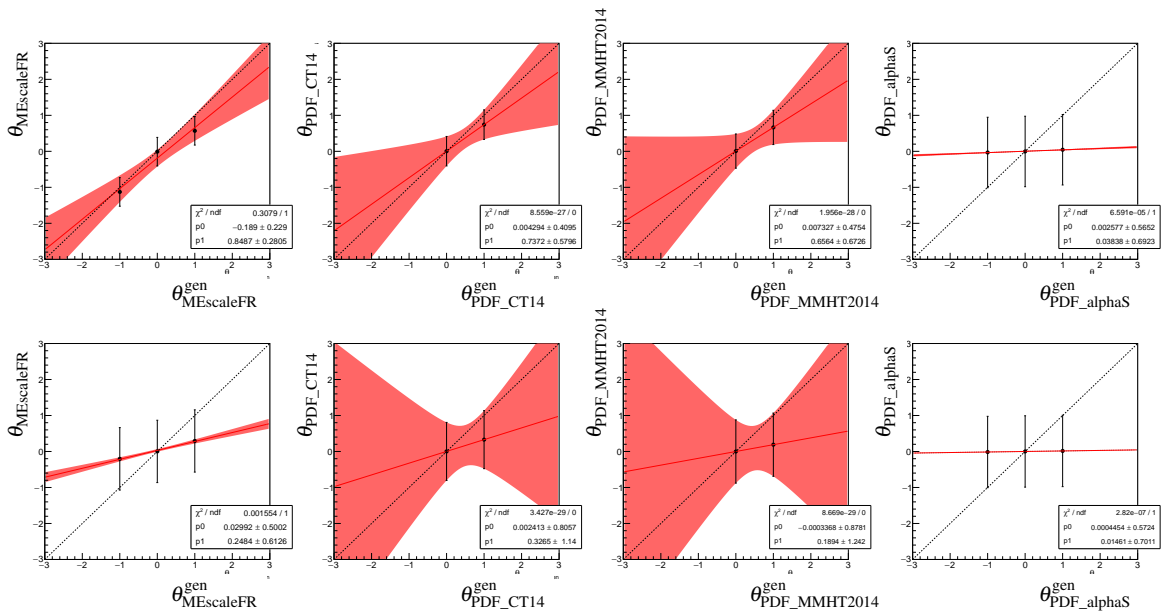


Figure D.4.: Closure test in muon+jets simulation of $\pm 1\sigma$ variation of one nuisance at the time while leaving only the corresponding nuisance free. The observable settings are upper row: 5D, lower row: 1D.

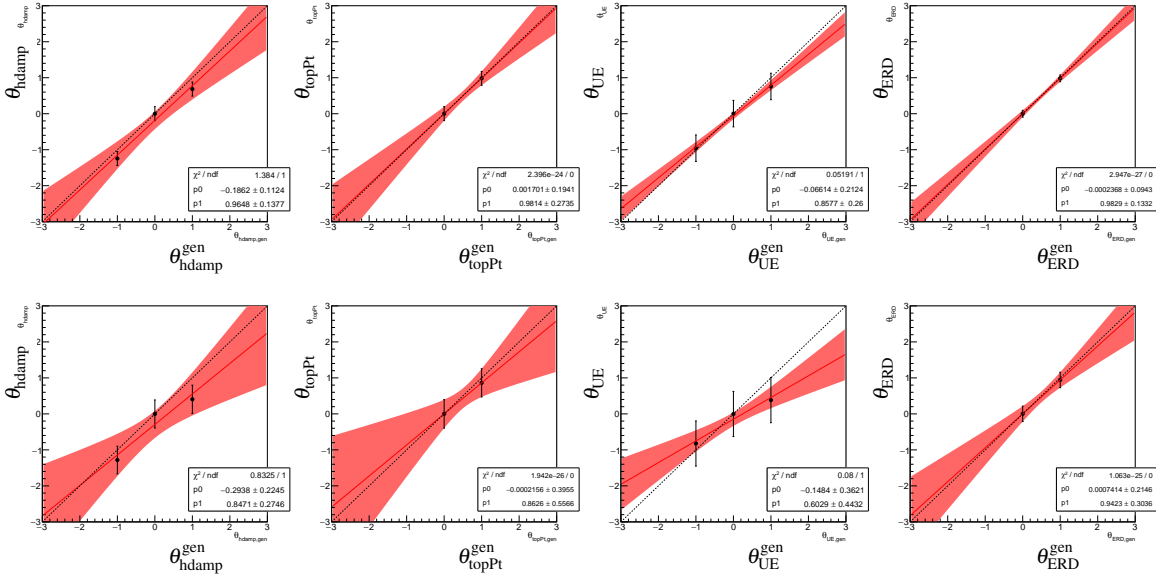


Figure D.5.: Closure test in muon+jets simulation of $\pm 1\sigma$ variation of one nuisance at the time while leaving only the corresponding nuisance free. The observable settings are upper row: 5D, lower row: 1D.

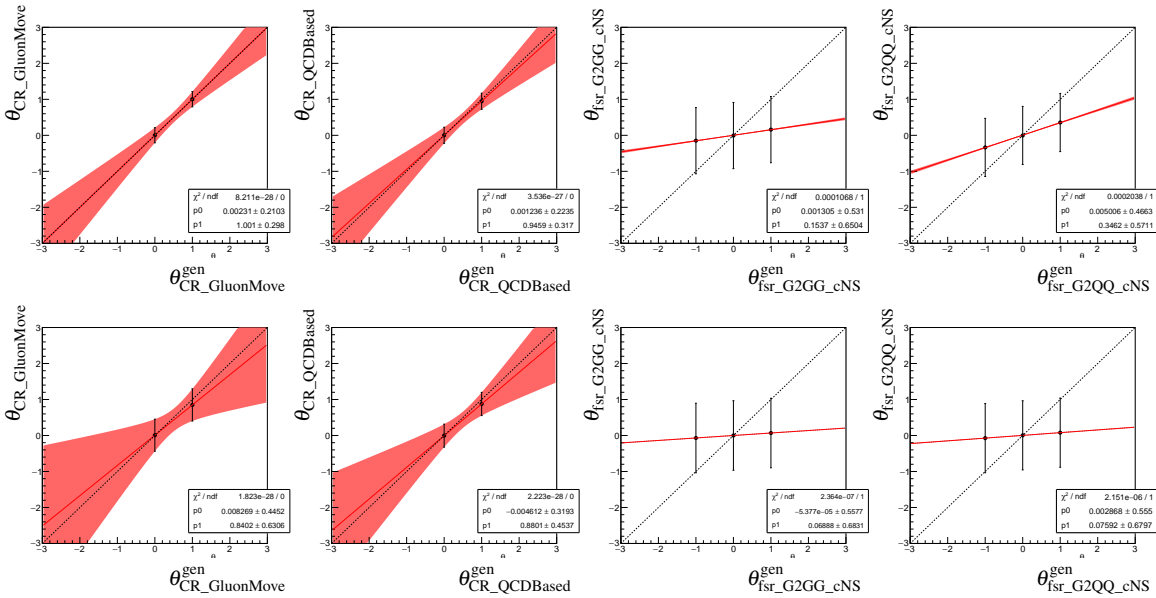


Figure D.6.: Closure test in muon+jets simulation of $\pm 1\sigma$ variation of one nuisance at the time while leaving only the corresponding nuisance free. The observable settings are upper row: 5D, lower row: 1D.

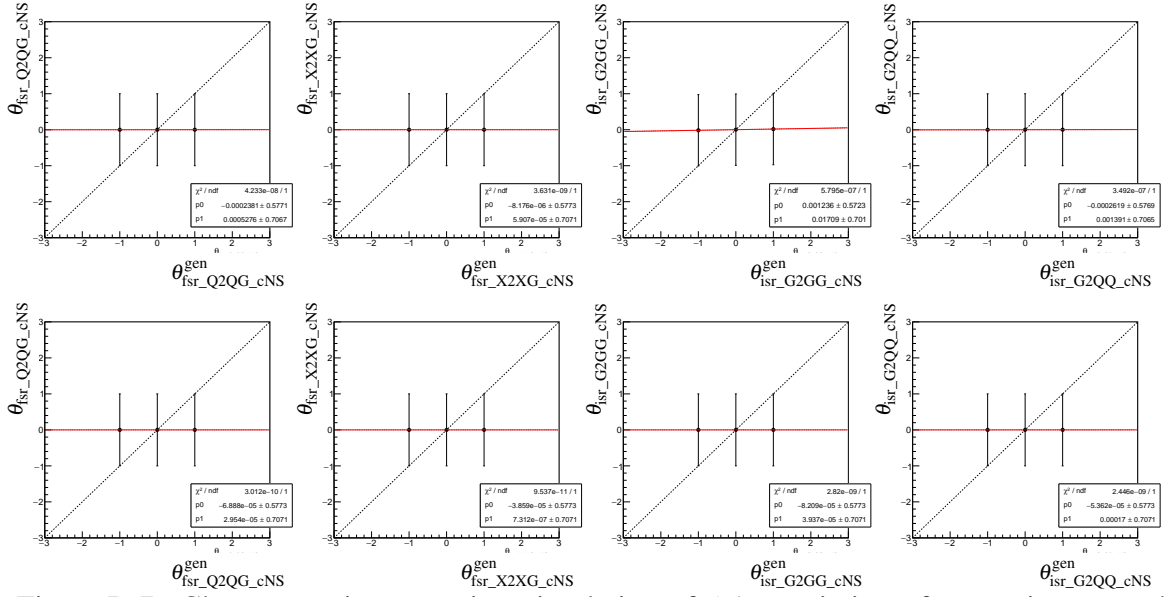


Figure D.7.: Closure test in muon+jets simulation of $\pm 1\sigma$ variation of one nuisance at the time while leaving only the corresponding nuisance free. The observable settings are upper row: 5D, lower row: 1D.

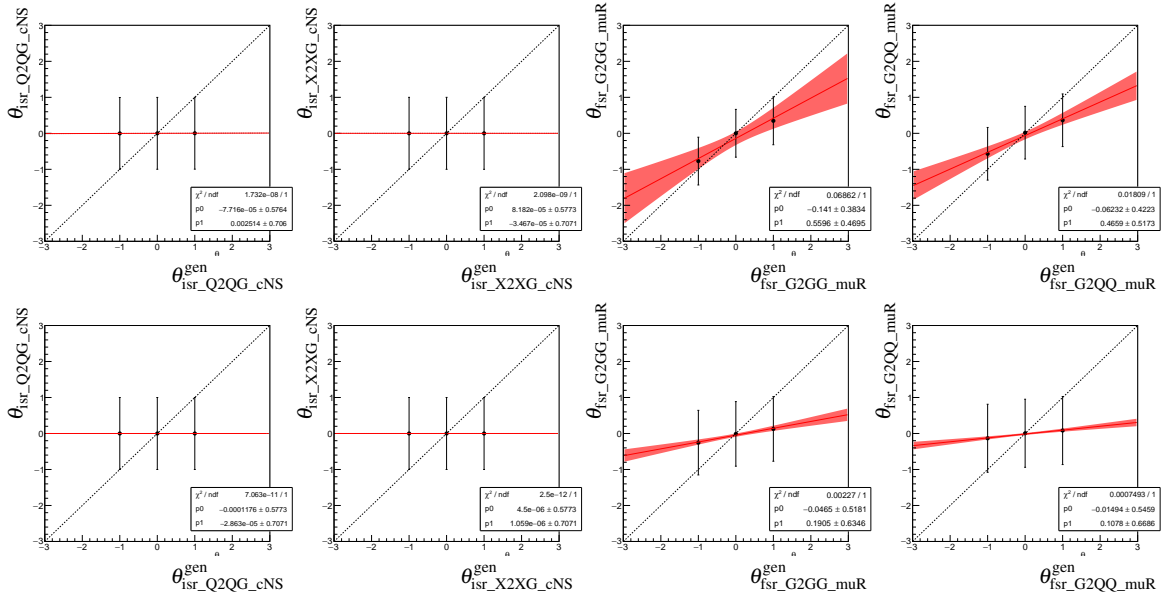


Figure D.8.: Closure test in muon+jets simulation of $\pm 1\sigma$ variation of one nuisance at the time while leaving only the corresponding nuisance free. The observable settings are upper row: 5D, lower row: 1D.

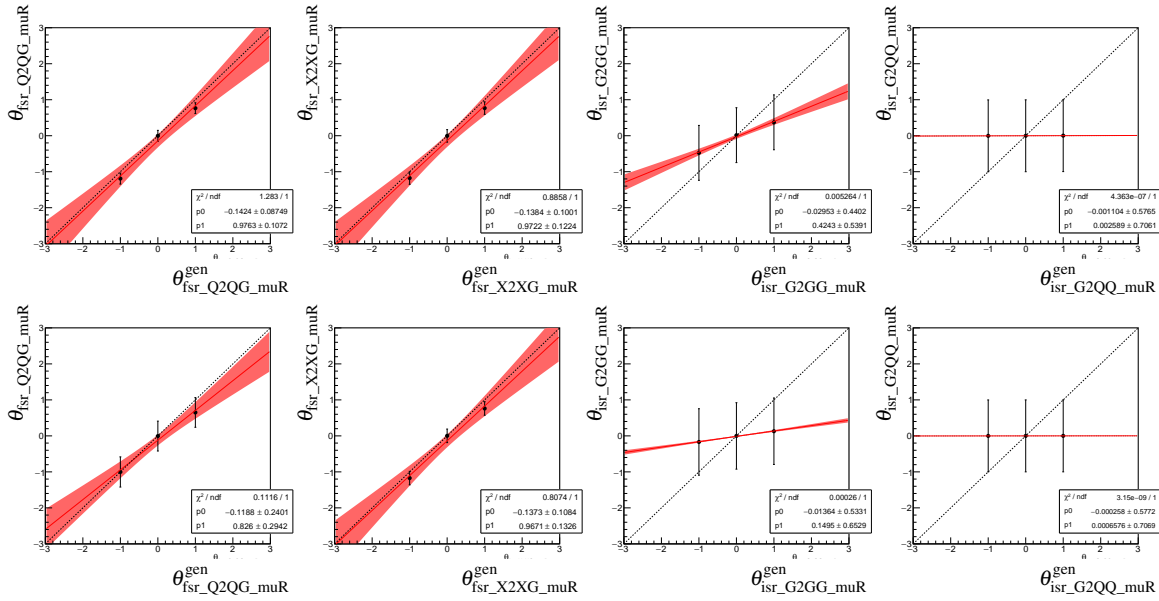


Figure D.9.: Closure test in muon+jets simulation of $\pm 1\sigma$ variation of one nuisance at the time while leaving only the corresponding nuisance free. The observable settings are upper row: 5D, lower row: 1D.

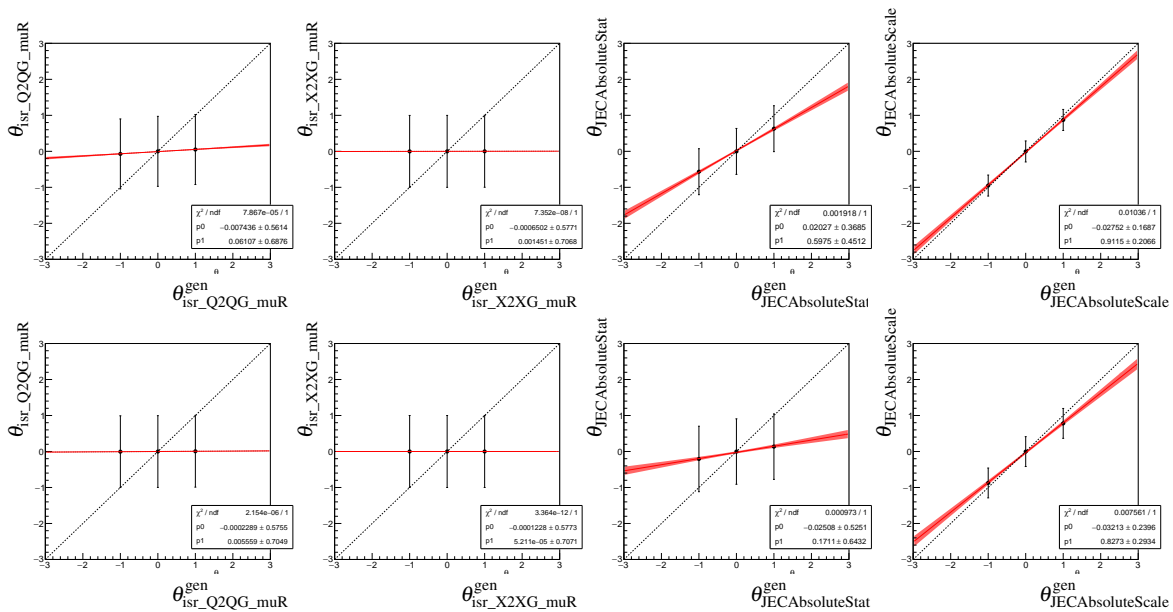


Figure D.10.: Closure test in muon+jets simulation of $\pm 1\sigma$ variation of one nuisance at the time while leaving only the corresponding nuisance free. The observable settings are upper row: 5D, lower row: 1D.

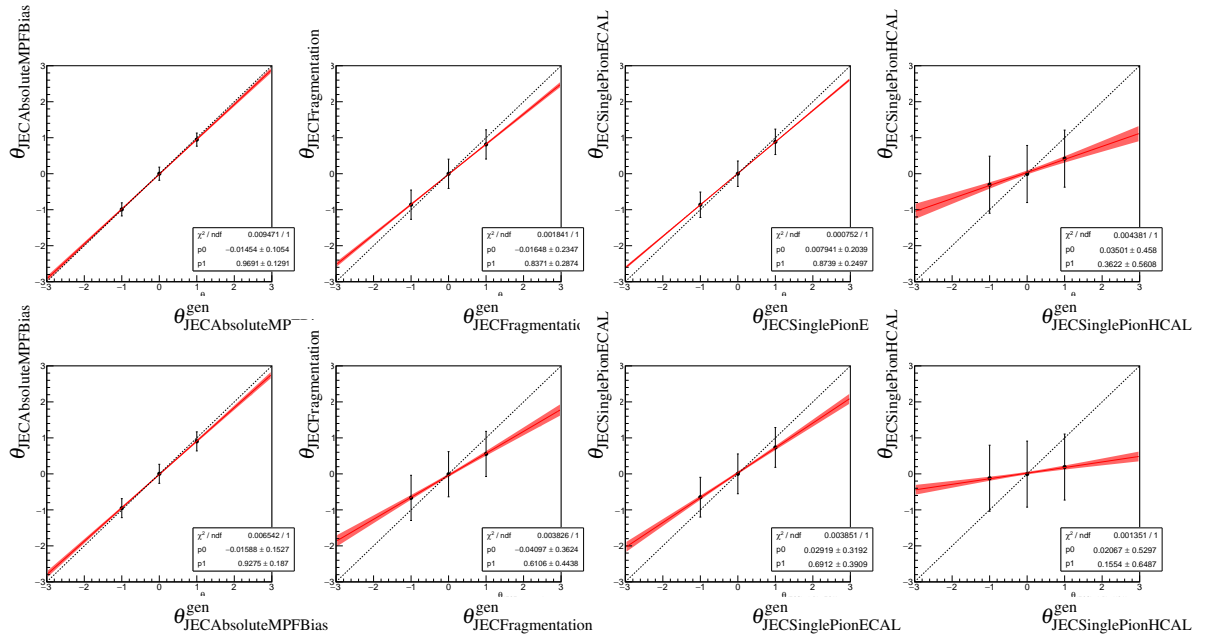


Figure D.11.: Closure test in muon+jets simulation of $\pm 1\sigma$ variation of one nuisance at the time while leaving only the corresponding nuisance free. The observable settings are upper row: 5D, lower row: 1D.

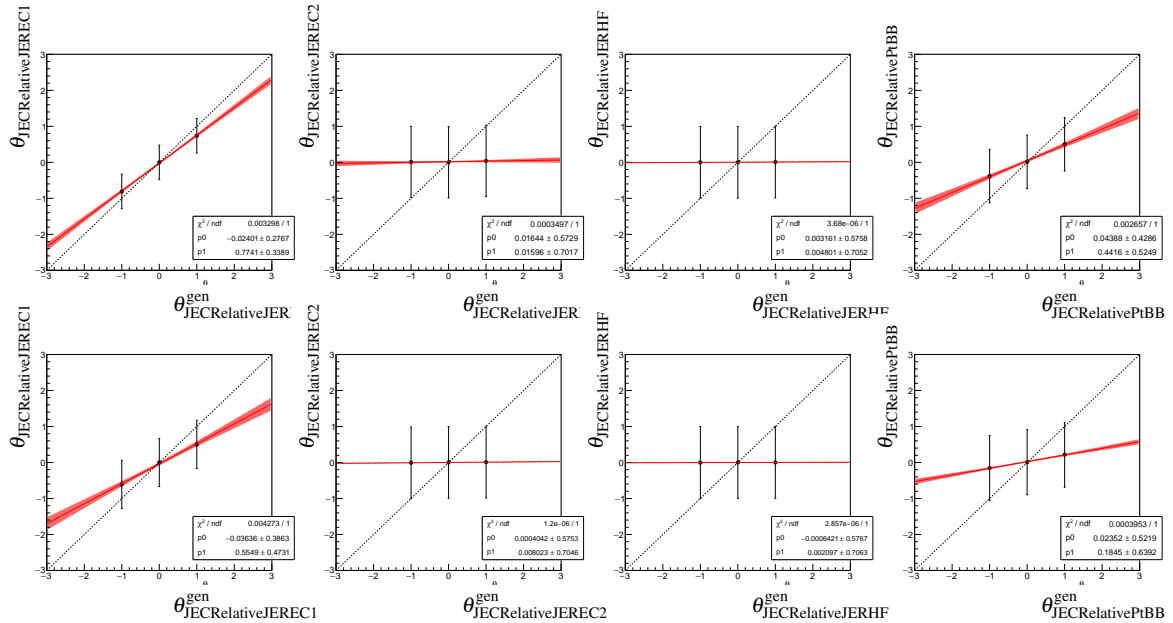


Figure D.12.: Closure test in muon+jets simulation of $\pm 1\sigma$ variation of one nuisance at the time while leaving only the corresponding nuisance free. The observable settings are upper row: 5D, lower row: 1D.

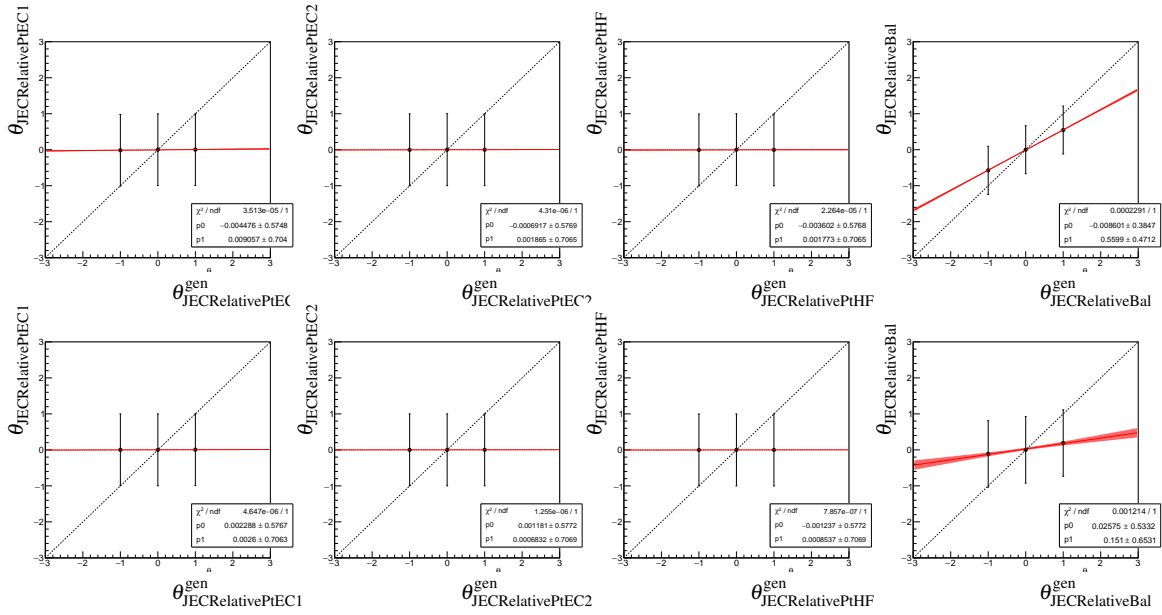


Figure D.13.: Closure test in muon+jets simulation of $\pm 1\sigma$ variation of one nuisance at the time while leaving only the corresponding nuisance free. The observable settings are upper row: 5D, lower row: 1D.

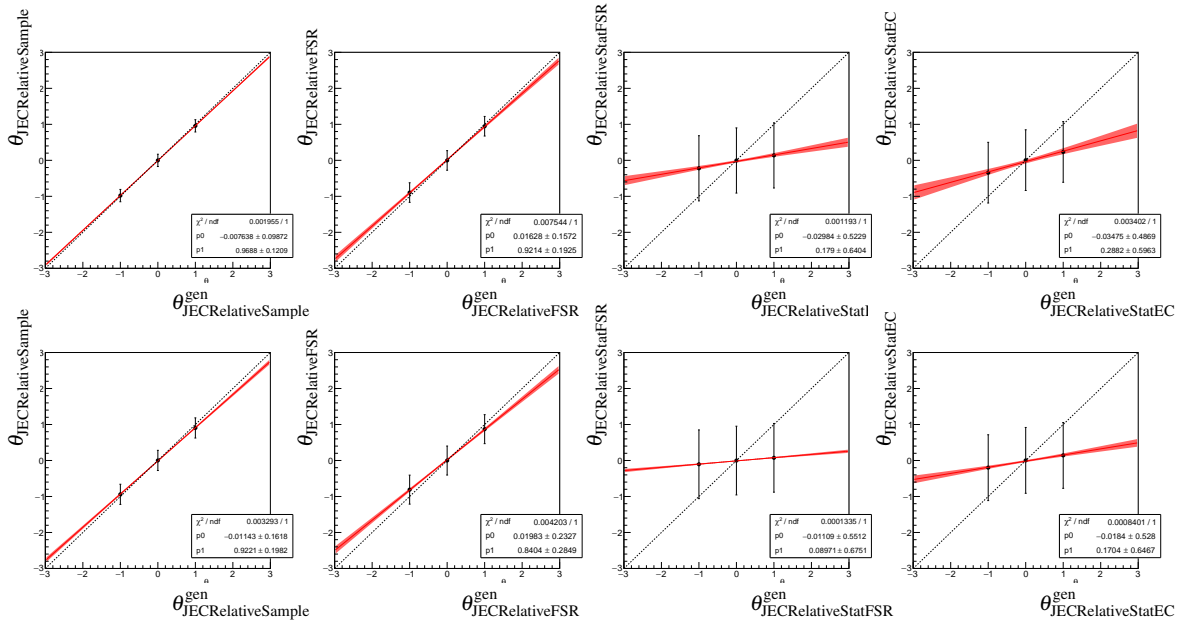


Figure D.14.: Closure test in muon+jets simulation of $\pm 1\sigma$ variation of one nuisance at the time while leaving only the corresponding nuisance free. The observable settings are upper row: 5D, lower row: 1D.

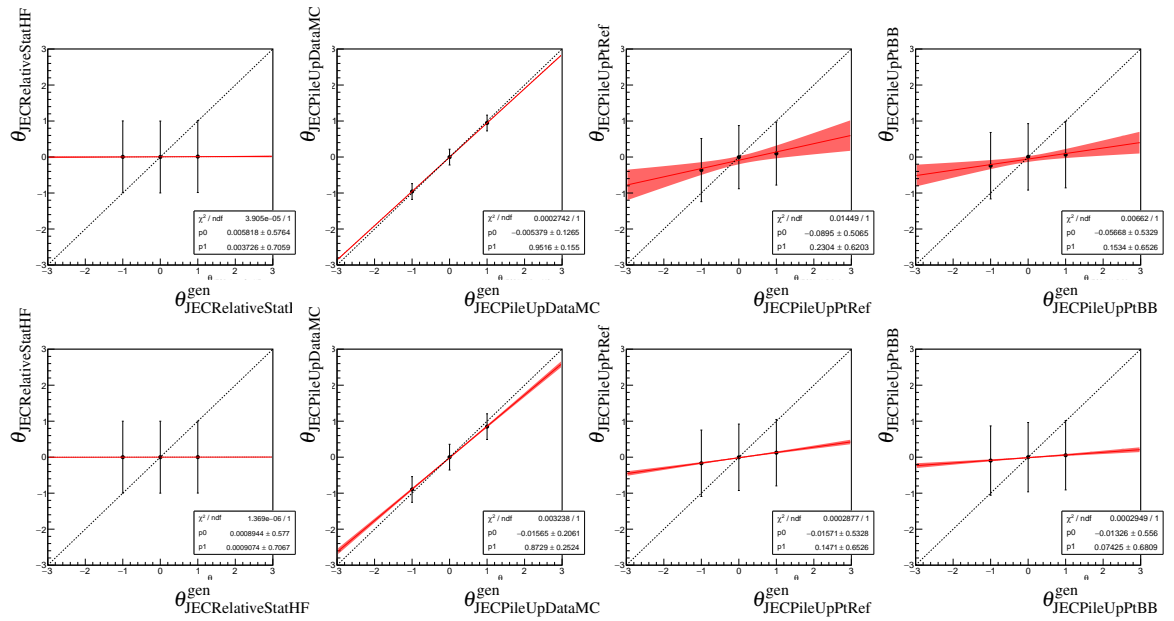


Figure D.15.: Closure test in muon+jets simulation of $\pm 1\sigma$ variation of one nuisance at the time while leaving only the corresponding nuisance free. The observable settings are upper row: 5D, lower row: 1D.

D.2. Template variation distributions

In this section the effect of the uncertainty variations on the templates is shown. For variation from dedicated samples a 1σ error band corresponding to the statistic uncertainty due to its sample size is shown.

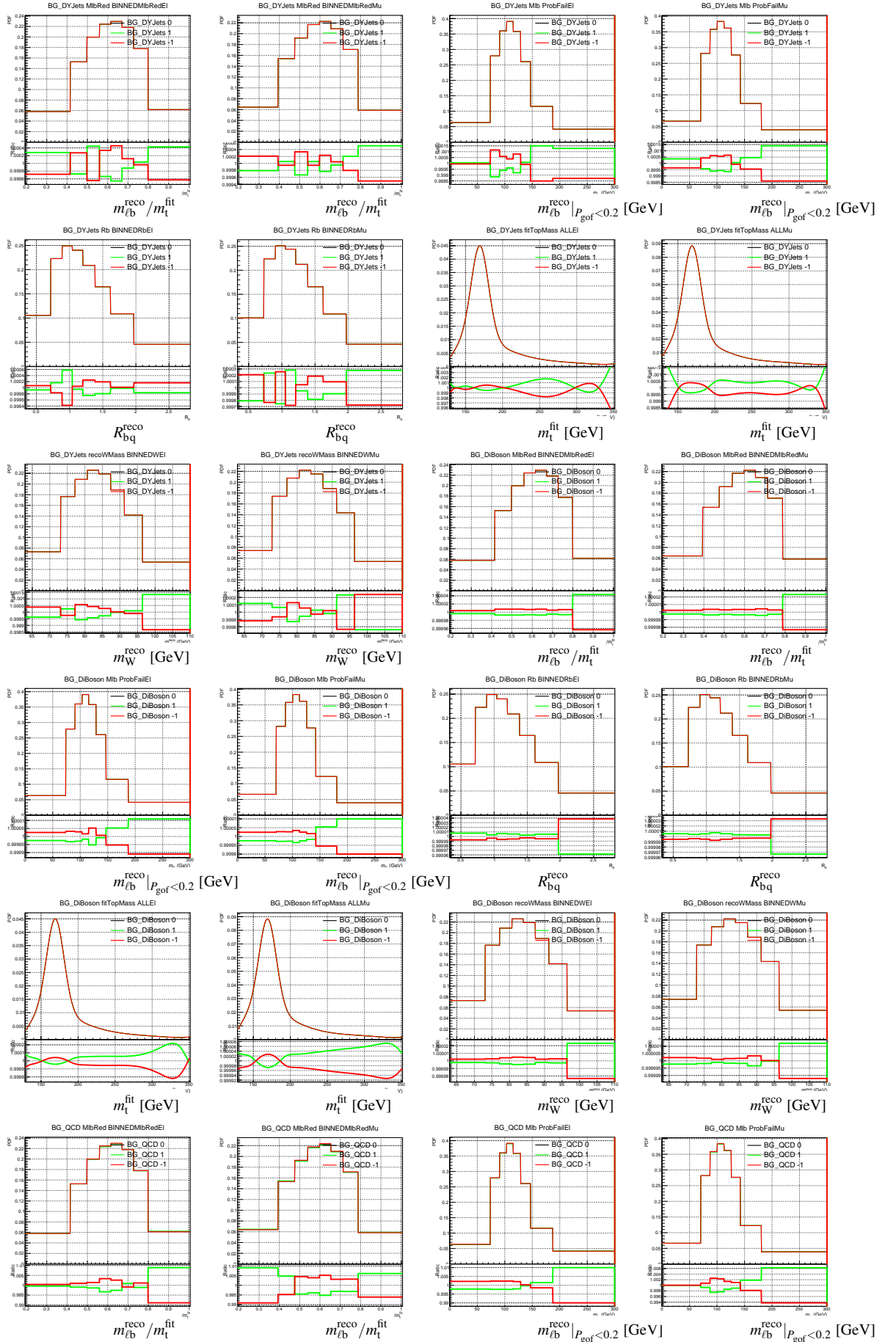


Figure D.16.: Template distribution for different observables and variations with the ratio to the template from the default simulation.

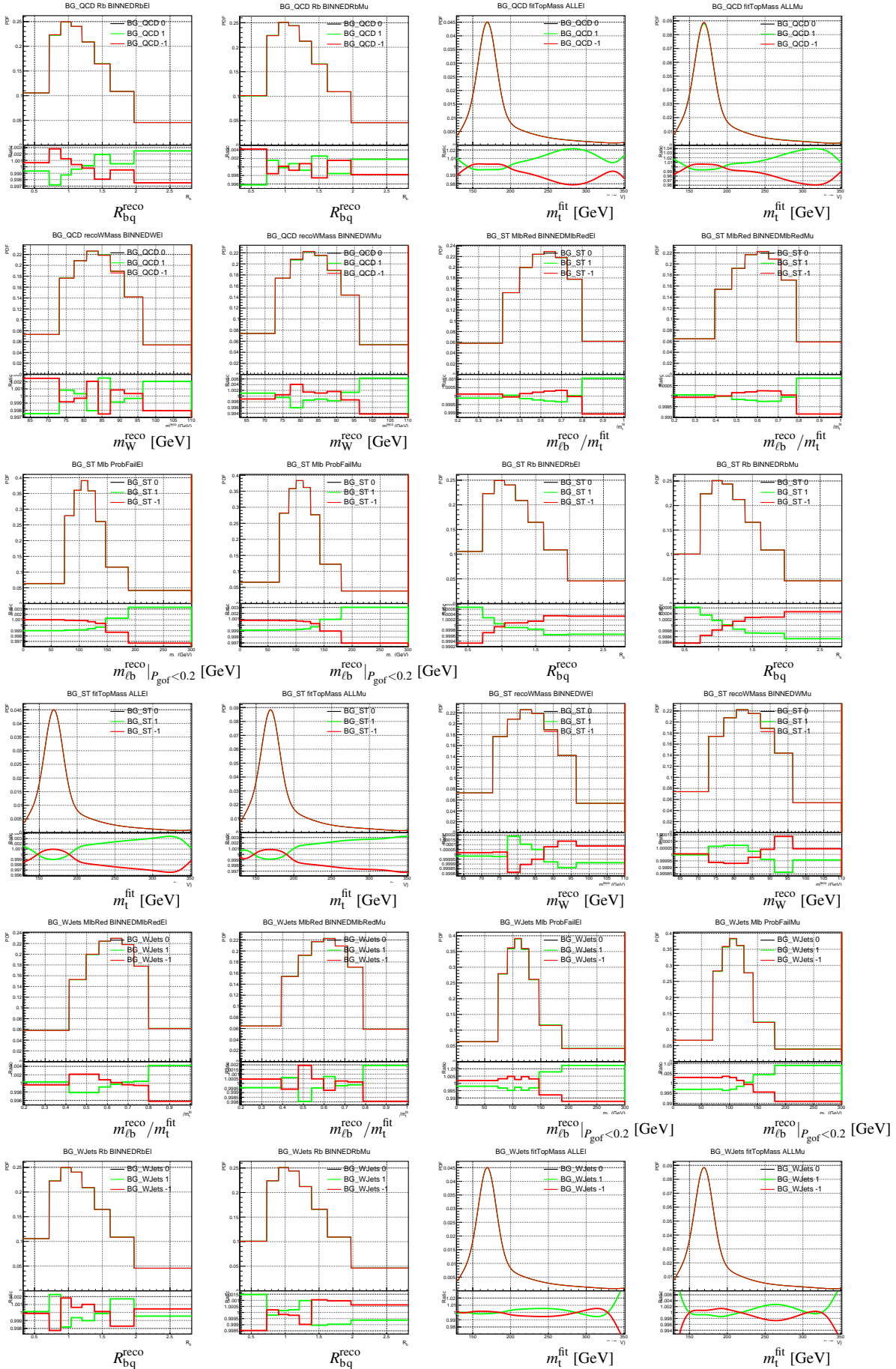


Figure D.17.: Template distribution for different observables and variations with the ratio to the template from the default simulation.

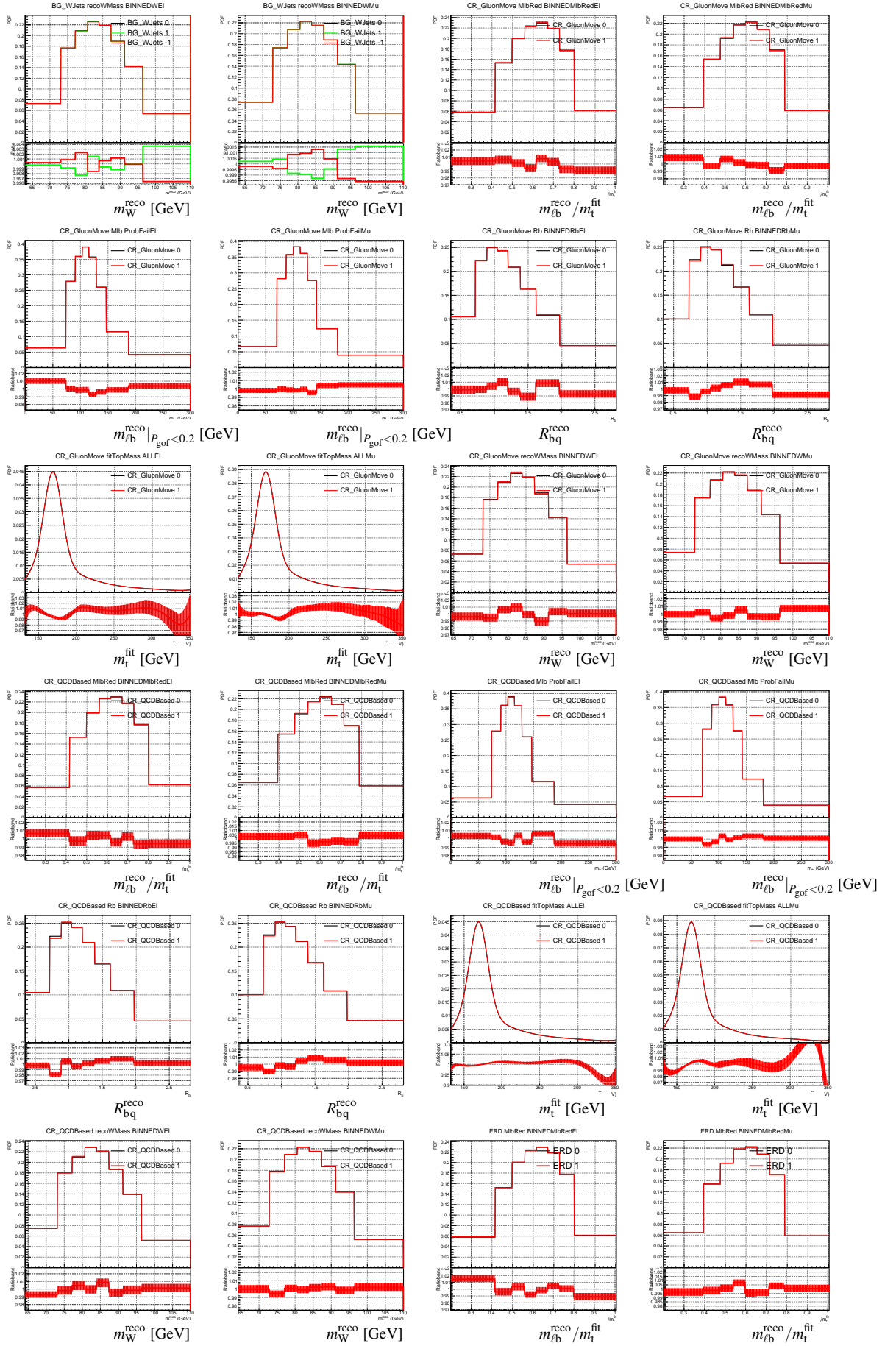


Figure D.18.: Template distribution for different observables and variations with the ratio to the template from the default simulation.

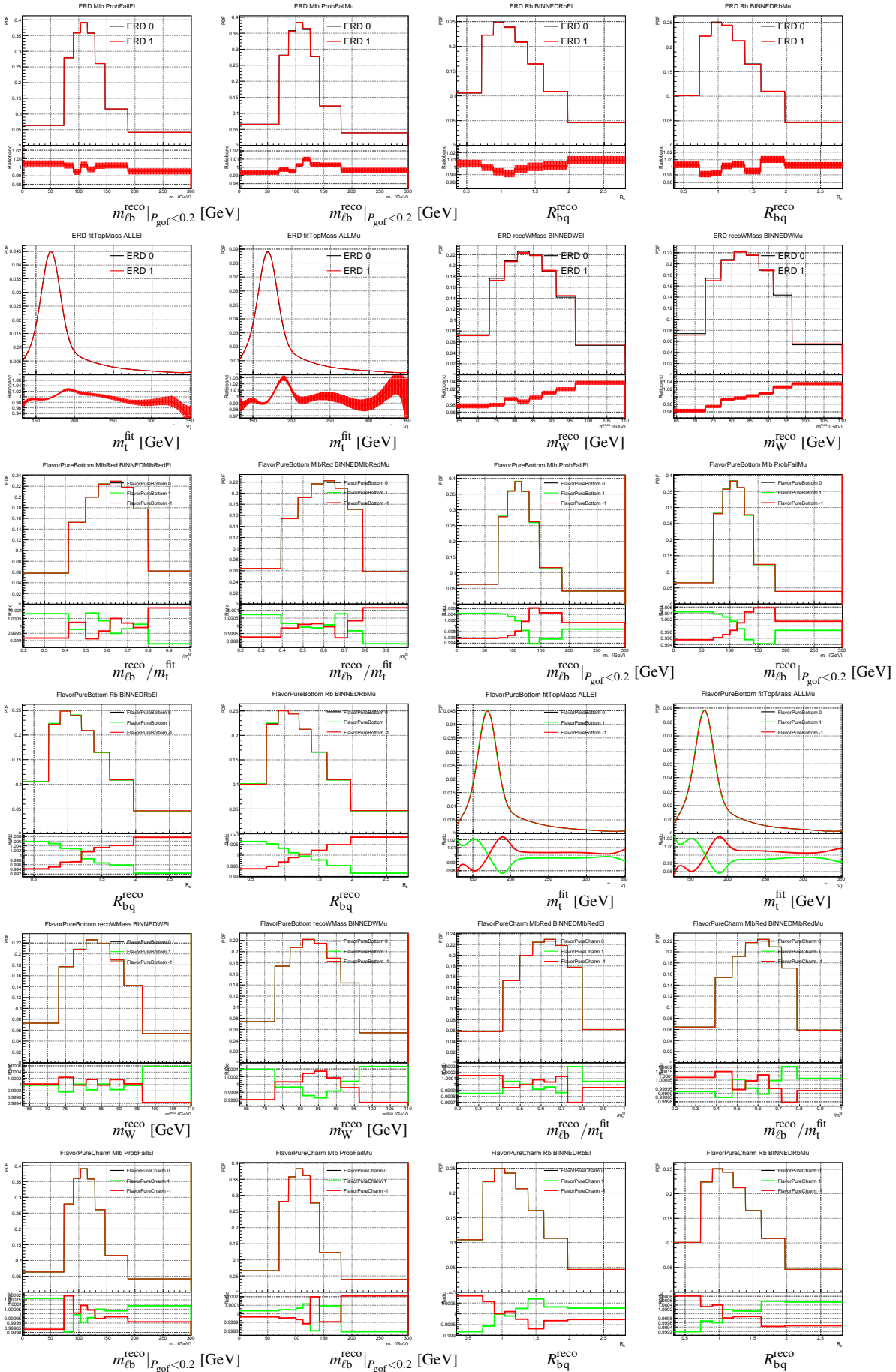


Figure D.19.: Template distribution for different observables and variations with the ratio to the template from the default simulation.

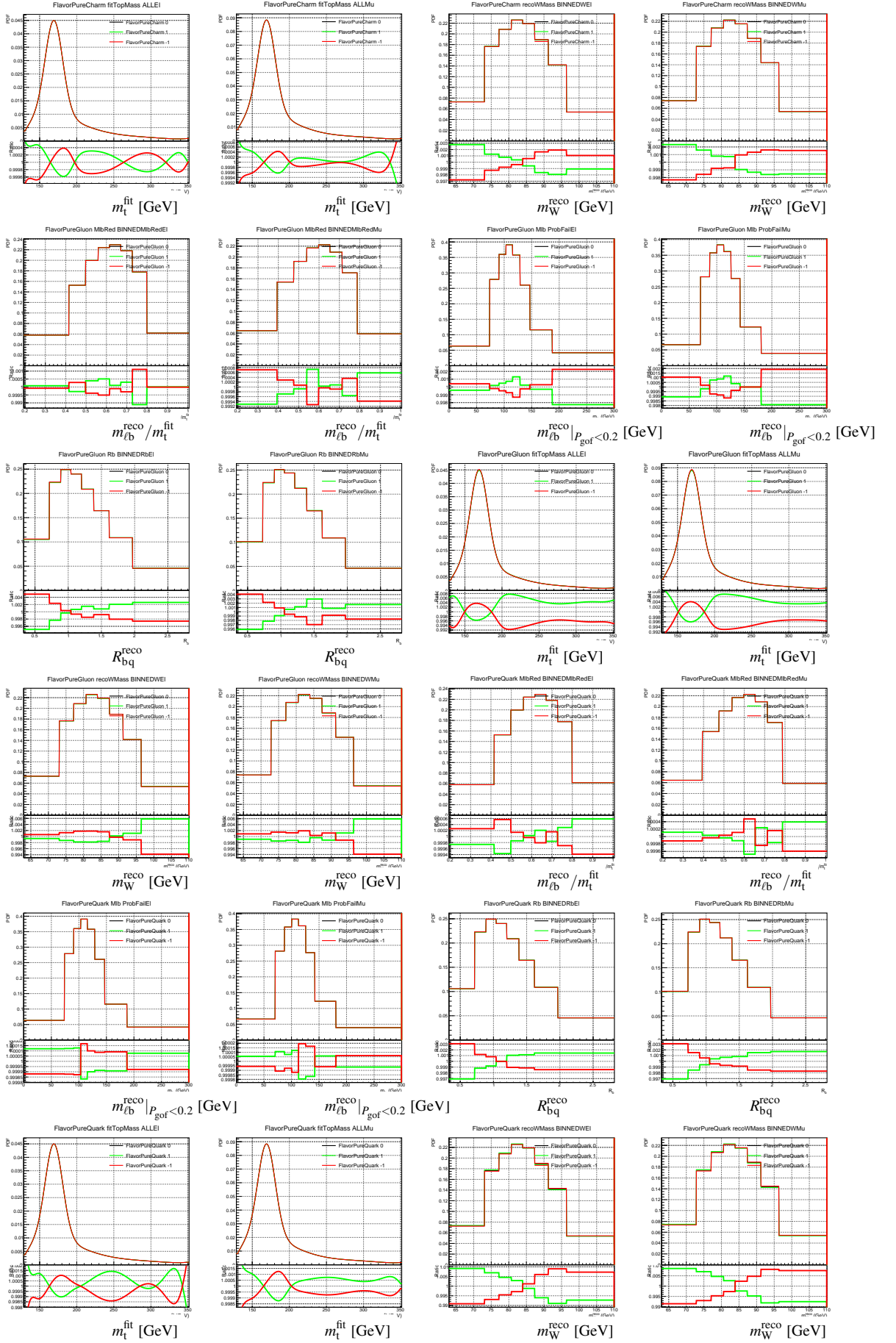


Figure D.20.: Template distribution for different observables and variations with the ratio to the template from the default simulation.

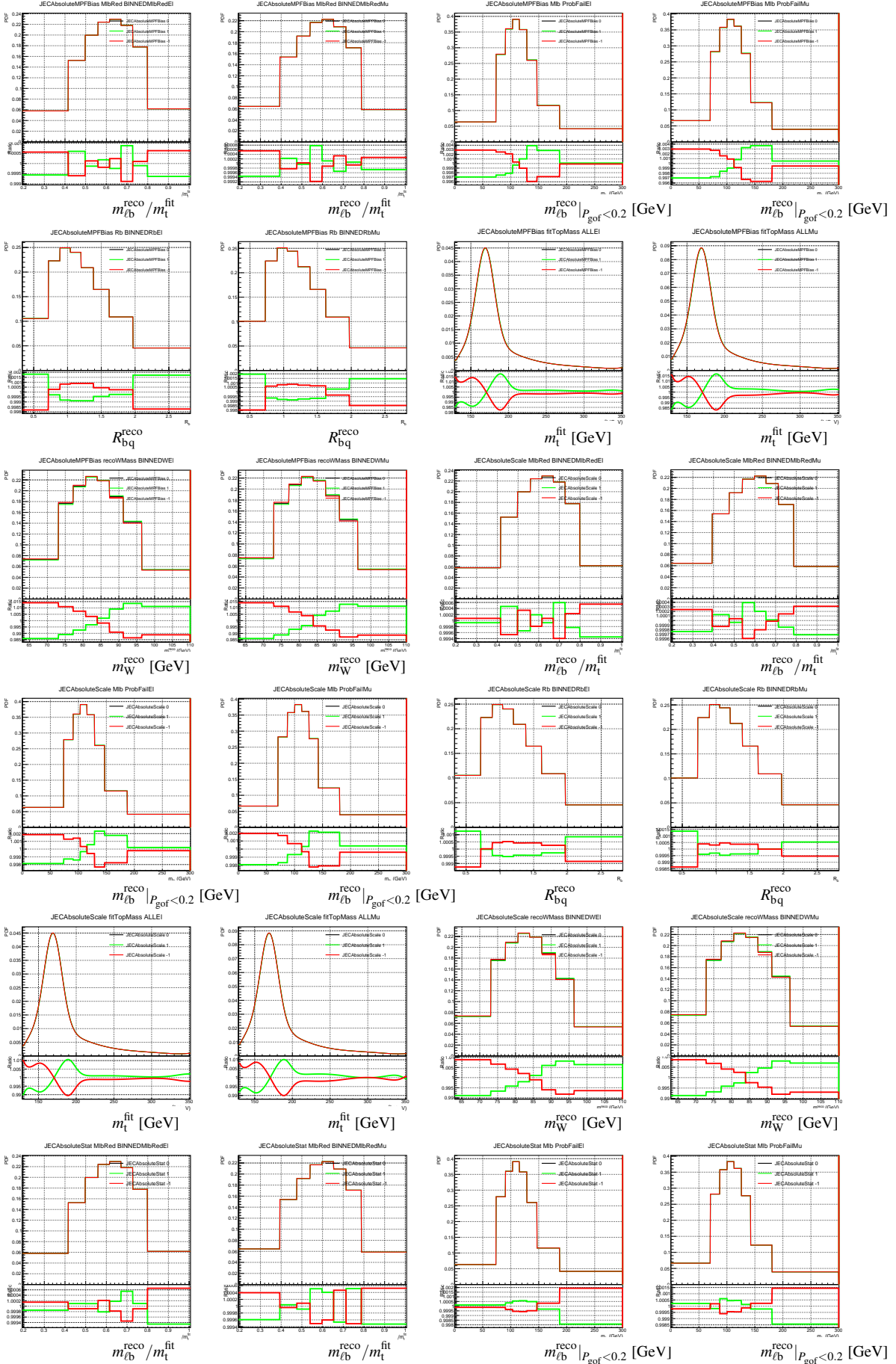


Figure D.21.: Template distribution for different observables and variations with the ratio to the template from the default simulation.

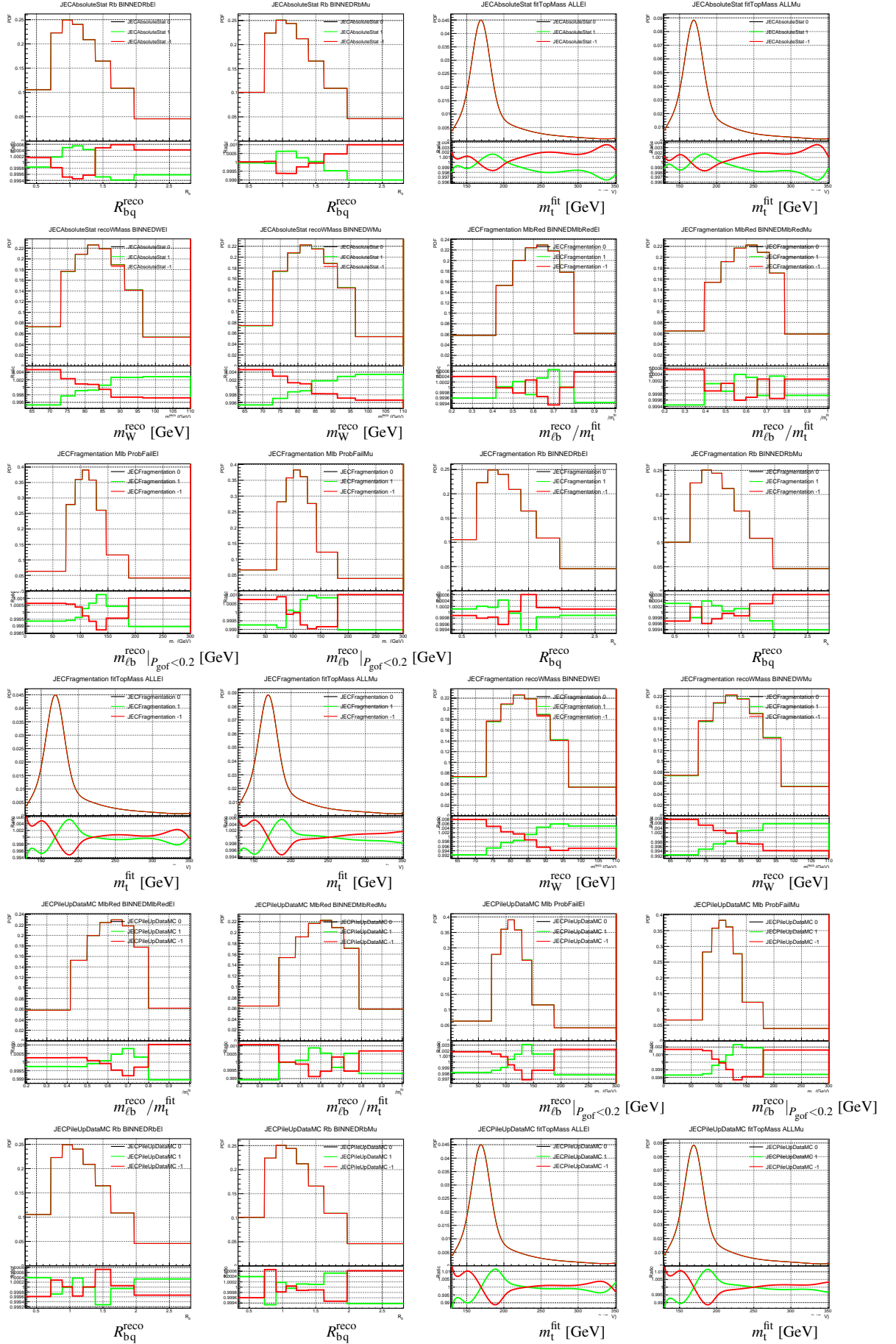


Figure D.22.: Template distribution for different observables and variations with the ratio to the template from the default simulation.

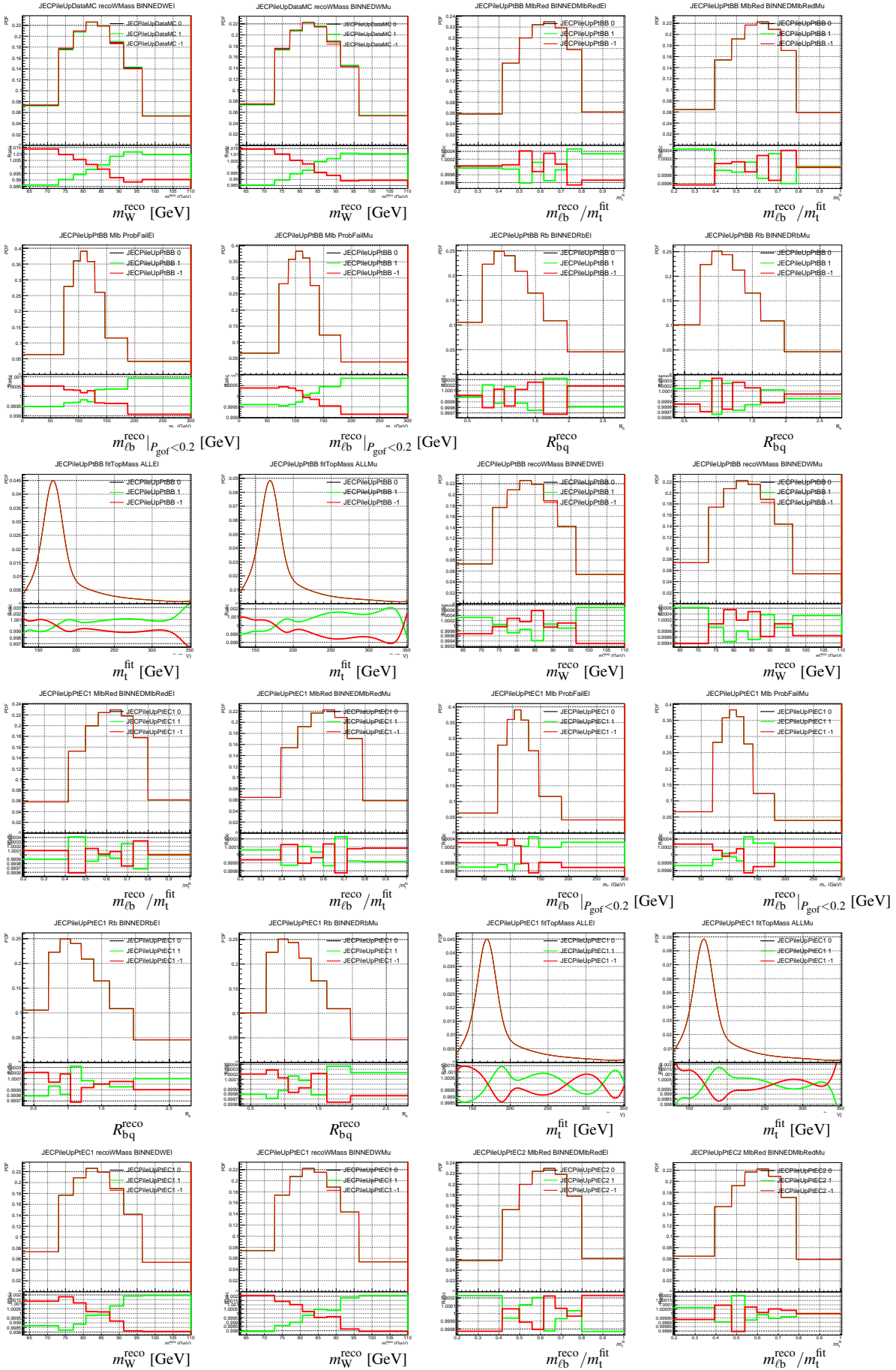


Figure D.23.: Template distribution for different observables and variations with the ratio to the template from the default simulation.

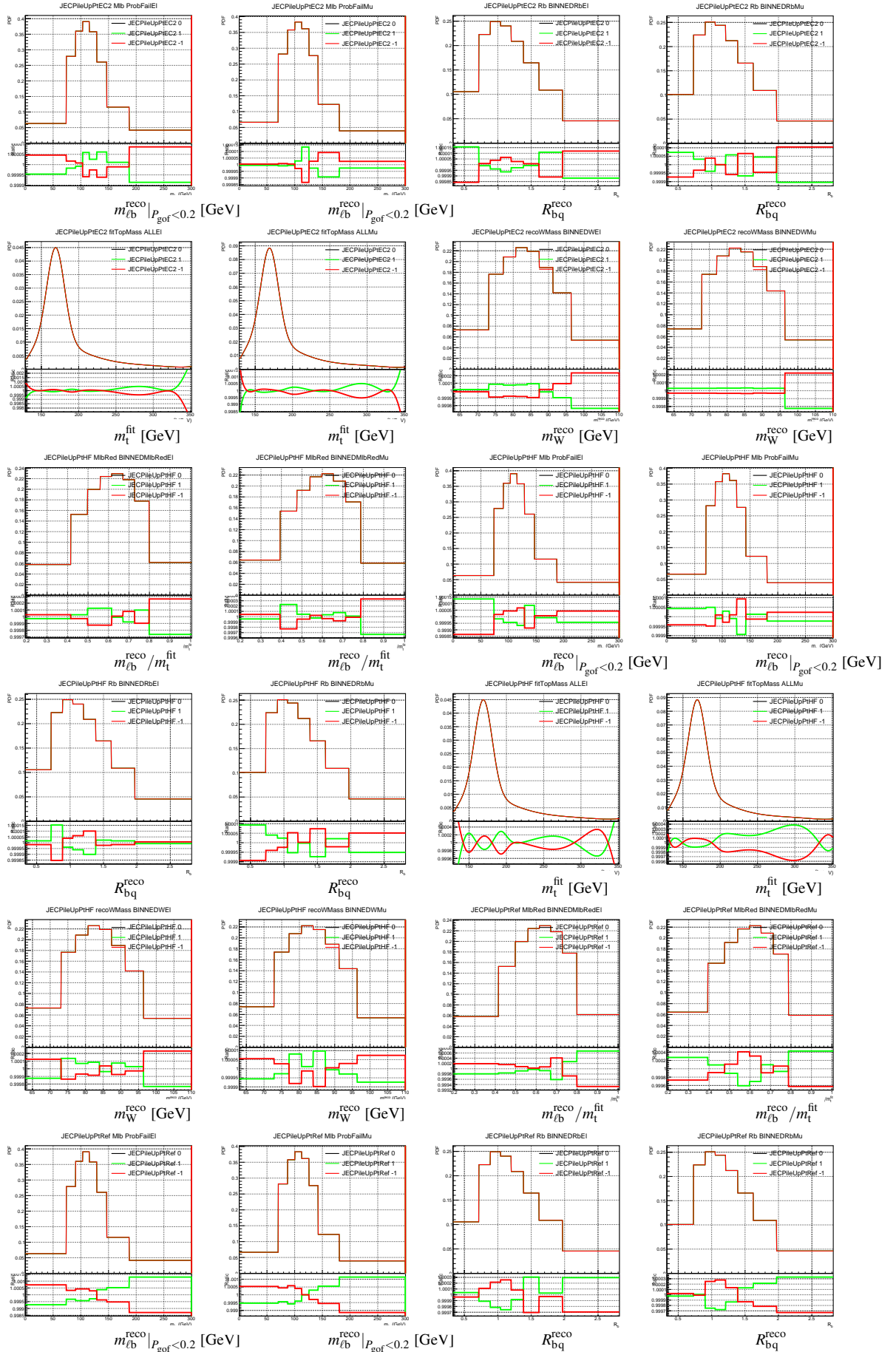


Figure D.24.: Template distribution for different observables and variations with the ratio to the template from the default simulation.

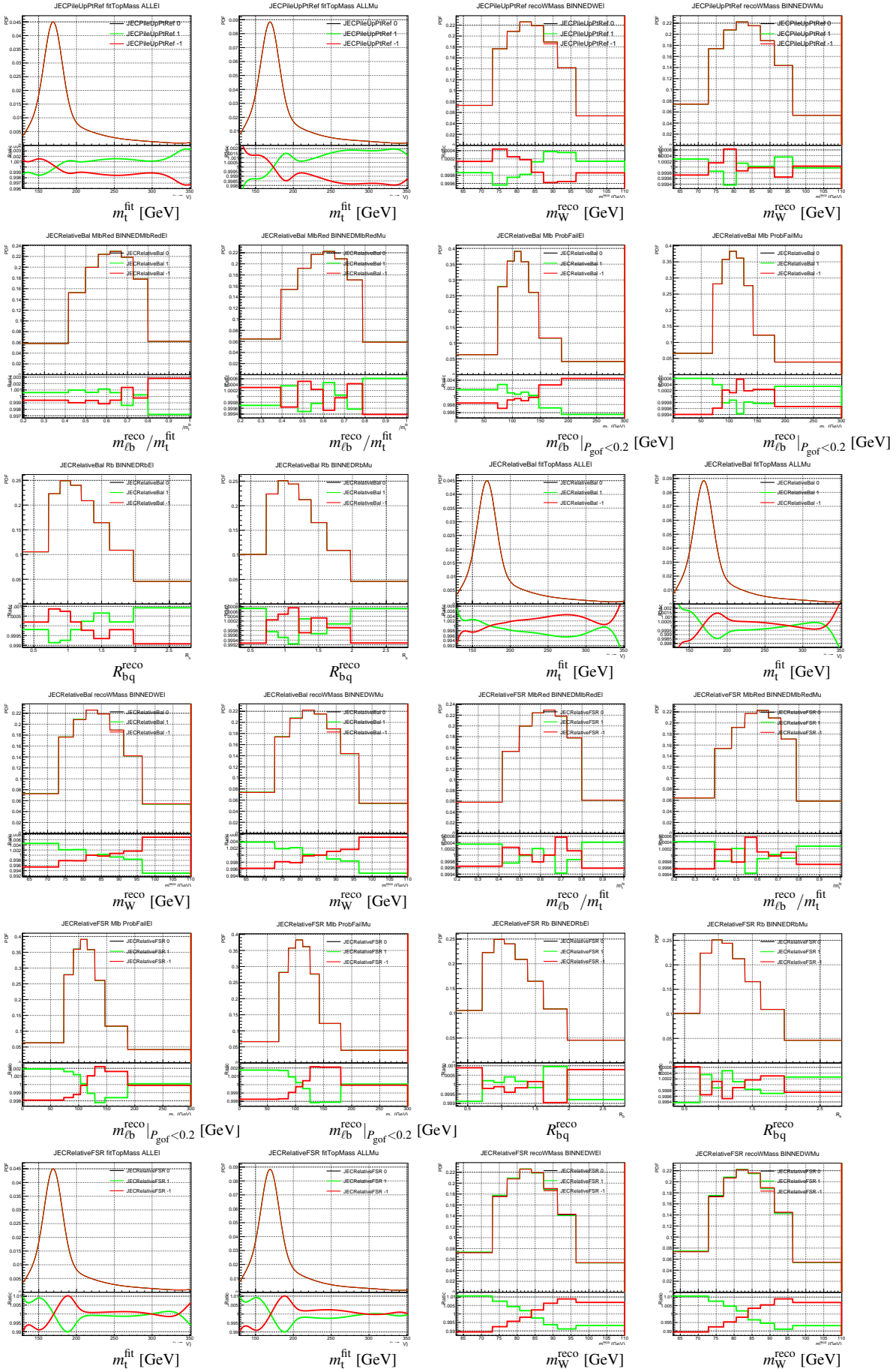


Figure D.25.: Template distribution for different observables and variations with the ratio to the template from the default simulation.

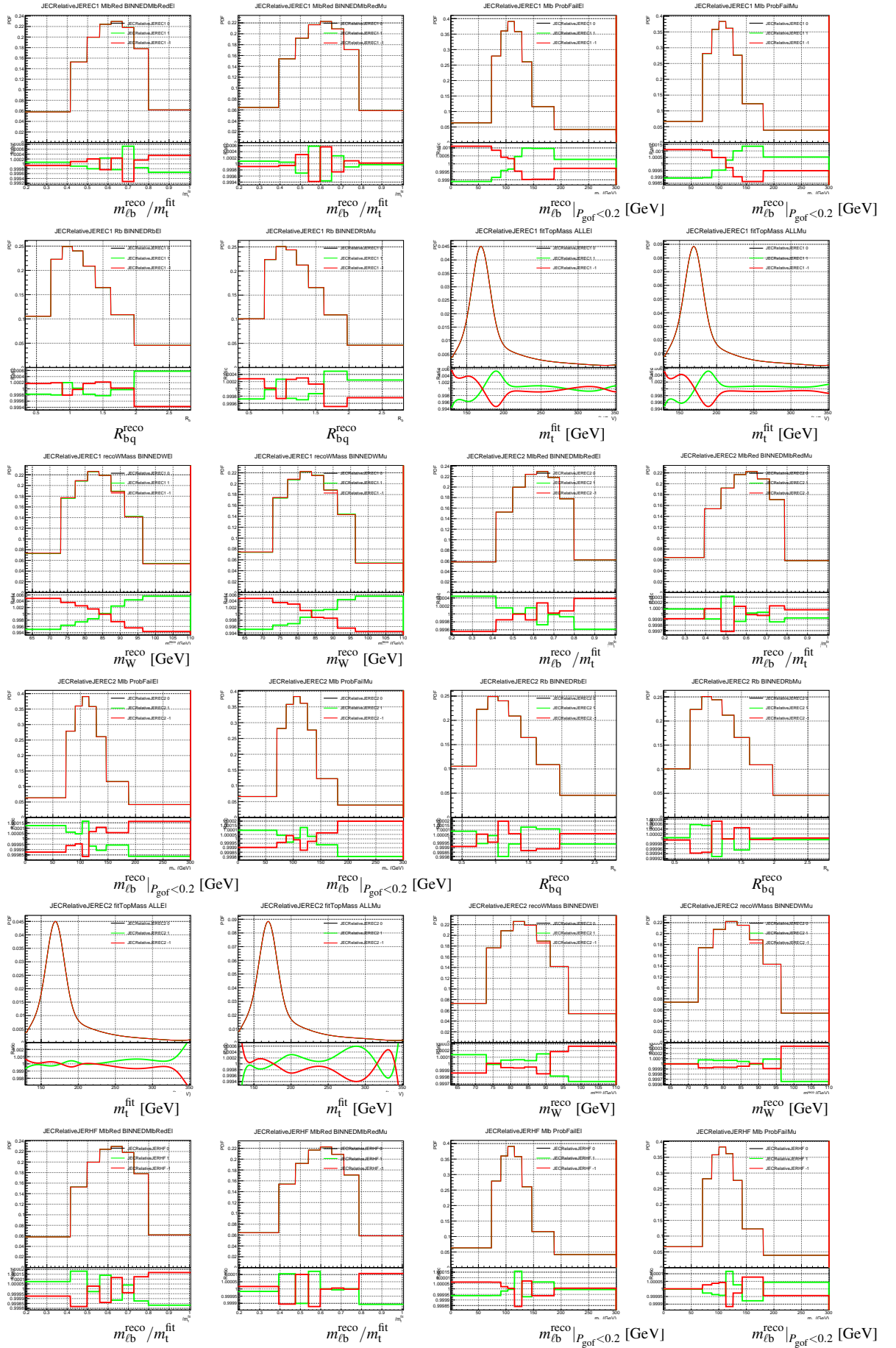


Figure D.26.: Template distribution for different observables and variations with the ratio to the template from the default simulation.

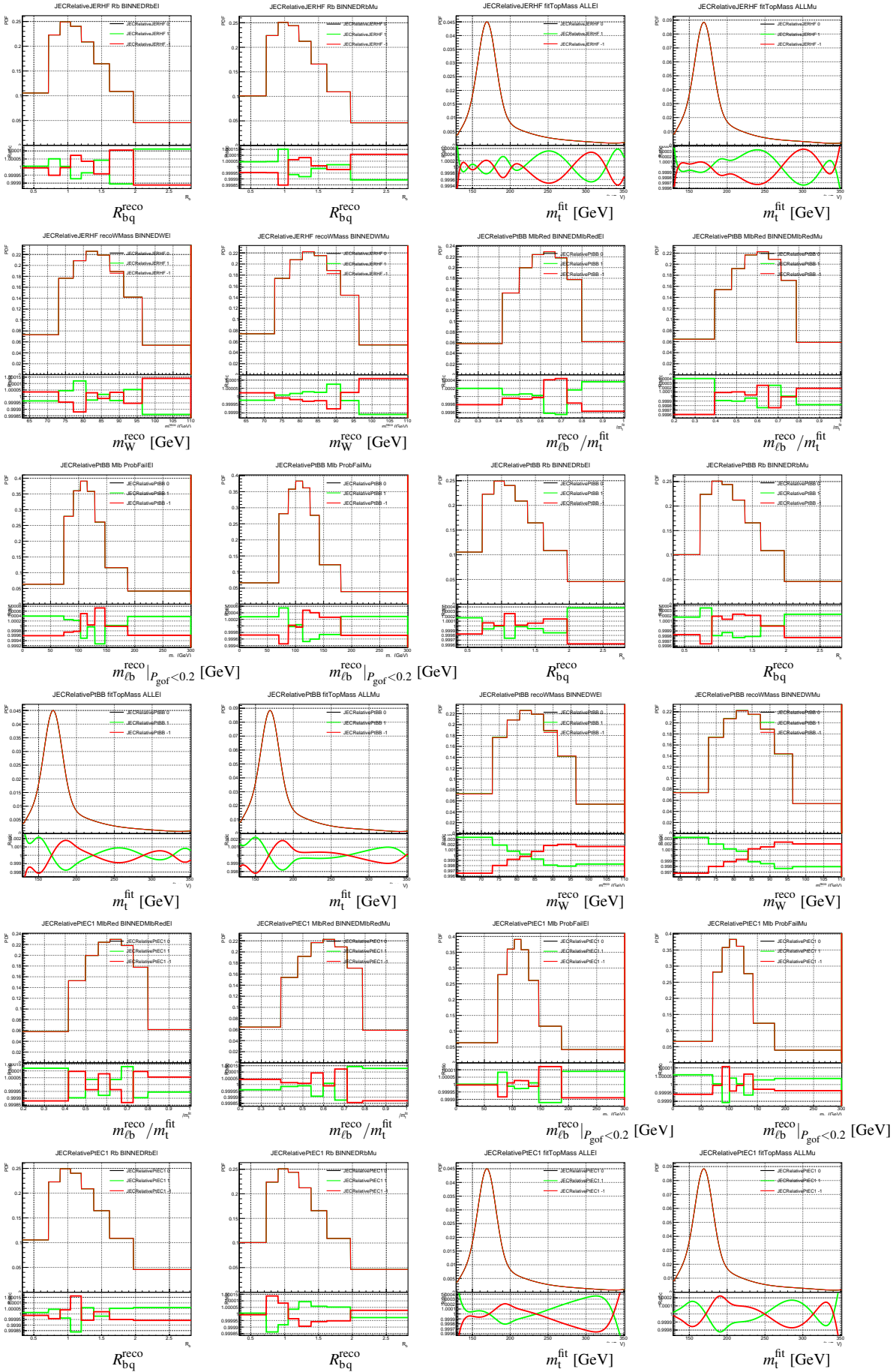


Figure D.27.: Template distribution for different observables and variations with the ratio to the template from the default simulation.

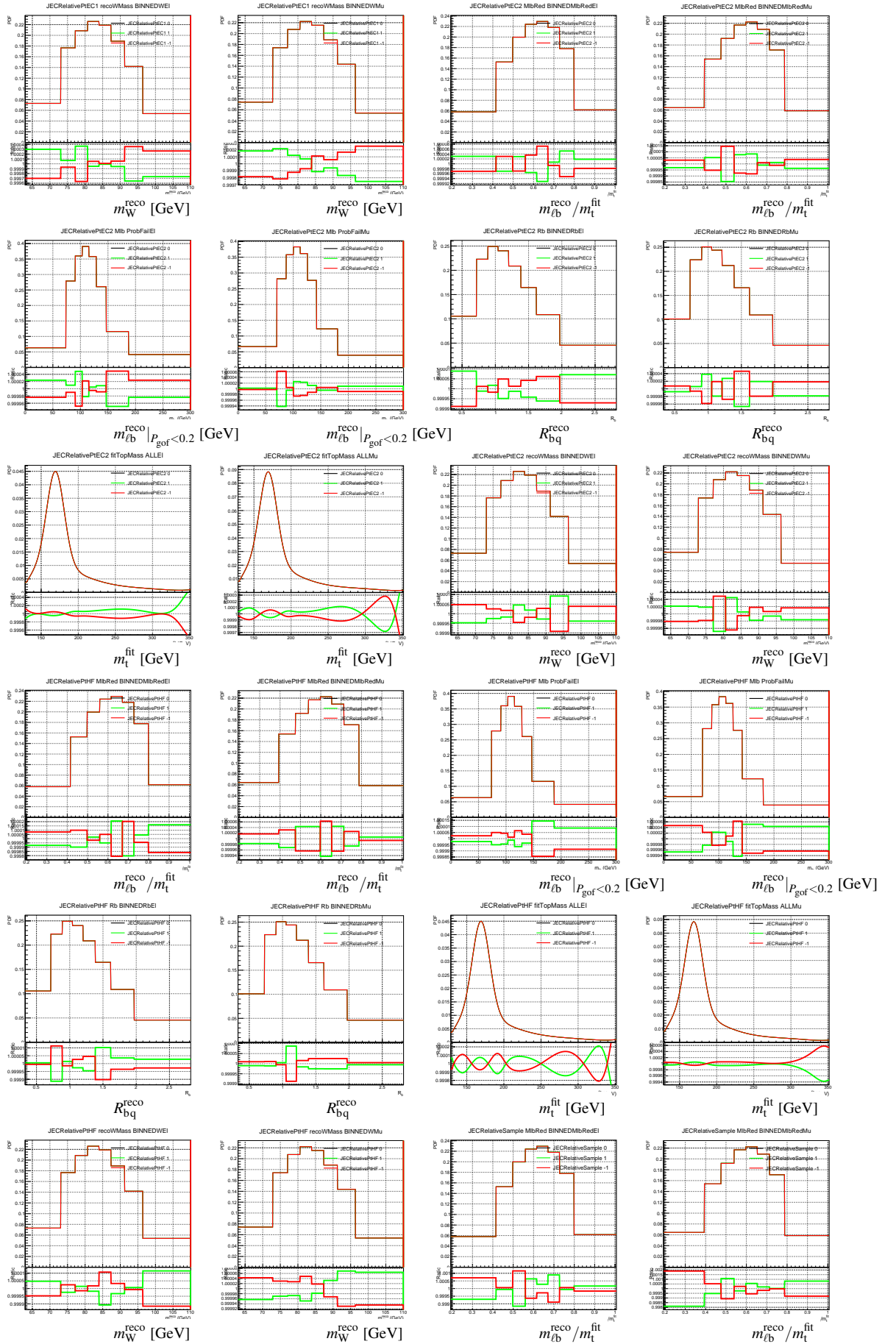


Figure D.28.: Template distribution for different observables and variations with the ratio to the template from the default simulation.

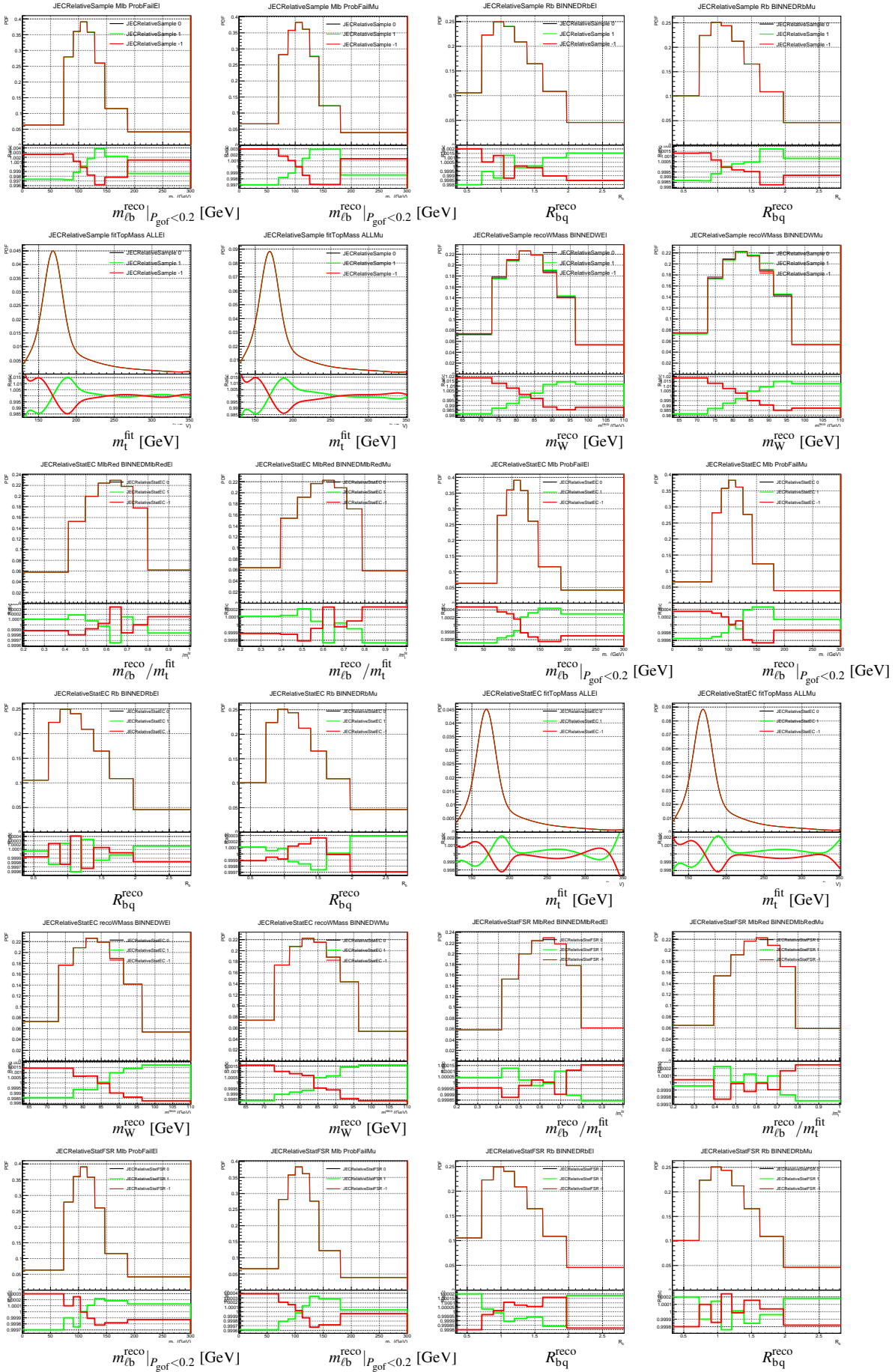


Figure D.29.: Template distribution for different observables and variations with the ratio to the template from the default simulation.

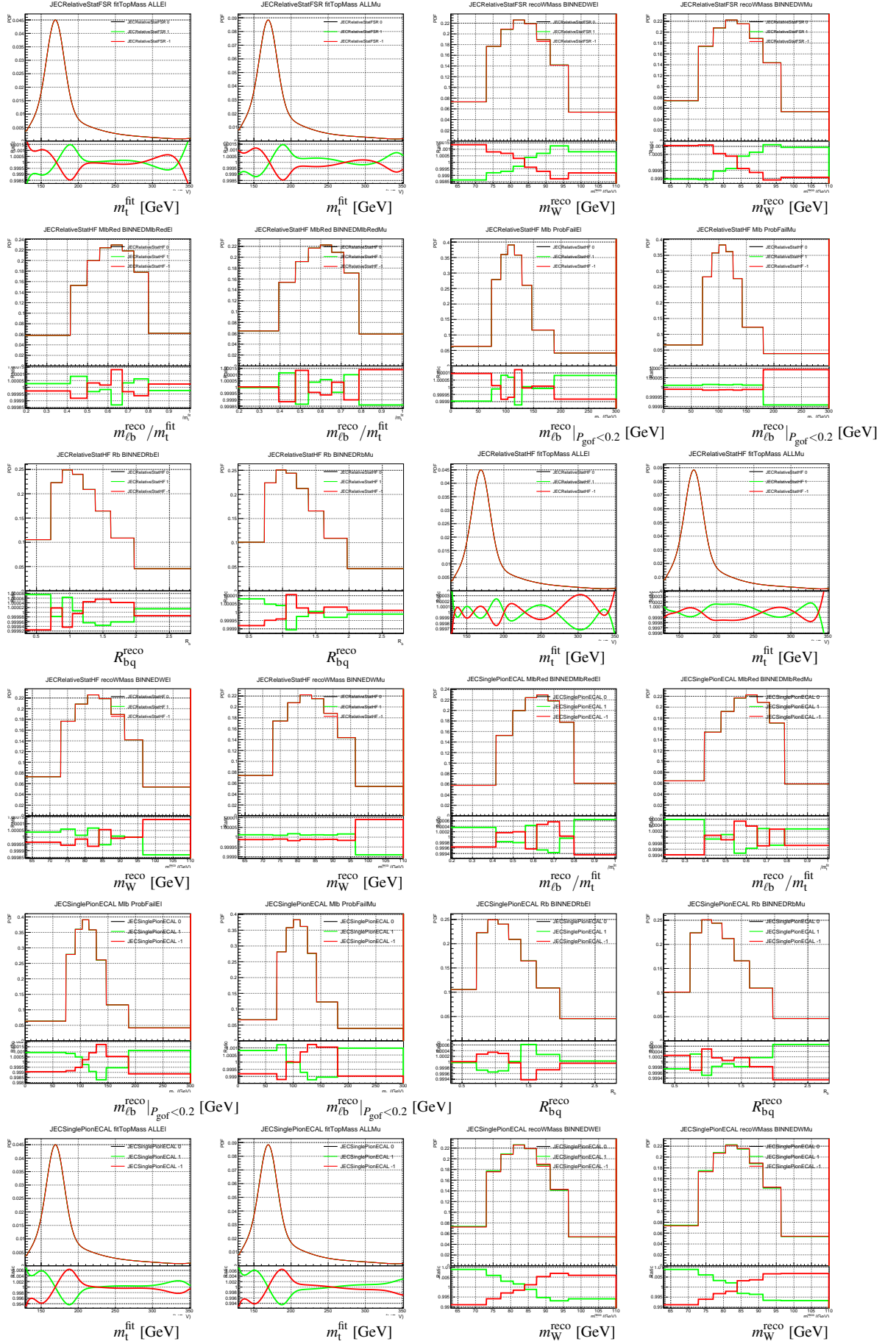


Figure D.30.: Template distribution for different observables and variations with the ratio to the template from the default simulation.

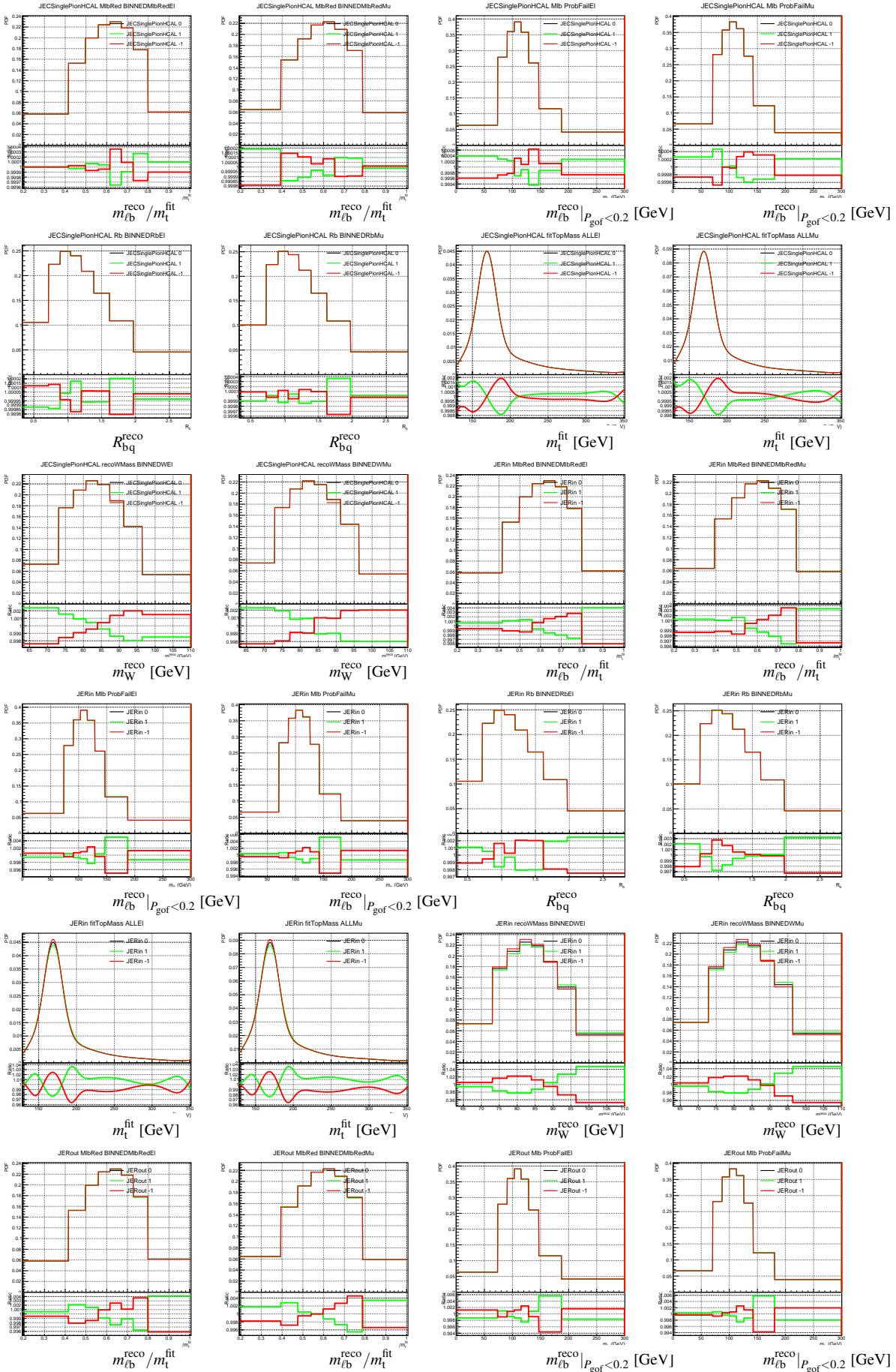


Figure D.31.: Template distribution for different observables and variations with the ratio to the template from the default simulation.

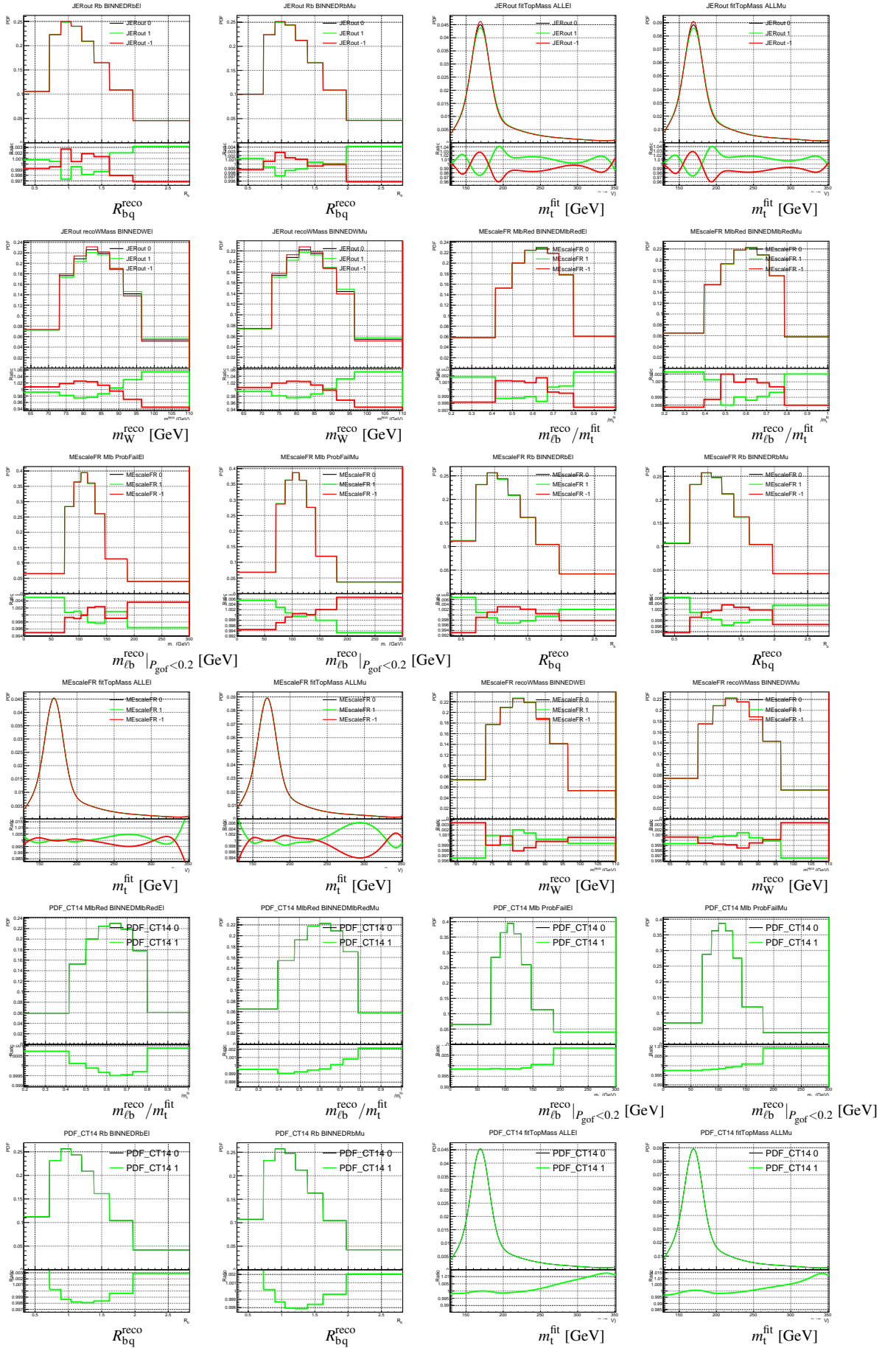


Figure D.32.: Template distribution for different observables and variations with the ratio to the template from the default simulation.

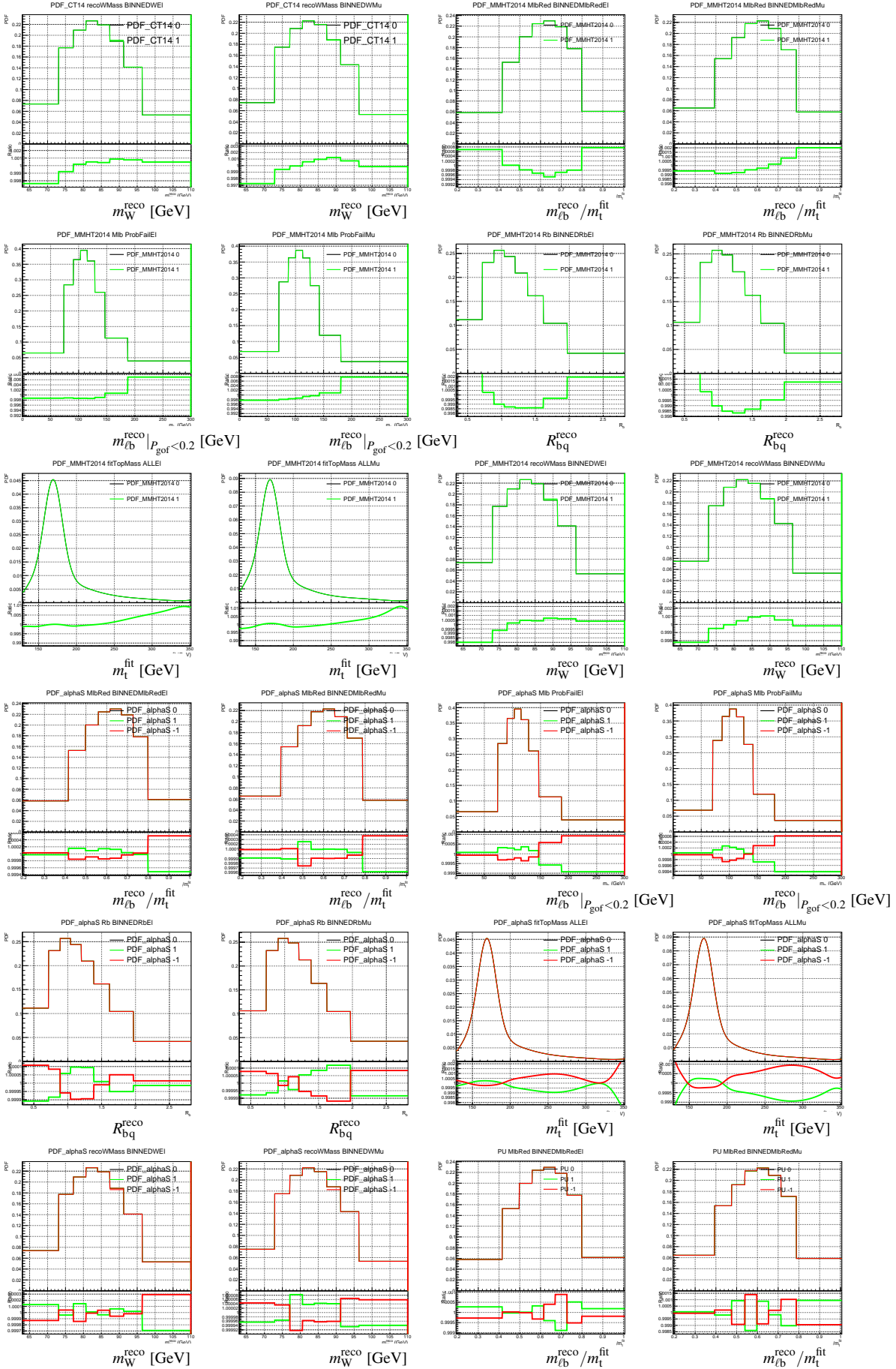


Figure D.33.: Template distribution for different observables and variations with the ratio to the template from the default simulation.

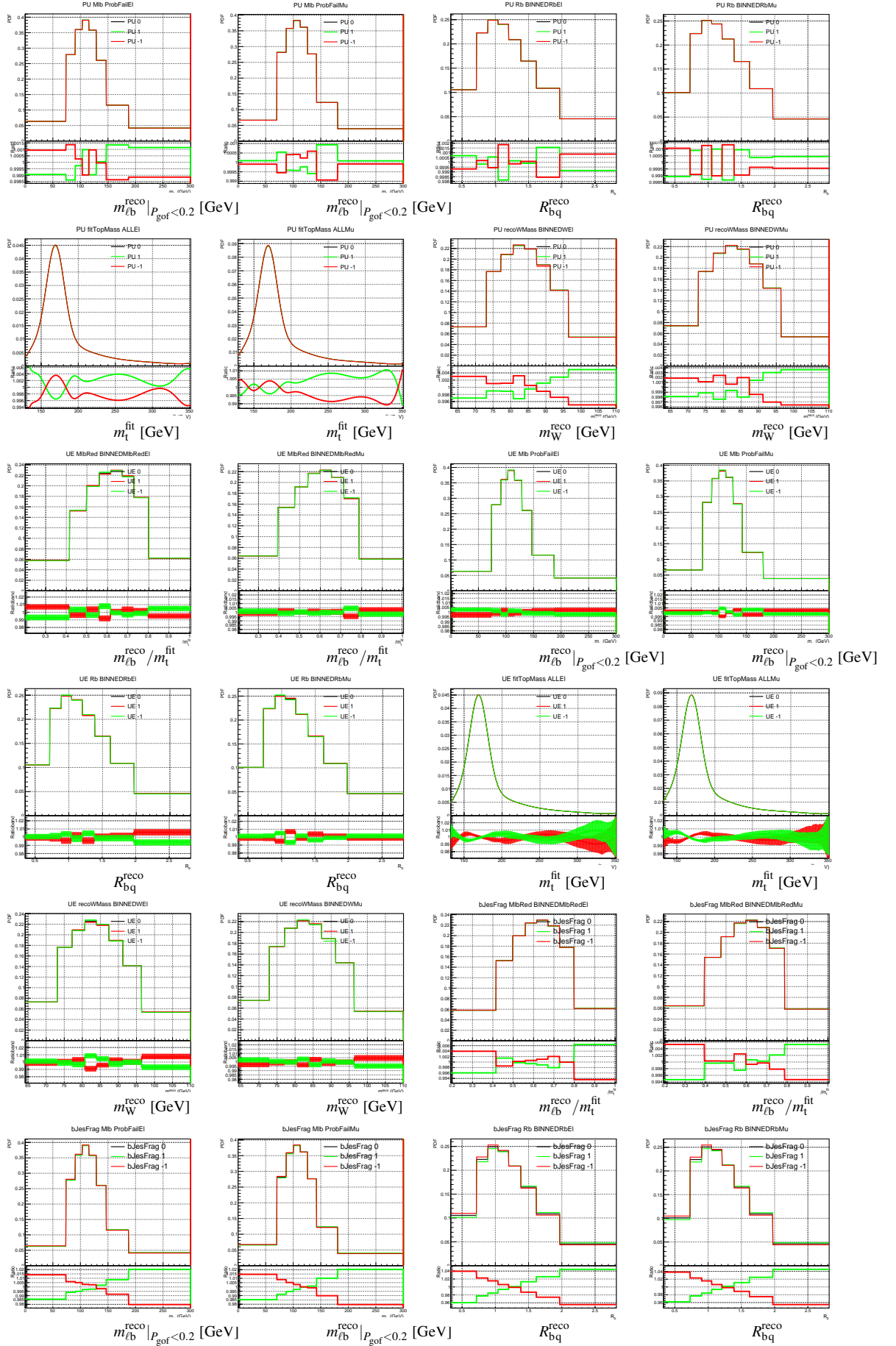


Figure D.34.: Template distribution for different observables and variations with the ratio to the template from the default simulation.

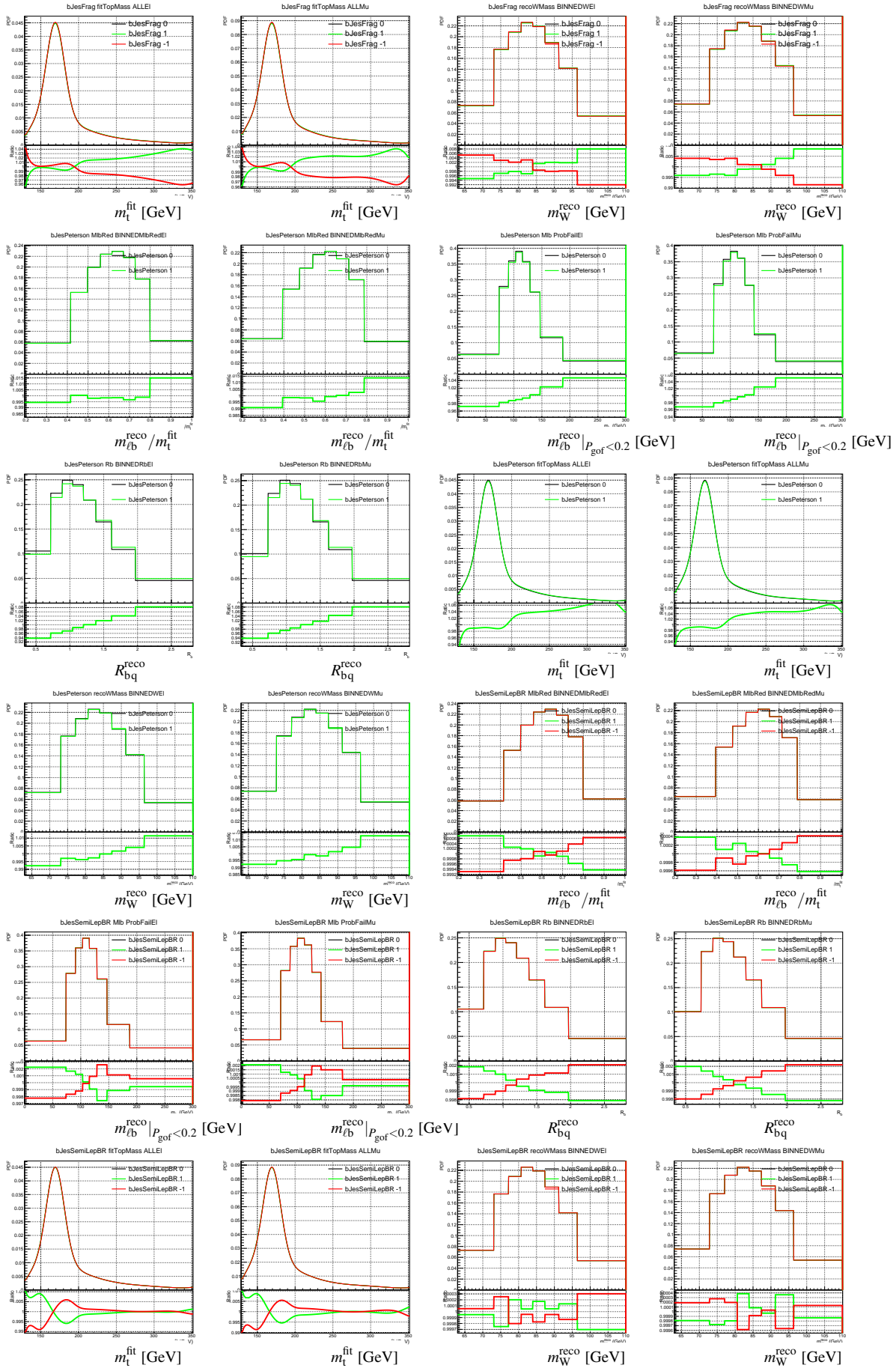


Figure D.35.: Template distribution for different observables and variations with the ratio to the template from the default simulation.

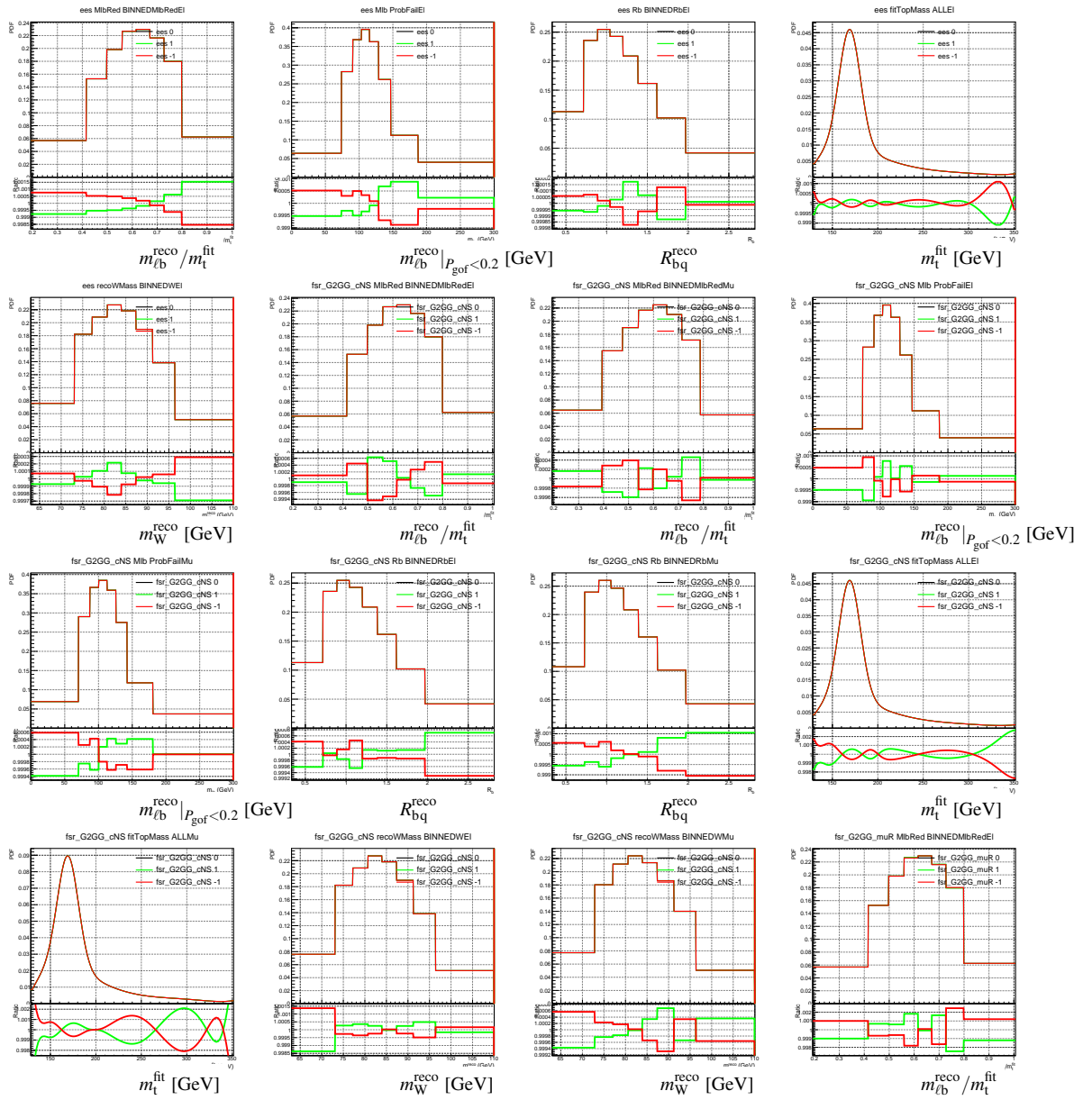


Figure D.36.: Template distribution for different observables and variations with the ratio to the template from the default simulation.

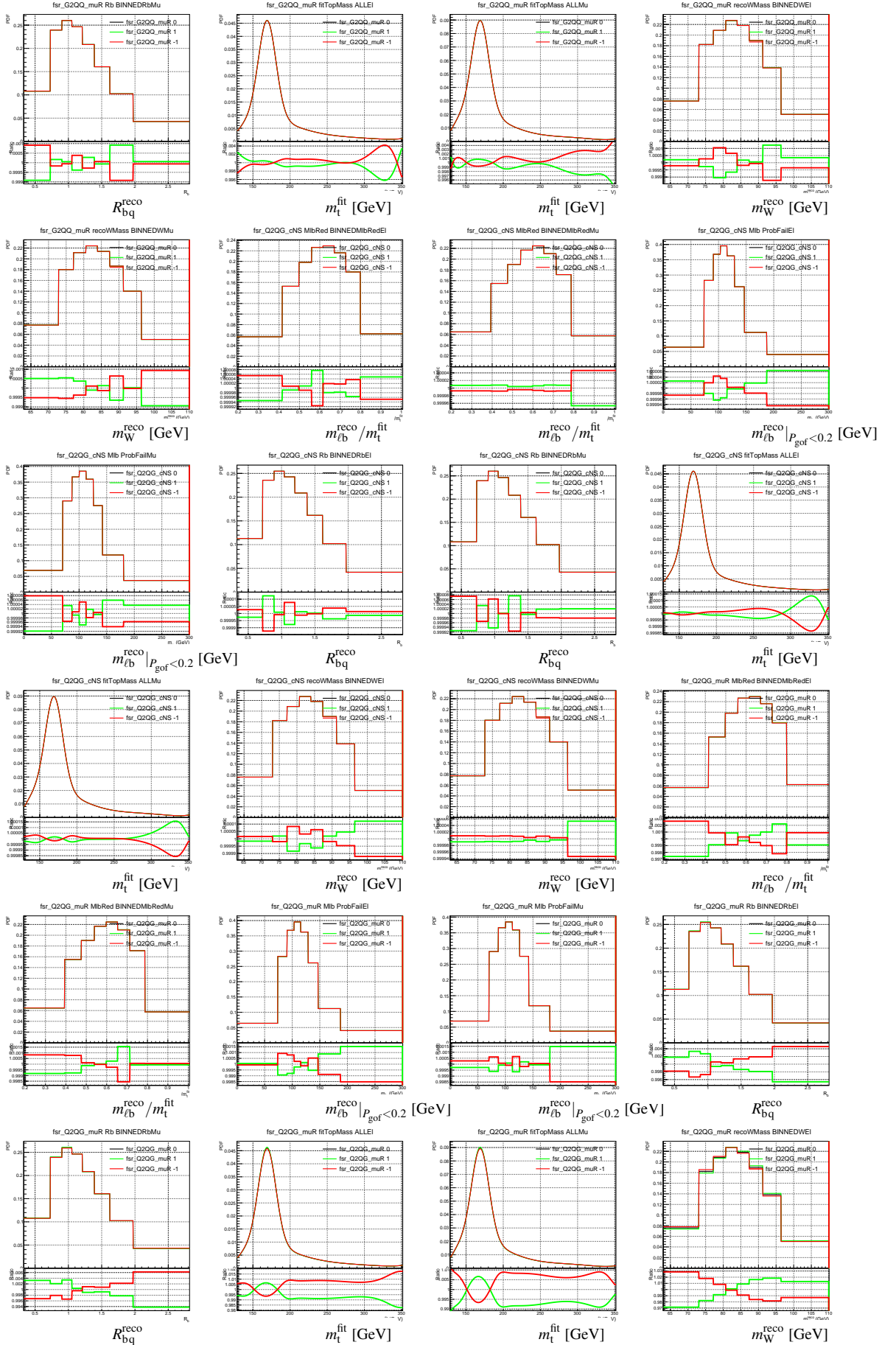


Figure D.38.: Template distribution for different observables and variations with the ratio to the template from the default simulation.

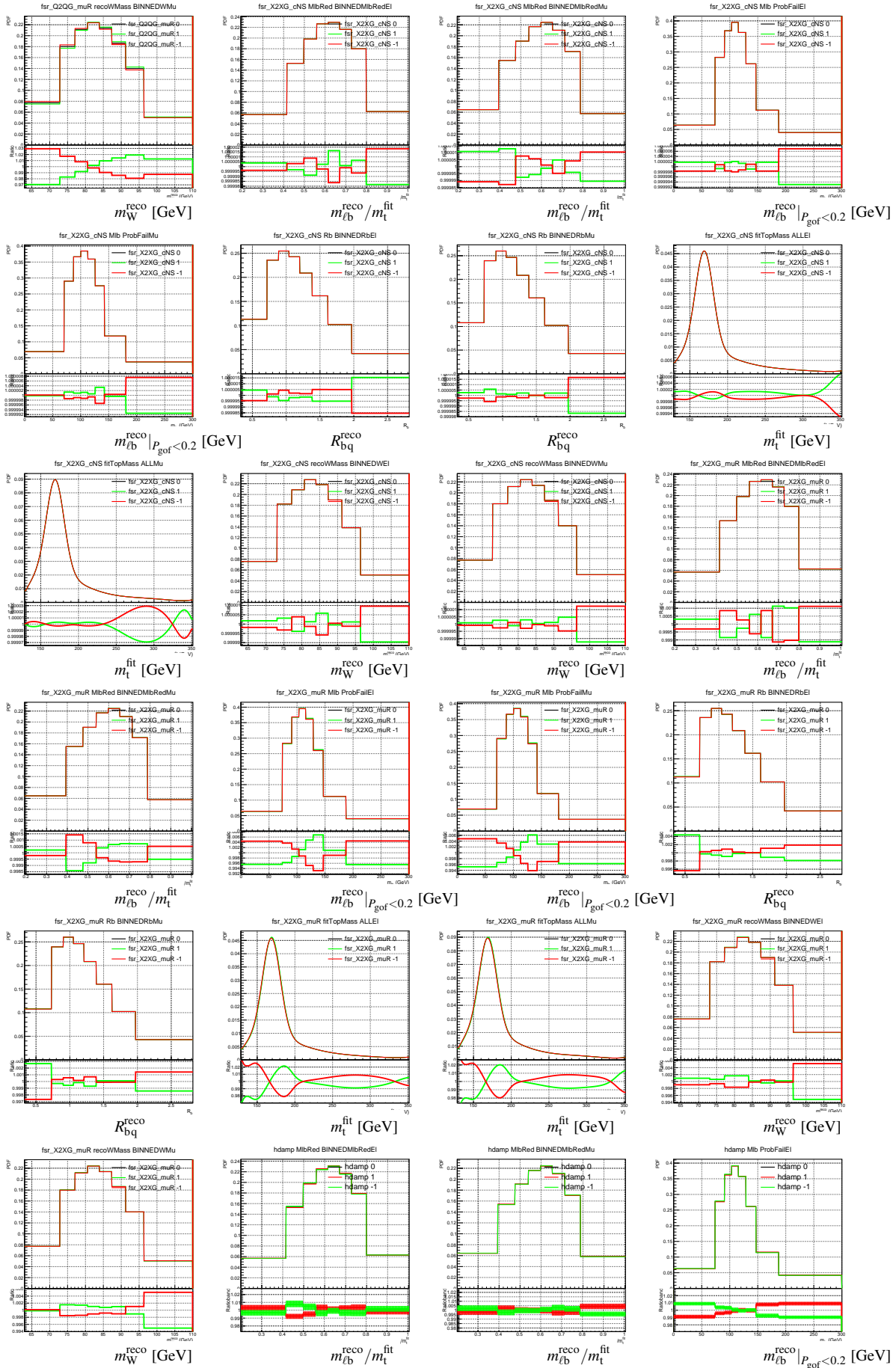


Figure D.39.: Template distribution for different observables and variations with the ratio to the template from the default simulation.

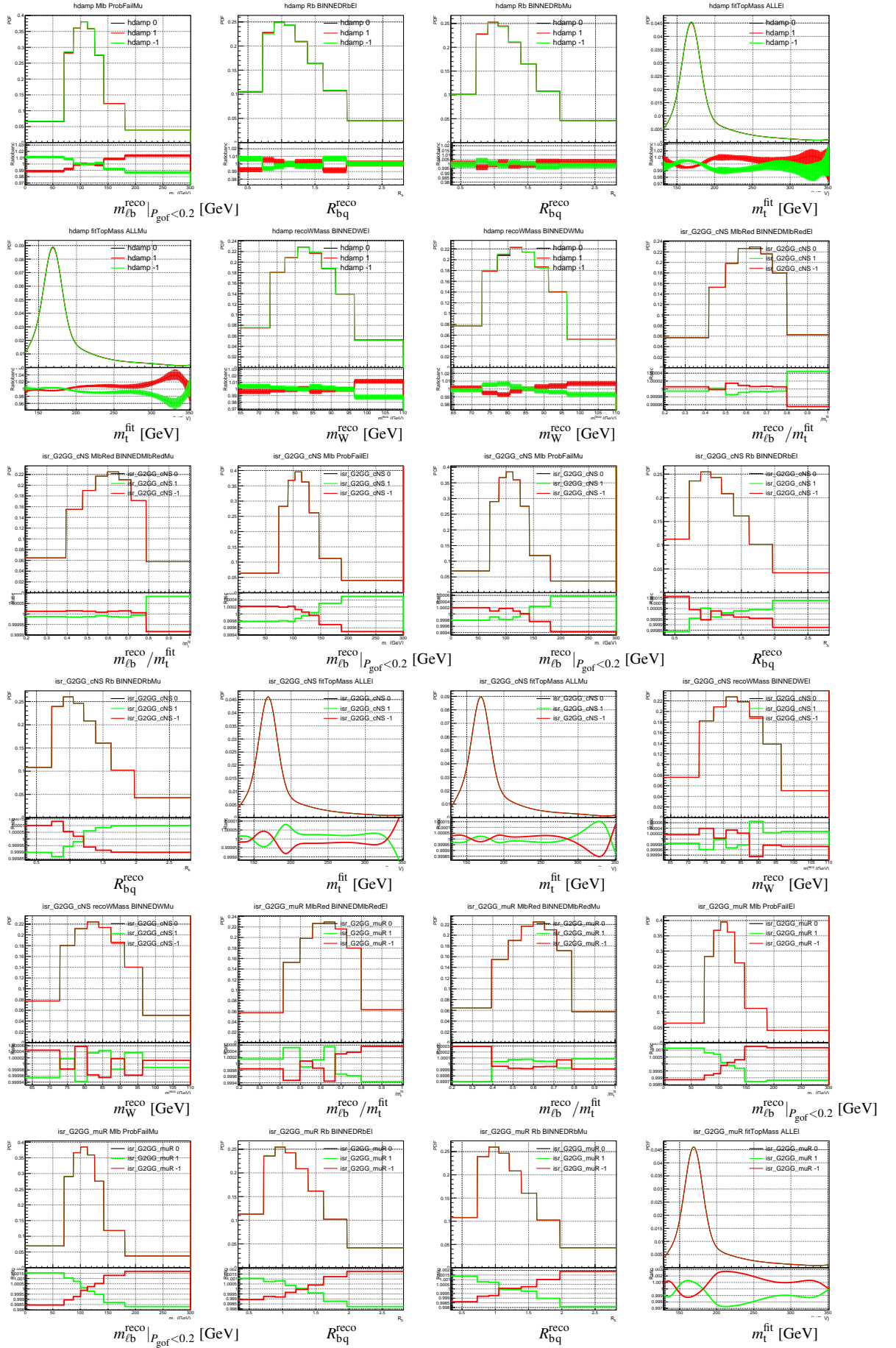


Figure D.40.: Template distribution for different observables and variations with the ratio to the template from the default simulation.

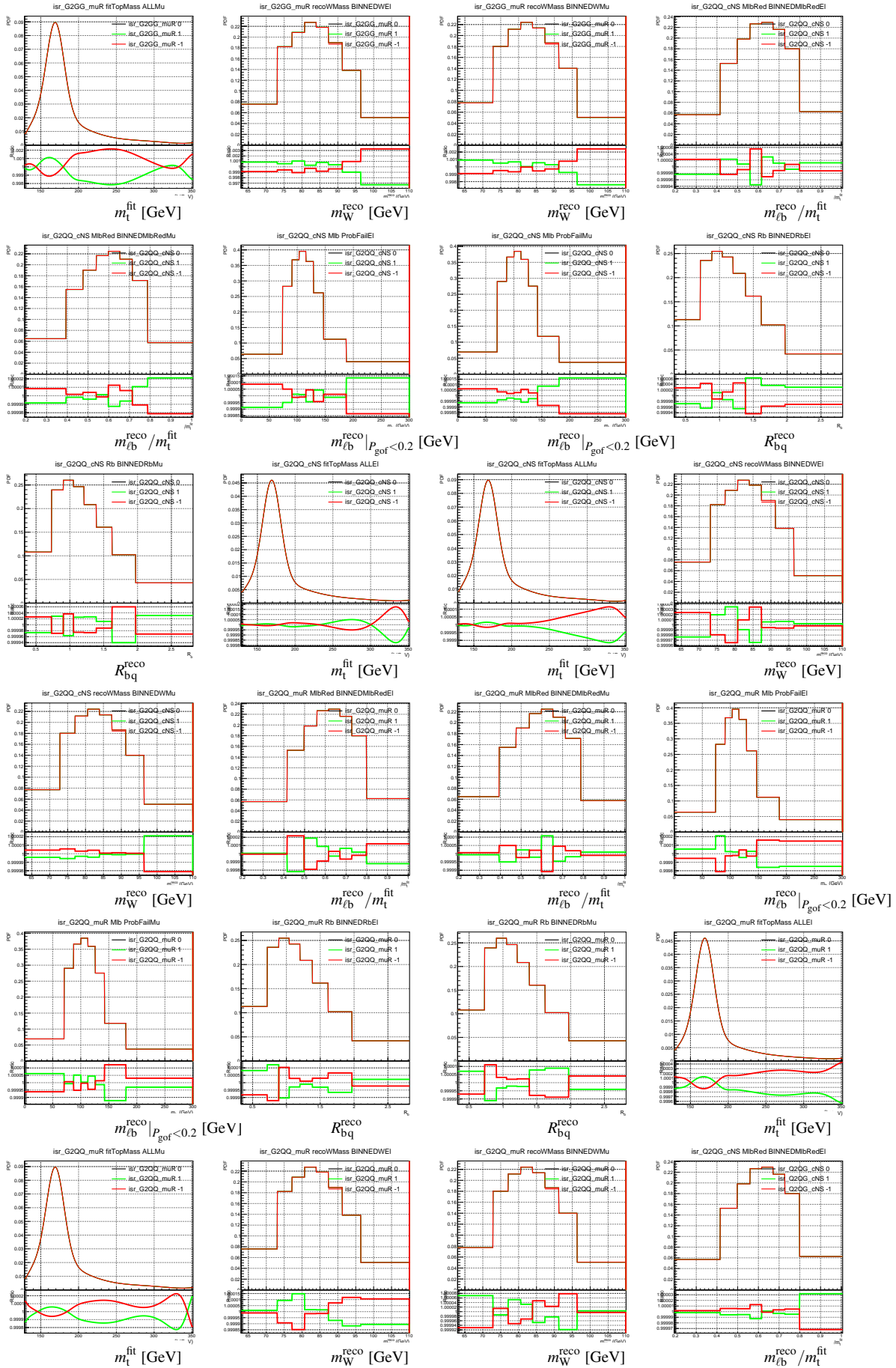


Figure D.41.: Template distribution for different observables and variations with the ratio to the template from the default simulation.

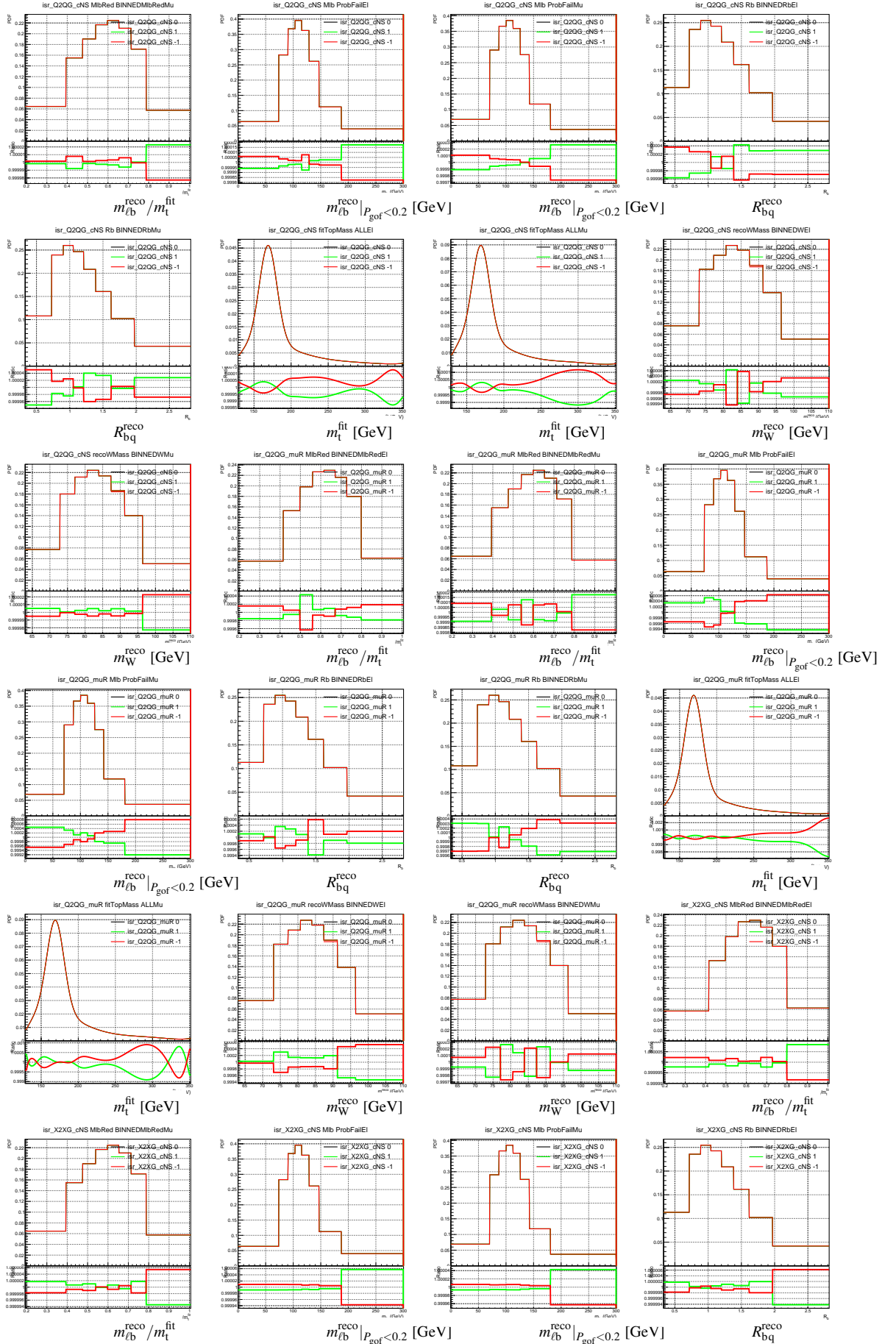


Figure D.42.: Template distribution for different observables and variations with the ratio to the template from the default simulation.

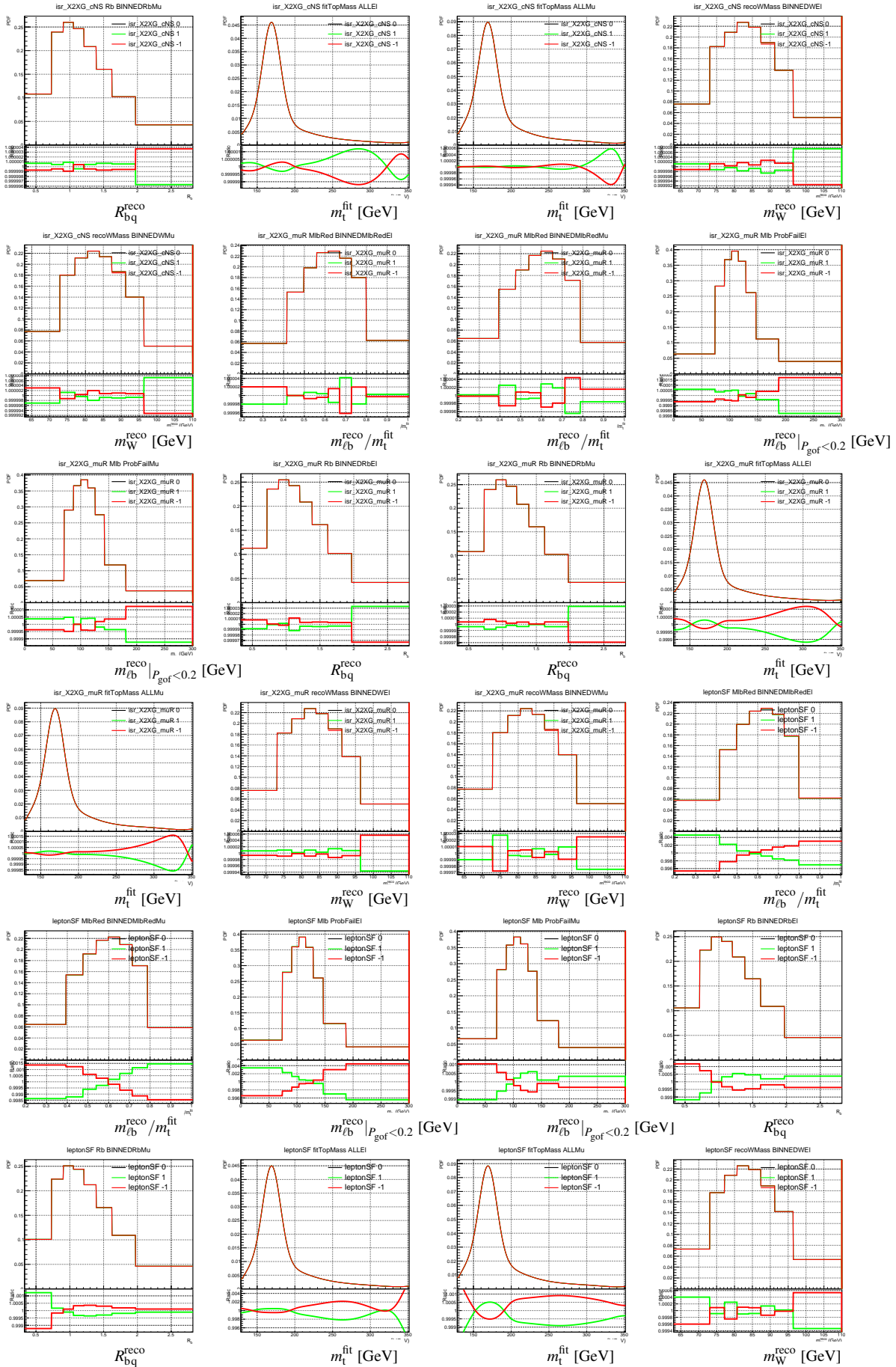


Figure D.43.: Template distribution for different observables and variations with the ratio to the template from the default simulation.

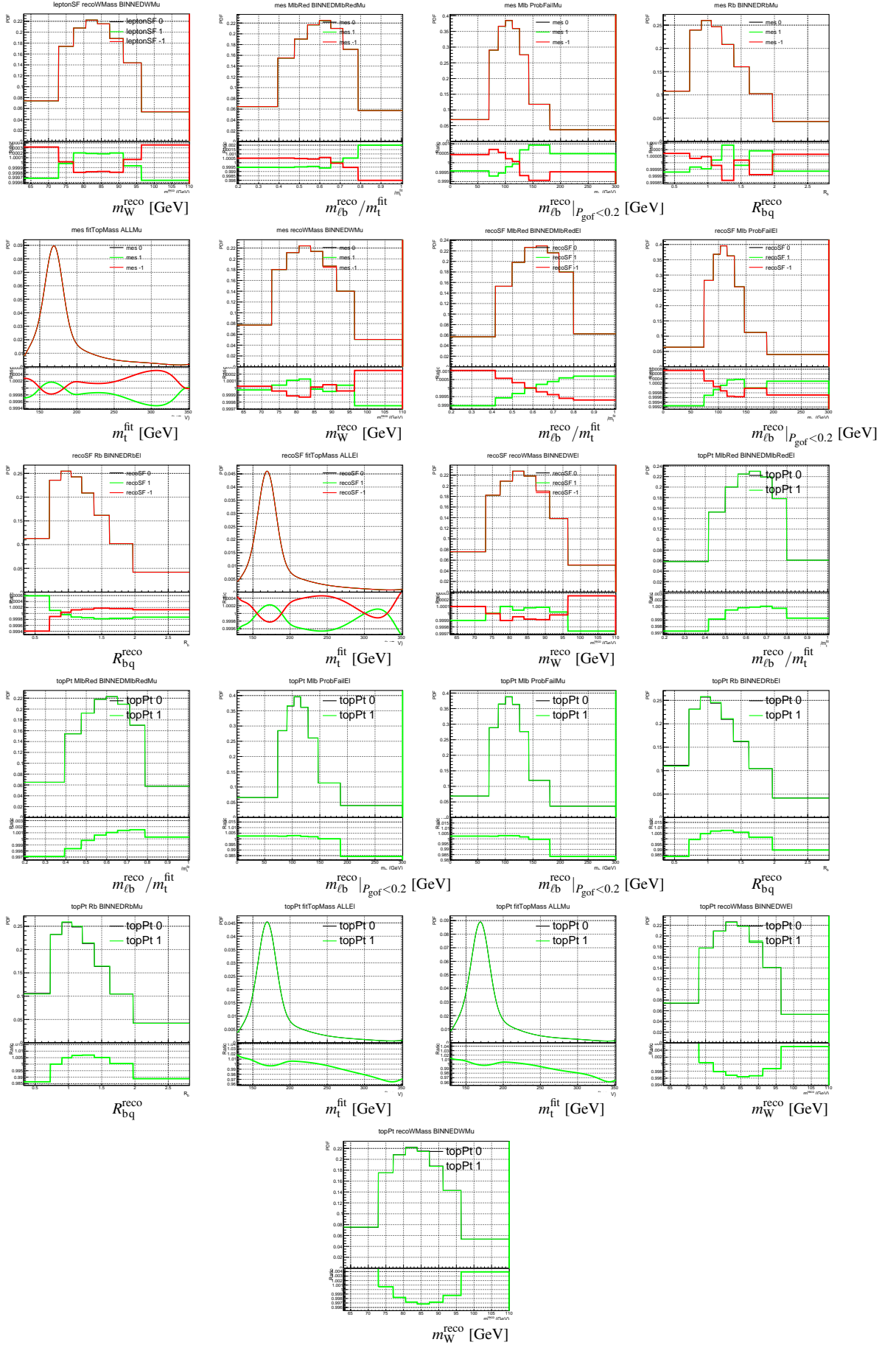


Figure D.44.: Template distribution for different observables and variations with the ratio to the template from the default simulation.

E. Bibliography

- [1] F. Abe, H. Akimoto, A. Akopian, M. G. Albrow, S. R. Amendolia, D. Amidei, J. Antos, C. Anway-Wiese, S. Aota, G. Apollinari, and et al. Observation of top quark production in $p\bar{p}$ collisions with the collider detector at fermilab. *Physical Review Letters*, 74(14):2626–2631, Apr 1995.
- [2] S. Abachi, B. Abbott, M. Abolins, B. S. Acharya, I. Adam, D. L. Adams, M. Adams, S. Ahn, H. Aihara, J. Alitti, and et al. Observation of the top quark. *Physical Review Letters*, 74(14):2632–2637, Apr 1995.
- [3] ATLAS Collaboration. First combination of Tevatron and LHC measurements of the top-quark mass. 2014.
- [4] CMS. Measurement of the top quark mass using proton-proton data at $\sqrt{s} = 7$ and 8 tev. *Phys. Rev. D*, 93:072004, Apr 2016.
- [5] S. Chatrchyan et al. The cms experiment at the cern lhc. *JINST*, 3:S08004, 2008.
- [6] Markus Seidel. *Precise measurement of the top-quark mass at the CMS experiment using the ideogram method*. PhD thesis, U. Hamburg, Dept. Phys., Hamburg, 2015.
- [7] A. M. Sirunyan, A. Tumasyan, W. Adam, F. Ambrogi, E. Asilar, T. Bergauer, J. Brandstetter, E. Brondolin, M. Dragicevic, and et al. Measurement of the top quark mass with lepton+jets final states using pp collisions at $\sqrt{s} = 13$ TeV. *The European Physical Journal C*, 78(11), Nov 2018.
- [8] Nataliia Kovalchuk, Christoph Garbers, Hartmut Stadie, Peter Schleper, Markus Seidel, and Fred Stober. Measurement of the top-quark mass in $t\bar{t}$ events with lepton+jets final states in pp collisions at $\sqrt{s} = 13$ TeV using 2016 data. CMS Analysis Note CMS AN-2016/327 [CMS internal], CERN, Geneva, 2016.
- [9] A profile likelihood approach to measure the top quark mass in the lepton+jets channel at $\sqrt{s} = 13$ TeV. Technical report, CERN, Geneva, 2022.
- [10] Cush MissMJ. Overview over the standart model of particle physics. <https://commons.wikimedia.org/w/index.php?curid=4286964>.

- [11] Particle Data Group, P A Zyla, R M Barnett, J Beringer, O Dahl, D A Dwyer, D E Groom, C J Lin, K S Lugovsky, E Pianori, D J Robinson, C G Wohl, and et al. Review of Particle Physics. *Progress of Theoretical and Experimental Physics*, 2020(8), 08 2020. 083C01.
- [12] Morad Aaboud et al. Measurement of the top quark mass in the $t\bar{t} \rightarrow$ lepton+jets channel from $\sqrt{s} = 8$ TeV ATLAS data and combination with previous results. *Eur. Phys. J. C*, 79(4):290, 2019.
- [13] Albert M Sirunyan et al. Measurement of the top quark mass in the all-jets final state at $\sqrt{s} = 13$ TeV and combination with the lepton+jets channel. *Eur. Phys. J. C*, 79(4):313, 2019.
- [14] Albert M Sirunyan et al. Measurement of the $t\bar{t}$ production cross section, the top quark mass, and the strong coupling constant using dilepton events in pp collisions at $\sqrt{s} = 13$ TeV. *Eur. Phys. J. C*, 79(5):368, 2019.
- [15] Albert M Sirunyan et al. Measurement of the top quark mass using single top quark events in proton-proton collisions at $\sqrt{s} = 8$ TeV. *Eur. Phys. J. C*, 77(5):354, 2017.
- [16] Vardan Khachatryan et al. Measurement of the top quark mass using proton-proton data at $\sqrt{s} = 7$ and 8 TeV. *Phys. Rev. D*, 93(7):072004, 2016.
- [17] D0 Collaboration CDF Collaboration. Combination of CDF and D0 results on the mass of the top quark using up 9.7 fb^{-1} at the Tevatron. 8 2016.
- [18] G. L. Fogli, E. Lisi, A. Marrone, D. Montanino, A. Palazzo, and A. M. Rotunno. Global analysis of neutrino masses, mixings and phases: entering the era of leptonic CP violation searches. *Phys. Rev.*, D86:013012, 2012.
- [19] S. Schael et al. Precision electroweak measurements on the Z resonance. *Phys. Rept.*, 427:257–454, 2006.
- [20] GORDON KANE and SCOTT WATSON. Dark matter and lhc: What is the connection? *Modern Physics Letters A*, 23(26):2103–2123, Aug 2008.
- [21] T. Aaltonen, S. Amerio, and et. al. High-precision measurement of the W boson mass with the cdf ii detector. *Science*, 376(6589):170–176, 2022.
- [22] Bernat Capdevila, Andreas Crivellin, Sébastien Descotes-Genon, Joaquim Matias, and Javier Virto. Patterns of new physics in $b \rightarrow sl+l-$ transitions in the light of recent data. *Journal of High Energy Physics*, 2018(1), Jan 2018.

- [23] B. Abi, T. Albahri, and et al. Measurement of the positive muon anomalous magnetic moment to 0.46 ppm. *Phys. Rev. Lett.*, 126:141801, Apr 2021.
- [24] B. P. Abbott and et al. Observation of gravitational waves from a binary black hole merger. *Phys. Rev. Lett.*, 116:061102, Feb 2016.
- [25] Jens Erler. Calculation of the qed coupling $\alpha(m_Z)$ in the modified minimal-subtraction scheme. *Physical Review D*, 59(5), feb 1999.
- [26] F. Abe et al. Observation of top quark production in $\bar{p}p$ collisions. *Phys.Rev.Lett.*, 74:2626–2631, 1995.
- [27] The CDF Collaboration. Observation of top quark production in pp-collisions. *Phys. Rev. Lett.*, 1995.
- [28] Scott S. Snyder. Measurement of the top quark mass at d0. Technical report, D0, 1995.
- [29] A. Quadt. Top quark physics at hadron colliders. *The European Physical Journal C - Particles and Fields*, 48(3):835–1000, 2006. 10.1140/epjc/s2006-02631-6.
- [30] CMS Collaboration. <https://twiki.cern.ch/twiki/bin/view/LHCPhysics/LHCTopWGSummaryPlots>.
- [31] A. M. Sirunyan, A. Tumasyan, W. Adam, F. Ambrogi, E. Asilar, T. Bergauer, J. Brandstetter, M. Dragicevic, J. Erö, and et al. Measurement of the $t\bar{t}$ production cross section, the top quark mass, and the strong coupling constant using dilepton events in pp collisions at $\sqrt{s} = 13$ TeV. *The European Physical Journal C*, 79(5), Apr 2019.
- [32] ATLAS Collaboration. Measurements of the top quark branching ratios into channels with leptons and quarks with the atlas detector.
- [33] M. Beneke and Vladimir M. Braun. Heavy quark effective theory beyond perturbation theory: Renormalons, the pole mass and the residual mass term. *Nucl. Phys.*, B426:301–343, 1994.
- [34] S. Moch. Precision determination of the top-quark mass, 2014.
- [35] Peter Marquard, Alexander V. Smirnov, Vladimir A. Smirnov, and Matthias Steinhauser. Four-loop relation between the \overline{MS} and on-shell quark mass. In *Proceedings, 12th International Symposium on Radiative Corrections (Radcor 2015) and LoopFest XIV (Radiative Corrections for the LHC and Future Colliders): Los Angeles, CA, USA, June 15-19, 2015*, 2016.

- [36] A.M. Sirunyan, A. Tumasyan, W. Adam, F. Ambrogi, T. Bergauer, J. Brandstetter, M. Dragicevic, J. Erö, A. Escalante Del Valle, M. Flechl, and et al. Running of the top quark mass from proton-proton collisions at $s=13\text{TeV}$. *Physics Letters B*, 803:135263, Apr 2020.
- [37] Fred Jegerlehner, Mikhail Yu. Kalmykov, and Bernd A. Kniehl. Self-consistence of the Standard Model via the renormalization group analysis. *J. Phys. Conf. Ser.*, 608(1):012074, 2015.
- [38] Mathias Butenschoen, Bahman Dehnadi, André H. Hoang, Vicent Mateu, Moritz Preisser, and Iain W. Stewart. Top quark mass calibration for monte carlo event generators. *Physical Review Letters*, 117(23), Nov 2016.
- [39] Iain W. Stewart, Frank J. Tackmann, and Wouter J. Waalewijn. N-Jettiness: An Inclusive Event Shape to Veto Jets. *Phys. Rev. Lett.*, 105:092002, 2010.
- [40] A precise interpretation for the top quark mass parameter in ATLAS Monte Carlo simulation. Technical report, CERN, Geneva, Jul 2021. All figures including auxiliary figures are available at <https://atlas.web.cern.ch/Atlas/GROUPS/PHYSICS/PUBNOTES/ATL-PHYS-PUB-2021-034>.
- [41] André H. Hoang. What is the top quark mass? *Annual Review of Nuclear and Particle Science*, 70(1):225–255, Oct 2020.
- [42] V. Khachatryan et al. Measurement of the top quark mass using proton-proton data at $\sqrt{s} = 7$ and 8 TeV. *Physical Review D*, 93(7), apr 2016.
- [43] M. Aaboud et al. Measurement of the top quark mass in the $t\bar{t}$ lepton+jets channel from $\sqrt{s}=8$ TeV ATLAS data and combination with previous results. *European Physical Journal C*, 79(4):290, April 2019.
- [44] A. M. Sirunyan, A. Tumasyan, W. Adam, F. Ambrogi, E. Asilar, T. Bergauer, J. Brandstetter, M. Dragicevic, J. Erö, and et al. Measurement of the top quark mass in the all-jets final state at $\sqrt{s} = 13$ TeV and combination with the lepton+jets channel. *The European Physical Journal C*, 79(4), Apr 2019.
- [45] Armen Tumasyan et al. Measurement of the top quark mass using events with a single reconstructed top quark in pp collisions at $\sqrt{s} = 13$ TeV. *JHEP*, 12:161, 2021.
- [46] Measurement of the top quark mass using a leptonic invariant mass in pp collisions at $\sqrt{s} = 13$ TeV with the ATLAS detector. Technical report, CERN, Geneva, Oct 2019. All figures including auxiliary figures are avail-

able at <https://atlas.web.cern.ch/Atlas/GROUPS/PHYSICS/CONFNOTES/ATLAS-CONF-2019-046>.

- [47] CMS Collaboration. Measurement of $t\bar{t}$ normalised multi-differential cross sections in pp collisions at $\sqrt{s} = 13$ tev, and simultaneous determination of the strong coupling strength, top quark pole mass, and parton distribution functions, 2019.
- [48] Sebastian Wuchterl, Katerina Lipka, and Matteo Defranchis. Measurement of the top quark pole mass using $t\bar{t}+1$ jet events with the CMS experiment. Virtual Spring Meeting of the German Physical Society, (Heidelberg) (Germany), 21 Mar 2022 - 25 Mar 2022, Mar 2022.
- [49] A. M. Sirunyan, A. Tumasyan, W. Adam, F. Ambrogi, T. Bergauer, J. Brandstetter, M. Dragicevic, J. Erö, A. Escalante Del Valle, M. Flechl, and et al. Measurement of the jet mass distribution and top quark mass in hadronic decays of boosted top quarks in pp collisions at $\sqrt{s} = 13$ tev. *Physical Review Letters*, 124(20), May 2020.
- [50] J. Haller, A. Hoecker, R. Kogler, K. Mönig, T. Peiffer, and J. Stelzer. Update of the global electroweak fit and constraints on two-higgs-doublet models. *The European Physical Journal C*, 78(8), Aug 2018.
- [51] Anders Andreassen, William Frost, and Matthew D. Schwartz. Scale-invariant instantons and the complete lifetime of the standard model. *Physical Review D*, 97(5), Mar 2018.
- [52] Stephen Myers. *The LEP Collider, from design to approval and commissioning*. John Adams' Lecture. CERN, Geneva, 1991. Delivered at CERN, 26 Nov 1990.
- [53] CERN collaboration. *Fifty years of the CERN Proton Synchrotron: Volume 1*. CERN, Geneva, 2011.
- [54] Lefèvre. Lhc preaccelerator chain. www.stfc.ac.uk/research/particle-physics-and-particle-astrophysics/large-hadron-collider/cern-accelerator-complex/.
- [55] CMS Collaboration. CMS Luminosity Measurements for the 2016 Data Taking Period. Technical Report CMS-PAS-LUM-17-001, CERN, Geneva, 2017.
- [56] CMS Collaboration. CMS luminosity measurement for the 2017 data-taking period at $\sqrt{s} = 13$ TeV. Technical Report CMS-PAS-LUM-17-004, CERN, Geneva, 2018.
- [57] CMS Collaboration. CMS luminosity 2016. https://twiki.cern.ch/twiki/bin/view/CMSPublic/LumiPublicResults#2016_proton_proton_collisions.

- [58] CERN. LHC basics. <https://press.cern/backgrounders/lhc-season-2-facts-figures>.
- [59] Oliver Sim Brüning, Paul Collier, P Lebrun, Stephen Myers, Ranko Ostojic, John Poole, and Paul Proudlock. *LHC Design Report*. CERN, Geneva, 2004.
- [60] CMS Collaboration. *CMS Physics: Technical Design Report Volume 1: Detector Performance and Software*. Technical Design Report CMS. CERN, Geneva, 2006. There is an error on cover due to a technical problem for some items.
- [61] CMS Collaboration. *CMS Physics: Technical Design Report Volume 2: Physics Performance*. Technical Design Report CMS. CERN, Geneva, 2006.
- [62] CMS Collaboration. CMS 3-d image for inclusion in presasntations - white background. <https://cms-docdb.cern.ch/cgi-bin/DocDB/ShowDocument?docid=2716>.
- [63] CMS Collaboration. CMS slice. http://commons.wikimedia.org/wiki/File:CMS_Slice.gif.
- [64] The CMS Collaboration. The CMS experiment at the CERN LHC. *Journal of Instrumentation*, 3(08):S08004–S08004, aug 2008.
- [65] Q Ingram. Energy resolution of the barrel of the CMS electromagnetic calorimeter. *Journal of Instrumentation*, 2(04):P04004–P04004, apr 2007.
- [66] *Journal of Instrumentation*, 8(09):P09009–P09009, Sep 2013.
- [67] Florian Beaudette. The CMS Particle Flow Algorithm. page 10 p, Jan 2014. Comments: 10 pages, 12 figures, proceedings for CHEF2013, Paris, France, April 2013.
- [68] CMS Collaboration. tt event display example. https://twiki.cern.ch/twiki/bin/view/CMSPublic/PhysicsResultsTOPEventDisplays#top_pair_production.
- [69] Frank Siegert. *Monte-Carlo event generation for the LHC*. PhD thesis, Durham U., 2010.
- [70] A. M. Cooper-Sarkar. PDF Fits at HERA. *PoS*, EPS-HEP2011:320, 2011.
- [71] Stefano Forte and Stefano Carrazza. Parton distribution functions, 2020.

- [72] L. A. Harland-Lang, A. D. Martin, P. Motylinski, and R. S. Thorne. Parton distributions in the LHC era: MMHT 2014 PDFs. *The European Physical Journal C*, 75(5), May 2015.
- [73] The NNPDF Collaboration, Richard D. Ball, Valerio Bertone, Stefano Carrazza, Luigi Del Debbio, Stefano Forte, Patrick Groth-Merrild, Alberto Guffanti, Nathan P. Hartland, Zahari Kassabov, José I. Latorre, Emanuele R. Nocera, Juan Rojo, Luca Rottoli, Emma Slade, and Maria Ubiali. Parton distributions from high-precision collider data, 2017.
- [74] Simone Alioli, Paolo Nason, Carlo Oleari, and Emanuele Re. A general framework for implementing NLO calculations in shower Monte Carlo programs: the POWHEG BOX. *JHEP*, 06:043, 2010.
- [75] Johan Alwall, Michel Herquet, Fabio Maltoni, Olivier Mattelaer, and Tim Stelzer. Madgraph 5 : Going beyond. *JHEP*, 1106:128, 2011.
- [76] J. Alwall, R. Frederix, S. Frixione, V. Hirschi, F. Maltoni, O. Mattelaer, H.-S. Shao, T. Stelzer, P. Torrielli, and M. Zaro. The automated computation of tree-level and next-to-leading order differential cross sections, and their matching to parton shower simulations. *Journal of High Energy Physics*, 2014(7):1–157, 2014.
- [77] John C. Collins. Sudakov form-factors. *Adv. Ser. Direct. High Energy Phys.*, 5:573–614, 1989.
- [78] Bo Andersson, G. Gustafson, G. Ingelman, and T. Sjostrand. Parton Fragmentation and String Dynamics. *Phys. Rept.*, 97:31–145, 1983.
- [79] The Atlas Collaboration. Comparison of Monte Carlo generator predictions for bottom and charm hadrons in the decays of top quarks and the fragmentation of high p_T jets. Technical report.
- [80] T. Aaltonen, M. Albrow, S. Amerio, D. Amidei, A. Anastassov, A. Annovi, J. Antos, G. Apollinari, J. A. Appel, T. Arisawa, and et al. Study of the energy dependence of the underlying event in proton-antiproton collisions. *Physical Review D*, 92(9), Nov 2015.
- [81] The CMS Collaboration. Measurement of the Underlying Event Activity at the LHC at 7 TeV and Comparison with 0.9 TeV. Technical Report CMS-PAS-FSQ-12-020, CERN, Geneva, 2012.
- [82] CMS Collaboration. Investigations of the impact of the parton shower tuning in Pythia 8 in the modelling of $t\bar{t}$ at $\sqrt{s}=8$ and 13 TeV. Technical Report CMS-PAS-TOP-16-021, CERN, Geneva, 2016.

- [83] A. M. Sirunyan, A. Tumasyan, W. Adam, F. Ambroggi, E. Asilar, T. Bergauer, J. Brandstetter, M. Dragicevic, J. Erö, and et al. Extraction and validation of a new set of cms pythia8 tunes from underlying-event measurements. *The European Physical Journal C*, 80(1), Jan 2020.
- [84] T Sjöstrand and P Skands. Multiple interactions and the structure of beam remnants. *Journal of High Energy Physics*, 2004(03):053–053, Mar 2004.
- [85] Jesper R. Christiansen and Peter Z. Skands. String formation beyond leading colour. *Journal of High Energy Physics*, 2015(8), Aug 2015.
- [86] Spyros Argyropoulos and Torbjörn Sjöstrand. Effects of color reconnection on $t\bar{t}$ final states at the LHC. *Journal of High Energy Physics*, 2014(11), Nov 2014.
- [87] CMS collaboration. Extraction and validation of a new set of CMS tunes with new color reconnection models in PYTHIA8 from underlying-event measurements. 2020.
- [88] S. Agostinelli et al. Geant4—a simulation toolkit. *Nuclear Instruments and Methods in Physics Research Section A: Accelerators, Spectrometers, Detectors and Associated Equipment*, 506(3):250 – 303, 2003.
- [89] Fons Rademakers. root-project/root: v6.18/02, 2019.
- [90] G Petrucciani, A Rizzi, and C Vuosalo. Mini-AOD: A new analysis data format for CMS. *Journal of Physics: Conference Series*, 664(7):072052, dec 2015.
- [91] Serguei Chatrchyan et al. Description and performance of track and primary-vertex reconstruction with the CMS tracker. *JINST*, 9(10):P10009, 2014.
- [92] The CMS Collaboration. Particle-Flow Event Reconstruction in CMS and Performance for Jets, Taus, and MET. Technical Report CMS-PAS-PFT-09-001, CERN, 2009. Geneva, Apr 2009.
- [93] CMS Collaboration. Commissioning of the particle-flow reconstruction in minimum-bias and jet events from pp collisions at 7 TeV. CMS Physics Analysis Summary CMS-PAS-PFT-10-002, CERN, 2010.
- [94] Serguei Chatrchyan et al. Performance of CMS muon reconstruction in pp collision events at $\sqrt{s} = 7$ TeV. *JINST*, 7:P10002, 2012.
- [95] A. Bodek, A. van Dyne, J. Y. Han, W. Sakumoto, and A. Strelnikov. Extracting muon momentum scale corrections for hadron collider experiments. *The European Physical Journal C*, 72(10), Oct 2012.

- [96] Aleko Khukhunaishvili Arie Bodek. Rochester corrections for 2017 ul. <https://indico.cern.ch/event/926898/contributions/3897122/attachments/2052816/3441285/roccor.pdf>.
- [97] CMS collaboration. Particle-flow reconstruction and global event description with the CMS detector. *Journal of Instrumentation*, 12(10):P10003–P10003, Oct 2017.
- [98] Matteo Cacciari and Gavin P. Salam. Dispelling the N^3 myth for the kt jet-finder. *Phys. Lett. B*, 641:57, 2006.
- [99] Matteo Cacciari, Gavin P. Salam, and Gregory Soyez. The Anti-k(t) jet clustering algorithm. *JHEP*, 0804:063, 2008.
- [100] Maryam Zeinali. Measurement of the Jet Energy Scale in the CMS experiment with the First LHC Proton Collisions.
- [101] S. Eno, D. Ferencek, I. Iashvili, and M. Zielinski. Offset Energy Correction for Cone Jets. http://cms.cern.ch/iCMS/jsp/db_notes/noteInfo.jsp?cmsnoteid=CMS%20AN-2009/035, May 2009.
- [102] The CMS Collaboration. Jet energy scale and resolution performance with 13 TeV data collected by CMS in 2016.
- [103] Henning Kirschenmann. Jet performance in CMS. Technical Report CMS-CR-2013-325, CERN, Geneva, Oct 2013.
- [104] Matteo Cacciari and Gavin P. Salam. Pileup subtraction using jet areas. *Phys. Lett. B*, 659:119, 2008.
- [105] Matteo Cacciari, Gavin P. Salam, and Gregory Soyez. The catchment area of jets. *JHEP*, 04:005, 2008.
- [106] Matteo Cacciari, Gavin P. Salam, and Gregory Soyez. FastJet user manual. , 2011.
- [107] V. Khachatryan, A.M. Sirunyan, A. Tumasyan, W. Adam, E. Asilar, T. Bergauer, J. Brandstetter, E. Brondolin, M. Dragicevic, J. Erö, and et al. Jet energy scale and resolution in the cms experiment in pp collisions at 8 tev. *Journal of Instrumentation*, 12(02):P02014–P02014, Feb 2017.
- [108] The CMS collaboration. Determination of jet energy calibration and transverse momentum resolution in cms. *Journal of Instrumentation*, 6(11):P11002–P11002, Nov 2011.

- [109] CMS Collaboration. Jet resolution 2016. <https://twiki.cern.ch/twiki/bin/viewauth/CMS/JetResolution>.
- [110] Vardan Khachatryan et al. Performance of the CMS missing transverse momentum reconstruction in pp data at $\sqrt{s} = 8$ TeV. *JINST*, 10(02):P02006, 2015.
- [111] F Stober, M Fischer, P Schleper, H Stadie, C Garbers, J Lange, and N Kovalchuk. The swiss army knife of job submission tools: grid-control. *Journal of Physics: Conference Series*, 898:092052, Oct 2017.
- [112] Torbjörn Sjöstrand, Stefan Ask, Jesper R. Christiansen, Richard Corke, Nishita Desai, Philip Ilten, Stephen Mrenna, Stefan Prestel, Christine O. Rasmussen, and Peter Z. Skands. An Introduction to PYTHIA 8.2. *Comput. Phys. Commun.*, 191:159–177, 2015.
- [113] The CMS Collaboration. Extraction and validation of a new set of CMS PYTHIA8 tunes from underlying-event measurements. Technical report.
- [114] S. Agostinelli et al. GEANT4 – a simulation toolkit. *Nucl. Instrum. Meth. A*, 506:250, 2003.
- [115] Michał Czakon, Paul Fiedler, and Alexander Mitov. Total Top-Quark Pair-Production Cross Section at Hadron Colliders Through $O(\alpha_s^4)$. *Phys. Rev. Lett.*, 110:252004, 2013.
- [116] Nikolaos Kidonakis. Next-to-next-to-leading soft-gluon corrections for the top quark cross section and transverse momentum distribution. *Phys. Rev. D*, 82:114030, 2010.
- [117] Nikolaos Kidonakis. Differential and total cross sections for top pair and single top production. In *Proceedings, 20th International Workshop on Deep-Inelastic Scattering and Related Subjects (DIS 2012)*, pages 831–834, 2012. [,831(2012)].
- [118] Kirill Melnikov and Frank Petriello. Electroweak gauge boson production at hadron colliders through $O(\alpha_s^2)$. *Phys. Rev. D*, 74:114017, 2006.
- [119] John M. Campbell and R. K. Ellis. MCFM for the Tevatron and the LHC. *Nucl. Phys. Proc. Suppl.*, 205-206:10, 2010.
- [120] John M. Campbell, J. W. Huston, and W. J. Stirling. Hard Interactions of Quarks and Gluons: A Primer for LHC Physics. *Rept. Prog. Phys.*, 70:89, 2007.
- [121] Michał Czakon and Alexander Mitov. Top++: A Program for the Calculation of the Top-Pair Cross-Section at Hadron Colliders. *Comput. Phys. Commun.*, 185:2930, 2014.

- [122] J. Ohnemus. Order α^{-s} calculations of hadronic $W^{\pm}\gamma$ and $Z\gamma$ production. *Phys. Rev.*, D47:940–955, 1993.
- [123] U. Baur, Tao Han, and J. Ohnemus. QCD corrections to hadronic $W\gamma$ production with nonstandard $WW\gamma$ couplings. *Phys. Rev.*, D48:5140–5161, 1993.
- [124] Nikolaos Kidonakis. Top quark production, 2013.
- [125] Dominic Hirscheuhl. t-channel cross section calculations. <https://indico.cern.ch/event/301787/contributions/690341/>.
- [126] CMS Collaboration. Muon isolation. https://twiki.cern.ch/twiki/bin/view/CMS/SWGuideMuonIdRun2#Muon_Isolation.
- [127] CMS Collaboration. Cms top egamma coordination (run2). <https://twiki.cern.ch/twiki/pub/CMS/TopEGM>.
- [128] Gaël L. Perrin and Luca Perrozzi. Update on Muon reRECO Scale-Factors, 2016.
- [129] M. Goerner M. Aldaya. Measurement of differential top-quark-pair production cross sections in e/μ +jets final states at $\sqrt{s} = 8$ TeV. CMS Analysis Note CMS AN-2013/267 [CMS internal], CERN, Geneva, 2014.
- [130] CMS Collaboration. Summary performance plots for 2016 data. <https://twiki.cern.ch/twiki/bin/view/CMSPublic/HLTplotsSummary2016>.
- [131] Andrey Popov. Sf of hlt_ele25_eta2p1_wptight_gsf and hlt_ele27_wptight_gsf for heavy higgs analysis. <https://indico.cern.ch/event/604912/contributions/2490011/>.
- [132] CMS Collaboration. Top muon information for analysis (run 2). <https://twiki.cern.ch/twiki/pub/CMS/TopMU0>.
- [133] T. Chwalek and A. De Iorio and N. Faltermann, A. Giammanco, Alberto Orso Maria Iorio, W.A. Khan, M. Komm, L. Lista, Th. Muller, , and P. Ott. Selection for the single top t-channel analyses with the 2016 dataset at 13 tev. CMS Note 2017/057 [CMS internal], CERN, 2019.
- [134] CMS Collaboration. 94x series - fall17v2 scale factors for 2016 legacy re-reco. https://twiki.cern.ch/twiki/bin/view/CMS/EgammaIDRecipesRun2#94X_series_Fall17V2_Scale_fa_AN1.
- [135] CMS Collaboration. Jet identification for the 13 tev data run2016. <https://twiki.cern.ch/twiki/bin/view/CMS/JetID13TeVRun2016>.

- [136] Verzetti, Mauro. Machine learning techniques for jet flavour identification at cms. *EPJ Web Conf.*, 214:06010, 2019.
- [137] Gouskos Loukas, Kieseler Jan, Qu Huilin, Stoye Markus, Verzetti Mauro, Majumder Devdatta, Moortgat Seth, Sphicas Paris, Stakia Anna, and Vernieri Caterina. Deep learning for jet reconstruction. CMS Analysis Note CMS AN-2017/188 [CMS internal], CERN, Geneva, 2017.
- [138] Mauro Verzetti Jan Kieseler, Markus Stoye. DeepJet: Framework for the development of deep-neural-network based reconstruction in high-energy-physics. CMS Analysis Note CMS AN-2017/126 [CMS internal], CERN, Geneva, 2017.
- [139] CMS Collaboration. Heavy flavour tagging for 13 tev 2016 legacy data (run2). <https://twiki.cern.ch/twiki/bin/viewauth/CMS/BtagRecommendation2016Legacy>.
- [140] CMS Collaboration. Methods to apply b-tagging efficiency scale factors. https://twiki.cern.ch/twiki/bin/viewauth/CMS/BTagSfMethods#1a_Event_reweighting_using_scale.
- [141] Measurement of the energy asymmetry in top quark pair production at 13 TeV. Chwalek, Thorsten and Faltermann, Nils and Rauser, Johann Vincent. CMS Analysis Note CMS AN-2019/223 [CMS internal], CERN, Geneva, 2021.
- [142] B. et al. Abbott. Direct measurement of the top quark mass at d0. *Phys.Rev.*, D58:052001, 1998.
- [143] CMS Collaboration. Measurement of the top-quark mass in $t\bar{t}$ events with lepton+jets final states in pp collisions at $\sqrt{s}=7$ tev. *J. High Energy Phys.*, 12(arXiv:1209.2319. CMS-TOP-11-015. CERN-PH-EP-2012-250):105. 33 p, Sep 2012.
- [144] Markus Seidel. *Precise measurement of the top-quark mass at the CMS experiment using the ideogram method*. PhD thesis, U. Hamburg, Dept. Phys., Hamburg, 2015.
- [145] S. Chatrchyan, V. Khachatryan, A. M. Sirunyan, A. Tumasyan, W. Adam, E. Aguilo, T. Bergauer, M. Dragicevic, J. Erö, and et al. Measurement of the top-quark mass in $t\bar{t}$ events with lepton+jets final states in pp collisions at $\sqrt{s} = 7$ tev. *Journal of High Energy Physics*, 2012(12), Dec 2012.
- [146] Albert M Sirunyan et al. Measurement of the top quark mass with lepton+jets final states using pp collisions at $\sqrt{s} = 13$ TeV. *Eur. Phys. J. C*, 78:891, 2018.
- [147] Vardan Khachatryan et al. Jet energy scale and resolution in the CMS experiment in pp collisions at 8 TeV. *JINST*, 12:P02014, 2017.

- [148] CMS Collaboration. Jec uncertainty sources 2016. https://twiki.cern.ch/twiki/bin/view/CMS/JECUncertaintySources#Main_uncertainties_2016_80X.
- [149] S. Abdullin, P. Azzi, F. Beaudette, P. Janot, and A. Perrotta. The fast simulation of the CMS detector at LHC. *J. Phys. Conf. Ser.*, 331:032049, 2011.
- [150] Serguei Chatrchyan et al. The performance of the CMS muon detector in proton-proton collisions at $\sqrt{s} = 7$ TeV at the LHC. *JINST*, 8:P11002, 2013.
- [151] CMS Collaboration. Muon scale factor. <https://twiki.cern.ch/twiki/bin/view/CMS/MuonReferenceEfts2016LegacyRereco>.
- [152] CMS Collaboration. Electron scale factor. https://twiki.cern.ch/twiki/bin/view/CMS/EgammaIDRecipesRun2#94X_series_Fall17V2_Scale_fa_AN1.
- [153] Emil Bols, Jan Kieseler, Mauro Verzetti, Markus Stoye, and Anna Stakia. Jet Flavour Classification Using DeepJet. *Submitted to: JINST*, 2020.
- [154] CMS Collaboration. Performance of the DeepJet b tagging algorithm using 41.9/fb of data from proton-proton collisions at 13 TeV with Phase 1 CMS detector. CMS Detector Performance Note CMS-DP-2018-058, CMS, 2018.
- [155] et al. Shima Abu Zeid. Performance of b-tagging algorithms at 13 TeV. CMS Analysis Note CMS AN-2016/036 [CMS internal], CERN, Geneva, 2016.
- [156] Hesham El Faham, Hamed Bakhshiansohi, and Andrea Giammanco. Pileup 2016-2018 studie. <https://indico.cern.ch/event/866775/#2-2016-2018-pileup-reweighting>.
- [157] Vardan Khachatryan et al. Measurement of the WZ production cross section in pp collisions at $\sqrt{s} = 13$ TeV. *Phys. Lett. B*, 766:268, 2017.
- [158] Albert M Sirunyan et al. Measurements of the $pp \rightarrow ZZ$ production cross section and the $Z \rightarrow 4\ell$ branching fraction, and constraints on anomalous triple gauge couplings at $\sqrt{s} = 13$ TeV. *Eur. Phys. J. C*, 78:165, 2018.
- [159] V. Khachatryan et al. Measurements of the associated production of a Z boson and b jets in pp collisions at $\sqrt{s} = 8$ TeV. *Eur. Phys. J. C*, 77:751, 2017.
- [160] Vardan Khachatryan et al. Measurement of the t-channel single-top-quark production cross section and of the $|V_{tb}|$ CKM matrix element in pp collisions at $\sqrt{s} = 8$ TeV. *JHEP*, 06:090, 2014.

- [161] Albert M Sirunyan et al. Cross section measurement of t -channel single top quark production in pp collisions at $\sqrt{s} = 13$ TeV. *Phys. Lett. B*, 772:752, 2017.
- [162] Vardan Khachatryan et al. Measurement of the production cross section of a W boson in association with two b jets in pp collisions at $\sqrt{s} = 8$ TeV. *Eur. Phys. J. C.*, 77:92, 2017.
- [163] Torbjorn Sjostrand, Stephen Mrenna, and Peter Z. Skands. PYTHIA 6.4 Physics and Manual. *JHEP*, 05:026, 2006.
- [164] Manuel Bähr, Stefan Gieseke, Martyn A. Gigg, David Grellscheid, Keith Hamilton, Oluseyi Latunde-Dada, Simon Plätzer, Peter Richardson, Michael H. Seymour, Alexander Sherstnev, and Bryan R. Webber. Herwig++ physics and manual. *Eur. Phys. J. C*, 58:639, 2008.
- [165] The CMS Collaboration. Measurement of the inclusive and differential tt production cross sections in lepton + jets final states at 13 TeV. Technical Report CMS-PAS-TOP-16-008, CERN, Geneva, 2016.
- [166] A. Heister et al. Study of the fragmentation of b quarks into B mesons at the Z peak. *Phys. Lett. B*, 512:30–48, 2001.
- [167] J. Abdallah et al. A study of the b-quark fragmentation function with the DELPHI detector at LEP I and an averaged distribution obtained at the Z Pole. *Eur. Phys. J. C*, 71:1557, 2011.
- [168] Sébastien Wertz. Update on b fragmentation uncertainties. https://indico.cern.ch/event/1004752/contributions/4222610/attachments/2186283/3694054/210208_bFragmentation.pdf.
- [169] C. Peterson, D. Schlatter, I. Schmitt, and P. M. Zerwas. Scaling violations in inclusive e^+e^- annihilation spectra. *Phys. Rev. D*, 27:105–111, Jan 1983.
- [170] Particle Data Group, P. A. Zyla, et al. Review of particle physics. *Prog. Theor. Exp. Phys.*, 2020:083C01, 2020.
- [171] Sayipjamal Dulat, Tie-Jiun Hou, Jun Gao, Marco Guzzi, Joey Huston, Pavel Nadolsky, Jon Pumplin, Carl Schmidt, Daniel Stump, and C.-P. Yuan. New parton distribution functions from a global analysis of quantum chromodynamics. *Physical Review D*, 93(3), Feb 2016.
- [172] The CMS Collaboration. Measurement of t t-bar production with additional jet activity, including b quark jets, in the dilepton channel using pp collisions at $\sqrt{s} = 8$ tev. *The European Physical Journal C*, 76(7), jul 2016.

- [173] Josh Bendavid. New mc features for analysis in 74x plus more details on scale/pdf uncertainties. <https://indico.cern.ch/event/494682/contributions/1172505/>.
- [174] W. T. Giele, D. A. Kosower, and P. Z. Skands. Higher-order corrections to timelike jets. *Physical Review D*, 84(5), Sep 2011.
- [175] S. Mrenna and P. Skands. Automated parton-shower variations in pythia 8. *Physical Review D*, 94(7), Oct 2016.
- [176] Serguei Chatrchyan et al. Measurement of differential top-quark pair production cross sections in pp collisions at $\sqrt{s} = 7$ TeV. *Eur. Phys. J. C*, 73:2339, 2013.
- [177] CMS Collaboration. Measurement of differential top-quark pair production cross sections in the lepton+jets channel in pp collisions at 8 TeV. Technical Report CMS-PAS-TOP-12-027, CERN, Geneva, 2013.
- [178] CMS Collaboration. Measurement of the differential $t\bar{t}$ cross section in the dilepton channel at 8 TeV. Technical Report CMS-PAS-TOP-12-028, CERN, Geneva, 2013.
- [179] The CMS Collaboration. Top quark pair differential cross sections in the dilepton channel at 13 TeV. Technical Report CMS-PAS-TOP-16-011, CERN, Geneva, 2016.
- [180] CMS Collaboration. Top pag corrections based on data aka data-nlo and data-nnlo weights. https://twiki.cern.ch/twiki/bin/view/CMS/TopPtRewighting#TOP_PAG_corrections_based_on_dat.
- [181] Peter Skands, Stefano Carrazza, and Juan Rojo. Tuning PYTHIA 8.1: the Monash 2013 Tune. *Eur. Phys. J. C*, 74:3024, 2014.
- [182] Albert M Sirunyan et al. Extraction and validation of a new set of CMS PYTHIA8 tunes from underlying-event measurements. *Eur. Phys. J. C*, 80(1):4, 2020.
- [183] Peter Z. Skands and Daniel Wicke. Non-perturbative QCD effects and the top mass at the Tevatron. *Eur. Phys. J. C*, 52:133, 2007.
- [184] A.M. Sirunyan, A. Tumasyan, W. Adam, E. Asilar, T. Bergauer, J. Brandstetter, E. Brondolin, M. Dragicevic, J. Erö, M. Flechl, and et al. Measurement of the top quark mass in the dileptonic $t\bar{t}$ decay channel using the mass observables m_{bl} , m_{t2} , and m_{blv} in pp collisions at $\sqrt{s}=8$ tev. *Physical Review D*, 96(3), Aug 2017.
- [185] Munira Khan. Lorentz-invariante observablen zur topquark-massenmessung am lhc.

- [186] Roger Barlow and Christine Beeston. Fitting using finite monte carlo samples. *Computer Physics Communications*, 77(2):219 – 228, 1993.
- [187] Christoph Garbers, Hartmut Stadie, Peter Schleper, and Seidel. A profiled likelihood approach to measure the top quark mass. CMS Analysis Note CMS AN-2019/284 [CMS internal], CERN, Geneva, 2021.
- [188] V. M. Abazov, B. Abbott, and et al. Precise measurement of the top-quark mass from lepton+jets events at d0. *Physical Review D*, 84(3), Aug 2011.
- [189] J. de Blas, M. Pierini, L. Reina, and L. Silvestrini. Impact of the recent measurements of the top-quark and w-boson masses on electroweak precision fits, 2022.
- [190] Electroweak measurements in electron–positron collisions at w-boson-pair energies at LEP. *Physics Reports*, 532(4):119–244, nov 2013.
- [191] ATLAS collaboration. Measurement of the w-boson mass in pp collisions at $\sqrt{s} = 7$ TeV with the ATLAS detector. *The European Physical Journal C*, 78(2), feb 2018.
- [192] LHCb collaboration. Measurement of the w boson mass. *Journal of High Energy Physics*, 36(1), jan 2022.
- [193] J. de Blas, M. Ciuchini, E. Franco, A. Goncalves, S. Mishima, M. Pierini, L. Reina, and L. Silvestrini. Global analysis of electroweak data in the standard model, 2021.
- [194] K. Nowak and A.F. Żarnecki. Optimising top-quark threshold scan at CLIC using genetic algorithm. *Journal of High Energy Physics*, 2021(7), jul 2021.

List of Figures

2.1. Overview over the standard model of particle physics	4
2.2. Leading order $t\bar{t}$ production diagrams	9
2.3. Summary of top-pair production cross section measurement	10
2.4. Dependence of the MSR mass on the input m_t^{MC} value	15
2.5. Summary of example top-quark mass measurement results.	16
2.6. Fit of the electroweak sector of the standard model	18
2.7. Phase diagram for stability in the $m_t^{\text{pole}}/m_h^{\text{pole}}$ plane of the SM	19
3.1. Schematic overview of the LHC pre-accelerator chain [54].	22
3.2. CMS Luminosity 2016	23
3.3. CMS detector overview	25
3.4. CMS detector cut through the ϕ -plane	26
3.5. CMS tracker schematic	27
3.6. Event display of a top-quark pair candidate in x-y views	29
3.7. Mean number of interactions per bunch crossing for the 2016 pp run at 13 TeV	30
4.1. Pictorial representation of a $t\bar{t}h$ event as produced by an event generator . .	32
4.2. The MMHT 2014 NNLO parton distribution function	33
4.3. PDF comparison	33

5.1. Consecutive stages of JEC	39
5.2. Properties of the jet performance	40
6.1. Comparison of UE tunes	45
6.2. The single-muon trigger efficiencies	50
6.3. The single-electron trigger efficiencies	50
6.4. Lepton identification and isolation scale factors	51
6.5. Schematic of the DEEPJET neural network algorithm [137].	53
6.6. Performance of the different heavy flavor tagging algorithms	53
6.7. Lepton+jets: lepton kinematic	56
6.8. Muon+jets: lepton kinematic	56
6.9. Electron+jets: lepton kinematic	56
6.10. Lepton+jets: jet properties	57
6.11. Muon+jets: jet properties	57
6.12. Electron+jets: jet properties	57
6.13. Lepton+jets: jet p_T	58
6.14. Muon+jets: jet p_T	58
6.15. Electron+jets: jet p_T	59
6.16. Lepton+jets: mass distributions of the W-boson and the top-quark	60
6.17. Lepton+jets: χ^2 and resulting P_{gof} from the kinematic fit	63
6.18. Muon+jets: χ^2 and resulting P_{gof} from the kinematic fit	63
6.19. Electron+jets: χ^2 and resulting P_{gof} from the kinematic fit	63
6.20. Lepton+jets: top-quark mass distribution	64

6.21. Muon+jets: top-quark mass distribution	64
6.22. Electron+jets: top-quark mass distribution	64
6.23. Muon+jets: Top quark decay channels in simulation	65
6.24. Electron+jets: Top quark decay channels in simulation	66
7.1. Number of pile up events	70
7.2. Ratio of the top p_T measured in CMS data to theory predictions	73
8.1. Mean errors of nuisance parameters with single observables	77
8.2. Correlation and profiles between different observables	79
8.3. Muon+jets simulation: independence checks between m_W^{reco} and $R_{\text{bq}}^{\text{reco}}$	79
8.4. Lepton+jets: Distributions of the used observables	80
8.5. Muon+jets: Distributions of the used observables	81
8.6. Electron+jets: Distributions of the used observables	82
8.7. Muon+Jets: Slopes in the template parameterization	88
8.8. Electron+Jets: Slopes in the template parameterization	89
8.9. Muon+jets: The observable distribution for different top-quark mass values	90
8.10. Electron+jets: The observable distribution for different top-quark mass values	91
8.11. Generated values for the three important example parameters.	92
8.12. Pull distributions $\frac{\theta - \theta^{\text{gen}}}{\Delta\theta}$ for the FlavorPureBottom nuisance	92
8.13. Pull distributions $\frac{\theta - \theta^{\text{gen}}}{\Delta\theta}$ for the CR_GluonMove nuisance	93
8.14. Pull distributions $\frac{\theta - \theta^{\text{gen}}}{\Delta\theta}$ for m_t	94
8.15. Validation of the overall mass extraction method	95

8.16. Closure test in muon+jets simulation	97
8.17. Lepton+jets 5D: Correlation matrix between the nuisance parameters	99
8.18. Lepton+jets single observables: Correlation matrices between nuisance parameters	100
9.1. The predicted and measured total uncertainty on m_t with different observable selections	102
9.2. Example comparisons of the predicted nuisance impacts and nuisance pull width	103
9.3. Lepton+jets simulation: Biggest predicted uncertainty nuisance impacts and pulls	104
9.4. Muon+jets simulation: Biggest predicted uncertainty nuisance impacts and pulls	105
9.5. Electron+jets simulation: Biggest predicted uncertainty nuisance impacts and pulls	106
9.6. Post-fit templates	107
9.7. The total uncertainty on m_t from single observables	108
9.8. Muon+jets: The pull mean and width and impacts when using all observables	110
9.9. Electron+jets: The pull mean and width and impacts when using all observables	111
9.10. Lepton+jets: The pull mean and width and impacts when using all observables	111
9.11. Blinded measured top quark mass when using quadratic parameterized fsr_*_muR nuisances	114
9.12. m_W^{reco} PDF for muon+jets	115
9.13. The FSR closure on muon+jets simulation using all observables	115
9.14. The fsr_Q2QG_muR closure on muon+jets simulation using all observables	116
9.15. Measurement of fsr_Q2QG_muR with different observable selections	117

9.16. Measurement of m_t in different channels, sets of observables and assumed correlation between the FSR PS scales 118

9.17. Lepton+jets 5D: Measurement of m_t with nuisance impacts and pulls 121

9.18. Comparison of the result to other measurements 122

List of Tables

2.1. Combinatoric branching ratios for all top quark pair decay modes in dependence of the W boson decays.	11
2.2. The top quark mass in the MSR scheme at different scales	13
2.3. Central values and uncertainties of the calibration for m^{MC} into theoretical mass schemes	14
3.1. LHC parameters	24
6.1. Single lepton data sets for RunII data at 13 TeV recorded in 2016.	43
6.2. Result of the fit to the top-quark mass dependence for the $t\bar{t}$ cross sections .	44
6.3. Simulation samples: signal and background	46
6.4. Simulation samples: QCD background	47
6.5. Simulation samples: systematic uncertainty variations	48
6.6. Muon+Jets event yields and fractions	62
6.7. Electron+Jets event yields and fractions	65
6.8. Final state permutation fractions.	65
6.9. Final selection $t\bar{t}$ decay channel fractions.	66
7.1. JER data/simulation scale factors	69

8.1. Lepton+jets: Correlation factor between all one-on-one combinations of the observable.	78
8.2. Bin Edges of the binned templates.	84
8.3. Used fixed constants of the parameterization	84
8.4. Response difference for different flavored jets caused by a $\pm 1\sigma$ variation of different uncertainties.	96
8.5. Estimation of the nuisance values for $\pm 1\sigma$ variation of different uncertainties using the response distributions.	96
9.1. Minimum likelihood values	112
9.2. Comparison of the uncertainty sources in the previous CMS measurement .	124

Acknowledgments

On hot summer days a few hours before handing in the thesis there is not much creativity and expression left for a proper acknowledgement of everyone who made my way to this thesis easier, better and more pleasant. First and foremost I want to thank my parents and my wife for the years of support. My parents especially for supporting and encouraging my academic studies as well as my music. And my wife for all her love and endurance during some of the more stressful weeks of the last years.

All this work would not be possible without my Professor Peter Schleper and the whole work group. Thank you everybody that I could join you starting with my Bachelor thesis. I cant name everyone who was part of the good time in the group and I want to especially point out Hartmut Stadie who I worked closely with on the topic of my Master and this PhD thesis and Torben Lange and Johannes Lange who were for the longest time my office colleges.

Thank you to everyone who proof-read parts of this documents.

And to the good friends of the last years, especially Mike Schipp and Lion Mohnke.

Prost to everyone I should have mentioned but missed, I owe you a beer!

Further I like to thank Andreas Meyer for certificating this thesis on short notice and all members of my defence committee.

Eidesstattliche Versicherung / Declaration on oath

Hiermit versichere ich an Eides statt, die vorliegende Dissertationsschrift selbst verfasst und keine anderen als die angegebenen Hilfsmittel und Quellen benutzt zu haben. Die eingereichte schriftliche Fassung entspricht der auf dem elektronischen Speichermedium. Die Dissertation wurde in der vorgelegten oder einer ähnlichen Form nicht schon einmal in einem früheren Promotionsverfahren angenommen oder als ungenügend beurteilt.

Ort, Datum

Unterschrift Christoph Garbers